



THE HONG KONG
POLYTECHNIC UNIVERSITY

香港理工大學

Pao Yue-kong Library

包玉剛圖書館

Copyright Undertaking

This thesis is protected by copyright, with all rights reserved.

By reading and using the thesis, the reader understands and agrees to the following terms:

1. The reader will abide by the rules and legal ordinances governing copyright regarding the use of the thesis.
2. The reader will use the thesis for the purpose of research or private study only and not for distribution or further reproduction or any other purpose.
3. The reader agrees to indemnify and hold the University harmless from and against any loss, damage, cost, liability or expenses arising from copyright infringement or unauthorized usage.

IMPORTANT

If you have reasons to believe that any materials in this thesis are deemed not suitable to be distributed in this form, or a copyright owner having difficulty with the material being included in our database, please contact lbsys@polyu.edu.hk providing details. The Library will look into your claim and consider taking remedial action upon receipt of the written requests.

**A STUDY OF VIBRATION BEHAVIOUR OF
WEFT-KNITTED SPACER FABRICS**

CHEN FUXING

Ph.D

The Hong Kong Polytechnic University

2016

THE HONG KONG POLYTECHNIC UNIVERSITY

INSTITUTE OF TEXTILES AND CLOTHING

**A STUDY OF VIBRATION BEHAVIOUR OF
WEFT-KNITTED SPACER FABRICS**

Chen Fuxing

**A thesis submitted in partial fulfilment of the requirements for the
degree of Doctor of Philosophy**

May 2015

CERTIFICATE OF ORIGINALITY

I hereby declare that this thesis is my own work and that, to the best of my knowledge and belief, it reproduces no material previously published or written, nor material that has been accepted for the award of any other degree or diploma, except where due acknowledgement has been made in the text.

_____ (Signed)

_____ CHEN Fuxing _____ (Name of student)

To my family

Abstract

Weft-knitted spacer fabrics are textile structures commonly consisting of two outer layers that are connected by spacer yarns. As a potential substitute for traditional foams in anti-vibration applications such as gloves and cushion pads, they are superior in terms of air permeability and thermoregulation. In former studies, spacer fabric with top-loaded mass was simply treated as a one-degree-of-freedom mass-spring-damper system. However, due to the nonlinear elastic force of spacer fabric, linear vibration models are only valid for very small excitation levels. To investigate its vibration performance under large excitations, nonlinear force-displacement relationship is considered in building the equation of motion, where models containing the symmetric elastic force and the asymmetric elastic force are compared. Besides, the viscoelasticity of spacer fabric is represented by a fractional derivative term.

This study follows a procedure as below. Firstly, weft-knitted spacer fabrics with structural variations are manufactured. Secondly, forced vibration experiments are carried out under different excitation levels and load mass. Thirdly, theoretical models concerned with the nonlinear elastic force-displacement relationship and the viscoelasticity of spacer fabric are established, and then model parameters are identified by fitting models with experimental results. Fourthly, the effects of model parameters on frequency response curves are analysed. Moreover, numerical simulations are also presented for solving the periodic solutions and the aperiodic solutions.

Weft-knitted spacer fabrics were firstly knitted on a STOLL CMS 822 computerized flat knitting machine of gauge 14. Polyester monofilaments tucked alternately on two outer layers, forming a convoluted structure. The difference in fabric structure was achieved by varying the tucking distance of monofilaments, and thus two fabric structures were obtained. Two identical fabrics were laminated into one sample in order to balance the transverse shift of fabric under vertical force.

In vibration experiments, sine sweep tests were carried out using an electromagnetic vibration exciter to record the acceleration transmissibility curves of the mass-spacer fabric systems. The influences of load mass, fabric structure and excitation level were studied. Results show that increasing the weight of load mass initially shifted the resonance frequency to lower values but then it rose again. Thicker spacer fabric exhibits better force isolation performance. It was also revealed that with a light load mass, increasing the vibration level could give rise to a nonlinear softening type of transmissibility curve, and a broadened isolation region could also be achieved.

To build the equation of motion under forced harmonic vibration, nonlinear stiffness terms were applied. Phenomenological models with the symmetric elastic force and with the asymmetric elastic force were studied separately. The major difference lies in the quadratic stiffness term which breaks symmetry in the elastic force-displacement relationship. Besides, viscoelasticity was expressed as a fractional derivative term in both models. The frequency-domain solutions to the equations of motion were obtained using harmonic balance method (HBM) with the first-order approximation. The effects of model

parameters on the transmissibility and amplitude-frequency curves were analysed.

Next, model parameters were identified by fitting theoretical models with experimental results. Root mean square error (RMSE) was adopted as the indicator of goodness of fit. Issues including the highest-order stiffness coefficient, the physical significance of the fractional order and the model redundancy were discussed. RMSEs using the symmetric model and the asymmetric model were compared. Results showed that the asymmetric model performed slightly better than the symmetric model. Moreover, the fractional derivative term improved the goodness of fit to a certain extent.

Following parameter identification, MATLAB/Simulink block diagram was utilized to obtain periodic solutions of the equation of motion. The difference in the frequency response curves between using numerical simulation and the HBM approximation was explained. Besides, bifurcation and chaotic motions are also observed numerically with varied conditions.

In brief, the vibration behavior of weft-knitted spacer fabric has been explored with the use of experimental, analytical and numerical methods. Nonlinear softening phenomenon is correlated with the polynomial force-displacement relationship. And the fractional derivative term is used to account for the viscoelasticity in the system. This study provides a better understanding of the vibration behavior of weft-knitted spacer fabric, and experimental data benefiting applied research in the future.

List of Publications Arising from the Thesis

Refereed Journal Papers

1. Fuxing Chen, Hong Hu and Yanping Liu. Development of Weft-Knitted Spacer Fabrics with Negative Stiffness Effect in a Special Range of Compression Displacement. *Textile Research Journal*. 2015; 85: 1720–31.
2. Fuxing Chen, Hong Hu. An Experimental Study on Vibration Isolation Performance of Weft-Knitted Spacer Fabrics. *Textile Research Journal*. In press.
3. Fuxing Chen, Hong Hu. Mathematical Modeling of the Vibration Behavior of Weft-Knitted Spacer Fabrics under Harmonic Excitation. *Applied Mathematical Modelling*. Manuscript under review.

Refereed Conference Papers

1. Fuxing Chen, Hong Hu and Lai Xu. Vibration Isolation Properties of Weft-Knitted Spacer Fabrics. *The Fiber Society 2013 Spring Conference*, Geelong, Australia, May 22–24.
2. Fuxing Chen, Hong Hu. Monofilament Morphology in the Weft-Knitted Spacer Fabric. *The 1st International Conference on Digital Technologies for the Textile Industries*, Manchester, UK, September 5-6, 2013.
3. Fuxing Chen, Yanping Liu and Hong Hu. Vibration Isolation Behavior of 3D Spacer Knitted Fabrics. *The 43rd Textile Research Symposium*, Christchurch, New Zealand, December 2-3, 2014.

Acknowledgements

First and foremost, I am deeply indebted to my chief supervisor, Prof. Hu Hong, to whom goes my deepest gratitude for offering me this research opportunity, for his invaluable guidance and greatest patience at every step of my development on this study.

Thank the lab technicians in the Institute of Textiles and Clothing, Dr. Zhou Jinyun, Mr. Chu W. M., Ms. Sun M. N., Mr. Hui Kevin, Mr. Choi K. O., and especially Ms. Liu Su, for their generous help in conducting experiments. And special thanks to my internal examiner Dr. Xu Bingang, and my external examiners Prof. Wang Lu and Prof. Wang Youjiang for their precious comments and suggestions in many aspects of this study.

My thanks are extended to Dr. Xiao Zhenlong, Dr. Qiu Canxing, Dr. Feng Weiqiang, Dr. Du Wei, Dr. Huang Xinxin, and especially Dr. Liu Yanping, for their help when I came across difficulties during research. These fragments of memories are treasures to me. Thanks also go to my friends, Dr. Luo Yimo, Dr. Kim Ken Ri, Xu Lai, and my colleagues, Dr. Ge Zhaoyang, Dr. Hou Xiaonan, Dr. Wang Zhengyue, Jiang Lili, Yang Yadie and countless others for being my companions, whose virtues have long inspired me. Also thank the funding support from the Research Grants Council of HK Special Administrative Region Government (Grant No. 516011).

Lastly, words can never express how grateful I am to my parents, my brother and my husband. It is their support, sacrifices and unconditional love that has sustained me thus far.

Table of Contents

ABSTRACT	I
LIST OF PUBLICATIONS ARISING FROM THE THESIS	IV
ACKNOWLEDGEMENTS	V
TABLE OF CONTENTS	VI
LIST OF FIGURES.....	X
LIST OF TABLES.....	XVII
NOMENCLATURE	XVIII
CHAPTER 1 INTRODUCTION	1
1.1 Motivations	1
1.2 Objectives.....	6
1.3 Methodology	7
1.4 Significance.....	10
1.5 Thesis outline	11
CHAPTER 2 LITERATURE REVIEW	14
2.1 Introduction.....	14
2.2 Knitted spacer fabrics.....	15
2.2.1 Types	15
2.2.2 Formation principles.....	16
2.2.3 Applications	19
2.2.4 Compression studies	20
2.2.5 Impact studies	27
2.3 HSLDS isolators.....	29
2.3.1 Euler column buckling.....	30
2.3.2 Negative stiffness mechanism	33
2.4 Helmholtz-Duffing equation	48
2.4.1 Duffing equation.....	48
2.4.2 Helmholtz-Duffing equation.....	52
2.4.3 Solutions to Helmholtz-Duffing equation.....	56

2.5 Fractional-order derivative	60
2.5.1 Definitions	61
2.5.2 Research approach	63
2.5.3 Duffing oscillator with fractional-order derivative.....	64
2.5.4 Helmholtz-Duffing oscillator with fractional-order derivative	65
2.6 Chapter summary	66
CHAPTER 3 EXPERIMENTAL DETAILS	68
3.1 Introduction	68
3.2 Fabric manufacture.....	68
3.2.1 Design idea	69
3.2.2 Structure optimization	70
3.2.3 Linking distance variation	74
3.2.4 Fabric lamination	78
3.3 Experimental setup and method	78
3.3.1 Test setup	79
3.3.2 Typical transmissibility curve.....	83
3.3.3 Sweep rate and direction.....	85
3.3.4 Material fatigue.....	88
3.4 Results and discussion.....	92
3.4.1 Effect of fabric thickness and load mass	92
3.4.2 Effect of excitation level.....	96
3.5 Chapter summary	99
CHAPTER 4 PARAMETER IDENTIFICATION BY CURVE FIT.....	100
4.1 Introduction	100
4.2 Approximate analytical models.....	100
4.2.1 Symmetric model with parameters $k k_3 k_5 k_7 c a \alpha$	100
4.2.2 Asymmetric model with parameters: $\beta \kappa k_3 c a \alpha$	103
4.2.3 Fitness function.....	107
4.2.4 Statistical indicator of the goodness of fit (RMSE).....	109
4.3 Results of data fitting	110
4.3.1 Excitation level	110

4.3.2 Load mass	123
4.4 Chapter summary	128
CHAPTER 5 PARAMETRIC ANALYSIS	129
5.1 Introduction	129
5.2 Symmetric model	129
5.2.1 Effect of excitation level G	135
5.2.2 Effect of viscous damping coefficient c	137
5.2.3 Effect of the fractional derivative term (a and α)	138
5.2.4 Effect of the linear stiffness k	139
5.2.5 Effect of the cubic stiffness k_3	141
5.2.6 Effect of the quintic stiffness k_5	142
5.3 Asymmetric model	143
5.3.1 Effect of the bias force β	151
5.3.2 Effect of the linear stiffness κ	153
5.3.3 Effect of the cubic stiffness k_3	156
5.4 Chapter summary	157
CHAPTER 6 NUMERICAL SIMULATION.....	160
6.1 Introduction	160
6.2 Periodic solutions	161
6.3 Model predictability	170
6.4 Bifurcation and chaotic motions	174
6.4.1 Bifurcation vs excitation frequency.....	175
6.4.2 Bifurcation vs excitation level	177
6.4.3 Bifurcation vs fractional order.....	181
6.5 Chapter summary	183
CHAPTER 7 CONCLUSIONS AND FUTURE WORK	184
7.1 Conclusions	184
7.1.1 Improved thickness of spacer fabric	185
7.1.2 Effects influencing the isolation performance	185
7.1.3 Improved performance of analytical model.....	186
7.1.4 Effects of nonlinear stiffness coefficients on frequency response curves	186

7.1.5 Bifurcation and chaotic behavior of the nonlinear system	187
7.2 Limitations	188
7.2.1 Model predictability.....	188
7.2.2 Phenomenological models	188
7.2.3 Fabric instability	189
7.2.4 Experiment condition.....	189
7.3 Recommendations for future work.....	190
7.3.1 Model improvement.....	190
7.3.2 Statistical analysis.....	190
7.3.3 Applied research	191
7.3.4 Time history	191
APPENDIXES	192
Introduction.....	192
Appendix 1 Frequency range.....	193
Appendix 2 Frequency step size	194
Appendix 3 Fitness function.....	196
Appendix 4 Optimization algorithm: least squares vs. jDE	200
Appendix 5 The initial value of the fractional order α	203
Appendix 6 The relative standard error (RSE)	206
REFERENCES.....	211

List of Figures

Figure 1.1 (a) Softening and hardening cubic nonlinearities cause resonance peak in the amplitude-frequency curve to bend to the left and to the right, respectively.	5
Figure 1.1 (b) The corresponding elastic force-displacement curves.	5
Figure 1.2 Flowchart of methodology in this study.	8
Figure 2.1 (a) Weft-knitted spacer fabric; (b) warp-knitted spacer fabric. ¹⁰	16
Figure 2.2 Machines for knitting weft-knitted spacer fabrics: (a) double circular knitting machine and (b) its dial and cylinder needle beds; (c) computerized flat knitting machine and (d) its front and back needle beds.	17
Figure 2.3 A schematic of Raschel knitting machine for producing warp-knitted spacer fabrics. ¹⁵	18
Figure 2.4 Transmissibility chart shows the Minus K isolation system can be 10-100 times better than the high-performance air table. ⁹³	34
Figure 2.5 Concept of a vertical-motion isolator by negative stiffness mechanism. ⁹⁴ ...	35
Figure 2.6 A schematic of vertical-motion isolator with means for accommodating changing weight loads. ⁹⁴	35
Figure 2.7 Concept of a horizontal-motion isolator by the “beam-column effect”. ⁹⁴	36
Figure 2.8 A schematic of horizontal-motion system with natural frequency independent of change in weight load. ⁹⁴	36
Figure 2.9 Schematic representation of the simplest system which can exhibit quasi-zero stiffness. ⁹⁸	39
Figure 2.10 Typical force-displacement characteristic of the isolator shown in Figure 2.9. ⁹⁸	39
Figure 2.11 Relationship of geometrical parameter γ and stiffness ratio α that yields QZS. ⁹⁸	40
Figure 2.12 A negative stiffness device for horizontal vibration isolation. ¹⁰³	42
Figure 2.13 (a) Model of a suspension seat and (b) a schematic of the proposed isolation system. ¹⁰⁴	43
Figure 2.14 Isolators with different types of negative stiffness systems. ¹⁰⁷	44

Figure 3.1 Design concept of weft-knitted spacer fabric structure: (a) before steaming treatment; (b) after steaming treatment.	70
Figure 3.2 Tuck patterns for constructing three candidate weft-knitted spacer fabrics: (a) Spacer-20f; (b) Spacer-20h; (c) Spacer-20h_var.	71
Figure 3.3 Tensile load vs. strain curves of three types of yarns used for knitting weft-knitted spacer fabrics.	72
Figure 3.4 Three candidate weft-knitted spacer fabrics in the course views: (a) Spacer-20f; (b) Spacer-20h; (c) Spacer-20h_var.	73
Figure 3.5 Fabric structures with different linking distance of spacer monofilaments: (a) Spacer-20h; (b) Spacer-12h.	74
Figure 3.6 Cross-sectional views of spacer fabrics produced: (a) and (c) Spacer-20h; (b) and (d) Spacer-12h.	75
Figure 3.7 Schematic of fabric structure with two identical fabrics laminated together: (a) before compression; (b) after compression.	78
Figure 3.8 Schematic of the vibration testing system.	80
Figure 3.9 Photo of the mass-spacer fabric system and the mounting of two accelerometers.	81
Figure 3.10 Amplitude-frequency curves for three excitation levels, 0.1g, 0.2g and 0.3g.	82
Figure 3.11 (a) Typical acceleration transmissibility curve and (b) the corresponding phase response curve for Spacer-12h under 0.3g excitation level and 2 kg load mass.	84
Figure 3.12 Effects of sweep rate and direction, where (b) is a magnified view of (a). .	87
Figure 3.13 Transmissibility curves for the forward sweep events (a) during the 1 st day and (b) during the 5 th day.	89
Figure 3.14 Transmissibility curves of (a) the 1 st sweep cycles and (b) the 10 th sweep cycles for five consecutive days.	90
Figure 3.15 Trends of (a) peak transmissibility and (b) resonance frequency for the forward sweep events (in solid lines) and the backward sweep events (in dashed lines) during each of five consecutive days.	91
Figure 3.16 (a) and (b) Transmissibility curves under 0.1g excitation level with load mass varied; (c) Variation of f_r and f_c with load mass.	94

Figure 3.17 Quasi-static compression curves (solid lines ‘—’) and stiffness curves k_s (dashed lines ‘- -’) of spacer fabrics..... 96

Figure 3.18 (a) and (b) Transmissibility curves under 2 kg load mass with excitation level varied; (c) Variation of f_r and f_c with load mass..... 98

Figure 4.1 Fitting results using the symmetric model with parameters $k, k_3, k_5, c, a, \alpha$ and the one with parameters k, k_3, c, a, α for the conditions of 2 kg load mass and: (a) and (d) 0.1g; (b) and (e) 0.2g; (c) and (f) 0.3g excitation level using Spacer-12h. 112

Figure 4.2 Fitting results using the symmetric model with parameters k, k_3, k_5, c and the one with parameters k, k_3, k_5, a, α for the conditions of 2 kg load mass and: (a) and (d) 0.1g; (b) and (e) 0.2g; (c) and (f) 0.3g excitation level using Spacer-12h. 113

Figure 4.3 Summary of RMSEs from curve fits using four variants of symmetric models. 115

Figure 4.4 Fitting results using the asymmetric model with parameters $\beta, \kappa, k_3, c, a, \alpha$, the one with parameters $\beta, \kappa, k_3, a, \alpha$ and the one with parameters β, κ, k_3, c for conditions of 2 kg load mass and: (a), (d) and (g) 0.1g; (b), (e) and (h) 0.2g; (c), (f) and (i) 0.3g excitation level using Spacer-12h. 117

Figure 4.5 Summary of RMSEs from curve fits using three variants of asymmetric models. 119

Figure 4.6 Comparison of RMSEs by asymmetric vs. symmetric models. 120

Figure 4.7 Reconstructed elastic force-displacement curves using fitted parameters under 0.1-0.3g excitation levels and 2 kg load mass for Spacer-12h: (a) the asymmetric model with parameters β, κ, k_3, c ; (b) the symmetric model with parameters k, k_3, k_5, c 122

Figure 4.8 Comparison of RMSEs for six model structures for the conditions of 1-5 kg load mass and 0.1g excitation level..... 123

Figure 4.9 Fitting using the symmetric model $k, k_3, k_5, c, a, \alpha$ for the conditions of 0.1g excitation level and the mass of: (a) 1 kg; (b) 2 kg; (c) 3 kg; (d) 4 kg; (e) 5 kg; and (f) is a

summary.	124
Figure 4.10 Fitting using the symmetric model k, k_3, k_5, c for the conditions of 0.1g excitation level and the mass of: (a) 1 kg; (b) 2 kg; (c) 3 kg; (d) 4 kg; (e) 5 kg; and (f) is a summary.	125
Figure 4.11 Fitting using the asymmetric model $\beta, \kappa, k_3, c, a, \alpha$ for the conditions of 0.1g excitation level and the mass of: (a) 1 kg; (b) 2 kg; (c) 3 kg; (d) 4 kg; (e) 5 kg; and (f) is a summary.	126
Figure 4.12 Fitting using the asymmetric model β, κ, k_3, c for the conditions of 0.1g excitation level and the mass of: (a) 1 kg; (b) 2 kg; (c) 3 kg; (d) 4 kg; (e) 5 kg, and (f) is a summary.	127
Figure 5.1 Effect of excitation level G on (a) harmonic amplitude $2 A $ vs. excitation frequency response and (b) acceleration transmissibility T	136
Figure 5.2 Effect of viscous damping coefficient c on (a) harmonic amplitude $2 A $ vs. excitation frequency response and (b) acceleration transmissibility T	137
Figure 5.3 Effect of fractional derivative order α on (a) harmonic amplitude $2 A $ vs. excitation frequency response and (b) acceleration transmissibility T	138
Figure 5.4 Effect of fractional derivative coefficient a on (a) harmonic amplitude $2 A $ vs. excitation frequency response and (b) acceleration transmissibility T	139
Figure 5.5 Effect of linear stiffness k on (a) harmonic amplitude $2 A $, (b) acceleration transmissibility T and (c) elastic force $kx + k_3x^3 + k_5x^5$	140
Figure 5.6 Effect of cubic stiffness k_3 on (a) harmonic amplitude $2 A $, (b) acceleration transmissibility T and (c) elastic force $kx + k_3x^3 + k_5x^5$	141
Figure 5.7 Effect of quintic stiffness k_5 on (a) harmonic amplitude $2 A $, (b) acceleration transmissibility T and (c) elastic force $kx + k_3x^3 + k_5x^5$	143
Figure 5.8 (a) Reconstructed elastic force-displacement curve $\kappa X + k_3X^3$ using fitted	

parameters of the model with parameters β, κ, k_3, c under 0.1g excitation level; (b) Converted into the compression force vs. compression displacement curve..... 151

Figure 5.9 Effect of bias force β on (a) static displacement $A_0 - \delta$, (b) harmonic amplitude $2|A|$, (c) acceleration transmissibility T and (d) elastic force $\kappa X + k_3 X^3$ 153

Figure 5.10 Effect of linear stiffness κ on (a) static displacement $A_0 - \delta$, (b) harmonic amplitude $2|A|$, (c) acceleration transmissibility T and (d) elastic force $\kappa X + k_3 X^3$ 155

Figure 5.11 Effect of cubic stiffness k_3 on (a) static displacement $A_0 - \delta$, (b) harmonic amplitude $2|A|$, (c) acceleration transmissibility T and (d) elastic force $\kappa X + k_3 X^3$ 157

Figure 6.1 MATLAB/Simulink block diagram, with the Oustaloup filter ^{151, 152} implemented for the approximation of the fractional derivative operator. 161

Figure 6.2 Numerical result ('+') in comparison with the experimental data ('o') and the HBM approximation ('•') using the asymmetric model with parameters β, κ, k_3, c : (a) static displacement; (b) harmonic amplitude. 164

Figure 6.3 Numerical result ('+') in comparison with the experimental data ('o') and the HBM approximation ('•') using the asymmetric model with parameters $\beta, \kappa, k_3, c, a, \alpha$: (a) static displacement; (b) harmonic amplitude. 165

Figure 6.4 Numerical result ('+') in comparison with the experimental data ('o') and the HBM approximation ('•') of harmonic amplitude using (a) the symmetric model with parameters k, k_3, k_5, c ; (b) the symmetric model with parameters $k, k_3, k_5, c, a, \alpha$ 166

Figure 6.5 Time series, phase portrait and Fourier amplitude spectrum for the dynamic displacement of spacer fabric using the asymmetric model with parameters β, κ, k_3, c 168

Figure 6.6 Time series, phase portrait and Fourier amplitude spectrum for the dynamic

displacement of spacer fabric using the symmetric model with parameters k, k_3, k_5, c .
..... 169

Figure 6.7 Numerical predictions ('+') and approximate analytical predictions ('•') for the other two excitation levels using the symmetric model with parameters $k, k_3, k_5, c, a, \alpha$ identified by fitting with experimental data ('o') of (a) the 0.1g excitation level; (b) the 0.2g excitation level; (c) the 0.3g excitation level. 172

Figure 6.8 Numerical predictions ('+') and approximate analytical predictions ('•') for the other two excitation levels using the asymmetric model with parameters $\beta, \kappa, k_3, c, a, \alpha$ identified by fitting with experimental data ('o') of (a) the 0.1g excitation level; (b) the 0.2g excitation level; (c) the 0.3g excitation level. 174

Figure 6.9 Bifurcation diagram with respect to excitation frequency under different excitation levels: (a) 0.1g; (b) 0.4g; (c) 0.6g; (d) 1.0g. 176

Figure 6.10 Time series, phase portrait, Poincaré map and Fourier amplitude spectrum for the dynamic displacement of spacer fabric using the asymmetric model with parameters β, κ, k_3, c , under the excitation frequency and the excitation level of: (a) 30 Hz, 0.6g; (b) 35 Hz, 0.6g; (c) 30 Hz, 1.0g; (d) 35 Hz, 1.0g. 177

Figure 6.11 Bifurcation diagram with respect to excitation level under different excitation frequencies: (a) 25 Hz; (b) 35 Hz; (c) 40 Hz; (d) 50 Hz. 179

Figure 6.12 Magnified bifurcation diagram in Figure 6.11(c) regarding excitation level under 40 Hz excitation frequency, showing period doubling bifurcation cascade to chaos. 179

Figure 6.13 Time series, phase portrait, Poincaré map and Fourier amplitude spectrum for the dynamic displacement of spacer fabric using the asymmetric model with parameters β, κ, k_3, c , under 40 Hz excitation frequency and the excitation level is: (a) 0.10g; (b) 1.00g; (c) 1.10g; (d) 1.25g; (e) 1.28g; (f) 1.35g. 180

Figure 6.14 Bifurcation diagram with respect to the fractional order under 1.35g excitation level and 40 Hz excitation frequency when the coefficient of the fractional derivative term α is: (a) 5; (b) 10; (c) 20; (d) 40. 182

Figure A.1 Effect of frequency range on the RMSE using the model with parameters $k, k_3, k_5, c, a, \alpha$	194
Figure A.2 Effect of frequency step size on the RMSE using the model with parameters $k, k_3, k_5, c, a, \alpha$	196
Figure A.3 Fitness function Type I for the asymmetric model $\beta, \kappa, k_3, c, a, \alpha$ with weighing factor: (a) $u = -1$; (b) $u = 0$; (c) $u = 1$	198
Figure A.4 Fitness function Type II for the asymmetric model $\beta, \kappa, k_3, c, a, \alpha$ with weighing factor: (a) $d = -1$; (b) $d = 0$; (c) $d = 1$	198
Figure A.5 Fitness function Type I for the symmetric model $k, k_3, k_5, c, a, \alpha$ with weighing factor: (a) $u = -1$; (b) $u = 0$; (c) $u = 1$	199
Figure A.6 Fitness function Type II for the symmetric model $k, k_3, k_5, c, a, \alpha$ with weighing factor: (a) $d = -1$; (b) $d = 0$; (c) $d = 1$	199
Figure A.7 RMSEs obtained by two algorithms.	202
Figure A.8 RMSE depends on the initial value of α : (a) $\alpha_0 = 0.1$; (b) $\alpha_0 = 0.2$; (c) $\alpha_0 = 0.4$; (d) $\alpha_0 = 0.5$; (e) $\alpha_0 = 0.8$; (f) $\alpha_0 = 1.0$	205
Figure A.9 RMSE and RSEs obtained using (a) the model with parameters $k, k_3, k_5, c, a, \alpha$; (b) the model with parameters k, k_3, k_5, c ; (c) the model with parameters k, k_3, k_5, a, α , for the 0.1g excitation level condition.	208
Figure A.10 RMSE and RSEs obtained using (a) the model with parameters $k, k_3, k_5, c, a, \alpha$; (b) the model with parameters k, k_3, k_5, c ; (c) the model with parameters k, k_3, k_5, a, α , for the 0.2g excitation level condition.	209
Figure A.11 RMSE and RSEs obtained using (a) the model with parameters $k, k_3, k_5, c, a, \alpha$; (b) the model with parameters k, k_3, k_5, c ; (c) the model with parameters k, k_3, k_5, a, α , for the 0.3g excitation level condition.	210

List of Tables

Table 2.1 An overview of the properties and performances of four types of negative stiffness systems.....	46
Table 3.1 Fabric basic properties.....	74
Table 3.2 Basic dimensional properties of two weft-knitted spacer fabrics with different linking distances.....	77
Table 3.3 k_d values of mass-spacer fabric system for a fixed excitation level at 0.1g...	96
Table 5.1 Parameter estimates by curve fit using the symmetric model.	134
Table 5.2 Parameter estimates by curve fit using the asymmetric model.	148
Table 6.1 Unit conversion: $1g = 9.81 \text{ m/s}^2$. The 1g is one gravitational acceleration.	181
Table A.1 Nine candidate frequency step sizes.	195
Table A.2 The goodness of fit (RMSEs) using different fitness functions.....	200
Table A.3 Comparison of the jDE algorithm and the method of least squares.	201

Nomenclature

T	acceleration transmissibility
T_{\max}	peak acceleration transmissibility
ϕ	phase angle
f_r	resonance frequency
f_c	crossover frequency
k_d	dynamic stiffness
k_s	static stiffness
m	load mass
G	magnitude of acceleration by the forced excitation
g	one gravitational acceleration
c	viscous damping coefficient
a	fractional derivative coefficient
α	fractional derivative order
x	dynamic change of the thickness of the laminated spacer fabric
\dot{x}	velocity
\ddot{x}	acceleration
x_0	initial displacement
\dot{x}_0	initial velocity
k	linear stiffness coefficient, tangent stiffness at the statically-loaded position
k_3	cubic stiffness coefficient
k_5	quintic stiffness coefficient
k_7	seventh-order stiffness coefficient
ω	angular frequency
t	time

A	one half of the harmonic displacement, a complex number
A_r	real part of A
A_i	imaginary part of A
\bar{A}	complex conjugate of A
$2 A $	harmonic amplitude
k_2	quadratic stiffness coefficient
κ	tangent stiffness at the center of symmetry of the elastic force
β	bias force
z	new coordinate generated due to coordinate transformation
δ	intermediate parameter generated due to coordinate transformation, $\delta = z - x$
A_0	static displacement
$A_0 - \delta$	new static displacement, the offset distance from the statically-loaded position to the center of oscillation
f_t	transmitted force
f_{t1}	harmonic amplitude of the transmitted force
f_{t0}	static component of the transmitted force
ϕ_t	phase angle of the transmitted force
Ω	driving frequency
peak _h	harmonic amplitude in the Fourier amplitude spectrum
peak _s	absolute value of the static displacement in the Fourier amplitude spectrum
$ X(f) $	Fourier amplitude

CHAPTER 1 INTRODUCTION

1.1 Motivations

Weft-knitted spacer fabric consists of two outer layers connected by spacer yarns. The outer layer can be regular weft-knitted structures, and the connecting yarns enable the tuck stitches to form a spacer layer. It provides excellent thermophysiological comfort due to its superior air permeability and thermoregulation. Besides, the outer layer structure, the spatial structure of spacer yarns and materials used can be readily changed during knitting. Thus, weft-knitted spacer fabric can adapt to the requirements of various mechanical properties. Due to its versatility and thermal comfort, it is made into various products such as compression bandages that prevent chronic leg ulcers.

In the similar context, it shows rising potentials in anti-vibration applications. Compared with regular passive vibration isolation materials such as rubber and polyurethane foams, weft-knitted spacer fabric is more suitable for uses that contact with human body. Different parts of the human body are sensitive to vibrations of different frequency components. To buffer sportive and occupational vibrations, spacer fabric can be made into knee braces, shoe materials, vehicle seats and anti-vibration gloves. For instance, for drillers working with electrical and pneumatic power tools, hand arm vibration syndrome (HAVS) such as pains and loss of strength in the joints and the vibration white finger (VWF) can occur in consequence of exposure to vibrations containing harmful

frequencies. Wearing anti-vibration gloves helps reduce the magnitude of vibration exposure so as to avoid occupational diseases.

There are a few studies on the vibration behaviors of knitted spacer fabrics, and most of them are concerned with free vibrations under impact force. For instance, Arabzadeh et al. ¹ built mathematical models for the free vibration of multi-layer warp-knitted spacer fabrics under impact. They found that decreasing the fineness and length of monofilaments and increasing their density will increase the transmitted force. Blaga et al. ^{2,3} used impact tests to study the dynamic response of weft-knitted and warp-knitted spacer fabrics regarding transmissibility curves in different fabric directions. Liu and Hu ⁴ studied the vibration isolation properties of warp-knitted spacer fabric top-loaded with mass, and found that the natural frequency measured by vibration test matched with the quasi-static compression curve. In these studies, spacer fabric with top-loaded mass was simply treated as a linear mass-spring-damper system. The same authors ⁵ also progressed the study by experimentally investigating the vibration isolation properties of different warp-knitted spacer fabrics top-loaded with varied masses under harmonic excitation by considering the spacer monofilaments as Euler springs, and found that a thicker fabric has better vibration isolation performance due to lower resonant and isolation frequencies.

Nevertheless, the linear mechanism only applies to the elastic force of weft-knitted spacer fabric for very small displacements. The linear vibration model loses its validity when the excitation force F is large. In fact, nonlinear mechanical behavior is a common phenomenon for many materials and systems, especially for the polymeric materials. The

nonlinear elastic force-displacement relationship for polymeric materials has been extensively studied. For instance, the LS model ⁶ divides the typical compression stress-strain response of polymer foam into three regions, elastic region, collapse region and densification region. Other models include the tangent function model ⁷ and the polynomial models of various types. These complex models are quite suitable for describing the quasi-static compression behavior of material. Nonlinear elastic force needs also to be taken in account in building the equation of motion under forced vibration. The topic of nonlinear vibration is not new, which has been studied widely for the design and optimization of nonlinear isolators that have a better performance in vibration isolation, as compared with the linear equivalent isolators. These nonlinear isolators include negative stiffness systems and buckled beams that exhibit high-static-low-dynamic stiffness, which will be reviewed in detail in Chapter 2.

For a linear system under harmonic excitation, the equation of motion has the form of

$$m\ddot{x} + c\dot{x} + kx = F\cos\omega t, \quad (1.1)$$

where c is the viscous damping coefficient, k is the linear stiffness coefficient, F is the excitation force, and ω is the driving angular frequency. The resonance frequency f_r of this system is

$$f_r = \frac{1}{2\pi} \sqrt{\frac{k}{m}}. \quad (1.2)$$

Assuming $m = c = F = 1$ and $k = 20$ in Equation (1.1), the black curve in Figure 1.1(a) illustrates the amplitude-frequency relationship for this linear mass-spring-damper system.

The resonance frequency f_r is 0.71, according to Equation (1.2). Vibration is amplified

at resonance and attenuated at higher frequencies. In fact, high frequency components are relatively easy to isolate, while low frequency components are relatively difficult to isolate. Thus, vibration isolation in the low frequency range calls for more attention. Figure 1.1(b) gives the corresponding elastic force-displacement curve of this linear system as shown also in black, which is obviously a straight line.

On the other hand, two examples of force nonlinearities are shown in Figure 1.1(b) in red and blue, assuming the absolute value of the cubic stiffness coefficient $|k_3|=100$. In a softening nonlinear system, the elastic force becomes $kx - |k_3|x^3$. The corresponding resonance peak of the amplitude-frequency curve deviates from the linear resonance peak and bends to the left, as shown in Figure 1.1(a) in red. In contrast, in a hardening nonlinear system, the elastic force becomes $kx + |k_3|x^3$. The corresponding resonance peak of the amplitude-frequency curve deviates from the linear resonance peak and bends to the right, as shown in Figure 1.1(a) in blue. The peak amplitudes for the three systems are different. The nonlinear system with softening elastic force exhibits the largest peak amplitude while the nonlinear system with hardening elastic force exhibits the smallest peak amplitude, which can be explained by the largest overall stiffness in a hardening system.

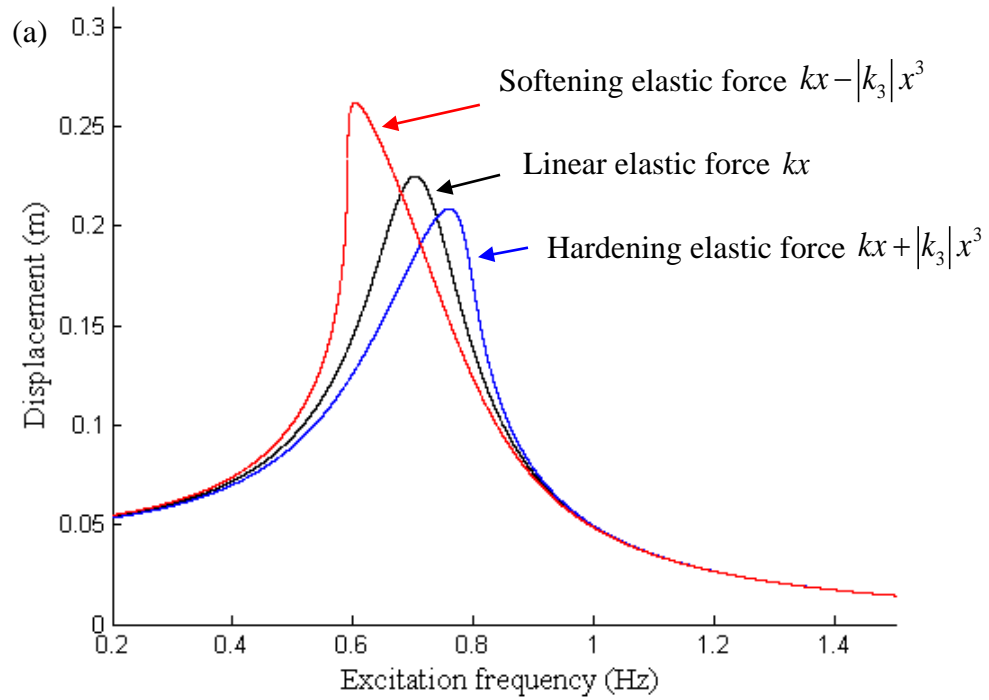


Figure 1.1 (a) Softening and hardening cubic nonlinearities cause resonance peak in the amplitude-frequency curve to bend to the left and to the right, respectively.

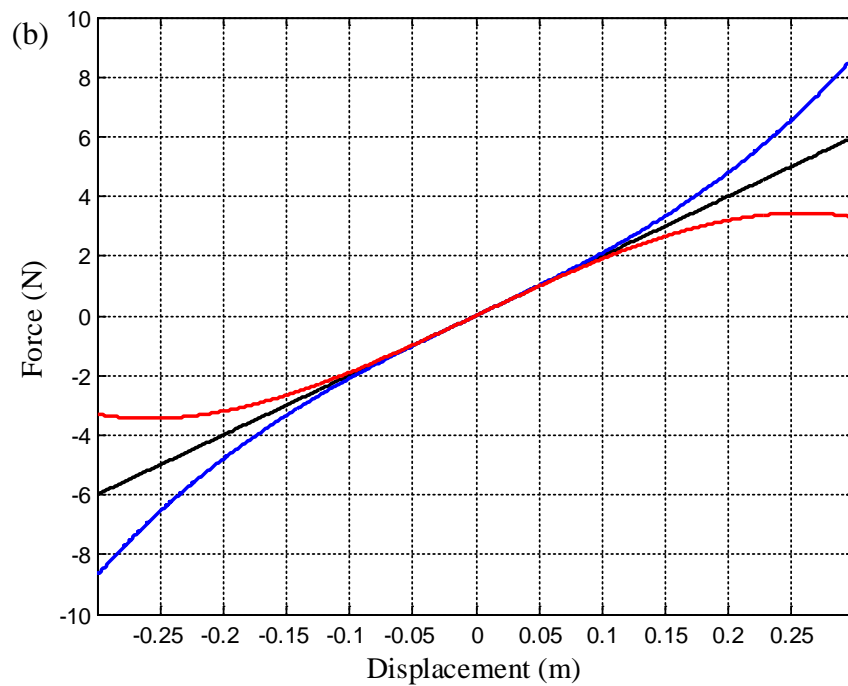


Figure 1.1 (b) The corresponding elastic force-displacement curves.

It is visible that the vibration behavior of weft-knitted spacer fabric is also nonlinear due to the nonlinearity of its elastic force. However, such phenomenon may not receive great attention. This study attempts to investigate the nonlinear response of weft-knitted spacer fabric under forced harmonic vibration. The vibration behavior of weft-knitted spacer fabric is closely related with fabric structure. Besides nonlinear elastic force, the time-dependent property of polymeric materials should be considered as well. For this, Deng et al.^{8,9} have used the hereditary model and the fractional derivative model for flexible polyurethane foam. In this study, the fractional derivative term will be adopted to represent the viscoelasticity of spacer fabric.

1.2 Objectives

This study attempts to fill the gap in the area of nonlinear vibration of the weft-knitted spacer fabric. Hopefully, the vibration isolation properties of knitted spacer fabric can be employed to protect the human body from vibration hazards in the environment. In brief, this study aims (i) to experimentally reveal how fabric structure and excitation conditions affect frequency responses; (ii) to build models that describe the vibration behavior of weft-knitted spacer fabric properly; and (iii) to explore its nonlinear vibration behavior both analytically and numerically. The objectives of this study are presented as follows.

- (1) To realize relatively thick weft-knitted spacer fabrics using electronic flatbed knitting machine. It is beneficial to increase its thickness as it achieves smaller dynamic stiffness during vibration. Thus, the resonance frequency of the mass-spacer fabric system can be reduced, and vibration isolation covers a wider range of frequencies;

- (2) To set up suitable and reliable experimental procedures for characterizing the vibration behaviors of weft-knitted spacer fabrics with fabric structure, excitation force and loaded mass varied;
- (3) To build analytical models that well describe periodic responses of the mass-spacer fabric system under harmonic excitation, and to find out how each model parameter affects the vibration behavior of the system. As it is known, weft-knitted spacer fabric has the properties of nonlinear elastic force and viscoelasticity. Hence, the linear mass-spring-damper model with one linear stiffness term is only suitable for very small excitation forces. To account for the two abovementioned properties under various excitation forces, this study attempts to use the polynomial elastic force-displacement relationship and the fractional-order derivative to describe the vibration behavior of weft-knitted spacer fabrics;
- (4) To determine suitable polynomial force-displacement relationship that better describes the vibration behavior of the system analytically;
- (5) To confirm the validity of approximate analytical solutions by numerical simulations for the periodic responses;
- (6) And, to predict the bifurcation and chaotic behaviors of the system by numerical method under different excitation frequency and excitation force conditions.

1.3 Methodology

Experimental, analytical and numerical approaches were used to investigate the steady-state responses of the mass-spacer fabric system under harmonic excitation in this study.

The methodology used is schematically shown in Figure 1.2.

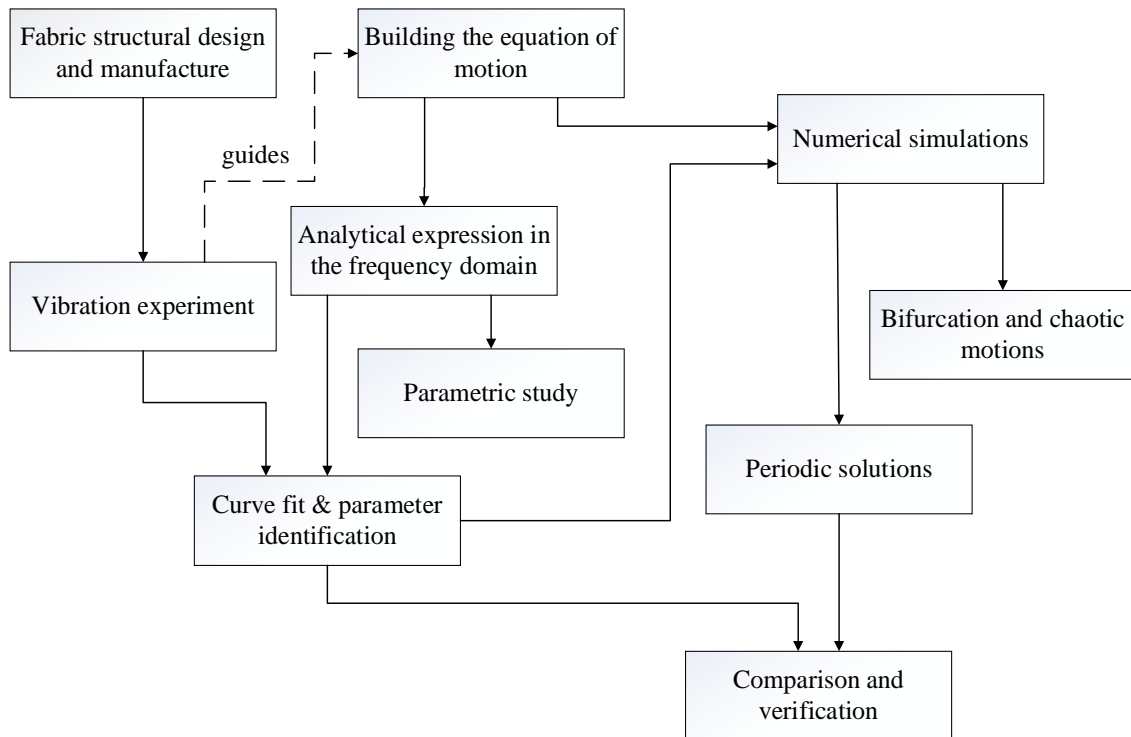


Figure 1.2 Flowchart of methodology in this study.

The three approaches were employed not in parallel but in a crosslinking and hierarchical manner. On the first level of the hierarchy, weft-knitted spacer fabrics were designed, manufactured and tested for their vibration responses under forced harmonic excitation. On the second level, based on the observation of nonlinear frequency responses, the dynamic equation of motion in the time domain was built with unknown model parameters. Then, the analytical expression in the frequency domain was derived. Curve fit between analytical model and experimental data was performed to identify model parameters. On the third level, parameter analysis was carried out to study the effect of each model parameter on the vibration behavior of the system. On the fourth level, with the equation

of motion in the time domain and model parameters identified, numerical simulation was carried out to obtain periodic solutions for the system. On the last level, frequency response curves (FRCs) by analytical and numerical methods were compared. Numerical solutions confirmed the validity of analytical solutions. Above mentioned are all the levels concerned with the periodic motions of the system. Additionally, the bifurcation and chaotic motions of the system, although not observed experimentally, were also studied using numerical method.

One advantage of the analytical method lies in that the underlying mechanism of how material and structural properties influence the vibration behavior of the system is reflected by model parameters including stiffness and damping coefficients. It is also noted that experimental, analytical and numerical results cannot be exactly the same. The discrepancies between experimental and analytical results come from fitting errors, and the discrepancies between analytical and numerical solutions come from the approximation of analytical solutions and the numerical errors. Above a brief introduction of the methodology is provided. Next, a description of the methodology is given.

(1) Firstly, weft-knitted spacer fabrics were designed and manufactured with structural variations. To test their vibration isolation performance, sinusoidal sweep tests were carried out with the excitation force fixed during one sweep cycle. The frequency response curve was recorded in the form of acceleration transmissibility. The effect of load mass, fabric structure and excitation level on the isolation performance of fabric were studied.

- (2) In order to theoretically model the vibration behavior, the dynamic equation of motion was built at first. Experimental results guided the modeling. Due to the viscoelasticity and the nonlinear elastic force of spacer fabric, a fractional derivative term and two different types of polynomial elastic force-displacement relationship were taken into consideration. The harmonic balance method (HBM) with the first-order approximation was used to solve the equation and obtain the approximate solution in the frequency domain.
- (3) Following this, curve fit was performed to identify parameter values and also to examine the performance of different model structures. Then, a parametric analysis was carried out to study the effects of varying model parameters and the excitation force on the frequency response curves.
- (4) In order to verify the approximate analytical solutions, the MATLAB/Simulink block diagram was used to obtain numerical results for the steady-state solutions in the frequency domain. Moreover, bifurcation and chaotic behaviors were also studied numerically using the bifurcation diagram, the phase portrait and the Poincaré map.

1.4 Significance

This study strengthens the understanding of vibration behavior of weft-knitted spacer fabrics. The nonlinear vibration dynamics of the mass-spacer fabric system has been explored in depth. It also acts as a valuable reference for the applied research concerning the design, manufacture and optimization of weft-knitted spacer fabrics that reduce vibrations in different working environments.

- (1) Although the analytical and numerical approaches to studying the nonlinear vibration problems are very common in a lot of research areas such as foams and buckled beams, the nonlinear vibration dynamics of spacer fabrics is under studied. This study presents a systematic investigation into the design, manufacture, testing and analysis of the mass-spacer fabric system.
- (2) The experimental results reveal how fabric structural variations affect the vibration isolation performance under forced harmonic excitation. This helps optimize fabric structural designs for specific applications such as anti-vibration gloves and car cushions which require vibration attenuation in different frequency bandwidths. With improvement, it is expected that they can be commercially used for vibration isolations in various fields.
- (3) Due to the great varieties of textile products, not only weft-knitted and warp-knitted spacer fabrics but also 3D woven and nonwoven fabrics can be designed as vibration isolators. Their stiffness and damping properties can be readily controlled by modifying the material and structure using textile technologies or by post-treatments on textile precursors. Thus, this study can be extended to other textile structures for vibration isolation purpose.

1.5 Thesis outline

After presenting Chapter 1 of an introductory nature, Chapter 2 firstly reviews literature on the mechanical performance of knitted spacer fabrics with regard to compression and impact behaviors, including the warp-knitted according to its prevalence. Next, different

high-static-low-dynamic-stiffness (HSLDS) isolators achieved by buckled Euler column and negative stiffness mechanisms (NSMs) are introduced. Their vibration behaviors are described using the Duffing equation and the Helmholtz-Duffing equation. Furthermore, the periodic and chaotic behaviors of the two equations with the inclusion of the fractional-order derivative are reviewed.

Chapter 3 presents experimental details for weft-knitted spacer fabric as a vibration isolator. Structural design and manufacture of spacer fabrics are presented first. Then, vibration tests using sinusoidal sweeps are carried out to study the effect of load mass, fabric structure and excitation level on the vibration isolation performance of these spacer fabrics under forced harmonic excitation. Acceleration transmissibility curves are compared.

Chapter 4 builds the equation of motion under forced harmonic excitation using two types of phenomenological models, one with the symmetric elastic force and the other with the asymmetric elastic force. Frequency-domain solutions are obtained using the harmonic balance method (HBM) with the first-order approximation. Then, model parameters are identified by curve fit, with discussions on the optimization algorithms used, the goodness of fit concerning two types of models, and the significance of the fractional derivative term.

Chapter 5 investigates the effects of model parameters and the excitation force on the frequency response curves of the mass-spacer fabric system.

Chapter 6 carries out numerical simulations on the periodic responses in the frequency domain and compares the numerical results with the approximate analytical solutions. The bifurcation and chaotic behaviors are also studied with respect to the excitation frequency, the excitation force and the fractional order. The period-doubling bifurcation route to chaos is observed numerically.

Chapter 7 draws conclusions and identifies the limitations of this study, and makes some recommendations for future research.

CHAPTER 2 LITERATURE REVIEW

2.1 Introduction

This chapter will review previous work related to this study. As the subject of this study is weft-knitted spacer fabrics, literature on knitted spacer fabrics will be first reviewed in Section 2.2. Since the vibration behavior of knitted spacer fabrics, especially the vibration behavior under forced harmonic excitation has been seldom studied, a detailed review on vibration related studies is also carried out. To study the vibration behavior of spacer fabrics under forced harmonic excitation, a proper equation of motion should be built first. Due to the nonlinear stiffness and the viscoelasticity of weft-knitted spacer fabrics, their vibration becomes very different from linear systems.

Nonlinearity is very common in materials and systems. To utilize this nonlinearity for better vibration isolation, high-static-low-dynamic-stiffness (HSLDS) structures and systems have been investigated by different researchers, which will be reviewed in Section 2.3. As the Duffing equation and the Helmholtz-Duffing equation are adopted to describe the vibration behavior of such isolators, the analytical and numerical approaches to study these equations will be reviewed in Section 2.4. For polymeric materials such as spacer fabrics, the time-dependent viscoelasticity property should be considered in building the equation of motion under forced vibration. One method to describe this property is to use the fractional-order derivative. For the fractional-order Duffing

oscillator and the fractional-order Helmholtz-Duffing oscillator, subjective literature on their periodic and chaotic responses will be reviewed in Section 2.5.

2.2 Knitted spacer fabrics

The types, formation principles, and mechanical properties of knitted spacer fabrics are reviewed in this section. Experimental, analytical and finite element modeling approaches to study the compression and impact behaviors will be presented.

2.2.1 Types

Knitted spacer fabrics are a kind of sandwiched textile structure consisting of two outer layers which are connected but kept apart by a spacer layer of yarns such as monofilaments. They can be produced by both weft knitting and warp knitting technologies. Figure 2.1(a) shows the schematic structure of the weft-knitted spacer fabric. Two face layers are knitted with single jersey stitches and the yarns in the spacer layer are tucked on face-layer loops. The tuck pillar constitutes the major thickness and transfers force when the fabric is deformed. Figure 2.1(b) shows the schematic structure of the warp-knitted spacer fabric. Two guide bars knit each of the two outer layers, and two other guide bars knit the spacer layer.

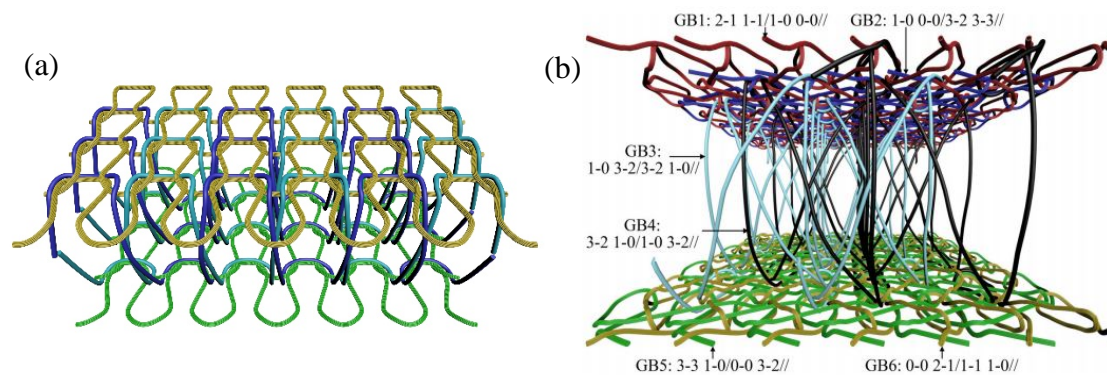


Figure 2.1 (a) Weft-knitted spacer fabric; (b) warp-knitted spacer fabric. ¹⁰

2.2.2 Formation principles

Weft-knitted spacer fabrics can be produced with double circular weft knitting machine and computerized flat knitting machine as shown in Figure 2.2. Although weft knitting process is simple and flexible, the upper limit of the dial height in a circular knitting machine, or the limit of the distance between two needle beds in a flat knitting machine obstructs the production of spacer fabrics with a thickness varied at a greater extent. Besides, the productivity of weft-knitted spacer fabrics with flat knitting machines is very low and weft-knitted fabrics have also a tendency to unravel due to the nature of weft loop constructions. However, the comparatively low speed of flat knitting machines conversely turns into an advantage when brittle and stiff yarns are used ¹¹. On a computerized flat knitting machine, knitting parameters such as cam setting can be easily altered. Weft-knitted spacer fabrics can be a priority for conducting a pilot study, since the preparation work is very simple and the required quantity of yarns for producing a sample is low, which is totally different from knitting warp-knitted spacer fabrics where a lot of time and yarns are required in the beam preparation and machine preparation. Besides, weft-knitted

spacer fabrics can be more competitive if texture effects such as color and jacquard pattern, or specified shapes are needed^{12,13}. Finally, the two-way stretch and the ability to conform to shape make weft-knitted spacer fabrics very promising in lingerie industries¹⁴ and for other next-to-skin applications such as medical bondages and knee braces.

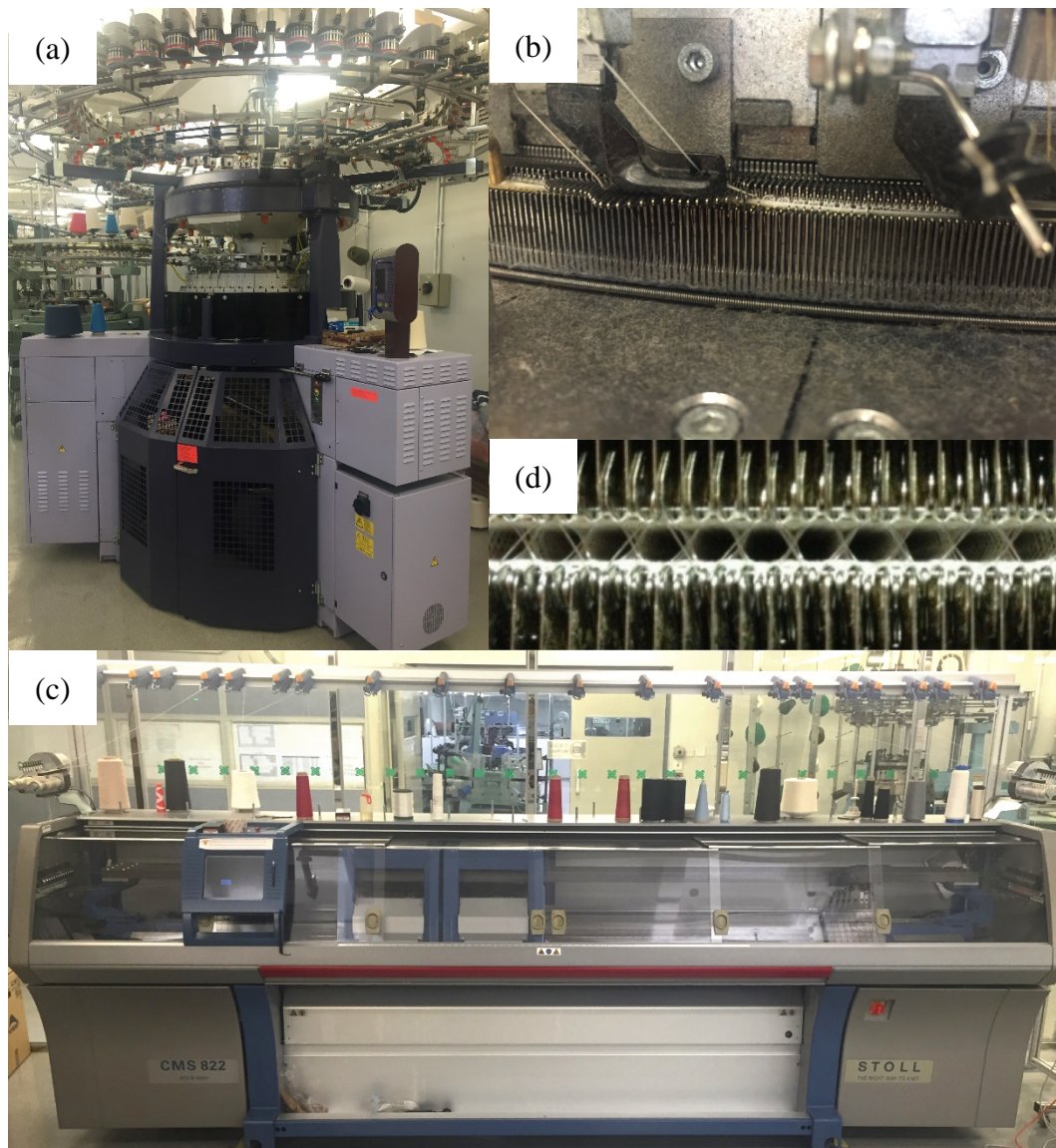


Figure 2.2 Machines for knitting weft-knitted spacer fabrics: (a) double circular knitting machine and (b) its dial and cylinder needle beds; (c) computerized flat knitting machine and (d) its front and back needle beds.

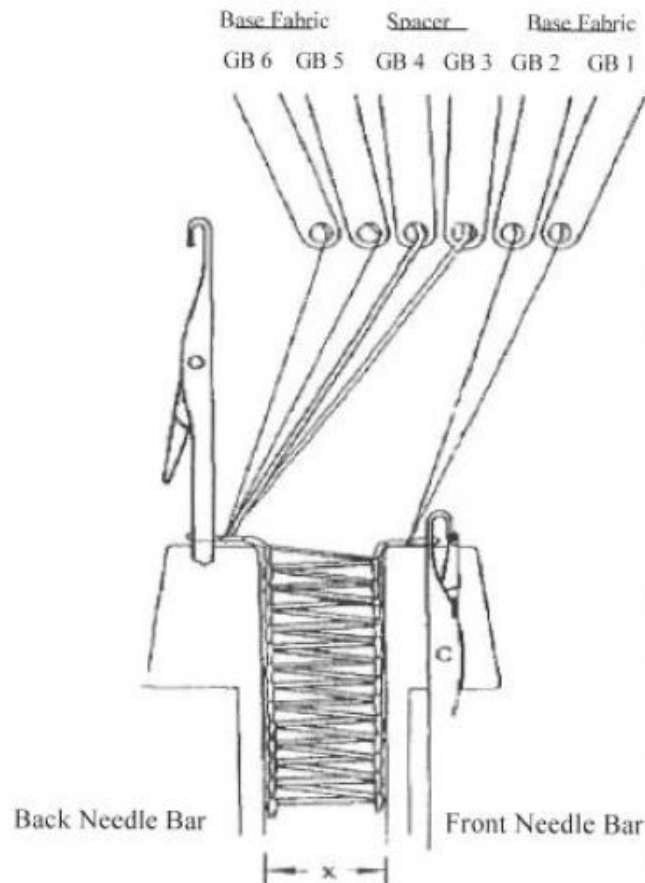


Figure 2.3 A schematic of Raschel knitting machine for producing warp-knitted spacer fabrics.¹⁵

However, knitted spacer fabrics found in the market are mostly warp-knitted, which are produced by double needle-bar Raschel knitting machines, as shown in Figure 2.3¹⁵. This is due to several reasons. Firstly, double needle-bar warp knitting machines have a greater capacity in adjusting the distance of two needle bars, possibly from 5 to 60 mm¹⁶, which permits to produce spacer fabrics with a large variation in thickness. Moreover, the adjustable shogging distance of yarn guide bars also adds to the advantage of using warp knitting machines to produce high-distance spacer fabric. For example, the HDR 6 EL (HighDistance®) warp knitting machine built by Karl Mayer could achieve a shogging

distances up to 65 mm. Another advantage of warp knitting machines comes from their high production efficiency. The maximum machine speeds for producing warp-knitted spacer fabrics range from 750 to 1000 r/min depending on the machine type¹⁷. In addition, warp knitting technology is very suitable for producing mesh and stable fabric structures. A large range of variations in fabric structure and thickness make warp-knitted spacer fabrics become one of the mostly used 3D fabrics in technical areas.

Bruer et al.¹² have reviewed production techniques and applications of knitted spacer fabrics, however, it should be noticed that with the progress of technology and techniques, innovated fabric structures and machine types are emerging. For instance, Włodarczyk and Kowalski¹⁸ presented a technology of multi-layered weft-knitted spacer fabrics. Pieklak and Mikołajczyk¹⁹ introduced a new concept of a multi-comb warp knitting machine for knitted spacer fabrics.

2.2.3 Applications

Knitted spacer fabric is attractive for many technical applications such as medical uses, composite reinforcement and impact protection. Its thermophysiological comfort regarding vapor permeability, liquid absorption and thermal insulation makes it very suitable for medical uses^{14, 20-33}. Fabric properties such as regain, dyeability and water drop absorption time on fabric surface can be modified by finishing³⁴. Knitted spacer fabric can be finished to possess antimicrobial function^{21, 23, 35}. Due to its good mechanical properties, it can also be made into intimate apparels³⁶ and cushions such as compression bandages and wound dressings^{22, 24, 26, 27, 32}. Moreover, its deformability allows it to be

easily made into curved shapes for applications such as art design ³⁷ and reinforced concrete ^{38,39}. Its functions in the fields of sound attenuation ⁴⁰⁻⁴², geotextile applications ^{43, 44}, thermal insulation for solar thermal applications ⁴⁵, and piezoelectric effect for energy harvesting applications ⁴⁶ have also been explored. Warp-knitted spacer fabrics with auxetic effect have also been reported ⁴⁷⁻⁴⁹.

2.2.4 Compression studies

Studies on the mechanical performance of knitted spacer fabrics incline to warp-knitted ones rather than weft-knitted ones. This may be caused by the dominance of warp-knitted spacer fabrics as highly flexible and commercial products, such as mattress beddings, which could again be traced back to its productive efficiency and product diversity. Besides, some studies on the analytical modeling of knitted spacer fabric do not specify whether it is warp-knitted or weft-knitted. Due to the over simplifications, warp-knitted and weft-knitted spacer fabrics may be not taken into consideration during modeling. In this section, the experimental, analytical and numerical studies of the compression behavior of warp-knitted and weft-knitted spacer fabrics are reviewed as follows.

2.2.4.1 Experimental approach

The compression behaviors of warp-knitted and weft-knitted spacer fabrics have been studied by different researchers. Compression mechanism is identified by dividing the deformation into different stages. With proper experimental design, parametric analysis

of fabric structure, yarn material and technological conditions can be directly applied. It is also noted that due to the large varieties of knitted spacer fabrics and their wide application fields, testing methods may need to be redefined.

Ye et al.⁵⁰ developed a warp-knitted spacer fabric produced on a Karl Mayer Raschel machine RD 6 DPLM/30, with two needle beds and six guide bars, and compared its performance with polyurethane foam for the pressure distributions in cushion testing, with the aid of a ClinSeat pressure measurement system manufactured by TekScan Inc. The result indicates spacer fabric achieves better pressure relief. Two other related studies also gave a comparison of different materials for pressure relief.^{51,52}

Liu and Hu⁵³ carried out a study on the compression properties of weft-knitted spacer fabric. The compression test was performed using the KES-FB3-A compression tester. This article analyzed the effect of NP value (i.e. stitch setting, a higher NP value results in a lower density of the fabric), knit pattern and monofilament diameter. It is shown that a higher NP value for the spacer layer provides higher compression resistance and better compression recovery.

Yip and Chung⁵⁴ and Yip and Ng⁵⁵ presented a study on the low stress mechanical properties of one warp-knitted spacer fabric and weft-knitted spacer fabrics with different inclination angle for spacer monofilament. The bending and compression properties were measured using the Kawabata evaluation system KES-F. They concluded that samples with higher inclination angle resulted in higher compression resistance. Besides, samples

using monofilaments as spacer yarns showed higher compression recovery compared with those using multifilament spacer yarns.

Mecit and Roye⁵⁶ investigated a testing method for compression behavior of warp-knitted spacer fabrics designed for concrete applications. They identified the issue that conventional testing standards are not appropriate for compression characteristics of spacer fabrics due to their structural features, so they defined and investigated the testing method in order to fill in this gap. They evaluated the effects of sample area, presser foot area and sample shape for the force-controlled test using the thickness measuring device, and evaluated the effects of test speed and stabilization form for the way-controlled test using Zwick/Roell 2.5 material testing machine. A similar study can also be found in Armakan and Roye^{16,57}.

Liu and Hu⁵⁸ carried out an experimental study on the compression behavior of warp-knitted spacer fabric. They evaluated the effects of the compression test boundary condition and the sample size. The deformation mechanism is identified by dividing the load-displacement curve into four stages. It is shown that the boundary condition influences fabric deformation in the plateau stage. Besides, sample walewise length has also an effect on the compression behavior.

2.2.4.2 Analytical approach

Due to the complexity of knitted spacer fabrics, analytical approach to solving the compression force-displacement relationship is carried out with simplifications. For

instance, the interactions of spacer yarn with face layer stitches and with other spacer yarns are often ignored. The boundary condition of spacer yarn fastened with face layer is assumed as pinned or fixed. Spacer yarn is treated as a perfect rod. Some works investigate the compression of a single spacer yarn, in which the classical beam theories can be applied. Other works investigate the compression of the whole spacer fabric, in which empirical models and phenomenological constitutive models can be applied.

Supel and Mikołajczyk⁵⁹ built a physical model for the spacer monofilament in a warp-knitted spacer fabric, with the assumption of having one rod fastened at both ends by articulated joints, being one immovable and the other slidable. Correspondingly, a mathematical model based on Euler's theory to describe compression process is formulated using fourth order differential equations. The resultant monofilament shape is a fragment of a sinusoid. They also proved that the force for higher order buckling form is greater than the first buckling form, which may occur due to the contact with neighboring monofilaments when the volume of monofilaments is great or when the compressive deformation is large. Supel and Mikołajczyk⁶⁰ also studied the compression process of spacer monofilament mathematically with two different boundary conditions, one model with one-side fixed and one-side articulated, the other model with both-sides fixed. Supel and Mikołajczyk⁶¹ later built a mechanical model based on Euler-Leaf theory, which is different from the abovementioned model. Spacer monofilament is treated as an "elastica" fastened at both ends by articulated joints and its bent shape is described using elliptic integrals, which is verified by experiment. During compression, the central angle of the curved monofilament keeps increasing until it reaches 90° and is maintained

constant afterwards. The ends of monofilament then undergo parallel displacement. This theoretical force-displacement curve is also compared with experiment.

Miao and Ge ⁶² derived an equation to calculate the pressure force on individual monofilament in the flat-wise compression. Besides, they modeled the monofilament spacing based on Love's ordinary approximate theory, which assumes the erect monofilament as an elastic rod as described in the Bernoulli-Euler theory. On the other hand, a modified equation of Love's is adopted for the initially curved rod. Sheikhzadeh et al. ⁶³ presented an analytical model based on the Van Wyk's equation, which showed that the variation of compressive pressure was directly proportional to the inverse thickness cubed of the fabric. This equation can be adapted to predict the lateral compressive behavior of spacer fabrics with an acceptable accuracy. Du and Hu ⁶⁴ studied the spherical compression properties of knitted spacer fabrics with a detailed theoretical analysis on compression force and fabric geometry. Köllner and Völlmecke ⁶⁵ built an analytical model for the compression of pile fibers in a spacer fabric based on rigid hinged struts. They used rotational springs to model the bending behavior of spacer yarn and used extension springs to model its interaction with fibers in the face layer. Then, the load-deformation behavior was obtained by calculating the total potential energy of the system. Liu and Hu ⁶⁶ proposed a constitutive model consisting of seven parameters to describe the compressive stress-strain relationship of warp-knitted spacer fabric. The proposed model outperforms three existing constitutive models by having the smallest fitting errors.

2.2.4.3 FE modeling approach

To realize finite element modeling, the geometry of knitted spacer fabric^{67, 68} should be built first. Zhang et al.⁶⁷ developed a realistic 3D special stitch model of warp-knitted spacer fabric using non-uniform rational B-spline (NURBS) curves and surfaces. With the aid of the Visual C++ language and usage of the OpenGL library, the geometric simulation of high accuracy is achieved. The 3D image help recognize complicated fabric structures. In many cases, however, the realistic geometry of spacer fabric is hard to be achieved. Simplifications are often used, such as taking outer layer as thin shell and assuming the spacer yarn is pin-ended with outer layers. Nevertheless, homogenization is usually not applied for the geometric modeling of knitted spacer fabrics. Last but not least, it is always critical to evaluate the validity of the constructed model. Below is a review of numerical studies on the compression behavior of knitted spacer fabrics using finite element modeling.

Lee et al.⁶⁹ presented the application of knitted spacer fabric as single-layer bandage system for the treatment of venous leg ulcers and they used honeycombed geometry to represent face sheets of warp-knitted spacer fabric. However, no information is provided on the element type choices and material properties adopted for mechanical simulation in ANSYS. Vassiliadis et al.⁷⁰ offered a detailed study on the numerical modeling of the compressional behavior of warp-knitted spacer fabrics. The simulation focuses on a two-scale mechanical analysis, micro and macro, using the Finite Element Method. Micromechanical analysis of the unit cell is based on the assumption that the spacer monofilament is bonded at the outer layers. Both of the inserted face yarns and spacer

monofilaments are simulated as beam element given that yarn bending dominates the deformation process during fabric compression. For the macromechanical modeling of the whole sample, inner spacer monofilaments are simplified as a solid volume and simulated with multi-linear isotropic elasticity, while the face layers are simulated using shell elements with linear orthotropic properties. This macromechanical simplification is encouraging and provides a direction for the homogenization of knitted spacer fabric during modeling. Kyosev and Renkens⁷¹ discussed about a truss-joint model of warp-knitted spacer fabric which excludes the influence of the bending stiffness of spacer yarns, but also quoted the literature⁷² of an exhaustive investigation on the influence of the bending stiffness of the spacer yarn. Hou et al.⁷³ simulated the transverse compression of warp-knitted spacer fabric using elasto-plastic beam elements for spacer monofilaments and using isotropic shell elements for face layers. In their study, spacer monofilament was fixed at the end with the face layer, and two face layers were allowed relative sliding in the horizontal plane in order to observe the effect of shear stress on the deformation mechanism of spacer fabric. Later, Hou et al.⁷⁴ also presented a detailed study revealing the factors that affect the compression deformation of 3D spacer fabrics using finite element modeling. The geometric model was developed with the aid of micro-CT scanner, so it represented a realistic monofilament configuration. Simulations revealed that the constraints, shearing, bending and collapses of monofilament and its contact with other monofilament and with outer layers all affect the compression mechanism. Qian et al.⁷⁵ simulated the flat compression stress-strain curve of one warp-knitted spacer fabric using ANSYS with reasonable assumptions that spacer yarn is ideal elastomer and surface fabrics are ideal elastic shell ignoring their thicknesses. Though the simulation result

conflated quite well with the experimental result complying with the poly-foam compression standard ASTM D3671-11, unfortunately, it lacks detailed information on the construction of its mechanical model. Dura Brisa et al.⁷⁶ carried out a FE modeling on the deformation of one spacer monofilament in the thick warp-knitted spacer fabric using ABAQUS. Hinged boundary condition was assumed and the contact with face layer was considered. On the other hand, the analytical solution which used Euler's equation for column buckling was obtained dividing the compression process into two zones, i.e. a free flexural buckling zone and a forced flexural buckling zone after contact with face layer. During the whole flexural buckling process, circular form was assumed for the free length of monofilament. Numerical and analytical solutions for the force-deformation curve were compared, and discrepancies were analyzed. Liu and Hu⁷⁷ developed a FE model for the compression of warp-knitted spacer fabric. The model corroborated the experiment, with the adjustment of constraints of spacer monofilament and outer layer thickness. It was found that the nonlinear compression behavior was due to the post-buckling, torsion, shear, rotation, contacts between spacer monofilament, and contacts between spacer monofilament and outer layers. Parametric study also showed that smaller monofilament inclination, coarser monofilament and smaller fabric thickness result in higher compression resistance.

2.2.5 Impact studies

The previous section reviewed literature on the quasi-static compression behavior of knitted spacer fabric. However, studies on the force vibration of knitted spacer fabric is still an open field. This section is concerned with experimental, analytical and finite

element modeling approaches for studying the impact behavior of knitted spacer fabric.

Guo et al.⁷⁸ investigated on the impact and compression-after-impact properties of warp-knitted spacer fabrics. Results showed that closed surface structure and coarser spacer yarns result in reduced peak force and higher energy absorption. Besides, higher fabric thickness has a better protective performance but at the cost of reduced comfort. Liu et al.⁷⁹ studied the effects of structural parameters on the peak transmitted force for warp-knitted spacer fabric used as impact protectors. It was found that higher inclination, higher fabric thickness, coarser spacer monofilament, and more stable outer layer structure performed better for impact force attenuation. Besides, the lamination of spacer fabric also improved force attenuation capacity. Marques et al.⁸⁰ found the warp-knitted spacer fabric embedded with silicone helps reduce peak force during a fall. Blaga et al.³ used an impact hammer to study the dynamic behavior of different types of warp-knitted spacer fabrics on three directions. Frequency response curves were obtained using fast Fourier transform. It was found that the responses on wale and course directions were comparable, while the perpendicular testing direction had significantly higher resonance frequencies. The authors² also studied the impact responses of weft-knitted spacer fabric in these three directions.

Arabzadeh et al.¹ provided a mathematical model in order to predict the damping behavior of warp-knitted spacer fabrics under impulsive loading. The uniqueness lies in that one spacer fabric was analytically modeled as a single-degree-of-freedom mass-spring-damper system. The results showed that coarser monofilament, smaller fabric thickness

and higher monofilament density would decrease the force transmitted. Analytical results provided a relevant understanding of the findings. However, the widely used viscous damping model is not necessarily appropriate for knitted spacer fabrics; for some polymers, a complex model including both viscous and hysteretic models may be more general for this analysis. Besides, the problem could be tougher if geometric nonlinearity of the spacer monofilament is considered. As a continuation of Liu and Hu's ⁶⁶ proposal of a constitutive model for the quasi-static compression of warp-knitted spacer fabric, they ⁸¹ also presented a dynamic model to describe its impact response based on the previous study. The dynamic model correlated with experimental results by drop-weight impact tests.

Lu et al. ⁸² studied the impact behavior of shear thickening fluid impregnated warp-knitted spacer fabric, which showed higher stiffness and lower peak force compared with pure warp-knitted spacer fabric. FE analysis showed that the main load carrier in pure warp-knitted spacer fabric is the monofilament. For the composite, however, the impact behavior and energy absorption mechanism were ruled by the thickening effect of shear thickening fluid and its interaction with yarns.

2.3 HSLDS isolators

In a linear vibration system, the stiffness, resonance frequency and the transmissibility do not change with the pre-load and the magnitude of excitation force. High stiffness is required to support the static load. On the other hand, low stiffness is preferred to reduce

resonance frequency so as to achieve a wider frequency bandwidth for vibration isolation. Thus, for a linear system exists an issue of having to choose between these two requirements. To solve this problem, a nonlinear system having high-static-low-dynamic-stiffness (HSLDS) can be designed. This section will review two mechanisms that exhibit HSLDS, Euler column buckling in Section 2.3.1 and negative stiffness mechanisms (NSMs) in Section 2.3.2.

2.3.1 Euler column buckling

Winterflood et al.⁸³ and Winterflood et al.⁸⁴ demonstrated that to achieve the same resonance frequency, a vertical vibration isolator using a linear coil spring requires to be stretched under load by the same length as the equivalent pendulum performed as a horizontal isolator. This is caused by the presence of the storage of gravitational potential energy in vertical vibration isolation. This problem can be mitigated by using the buckled Euler column working in its axial direction as a nonlinear isolator, since it does not require the storage of static energy. As stated by Virgin and Davis⁸⁵, buckling in most cases means collapse and the loss of stiffness, a phenomenon generally to be avoided. To the opposite, it can also be utilized herein to generate the high-static-low-dynamic-stiffness (HSLDS). With the assumption of a half-sine shape for the buckled beam, they used the approximate solution for the force-lateral deflection relation valid for mild oscillations,

$$\frac{P}{P_e} = 1 + \frac{\pi^2}{8} \left(\frac{Q}{L} \right)^2, \quad (2.1)$$

where P is the axial force, $P_e = EI \left(\frac{\pi}{L} \right)^2$ is the classical Euler critical load for a pin-ended beam, Q is the lateral deflection, and L is the beam length. Given the geometric relation between the lateral deflection Q and the end shortening L as,

$$\left(\frac{\delta}{L} \right) = \frac{\pi^2}{4} \left(\frac{Q}{L} \right)^2 + \frac{3\pi^4}{64} \left(\frac{Q}{L} \right)^4, \quad (2.2)$$

the non-dimensional post-buckled force-axial deformation relation can be approximated as,

$$\frac{P}{P_e} = \frac{1}{3} \left[2 + \sqrt{1 + 3 \left(\frac{\delta}{L} \right)^2} \right] \approx 1 + \frac{1}{2} \left(\frac{\delta}{L} \right)^2. \quad (2.3)$$

Assume the critical load to be $P_e = mg$, then at the onset of buckling, the approximate

stiffness is $k = \frac{P_e}{2L}$. Therefore, we have the angular resonance frequency $\omega = \sqrt{\frac{g}{2L}}$

where L is the length of the nonlinear beam. In comparison, the angular resonance

frequency for a linear vertical isolator is $\omega = \sqrt{\frac{g}{\Delta l}}$ where Δl is the length of compression

or extension of the linear spring under load. As shown by Winterflood et al.⁸³, not only is

the requirement on spring length greatly lightened using a buckled beam as the nonlinear isolator, the spring mass is also greatly reduced so as to avoid internal resonance.

Virgin and Davis⁸⁵ further incorporated the influence of initial geometric imperfection

Q_0 on the force-axial deformation relation. As a result, the stiffness becomes lower for

small oscillations at the vicinity of just above the critical buckling, compared with an initially straight beam; at relatively large deformation, it also shows a slightly lower axial force but with almost the same stiffness. Notably, as will be reviewed later for the realization of negative stiffness using oblique buckled beam, Liu et al.⁸⁶ found that a smaller imperfection is preferred because it yields smaller stiffness and a wider range of smaller overall stiffness.

Friswell and Flores⁸⁷ investigated the design of HSLDS isolation mounts using beams of tunable geometric nonlinear stiffness. Tuning was achieved by prescribed axial displacement and rotation to the ends of beam so as to implement internal stresses and reduce the linear stiffness. Shoup⁸⁸ utilized the suspension spring pair clamped in a semicircular shape to generate symmetrical hardening nonlinearity for shock and vibration isolation. Yabuno and Tsumoto⁸⁹ found that the buckled beam can be recovered to the straight shape due to high-frequency excitation, which is valid in the neighborhood of the straight shape. The phenomenon was theoretically interpreted that high-frequency excitation shifts the pitchfork bifurcation point and increases the buckling force.

Anti-spring⁹⁰ was used to generate anti-restoring force, reducing the natural frequency of system when added to a normal spring, so it can also be regarded as negative stiffness element. Winterflood et al.^{84,91} and Chin et al.⁹² proposed a simple structure for mounting a pair of Euler spring blades in their buckled mode. The one facing the pivot flexure provides negative stiffness, so employing a pair of matched spring blades that possess appropriate bending stiffness ratio can give the structure much reduced resonant

frequencies.

2.3.2 Negative stiffness mechanism

Negative stiffness mechanism uses negative stiffness spring combined in parallel with positive stiffness spring to achieve quasi-zero stiffness (QZS) at the statically loaded position of the system. The concept of using NSM for a vibration isolator to achieve the low resonance frequency has already reached a practical and commercialized level. Below will introduce three approaches to negative stiffness component, by using pre-stressed beams in Section 2.3.2.1, oblique springs in Section 2.3.2.2, and magnet in Section 2.3.2.3.

2.3.2.1 Pre-stressed beam

Platus designed and patented a negative-stiffness-mechanism vibration isolation system in 1992 ⁹³, and his company “Minus K Technology” offers vibration isolation products with payload capacities ranging from a 10-pound tabletop to 10,000-pound floor panels. To improve the reliability of precision instruments such as the turntable, SPM and AFM, environmental vibrations with frequencies as low as 2 Hz need to be isolated. Figure 2.4 shows the transmissibility chart for the high-performance air and the Minus K isolation system. The transmissibility is greater than one under low excitation frequencies, as shown in Figure 2.4, indicating vibration magnification. It reaches peak value at resonance and declines to below one at higher frequencies, indicating vibration isolation. The resonance frequency of a typical pneumatic isolation system is around 2.3 Hz. In comparison, the resonance frequency of the NSM isolator by the Minus K can reach as

low as 0.4 to 0.5 Hz. It exhibits a ten-fold to hundred-fold better isolation performance than high-performance air at certain frequencies.

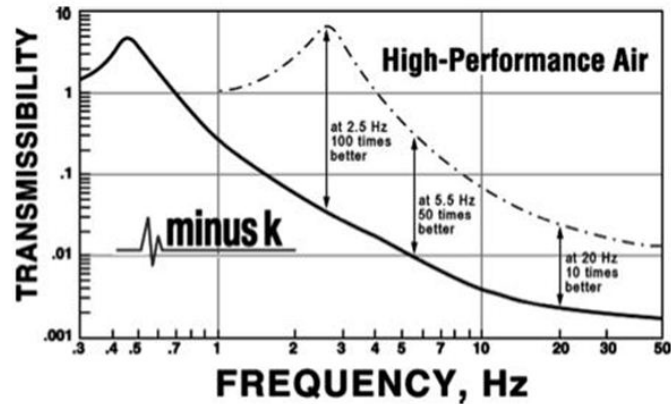


Figure 2.4 Transmissibility chart shows the Minus K isolation system can be 10-100 times better than the high-performance air table.⁹³

As shown in Figure 2.5, the vertical-motion isolation device by Platus⁹⁴ uses negative stiffness mechanism consisting of two bars hinged at the center connected in parallel with a regular positive linear spring. The vertical dynamic stiffness can be made to approach quasi-zero value by simply adjusting the loading screws as in Figure 2.6, in order to preset the compressive load P , thus to change the negative stiffness K_N .

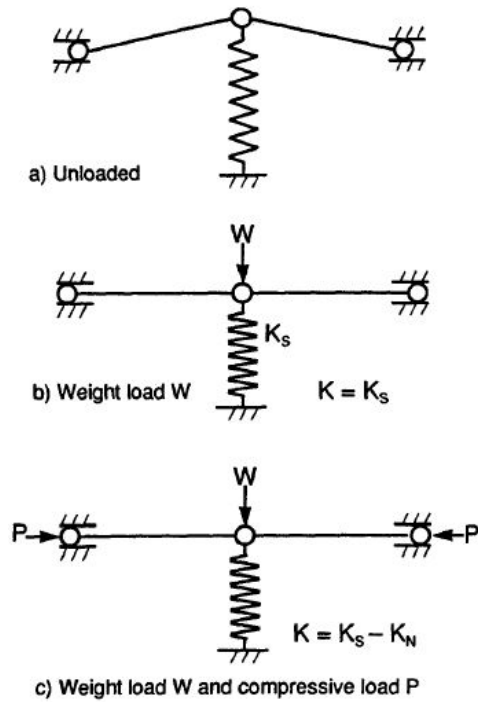


Figure 2.5 Concept of a vertical-motion isolator by negative stiffness mechanism. ⁹⁴

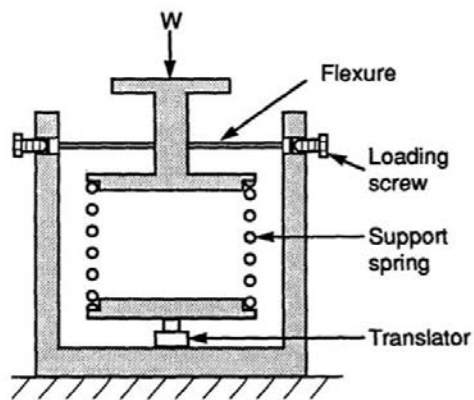


Figure 2.6 A schematic of vertical-motion isolator with means for accommodating changing weight loads. ⁹⁴

Shahan et al. ⁹⁵ adopted a similar design concept as above, but they fabricated the negative stiffness device using selective laser sintering (SLS), to leverage the geometric design freedoms. The prototype is made of a single piece of material, except the threaded rods

and screws. As a rapid prototyping technology, SLS offers convenience and geometric design freedom for model realization and theory proof. One advantage of using SLS for studies in vibration isolation is the minimized number of sources for losses that are not captured in the model.

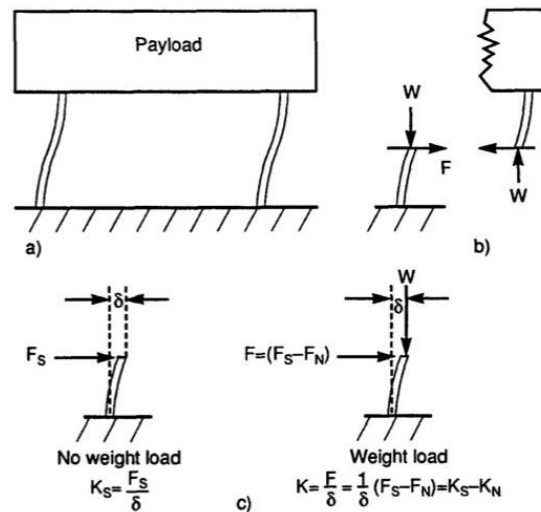


Figure 2.7 Concept of a horizontal-motion isolator by the “beam-column effect”.⁹⁴

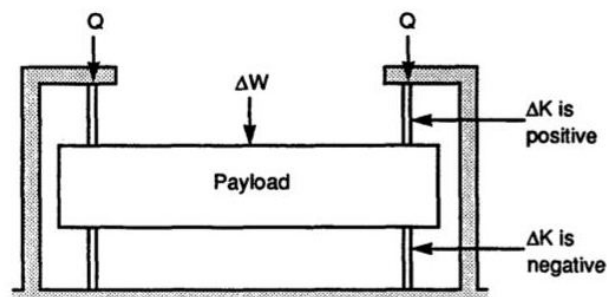


Figure 2.8 A schematic of horizontal-motion system with natural frequency independent of change in weight load.⁹⁴

Additional to the vertical-motion isolation, Plusus⁹⁴ also made use of the “beam-column effect” in order to provide the horizontal-motion isolation. The mechanism is illustrated

in Figure 2.7(c). Consider the fixed-free column, without the weight load W , the beam-column is just a cantilever beam acting as a horizontal spring with stiffness K_s as shown in Figure 2.7(c). Payload W adds bending moments on the laterally loaded beam, proportional to the deflection δ . Compared with the case when no weight load exists, to achieve the same lateral deflection δ , a reduced lateral force is needed when the payload W exists, which is equivalent to introducing a negative stiffness $K_N = F_N/\delta$, as in Figure 2.7(c). The net horizontal stiffness of the beam-column approaches zero as the payload W approaches the critical buckling load, thus K_N approaches K_s . Figure 2.8 illustrates a schematic of the horizontal-motion isolation system which is composed primarily of two sets of flexible columns preloaded with axial load Q . The payload sits between the upper and lower columns. Increasing payload weight decreases the negative stiffness effect and increases its horizontal stiffness of the upper column, while on the other hand, it increases the negative stiffness effect and reduces the horizontal stiffness of the lower column. Thus, by proper sizing of the upper and lower columns, the horizontal stiffness can be made proportional to the payload weight. The resulting horizontal natural frequency is then made independent of change in the weight load.

Based on Platus' vertical isolator device, the fundamental frequency of the isolator has been lowered to 0.4~0.5 Hz. However, a systematic design procedure is still necessary to act as design guidelines of the isolator. For this purpose, Ahn⁹⁶ initiated the nonlinear analysis on the performance limit, i.e. the fundamental frequency of the NSM vertical isolator using a nonlinear dynamic model, and presented an approximate design equation of the fundamental frequency as a meaningful guideline to improve the isolator

performance. According to his design equation, the stiffness of the horizontal spring should be kept as small as possible, while the vertical spring should be very stiff.

Besides, Liu et al.⁸⁶ used Euler buckled beams as the negative stiffness element instead of coil springs to achieve quasi-zero stiffness. The slender beam is axially loaded and pinned at two ends. With initial imperfection, the approximate relation between the axial force and the end shortening is built based on the classical Euler critical load. Although the exact solution for a classic Euler beam makes use of elliptic integrals which can be found in the book by Bazant and Cedolin⁹⁷, for small deflections the approximate expression achieves sufficient accuracy. The force-deflection relation of the isolator is derived satisfying zero stiffness at the static equilibrium position. It is found that a larger oblique angle and a smaller imperfection yield smaller stiffness and a wider range of smaller overall stiffness.

2.3.2.2 Oblique mechanical spring

Aside from using pre-stressed beam to realize negative stiffness and achieve quasi-zero net stiffness, a number of configurations generally making use of coil spring orientations have also been proposed⁹⁸⁻¹⁰⁴. Carrella et al.⁹⁸ studied the force-displacement characteristic of one quasi-zero-stiffness isolator, illustrated in Figure 2.9 shown in its unloaded condition.

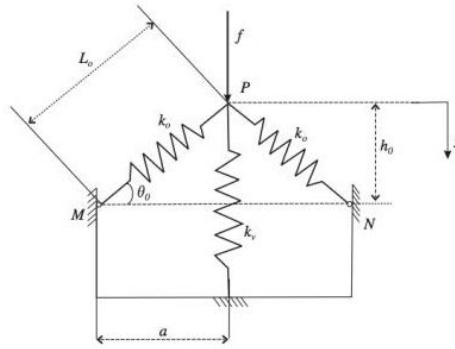


Figure 2.9 Schematic representation of the simplest system which can exhibit quasi-zero stiffness. ⁹⁸

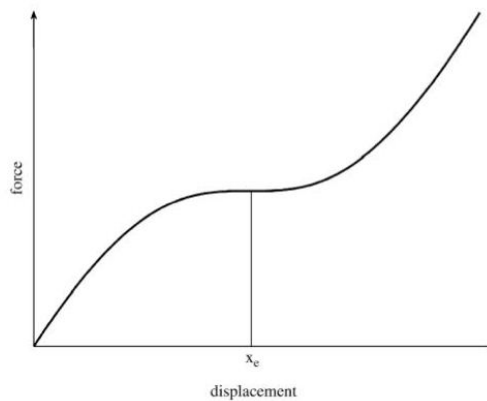


Figure 2.10 Typical force-displacement characteristic of the isolator shown in Figure 2.9. ⁹⁸

This quasi-zero-stiffness (QZS) isolator is composed of a vertical spring k_v acting in parallel with two oblique springs k_o . When it is loaded with a proper mass, the oblique springs k_o are compressed to the horizontal position and only the vertical spring k_v bears the static load. It is called the static equilibrium position. Figure 2.10 shows the typical force-deflection curve for the QZS isolator in Figure 2.9. It can be seen that at the static

equilibrium position x_e , the dynamic stiffness of the system is zero. Based on the equation of the non-dimensional stiffness of the system as a function of the non-dimensional vertical displacement they have derived, their study clearly identified the relationship between the geometrical parameter $\gamma = a/L_0 = \cos \theta_0$ and the spring coefficient ratio $\alpha = k_o/k_v$ that yields the desired stable QZS characteristic (i.e. zero dynamic stiffness at

the static equilibrium position): $\gamma_{QZS} = \frac{2\alpha}{2\alpha + 1}$.

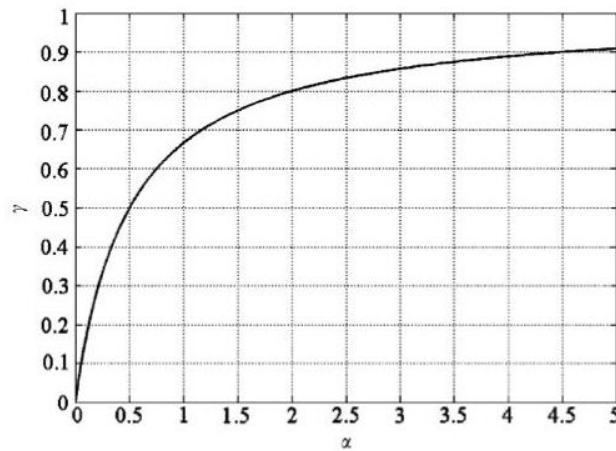


Figure 2.11 Relationship of geometrical parameter γ and stiffness ratio α that yields QZS. ⁹⁸

Figure 2.11 illustrates this relationship. When the initial angles of inclination are too small ($\gamma \approx 1$), the inclined springs need to be orders of magnitude stiffer than the vertical spring; when the initial angles are in the moderate range of $37^\circ \sim 66^\circ$ ($0.4 < \gamma < 0.8$), the inclined springs possess a similar stiffness as the vertical spring. To further optimize the QZS mechanism, they intensified the condition that to achieve a large excursion from the static

equilibrium position, while at the same time, over the range of displacement the stiffness of the system should also be kept smaller than the vertical spring alone. Satisfying this requirement, the resultant optimum stiffness ratio α_{opt} ranges from 1 to 0.6, and the corresponding initial angles of inclination ranges from $48^\circ \sim 57^\circ$.

As a continuation of the previous study, Kovacic et al.⁹⁹ analyzed the QZS isolator with nonlinear pre-stressed oblique springs. Unlike the previous model of a geometrically nonlinear but physically linear system, this study adopted a configuration possessing nonlinearity both geometrically and physically. In their study, they demonstrated the benefits of this update: 1) it achieves comparatively smaller stiffness at larger displacement about the static equilibrium position; 2) it also achieves very small stiffness around the equilibrium position. The penalty is, however, the possibility of exhibiting period-doubling bifurcations under an asymmetric excitation, but only within a specific frequency range.

Additional to the abovementioned static analyses of the QZS isolator composed of two oblique springs connected in parallel with a vertical spring, Carrella et al.^{100, 101} also investigated the transmissibility of three configurations of the same QZS system. They found that nonlinear and pre-stressed oblique springs acting as negative stiffness element exhibits advantages over either linear, or linear and pre-stressed oblique springs, which consolidated their earlier conclusions⁹⁸. Besides, all the QZS systems, with proper chosen system parameters, are capable of outperforming the linear system.

Pasala et al. ¹⁰³ presented a new structural modification approach for seismic protection using adaptive negative stiffness. The schematic of the negative stiffness device is as illustrated in Figure 2.12. The pre-stressed vertical spring with stiffness k_v is connected in parallel with a horizontal spring with stiffness k_h to reduce the base shear and achieve horizontal vibration isolation. It was noticed that while NSD reduces the net stiffness of the structure, its assembly also results in an increase in maximum deformation. To reduce the deformation, a viscous damper, among which a nonlinear one is preferred, is added in parallel with the NSD. Their study examined the effectiveness of the proposed NSD in both elastic and inelastic structural systems through numerical simulations for periodic and random input ground motions. Based on the prototype this research team designed, the first phase experiments involving an actual NSD device have already been completed for proof of the concept. Further experimental and analytical study is in progress in their NEESR-Adapt-Struct project.

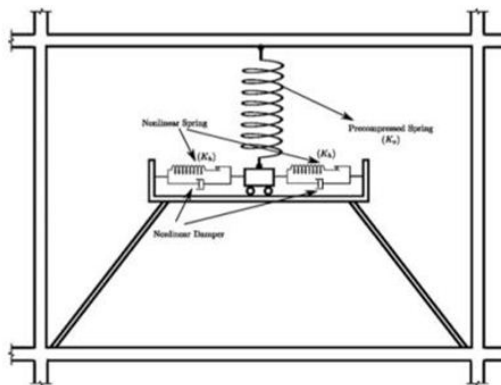


Figure 2.12 A negative stiffness device for horizontal vibration isolation. ¹⁰³

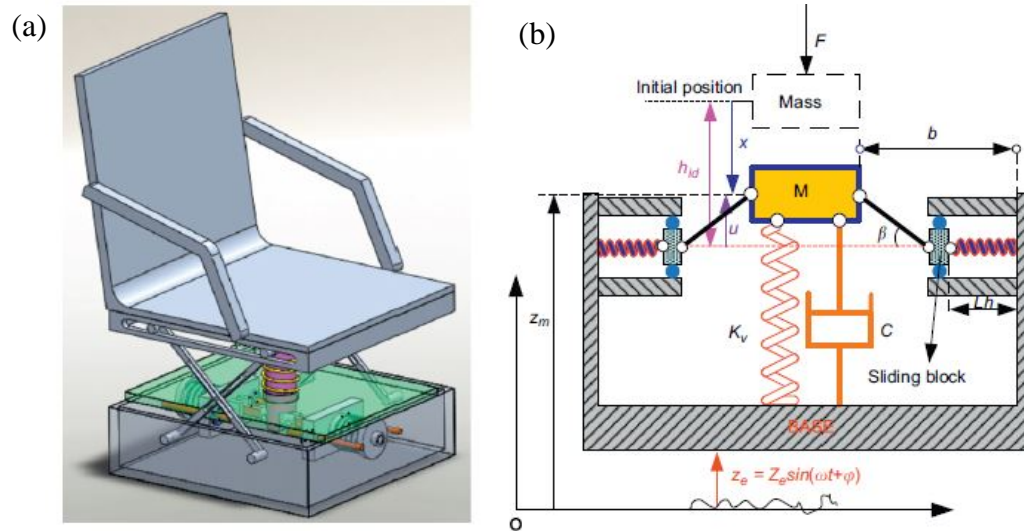


Figure 2.13 (a) Model of a suspension seat and (b) a schematic of the proposed isolation system. ¹⁰⁴

Figure 2.13 illustrates the model of a seat suspension system proposed by Le and Ahn ¹⁰⁴. The negative stiffness structure is realized through two horizontally aligned and compressed springs attached to two bars connecting with the payload. The restoring force generated by the horizontal springs acts on the mass, as the way to realize negative stiffness. Their mathematical analysis indicates that negative stiffness cannot be achieved when the ratio of the length of the bar to the original length of the horizontal spring is below 0.2, or when the ratio of the distance between the wall and the mass to the length of the horizontal spring is below 1.0 or above 1.75. They also made a detailed analysis of the influence of the spring ratio, i.e. the ratio of the horizontal spring stiffness to the vertical spring stiffness, on the occurrence of structural negative stiffness. When the ratio of the length of the bar to the original length of the horizontal spring equals 1.0 and the spring ratio equals 0.5, the proposed system offers optimum effectiveness for low-excitation-frequency excitations.

Another approach utilizing negative stiffness for seat suspension system involves solving the geometrically nonlinear problem of the large-amplitude post-buckling of rod-shaped elastic springs. Lee et al. ¹⁰⁵ identified the problem that the conventional seat suspensions with load-bearing springs (LBSs) possess a certain “negative” stiffness under only small-amplitude movement. Based on the consistent theory of thin shells, they presented an approach for designing compact springs in terms of their compatibility with the room available for mounting the vehicle suspensions and the extension of the height control region as well, and proposed a generic model of a simple springing element with negative stiffness in the large. The negative torsional stiffness was observed in experiment and it fits well with the computational result. Their generic spring module applies to various vehicle suspensions such as seat suspension, cab mounting, cargotainer platform or vehicle-borne mini-device. Similar approach to realize negative stiffness was applied to a multi-stage high-speed railroad vibration isolation system ¹⁰⁶.

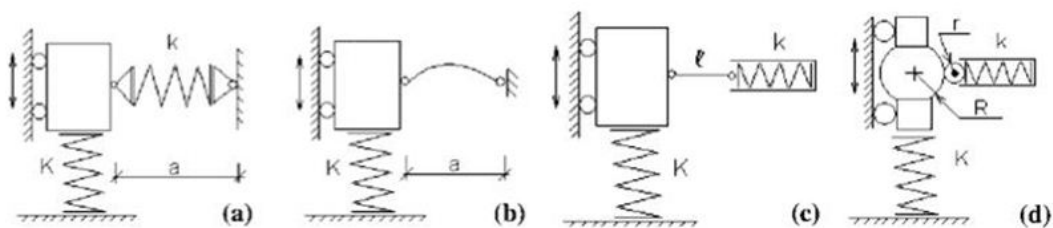


Figure 2.14 Isolators with different types of negative stiffness systems. ¹⁰⁷

Park and Luu ¹⁰⁷ summarized four typical types of passive negative stiffness systems based on their structure difference, illustrated in Figure 2.14 at their equilibrium position. They made a comparative study, both analytically and experimentally, of the abovementioned four NSD systems, with the goal of choosing the most reliable structure

that provides a low frequency, and that at the same time has a large working range. In the part of mathematical analyses, the equivalent stiffness of each NSD system was acquired either by calculating the second derivative of the potential function, or by calculating the first derivative of the restoring force. In the part of experimental evaluation, harmonic base excitation was performed and the fundamental frequency was determined based on the resultant transmissibility curve. Table 2.1 summarizes the properties and performance of these four types of negative stiffness systems.

Based on their study, Type III NSD consisting of a compressed spring connected to a bar, and Type IV NSD consisting of a compressed spring and a roller, were selected as the superior model among the four described herein since they gave stability and low natural frequency. One drawback as they described is, however, the system is bulky and complicated since the condition $l = \delta_0$ must be satisfied in order to achieve linearization. For this problem, they reconfigured the device by putting the NSD inside the main spring and changing the movement of the NSD from horizontal direction to vertical direction using a special joint.

The device of the abovementioned Type III NSD isolator in Figure 2.14(c) is very similar with the suspension system proposed by Le and Ahn¹⁰⁴ as shown in Figure 2.13. They approached the solution for optimizing the effect of negative stiffness from different perspectives. For comparison, the latter presented a more comprehensive analysis of the influence of different structural elements on isolation performance and also gave more insights guiding people on new structural NSD design for isolation purpose.

Table 2.1 An overview of the properties and performances of four types of negative stiffness systems.

	Type I isolator	Type II isolator	Type III isolator	Type IV isolator
NSD element	Compressed coil spring with stiffness k	Compressed leaf spring (nonlinear)	Compressed coil spring k connecting to a bar l	Compressed coil spring k and a roller with radius r
Mathematical analysis	$K_{eq=0} > 0$ for $x \neq 0$. The isolator is stable but cannot obtain the expected stiffness on all working ranges.	Similar with Type I isolator, it is stable but cannot obtain the expected stiffness on all working ranges.	When $l = \delta_0$, $K_{eq=0} = 0$, i.e. the isolator has zero stiffness at any point of x . The equivalent stiffness is a constant ($K_{eq=0} = K = k$).	When $\delta_0 = (R+r)$, $K_{eq=0} = 0$, i.e. the isolator has zero stiffness at any point of x , equivalent to Type III NSD.
NSD property	Non-linear	Non-linear	Linear	Linear
Natural frequency obtained from experiment	Not obtained due to the operational instability of the model	$f_n = 1.4$ Hz	$f_n = 0.6$ Hz	$f_n = 0.6$ Hz

Note: δ_0 is the initial deformation of the spring k .

2.3.2.3 Magnet

Aside from pre-stressed beam or oblique mechanical springs, negative stiffness spring can be realized by using magnets as well, which may be passive or active. Robertson et al.¹⁰⁸ carried out a theoretical analysis on a non-contact spring with inclined permanent magnets for load-independent resonance frequency, and their study investigated the influence of design parameters such as magnet shape, magnet angle, magnet offset and magnet volume on the natural frequency characteristics of the system. Carrelle et al.¹⁰² proposed a parallel connection of linear mechanical springs and magnets to achieve low dynamic stiffness. In their design, an isolated mass is mounted between two vertical mechanical springs. At the out edge of them two permanent magnets are introduced to provide negative stiffness. It was shown that for small oscillations this magnetic suspension could be treated as linear. A different approach utilizing negative stiffness from magnetic interaction was proposed by Zhou and Liu¹⁰⁹. The feature of the developed isolation design is its tunability regarding stiffness, acting either passively or semi-actively. The passive negative stiffness element is obtained from interaction between the permanent magnet and the steel cores of the electromagnets, in contrast with the negative stiffness mechanism in Carrella's work¹⁰². Their study showed that reducing the gap distance or increasing the current widens the isolation region. Besides, they demonstrated that a proper combination of the gap distance and the electromagnet current results in a low and near constant dynamic stiffness.

All the vibration isolation systems reviewed in Section 2.3 belong to the passive control category. Although the active-control of structures is more effective than passive-control, it has two major limitations: high power requirement to drive the actuator, and dependency

on the continuous feedback signal. Semi-active control combines the advantages of both active and passive control systems, without requiring high power supply, however, its operation still relies on battery power. In the critical case when the main power source to the structure fails, semi-active control system loses its reliability as well. Thus, passive negative stiffness systems is advantageous, as it does not need any feedback control or power supply.

2.4 Helmholtz-Duffing equation

The high-static-low-dynamic-stiffness (HSLDS) isolators reviewed in Section 2.3 have nonlinear stiffness terms. The equation of motion for such isolators under forced harmonic excitation can be described using the Duffing equation or the Helmholtz-Duffing equation. Except for negative stiffness systems, Euler buckled beam under transverse vibration can also be described using the latter equation. Using the Duffing equation to describe the vibration of negative stiffness systems will be reviewed in Section 2.4.1. Using the Helmholtz-Duffing equation to describe the vibration of other negative stiffness systems and Euler buckled beam under transverse vibration will be reviewed in Section 2.4.2. The steady-state periodic solutions of the Helmholtz-Duffing equation will be reviewed in Section 2.4.3, using approximate analytical and numerical methods.

2.4.1 Duffing equation

The QZS mechanism is one special case of the HSLDS isolator. It has high static stiffness

to support load and low dynamic stiffness to isolate vibration in a wide frequency range, particularly for low-frequency components. The Duffing equation is largely used to describe the dynamics of such isolators.

As described earlier for the oblique mechanical springs in a negative stiffness device^{98, 101}, when the geometrical parameter and the spring coefficient ratio satisfies a certain relationship, the linear term in the approximate force-deflection curve of the isolator will vanish and only a cubic term exists. At the static equilibrium position exhibits zero dynamic stiffness. This is the Duffing equation without linear term and with linear viscous damping, which can be written as

$$\ddot{y} + 2\zeta \dot{y} + c_3 y^3 = F \cos \Omega t . \quad (2.4)$$

The cubic stiffness coefficient is c_3 , the excitation force is F and the excitation angular frequency is Ω . Although the oblique springs, as negative stiffness element, offsets the linear stiffness of the vertical spring in the vicinity of the static equilibrium position and thus enlarges the vibration isolation region, it also introduces a cubic stiffness coefficient c_3 which leads to the bending of resonance peak to higher frequencies and deteriorates the performance of the isolator. This undesirable phenomenon is less pronounced with higher damping and smaller excitation amplitude. Although this stiffening effect due to cubic nonlinearity in the Duffing oscillator is viewed as undesirable, in another point of view, however, in circumstances of transient oscillations and shock, hard spring is preferred; otherwise, the large deflection arising from softness could lead to catastrophic damage^{88, 110}.

Carrella et al. ¹⁰⁰ studied the force transmissibility of the same vibration isolator. It is shown that using oblique springs which are pre-stressed and have a cubic softening nonlinearity is advantageous over using either linear, or linear and pre-stressed springs in that it reduces the undesirable hardening effect for large excursions from the static equilibrium position. As a result, the minimum frequency at which vibration isolation can occur is decreased. Furthermore, they showed that all the quasi-zero-stiffness (QZS) systems with appropriate parameters can outperform the linear system by having a lower jump-down frequency and a lower maximum force transmissibility.

Later, Carrella et al. ¹¹¹ showed the difference between the force transmissibility and the displacement transmissibility (corresponding to two types of excitations encountered, i.e. force excitation and base excitation) of a similar nonlinear isolator with high-static-low-dynamic-stiffness (HSLDS), in which the static equilibrium position locates at when two oblique springs are horizontal. The force-deflection curve of the isolator is approximated by a linear and a cubic term. Therefore, the equation of motion can be described by the Duffing equation

$$\ddot{y} + 2\zeta \dot{y} + c_1 y + c_3 y^3 = F \cos \Omega t . \quad (2.5)$$

The linear stiffness is c_1 . With cubic stiffness coefficient $c_3 = 0$, the equation reduces to a linear forced harmonic oscillator. In a different case with $c_1 = 0$, the cubic stiffness coefficient $c_3 = 1$ and $\Omega = 1$, it reduces to the Ueda oscillator and has a hardening nonlinearity ¹¹².

The Duffing equation was first introduced by the German electrical engineer Georg Duffing in 1918¹¹³. It is used for describing many physical, engineering and even biological problems¹¹⁴. Numerous studies have been carried out on the regular and chaotic motions of this oscillator. For example, Kalmar-Nagy and Balachandran¹¹² summarized the fundamental dynamic behaviors of the Duffing oscillator with linear viscous damping under harmonic excitation. Shen et al.¹¹⁵ stated that chaotic motion may exist when the linear or cubic stiffness coefficient is negative in the Duffing oscillator, especially with homoclinic orbit and/or heteroclinic orbit. Besides, as described by Rega et al.¹¹⁶, Duffing oscillators that have negative linear stiffness and hardening cubic stiffness are unstable, and exhibit multiple static equilibria. One example is the dynamics of a buckled beam or plate when only one mode of vibration is considered, i.e. the snap-through oscillation.¹¹⁶¹¹⁷ Also, as will be reviewed later, chaotic motions were observed in fractional-order Duffing oscillators with restoring force in the form of $-x + x^3$.¹¹⁷⁻¹¹⁹ On the contrary, stable Duffing oscillators exhibit only one equilibrium state¹¹⁶, such as the preceding HSLDS oscillators having positive values of linear and cubic stiffness.

The Duffing equation is also studied by Carrella et al.¹²⁰, in which the benefit from using a HSLDS isolator is demonstrated by a broadened isolation bandwidth and lowered peak transmissibility compared with an equivalent linear isolator, i.e. the one that supports the same mass with the same static deflection as the nonlinear isolator. The displacement transmissibility for a base excited nonlinear isolator with an identical form of dynamic equation is also studied by Milovanovic et al.¹²¹. They defined the regions in which the relative displacement has a finite, an infinite and a non-existent maximum value under the

combined effect of the cubic-to-linear stiffness ratio c_3/c_1 and the linear damping ratio ζ . The result showed that a finite value of damping is needed to give a bounded response for a given stiffness ratio. In contrast, in a linear isolator with $c_3 = 0$, no limit on the amount of damping is required to achieve a bounded response. Moreover, by replacing the linear damping with a cubic damping, the performance around the resonance region is improved while the performance at high frequencies is degraded. The vehicle suspension seat developed by Le and Ahn^{104, 122} also employed a similar negative stiffness structure in which system the Duffing equation is applied to describe its dynamic behavior. It also presented experiments with random and multi frequency excitations in the time domain, and performed numerical simulations of transmissibility curves of the system with and without negative stiffness structure.

2.4.2 Helmholtz-Duffing equation

Except the Duffing equation, the Helmholtz-Duffing equation can also be used to describe the vibration behaviors of some other nonlinear systems. These nonlinear systems include HSLDS isolators realized by negative stiffness mechanisms, and Euler buckled beam under transverse vibration. Literature on the approximate analytical solutions and numerical solutions of the Helmholtz-Duffing equation is also reviewed. Except for regular periodic motion, chaotic motion can also occur for such nonlinear isolators.

2.4.2.1 For NSM structures

Consisting with the QZS nonlinear isolator using Euler buckled beams as negative stiffness corrector by Liu et al.⁸⁶, Huang et al.¹²³ studied the same isolator but taking into account the effect of the detuning (overload or underload) of loaded mass, a practical case when the mass is not balanced at the static equilibrium point that has the lowest stiffness. This changes the system from a Duffing oscillator into a Helmholtz-Duffing oscillator since the restoring force is no longer symmetric. The resulting steady-state response contains a bias term. Besides, as suggested by the results of sinusoidal sweeping experiments, the system can be pure softening, mixed softening-hardening and pure hardening depending on the magnitude of excitation level. The Helmholtz-Duffing equation takes the form of

$$\ddot{y} + 2\zeta\dot{y} + c_1y + c_2y^2 + c_3y^3 = F \cos \Omega t. \quad (2.6)$$

Its difference with the Duffing equation is the addition of a quadratic stiffness term. Huang et al.¹²⁴ also studied the Helmholtz-Duffing equation for an ultra-low frequency nonlinear isolator using a positive mechanical spring and a horizontal sliding beam loaded vertically at the midpoint as negative stiffness element. For small displacements, the force-deflection curve and the stiffness-deflection curve of the system using the first three orders of deflection are comparable with the ones obtained using the full eleven terms. Therefore, for small oscillations it is adequate to use the approximate equation of Helmholtz-Duffing type; however, for large oscillations the frequency response curves (FRCs) obtained using this equation deviates from the ones using the full terms. For large excitations, double jump phenomenon takes place. The FRCs show both softening behavior at low frequency

and hardening behavior when approaching resonance. Besides, they found that the linear spring stiffness and the transverse deflection of beam in the midpoint affect the softening or hardening behavior of the FRCs. As noted by Kovacic et al.¹²⁵, the Helmholtz-Duffing oscillator can behave as hardening or softening depending on the sign of the expression $c_3 - 10c_2^2/9c_1$. Based on this rule, Huang et al.¹²⁴ explained the experimental results that the ultra-low frequency isolator using sliding beam as negative stiffness exhibited softening characteristic under a small static deflection, and vice versa.

As a continuation of static analysis of the QZS nonlinear isolator using linear and unstressed oblique springs to realize negative stiffness by Carrella et al.⁹⁸, Kovacic et al.⁹⁹ modified the oblique springs as reviewed earlier on Carrella et al.¹⁰⁰, and they considered an asymmetric excitation force comprised of a harmonic component and a static component. Consequently, the oscillator is changed from a symmetric Duffing type into an asymmetric Duffing type with no linear term and hardening nonlinearity, which is equivalent to a Helmholtz-Duffing oscillator with linear-quadratic-cubic stiffness terms after coordinate transformation. In this case, coupling between stiffness coefficients exists. The transformation along with the corresponding restoring force, energy level and phase trajectory was demonstrated in detail by Kovacic and Brennan¹²⁶.

2.4.2.2 For Euler buckled beam

Other than negative stiffness mechanisms, the Helmholtz-Duffing equation can also be employed to describe the vibration of buckled beam under transverse excitation. For instance, Mayoof and Hawwa¹²⁷ studied the chaotic behavior of a curved carbon nanotube

subjected to a transverse harmonic excitation. The governing differential equation is derived using an energy approach taking into account the kinetic energy, the energies due to the stretching and the bending of beam. They found that the quadratic term arises from the curvature of beam, and the cubic term arises from the mid-plane stretching. Increasing the curvature weakens the cubic nonlinearity, while its effect on the quadratic nonlinearity is non-monotonic. For a straight carbon nanotube, the equation of motion reduces to the Duffing type. Incidentally, Rega et al.¹¹⁶ also state that the even term arises due to the initial curvature of elastic system in structural applications, such as curved beams, shallow arches and suspended cables, and the cubic term arises due to the stretching of cable axis. They identified that these systems can have three physically admissible stable equilibrium positions in which two are stable; however, for a heavy suspended elastic cable vibrating in its plane, it exhibits only one physically admissible stable equilibrium position because it can resist only tensile forces.

The vibration of buckled beam under transverse excitation has been studied by different researchers. Friswell et al.¹²⁸ used a nonlinear buckled cantilever beam with a tip mass mounted vertically and excited in the transverse direction at its base as the energy harvester. When the mass is adjusted such that the beam is near the critical buckling, the nonlinear harvester has a low resonance frequency. The pre-buckled beam also gives rise to a high level of harvested power and a large bandwidth, compared with the linear harvester which is only efficient at resonance. They also made a comparison of the pre-buckled and post-buckled beam configurations by adjusting the tip mass. Both of experimental results and simulations by solving the equation of motion indicated that, the

pre-buckled system that exhibits hardening nonlinearity generated higher power output than the post-buckled system that exhibits softening nonlinearity. It was explained that for the post-buckled system, the dominant response locates in a single potential well; however, the double potential well should be utilized in order to achieve higher energy harvesting. Ghayesh and Amabili¹²⁹ also investigated the nonlinear dynamics of axially moving viscoelastic beams at the post-buckled state. A distributed transverse excitation load is applied when the beam is traveling with an axial speed large enough to cause its instability and situate it in the supercritical regime. The governing differential equation of motion is built with cubic and quadratic terms after discretization. And the resultant frequency response curves (FRCs) are of softening type. It is identified that the softening behavior is associated with the presence of quadratic nonlinear terms. The softening behavior also decreases as the axial speed increases. Contrarily, when the axial speeds belong in the subcritical regime, the FRCs will be of hardening type instead. Somnay and Ibrahim¹³⁰ studied the nonlinear dynamics of a Gospodnetic-Frisch-Fay beam under sinusoidal excitation. The restoring force was approximated by curve fit with the exact solution in terms of elliptic functions. The fitted curve obtained was a polynomial of the eleventh-order with all odd terms. Busby and Weingarten¹³¹ studied the steady-state response of a nonlinear beam under harmonic excitation. They pointed out the nonlinearity is due to the membrane tension effect induced when the deflection is not small compared with its thickness.

2.4.3 Solutions to Helmholtz-Duffing equation

The steady-state solutions of the Helmholtz-Duffing equation can be solved by

approximate analytical method and numerical method. Except for regular periodic response, chaotic motion may also arise in certain conditions.

2.4.3.1 Approximate analytical solution

Approximate analytical solutions of the steady-state response of the Helmholtz-Duffing oscillator are usually assumed to be a sum of the DC bias and the harmonic components. It involves perturbation techniques such as harmonic balance, averaging, multiple scales, etc. Harmonic balance method (HBM) with the first-order approximation is commonly used, such as in Ravindra and Mallik¹³², Kadji et al.¹³³, Kovacic et al.¹²⁵ and Kovacic et al.⁹⁹. Kovacic et al.¹³⁴ also included a second harmonic. The inclusion of the second harmonic in the solution changed the response but its effect was little in their case. Benedettini et al.¹³⁵ added the period-two and period-three harmonic responses in the HBM solutions, and obtained the FRCs for the amplitude of the corresponding 1/2-subharmonic and 1/3-subharmonic components; besides, the order two and three superharmonic responses were also analytically studied. In general, analytical solutions are concerned with frequency responses of the primary resonance and even of the secondary resonances using amplitude-frequency curves and transmissibility curves, in which the phenomena of curve bending, jump and resonant hysteresis may be observed. For example, Ravindra and Mallik¹³² obtained the force transmissibility in the case of force excitation and the displacement transmissibility in the case of base excitation for a nonlinear oscillator, considering both symmetric and asymmetric nonlinear restoring forces. They found that the asymmetric force may not perform satisfactorily for a base

excitation. Kovacic et al. ¹²⁵ and Kovacic et al. ¹³⁴ studied the resonance responses of an oscillator with quasi-zero stiffness under static and harmonic forces. They found that the system can have a maximum number of one, three, or five steady-state values depending on the static and harmonic forces. As the static force increased from zero, the system changed from pure hardening to mixed hardening and softening, and finally to pure softening. They also studied how the stiffness of system changed at specific points of the amplitude-frequency curves, and confirmed damping can be used to avoid the appearance of jumps.

Much of research work has considered steady-state responses of an asymmetric oscillator. However, studies on the transient responses are few due to the complexity involved. Elias-Zuniga and Martinez-Romero ¹¹⁰ pointed out that the amplitudes of transient oscillation must be estimated to avoid undesirable peaks that could violate design constraints or unstable system behavior. They obtained the time-dependent amplitude-frequency response curves for the primary resonance of the Helmholtz-Duffing oscillator by using Jacobi elliptic function, Fourier series and harmonic balance.

2.4.3.2 Numerical solution

Numerical results, usually obtained by the 4th order Runge-Kutta algorithm ^{116, 133}, can be used to evaluate or confirm analytical results in the frequency domain ^{125, 134}. Yet a greater significance of numerical simulations is to study the bifurcation and chaotic responses of a nonlinear oscillator, although the bifurcation study can also be realized by approximate analytical methods ⁹⁹. In respect of the dynamics of routes from periodic to chaotic

responses, a lot of studies showed that the Helmholtz-Duffing oscillator experienced the cascades of period-doubling bifurcations leading to chaos⁹⁹. Common dynamic measures such as time history, phase portrait, Poincaré section and bifurcation diagram contain rich and qualitative information on the transitions from periodic to chaotic motions. Poincaré map is the intersection, or return point, of a periodic orbit in the state space of a dynamic system, in which the period is determined by the driving force. As described by Cao et al.¹¹⁸, periodic motion forms n discrete points indicating the period of motion is nT ; quasi-periodic motion forms a closed curve; and chaotic motion forms a particular or geometrical structure. Bifurcation diagram provides an overview of essential dynamics with the change of parameters. For instance, these measures were used by Mayoof and Hawwa¹²⁷ to study the influence of increasing excitation amplitude on the dynamic response of the oscillator. They found that increasing excitation amplitude results in period-doubling bifurcation, followed by the chaotic behavior. Ghayesh and Amabili¹²⁹ constructed bifurcation diagrams for increasing the excitation amplitude on the nonlinear system of a post-buckled and axially moving viscoelastic beam with distributed transverse excitation load, with the variations of axial speed. It was shown that increasing the axial speed resulted in less complicated and strange attractors in the bifurcation diagrams. Besides, quasi-periodic, period- n and chaotic motions appeared as the excitation amplitude increased. Kovacic et al.⁹⁹ studied the appearance of period-bifurcation and its development into chaos with decreasing excitation frequency. Besides, they found that period-doubling bifurcation can be entirely eliminated by choosing a suitable damping coefficient. Kadji et al.¹³³ studied the chaotic behaviors of plasma oscillations, in which area the cause of chaotic motion is of interest. They found that increasing the quadratic

nonlinearity led to quasi-periodic oscillations, and the rate of chaos became more important and remained unchanged; while increasing the cubic nonlinearity decreased the windows of chaotic and regular motions. Thus, the quadratic and cubic parameters can be used to manipulate the rate of chaotic motions in a plasma system. Besides, the bifurcation diagram and phase portraits for increasing excitation amplitude showed a quasi-periodic evolution and finally a chaotic one. Rega et al.¹¹⁶ and Benedettini et al.¹³⁵ used control parameter spaces to study the influence of excitation amplitude and excitation frequency on the periodic and chaotic responses. The chaoticity of a system can be examined by the Lyapunov exponents of the system. Chaotic system has a positive Lyapunov exponent. As Sheu et al.¹¹⁷ stated, Lyapunov exponents can be used to distinguish chaotic motion from quasi-periodic motion. Other than the aforementioned tools, basin of attraction was also adopted by Kadji et al.¹³³ and Benedettini et al.¹³⁵ to study the presence of co-existing solutions with sensitivity to initial conditions. The abovementioned features exist in even apparently simple nonlinear system.¹³⁶

2.5 Fractional-order derivative

The fractional-order derivative was raised by Leibniz more than 300 years ago.¹³⁷ The fractional order operator is a nonlocal operator. It has unlimited memory, but can closely resemble the real world in a concise manner.^{118, 119} Fractional calculus has become a popular instrument in many scientific and engineering fields such as viscoelasticity, hereditary physics, structural hysteresis, rheology, electrochemistry, bioengineering, mechanics, automatic control, signal and image processing, quantum evolution of

complex system, etc.^{117, 137} For example, Bagley and Torvik¹³⁸ have used fractional derivative models to describe the frequency-dependent damping behavior of materials and systems very well. This section will review literature that considers fractional-order derivative in the Duffing oscillator and the Helmholtz-Duffing oscillator. Relevant studies using approximate analytical and numerical approaches to study the periodic and chaotic behaviors of such nonlinear systems will be presented. First of all, the definitions of the fractional-order derivative is introduced as below.

2.5.1 Definitions

Several definitions of fractional-order derivative are widely used. One of them is the Riemann-Liouville (RL) definition,^{8, 118, 139}

$${}_a D_t^\alpha f(t) = \frac{1}{\Gamma(n-\alpha)} \frac{d^n}{dt^n} \int_a^t \frac{f(\tau)}{(t-\tau)^{\alpha-n+1}} d\tau, \quad \alpha > 0, \quad n-1 < \alpha < n, \quad n \in \mathbb{N}, \quad (2.7)$$

where α has non-integer values, n is the smallest integer larger than q , and $\Gamma(\cdot)$ is the Gamma function; the subscripts to the left and right of D are the lower- and upper-bounds in the integral. The equation implies that the history has an impact on the current state. Moreover, due to the $(t-\tau)^{n-\alpha-1}$ term, the integro-differential operator has fading or decaying memory in that it weighs the recent past more heavily than the distant past.^{8, 140} As noted by Zhang and Shimizu¹⁴¹, the RL definition renders an infinite value for the integrand at upper limit $\tau = t$; besides, the resulting integral will diverge if the sequence of integration and differentiation is switched. The RL definition usually causes difficulties for practical application, albeit meaningful in physics. Furthermore, at $t = 0$ it may

encounter trouble to the instantaneous response of system due to the fact that the fractional derivative of a constant is not identically zero.¹³⁷ Shokooh and Suarez¹⁴² proposed to use the initial velocity to replace the fractional derivative at $t = 0$, since the value of the latter is unknown. They verified that small variations in the initial data would not affect the result since the numerical models adopted are sufficiently stable. This problem can also be avoided by using the Caputo's definition, which takes the form

$${}_a D_t^\alpha f(t) = \frac{1}{\Gamma(n-\alpha)} \int_a^t (t-\tau)^{n-\alpha-1} \frac{d^n f(\tau)}{d\tau^n} d\tau, \quad \alpha > 0, \quad n-1 < \alpha < n, \quad n \in \mathbb{N}. \quad (2.8)$$

However, due to the presence of the integral and the gamma function, numerical techniques are difficult to operate on the RL definition and the Caputo's definition.¹³⁷ To realize discretization of the fractional order operators, the Grunwald-Letnikov (GL) definition is the most straightforward to use numerically.¹¹⁸ It takes the form

$${}_a D_t^\alpha f(t) = \lim_{h \rightarrow 0} h^{-\alpha} \sum_{j=0}^{[(t-a)/h]} (-1)^j \binom{\alpha}{j} f(t-jh), \quad (2.9)$$

where h is the time increment, $[x]$ is the truncation of x , and the binomial coefficients

$$\binom{\alpha}{j} = \frac{(-1)^{j-1} \alpha \Gamma(j-\alpha)}{\Gamma(1-\alpha) \Gamma(j+1)}.$$

For a great varieties of functions in real physical and engineering applications, the three definitions are equivalent.¹³⁷ Consequently, one can use the RL definition for problem formulation, and turn to the GL definition for numerical solution.¹⁴³

Here below shows two basic properties of the fractional-order derivative:¹⁴⁴

(1) Linearity. For any constants c and d we have

$${}_a D_t^\alpha [cf(t) + dg(t)] = c {}_a D_t^\alpha f(t) + d {}_a D_t^\alpha g(t). \quad (2.10)$$

(2) Index law. With restrictions on initial values, the fractional-order differentiation operators commute, i.e.

$${}_a D_t^\alpha [{}_a D_t^\beta f(t)] = {}_a D_t^\beta [{}_a D_t^\alpha f(t)] = {}_a D_t^{\alpha+\beta} f(t). \quad (2.11)$$

On the other hand, it is usually easier to describe the fractional integro-differential operation in the Laplace domain.¹¹⁸ With vanishing initial conditions, i.e. all of the derivatives of the function $f(t)$ equals to zero at $t = a$, the Laplace transform has a simplified form as,

$$L\{{}_a D_t^\alpha f(t)\} = s^\alpha L\{f(t)\}. \quad (2.12)$$

2.5.2 Research approach

Based on these definitions, numerical simulations and approximate analytical methods can be used to solve the fractional-order differential equations (FODEs). Numerical methods for fractional order oscillators are quite a few, for instance, multi-step numerical schemes for a single-degree-of-freedom (SDOF) fractional oscillator in the time domain¹⁴⁵, discretization¹⁴⁶, predictor-corrector method¹¹⁷, linear approximation of fractional order transfer function in the frequency domain^{143, 147}, etc. Nevertheless, frequency domain methods are said to be not always reliable in detecting chaos.¹¹⁹ One disadvantage of numerical simulations is that they are unable to relate structural parameters with the

underlying physics of the problem.¹⁴⁸ Moreover, they cannot arrive at unstable solutions. Although these solutions are not physically realizable, they do offer insight into the global behavior, such as the determination of domains of attraction.¹³⁶ On the other side, approximate analytical approach has no such problems. It usually uses different perturbation techniques, such as Multiple Scales and Averaging methods that are developed in the time domain. Frequency domain methods can also be used for solving FODEs, e.g., the Multiple Time Scales and the Lindstedt Poincaré perturbation methods (MSLP), thus nonlinear behaviors can be readily interpreted.¹⁴⁸

As we are interested to learn about the periodic and chaotic behaviors of the Duffing oscillator and the Helmholtz-Duffing with fractional-order derivative, literature on the two kinds of oscillators is reviewed as follows.

2.5.3 Duffing oscillator with fractional-order derivative

Shen et al.¹¹⁵ adopted the averaging method with the separation of periodic and aperiodic components to obtain the frequency response equation for steady-state solutions of the Duffing oscillator with fractional-order derivative. Equivalent damping coefficient and equivalent stiffness coefficient were calculated involving the effect of fractional-order derivative. The FRCs obtained by approximate analytical and numerical solutions showed that the fractional-order parameters could affect both of the resonance amplitude and the bending degree simultaneously. Based on the property of sequential fractional derivatives, Cao et al.¹¹⁸ transformed the Duffing equation with fractional order damping into three state-space equations with zero initial conditions. As the fractional order operator cannot

be implemented directly in time-domain simulations, by direct discretization using the 10th order CFE-Euler methods to approximate the fractional order operator and by using the 4th order Runge-Kutta method, the dynamics was simulated in MATLAB/Simulink. Bifurcation diagrams for increasing the fractional order, excitation frequency and excitation amplitude were generated. The oscillator exhibited alternating periodic and chaotic motions with the increase of the fractional order, during which a period doubling route to chaos and an inverse period doubling route leaving chaos were observed. El-Sayed et al. ¹¹⁹ proposed a discretization method to approximate the right-hand side of the state-space equations with piecewise constant arguments for the fractional-order Duffing oscillator. Bifurcation diagrams of the discrete system showed that increasing the fractional order stabilized the chaotic system. Sheu et al. ¹¹⁷ used a predictor-corrector method for the numerical solution of fractional integral equations transformed from the original fractional-order Duffing equation. The bifurcation diagram showed that the size of attractor trended to enlarge as the fractional order increased. Besides, a period doubling route to chaos was found, with many period-three windows observed.

2.5.4 Helmholtz-Duffing oscillator with fractional-order derivative

Dal ¹⁴⁹ used the Multiple Time Scales method (MS) to study the free vibration of the Helmholtz-Duffing equation with fractional-order damping. The approximate analytical result was compared with numerical solutions by both variational iteration method (VIM) and finite difference method (FDM). Ogam et al. ¹⁴⁸ derived the frequency response equation for the cracked structure dynamics, described by the Helmholtz-Duffing

equation with a fractional-order derivative term close to unity. The Multiple Time Scales-Lindstedt Poincaré perturbation method (MSLP) was employed to solve the dynamic equation in the frequency domain, valid for both weakly and strongly nonlinear systems. The stiffness nonlinearity arose from the contact of cracked surfaces, and was modeled using the Hertz contact theory. The cubic term gave a soft spring behavior, which explained the downward shift of resonance frequency as the excitation amplitude increased. This study has a practical significance in the prevention of catastrophic failure due to the development of crack-like defects in critical complex installations like aircraft and steel bridges during service. Yang and Zhu ¹³⁷ studied the vibrational resonance (VR) phenomenon in over- and under-damped Duffing systems with fractional-order damping. Kovacic and Brennan ¹²⁶ summarized current studies on the resonance, bifurcation and chaotic motions of the Helmholtz-Duffing oscillator.

2.6 Chapter summary

This chapter firstly reviews mechanical properties of knitted spacer fabrics regarding compression and impact behaviors. Secondly, high-static-low-dynamic-stiffness (HSLDS) structures and systems, and the Duffing equation and the Helmholtz-Duffing equation adopted to describe the vibration behavior of such isolators are reviewed, using analytical and numerical approaches. Moreover, the time-dependent viscoelasticity property can be described using the fractional-order derivative. Relevant literature on periodic and chaotic responses of the fractional-order Duffing oscillator and the fractional-order Helmholtz-Duffing oscillator is lastly reviewed.

Weft-knitted spacer fabrics exhibit both nonlinear stiffness and the viscoelasticity. Their vibration behavior under forced vibration has not been studied by researchers yet. However, nonlinearity is very common for materials and systems. Different nonlinear vibration systems have been extensively studied. Nonlinear isolator designed to have HSLDS helps improve vibration isolation. Thus, the mechanisms of such systems including Euler buckled beam and negative stiffness devices are reviewed here. Models to describe their vibration behaviors and the methods of solving them are also presented to guide the solutions of vibration models for weft-knitted spacer fabrics in this study.

CHAPTER 3 EXPERIMENTAL DETAILS

3.1 Introduction

This chapter presents experimental details, including the design and fabrication of weft-knitted spacer fabric samples in Section 3.2, and the setup, methodology and results of vibration experiment in Sections 3.3 and 3.4. Firstly, to fulfill the objective of obtaining relatively high thickness of weft-knitted spacer fabric thus reducing the dynamic stiffness and the resonance frequency, fabric structure is conceptualized and optimized. Based on the design idea, weft-knitted spacer fabrics having different fabric thicknesses are fabricated on a computerized flat knitting machine in which the distance between the front needle bed and the back needle bed cannot be changed. Next, to study the vibration isolation performance of spacer fabric, the sinusoidal sweep test is carried out using an electromagnetic vibration exciter to record the transmissibility curves of the mass-spacer fabric systems. Factors of sweep rate and direction, and material fatigue of spacer fabrics are evaluated. The effects of load mass, fabric thickness and excitation level on transmissibility curves are then analyzed.

3.2 Fabric manufacture

The section will present the design and fabrication of weft-knitted spacer fabrics using flat knitting technology. First, to achieve the objective of high fabric thickness for weft-

knitted spacer fabric, a design idea is presented in Section 3.2.1 by increasing the linking distance of spacer monofilament and using elastic yarns to knit two outer layers. Secondly, an optimized fabric structure is chosen by comparing the thickness and appearance of three candidates in Section 3.2.2. Following this, two different spacer fabrics are manufactured with linking distance varied in Section 3.2.3. Dimensional properties such as fabric thickness, areal mass and stitch densities are then measured. Section 3.2.4 presents the lamination of two identical spacer fabrics as one sample for vibration test.

3.2.1 Design idea

To reduce the stiffness of weft-knitted spacer fabrics and obtain a low resonance frequency, relatively thick spacer fabric should be used. However, as discussed in Section 2.2.2 of the previous chapter, the thickness of weft-knitted spacer fabrics is usually not high due to limited adjustment of the distance between two needle systems in a weft knitting machine. Besides, the length of continuous float stitches which crosslink two face layers on the needle beds could not be too long. Due to these twofold limitations, the thickness of a regular weft-knitted spacer fabric is within 10 mm for the knitting machine used in this study.

To achieve the objective of higher thickness, a special structure concept is firstly suggested. As shown in Figure 3.1(a), the spacer structure suggested is constructed with two outer layers knitted from elastic yarn and an inner or spacer layer knitted with symmetrical monofilaments in “X” shape. As the outer layers are knitted from elastic yarn, after a steaming treatment, the outer layers would shrink, resulting in a rotation of the

inclined monofilament yarns to the thickness direction of the fabric, as shown in Figure 3.1(b). As a result, fabric thickness is increased. If a different linking distance of spacer yarns is used, spacer fabric with different thickness can be easily obtained.

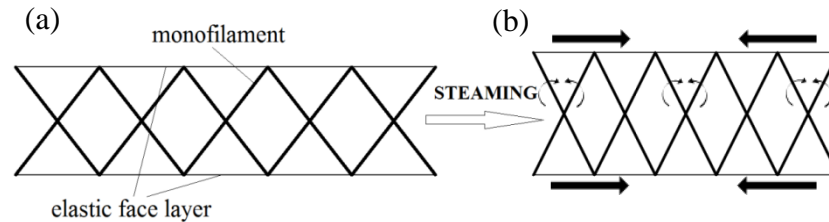


Figure 3.1 Design concept of weft-knitted spacer fabric structure: (a) before steaming treatment; (b) after steaming treatment.

3.2.2 Structure optimization

As previously discussed, the linking distance of spacer monofilament should be long enough to obtain high fabric thickness. Thus, a linking distance of 20 needle stitches is used here. Fabric structure is varied by changing the density and tuck position of spacer monofilament, while the face layer is identical. This trial test is carried out in order to select a suitable fabric structure as vibration isolator.

Three candidate weft-knitted spacer fabrics, i.e. Spacer-20f, Spacer-20h and Spacer-20h_var, are designed. The number indicates the stitches between two tucking points on the same needle bed for one monofilament. In the case when all needles knit tuck stitches, “f” is designated, which means full linking density. In the case when only half numbers of needles knit tuck stitches, “h” is designated, which means half linking density. Figure 3.2(c) shows the variants by changing tuck locations.

All of them have spacer monofilaments tuck every other nine needles on two needle beds alternately. In Spacer-20h, ten monofilaments comprise one course, in which the tuck positions are evenly distributed. Its periodic pattern is captured in Figure 3.2(b). By rearranging the tuck positions, Spacer-20h_var is obtained as in Figure 3.2(c). Spacer-20f, as shown in Figure 3.2(a), has twofold monofilament picks, and twofold evenly distributed tuck stitches.

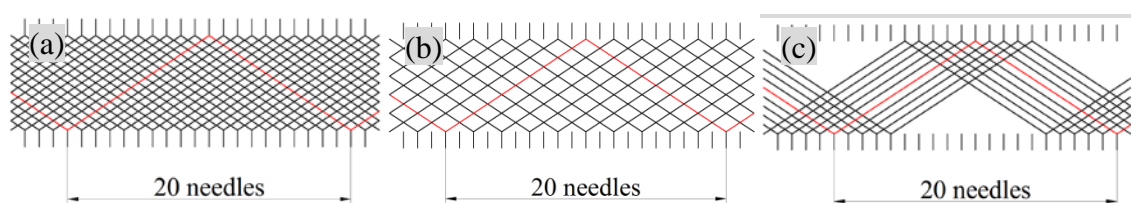


Figure 3.2 Tuck patterns for constructing three candidate weft-knitted spacer fabrics: (a) Spacer-20f; (b) Spacer-20h; (c) Spacer-20h_var.

These fabrics are knitted on a STOLL CMS 822 computerized flat knitting machine of gauge 14. Monofilaments tuck and link together two outer single jersey layers separately knitted on the front and back needle beds of the machine. Outer layer structures are single jersey stitches using the multifilament containing one 100D nylon multifilament yarn and one 30D Spandex/70D nylon covering yarn. Polyester monofilament of 0.12 mm in diameter produced by the Nantong Xindike Special Fibre Co., Ltd. is used as the spacer yarn. The tensile behaviors of these yarns are shown in Figure 3.3. It is found that the Spandex nylon covering yarn used has a very small tensile modulus in a wide range of strain.

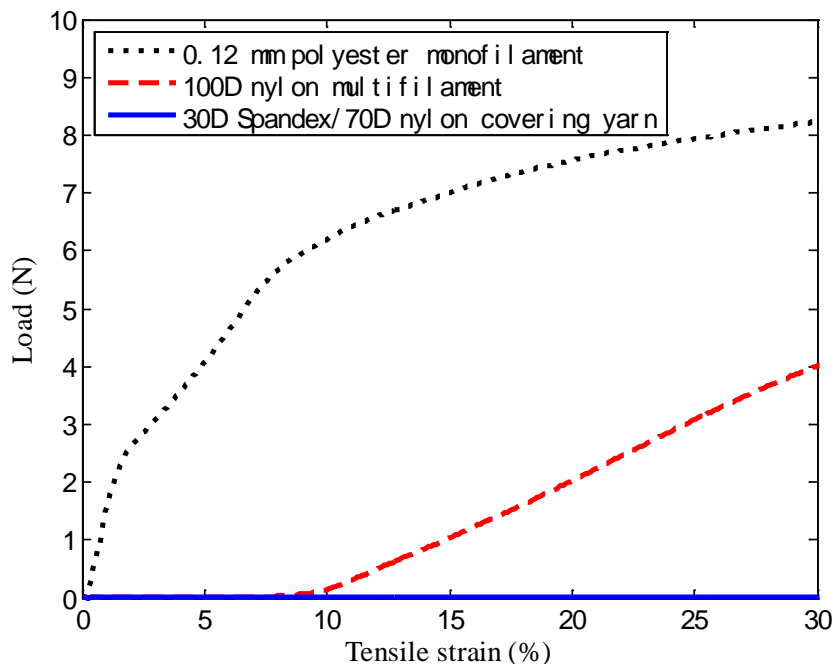


Figure 3.3 Tensile load vs. strain curves of three types of yarns used for knitting weft-knitted spacer fabrics.

In order to knit the spacer fabrics with required quality, proper settings of knitting parameters are important. Among a series of knitting parameters, NP value, i.e. cam setting, is the most important parameter demanding correctly be set as it directly determines fabric density and loop length. Based on trial tests, it is found that NP value set at 9.0 for spacer layer, and NP value set at 11.0 for outer layers could give a better knitting effect. Too large or too small NP value for spacer layer could make outer layers rough or cause the damage of monofilaments. Special care should also be taken of for other machine settings such as yarn feeding routes and tension, fabric take-down tension and machine speed to minimize fabric defects.

After knitting, all fabric samples are subjected to a steaming treatment using a steam iron

at a free state. The temperature of the steam iron is kept at around 50°C to avoid yarn damages. Elastic yarns in the outer layers shrink during this process, which leads to fabric thickening. After the steaming treatment, the fabric samples are relaxed under a constant temperature and humidity condition of 20°C and 65% relative humidity for one week to allow for further shrinkage, but at a lesser and slower extent. After full relaxation, spacer fabrics of stable dimensions are obtained. Fabric basic properties are listed in Table 3.1.

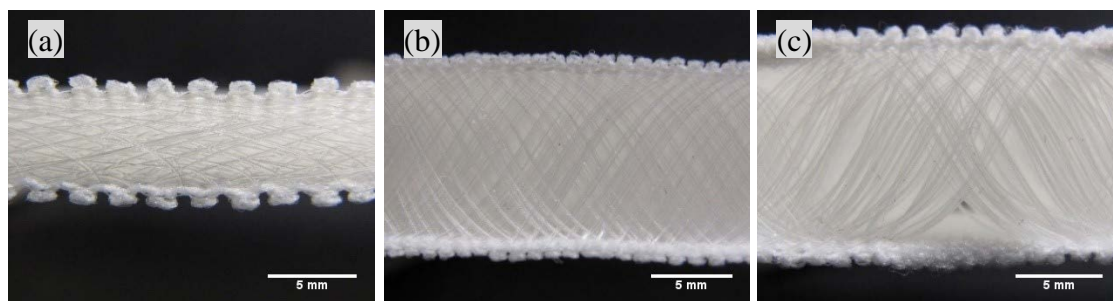


Figure 3.4 Three candidate weft-knitted spacer fabrics in the course views: (a) Spacer-20f; (b) Spacer-20h; (c) Spacer-20h_var.

Figure 3.4 shows the course views of these spacer fabrics. Their structural parameters are also listed in Table 3.1. Spacer-20f has relatively small thickness which limits the range of displacement under axial vibration. Spacer-20h_var generates empty areas void of tuck stitches, making it unsuitable for bearing axial load. For Spacer-20h as shown in Figure 3.4(b), the cross-over structure of spacer monofilaments in the course direction balances axial forces so that transverse shift along the courses of fabric does not arise. As a result, Spacer-20h is selected as the basal samples for vibration tests.

Table 3.1 Fabric basic properties.

Fabric type	Course density (wales/cm)	Wale density (courses/cm)	Areal mass (g/m ²)	Thickness (mm)
Spacer-20f	5.63 (0.08)	23.37 (0.53)	1102.27 (18.11)	7.10 (0.13)
Spacer-20h	7.15 (0.12)	26.10 (0.91)	1020.15 (21.99)	12.01 (0.17)
Spacer-20h_var	7.82 (0.19)	28.26 (0.90)	612.67 (14.58)	13.23 (0.21)

Note: Standard deviations are given in parentheses.

3.2.3 Linking distance variation

The difference in fabric structure is achieved by varying the linking distance of monofilaments from 20 needles to 12 needles long, while keeping materials and the other knitting conditions identical. Two structures are used in the vibration experiments. The knitting notations are shown in Figure 3.5.

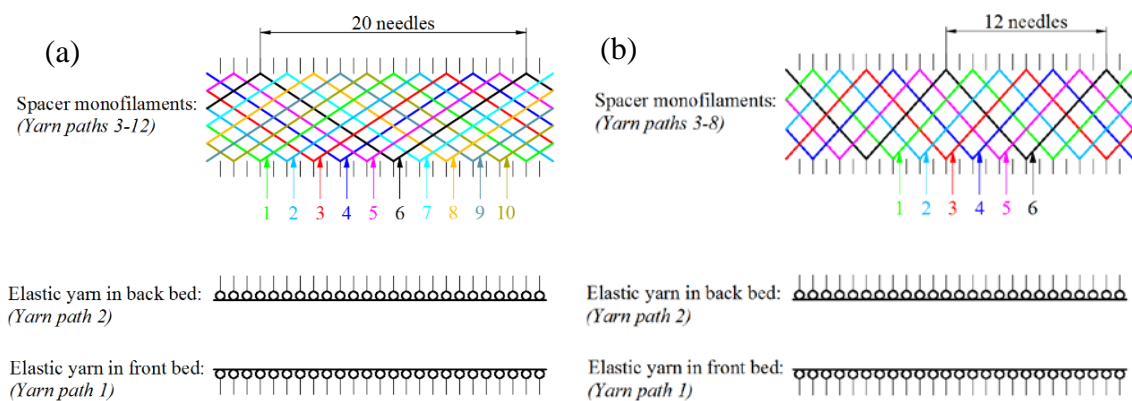


Figure 3.5 Fabric structures with different linking distance of spacer monofilaments: (a) Spacer-20h; (b) Spacer-12h.

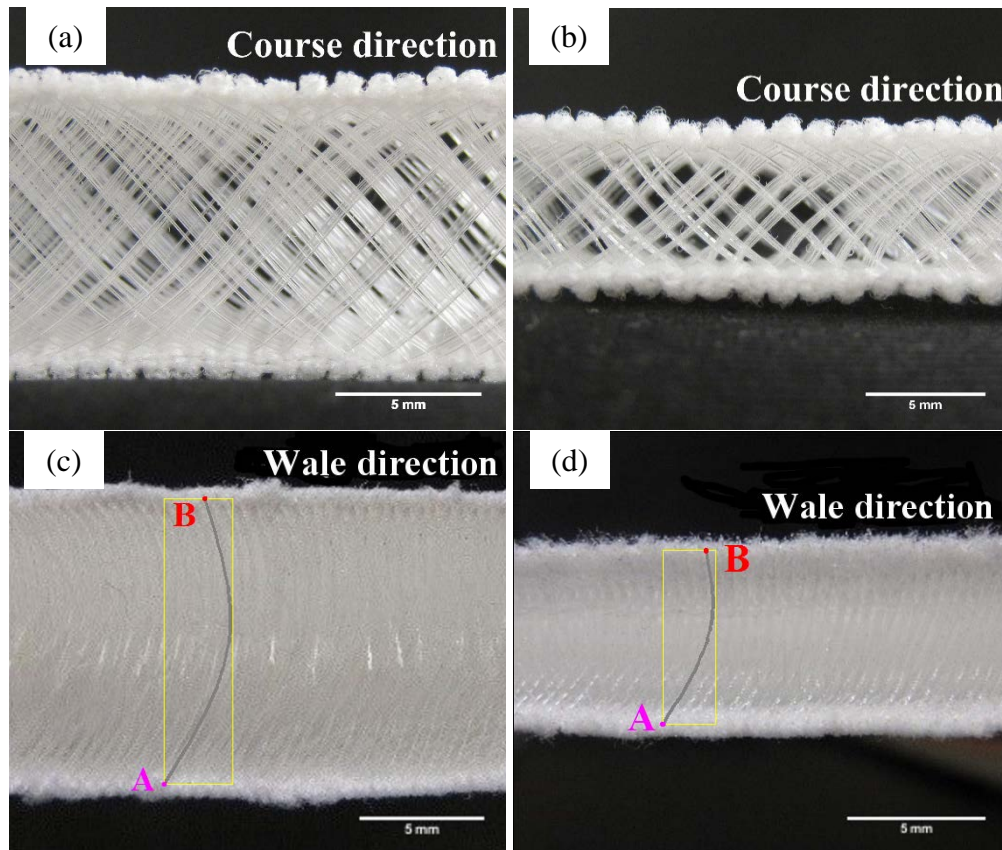


Figure 3.6 Cross-sectional views of spacer fabrics produced: (a) and (c) Spacer-20h; (b) and (d) Spacer-12h.

Figure 3.6 also shows the cross-sectional views of the as-fabricated weft-knitted spacer fabrics. It can be found that the cross-sectional views along the course direction and the wale direction are different. Along the course direction, spacer monofilaments have a crossed structure. However, along the wale direction, i.e. the take-up direction for the whole fabric, spacer monofilaments have a curved shape. Moreover, linking points A and B of each monofilament with two outer layers are not located on the same vertical line.

Along the wale direction (Figure 3.6(c) and (d)), the monofilaments should have exhibited

bilateral symmetry characteristic of “C”-shapes in an ideal-case scenario. Monofilaments connect two outer layers by tuck stitches. The floating length between adjacent tuck stitches forms a shallow arc, stemming from the bending moment developed on tuck stitches. However, the two endpoints of a monofilament segment may not be in a strictly vertical alignment in reality. As a result, transverse instability exists along the wale direction of fabric. The reasons are as follows:

- (1) The knitting of stitches in one outer layer always lags behind that in the other outer layer of spacer fabric. Due to the pulling force by the draw-off roll, the earlier knitted stitches will be drawn off first. As a result, the two opposite stitches from the two outer layers cannot be aligned. For the same reason, the two endpoints of a monofilament segment is also not aligned. Moreover, due to the limited control over steaming skills, imperfections are easily introduced to spacer fabrics. Consequently, one uncut piece of spacer fabric exhibits a preference regarding to the right or to the left along the wales would the monofilaments flatten under the perturbation of axial force. In addition, another source of imperfection comes from a tilted load mass.
- (2) Another important reason is the uncertain boundary conditions (neither pin-ended nor fixed-ended) of monofilament segment with two outer layers. Monofilament segments are in a continuous filament but only separated by tuck stitches at periodic intervals. Consequently, one uncut piece of spacer fabric exhibits a preference regarding to the right or to the left along the wales would the monofilaments flatten under the perturbation of axial force. Accompanying axial deformation, the aforementioned imperfection of the monofilament arc shape leads to lateral shifting of one outer layer relative to the other. As the compression force increases, it resembles the buckling of

a fixed-free column. Under stress, the monofilament segments depart readily from the original “C”-shaped symmetric construction, and transform into half “C” shapes, i.e. the tangent of one endpoint forms a right angle with the connected outer layer.

Transverse instability could happen to certain types of warp-knitted spacer fabric as well, both along the wale and course directions. This adverse behavior could be avoided by proper design, so as to incorporate balanced and stable structures for monofilaments. Yet for weft-knitted spacer fabric, few countermeasures could be taken against transverse shift along the wale direction. Therefore, the dislocation between linking points A and B should be taken into consideration when preparing the fabric samples for vibration testing.

Basic dimensional properties such as fabric thickness, areal mass, course density and wale density of two kinds of weft-knitted spacer fabrics are shown as in Table 3.2. As spacer fabric has longer linking distance, fabric thickness, areal mass are both increased. Besides, course density is slightly increased as well. However, wale density does not change much when linking distance is varied.

Table 3.2 Basic dimensional properties of two weft-knitted spacer fabrics with different linking distances.

Fabric type	Course density (wales/cm)	Wale density (courses/cm)	Areal mass (g/m ²)	Thickness (mm)
Spacer-20h	7.15 (0.12)	26.10 (0.91)	1020.15 (21.99)	12.01 (0.17)
Spacer-12h	6.66 (0.06)	25.90 (0.42)	673.27 (31.33)	6.66 (0.18)

Note: Standard deviations are given in parentheses.

3.2.4 Fabric lamination

It is learned earlier that under the perturbation of axial force, an imperfect weft-knitted spacer fabric exhibits a preference regarding to the right or to the left along the wales that it would flatten. In order to circumvent the undesirable transverse shift along the wale direction of the spacer fabric structure during vibration tests, two identical spacer fabrics were bonded together using a double-sided adhesive tape as shown in Figure 3.7(a). Thus, point A and point C are located on the same vertical line. In this case, the topmost layer and the base layer of the laminated fabric can maintain opposite to each other under the mass loaded, as shown in Figure 3.7(b). By this way, the transverse motion of the spacer fabric has no interference on the vertical motion of the mass-spacer fabric system.

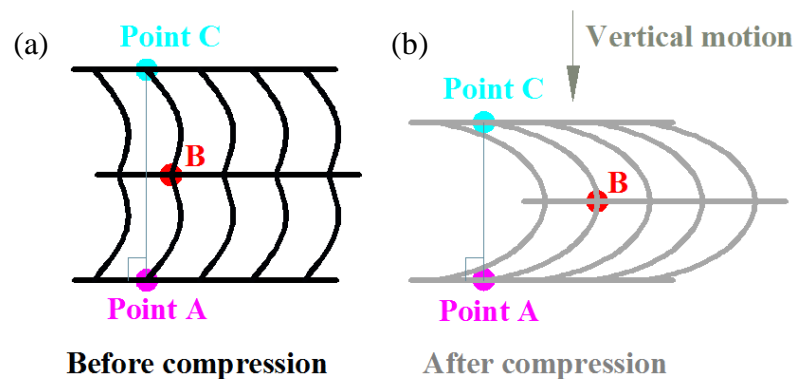


Figure 3.7 Schematic of fabric structure with two identical fabrics laminated together:

(a) before compression; (b) after compression.

3.3 Experimental setup and method

Below introduces the test setup, the typical transmissibility curve, the evaluation of the factors of sweep rate, sweep direction and material fatigue on the transmissibility curve, and the quasi-static compression test method.

3.3.1 Test setup

A vibration test system EM-400F3K-30N80 manufactured by the King Design Instrument Technology (Kun Shan) Co., Ltd was used to measure the vibration transmissibility of laminated weft-knitted spacer fabrics. The system mainly consists of an electromagnetic vibration shaker equipped with a vertically connected 35 cm × 35 cm square platform made of aluminum, a digital vibration controller VCS 102, a high power amplifier and protector, and a cooling blower. The schematic of the system is shown in Figure 3.8. The controller VCS 102 has one output channel (Output) and two input channels (Input 1 and Input 2), and generates voltage signals transmitted through the power amplifier to drive the shaker platform to vibrate at predefined frequencies and excitation levels. Then, acceleration signals measured by two accelerometers respectively mounted on the shaker platform (Accelerometer 1) and the load mass (Accelerometer 2) were sent back through Input 1 and Input 2 to the controller for data acquisition. It should be noted that the Accelerometer 1, Input 1, controller, and Output form a feedback control system to ensure that the shaker platform vibrates correctly according to the predefined profile. The controller was also connected to the test software of PC for waveform display and analysis. The cooling blower cooled down the shaker for safety purpose.

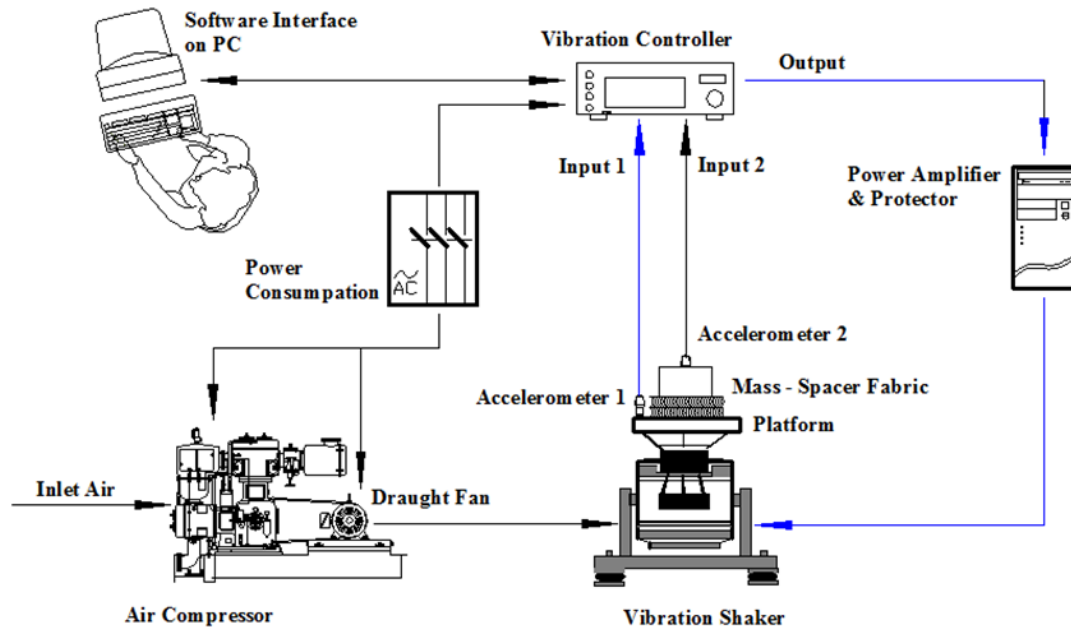


Figure 3.8 Schematic of the vibration testing system.

The mounting of two accelerometers for measuring the acceleration transmissibility of the mass-spacer fabric system is shown in Figure 3.9. The spacer fabric to be tested is placed on the center of the shaker platform and top-loaded with a metallic mass. The accelerometer stud-mounted on the shaker platform was an accelerometer Brüel & Kjær 4514-004 with a sensitivity of 50.9 mV/g and an acceleration range of 100g, where g is the gravitational acceleration (9.81 m/s^2). The other accelerometer PCB 352A56 with a sensitivity of 101.7 mV/g and an acceleration range of 50g was adhesively mounted on the center of the load mass using petro wax.

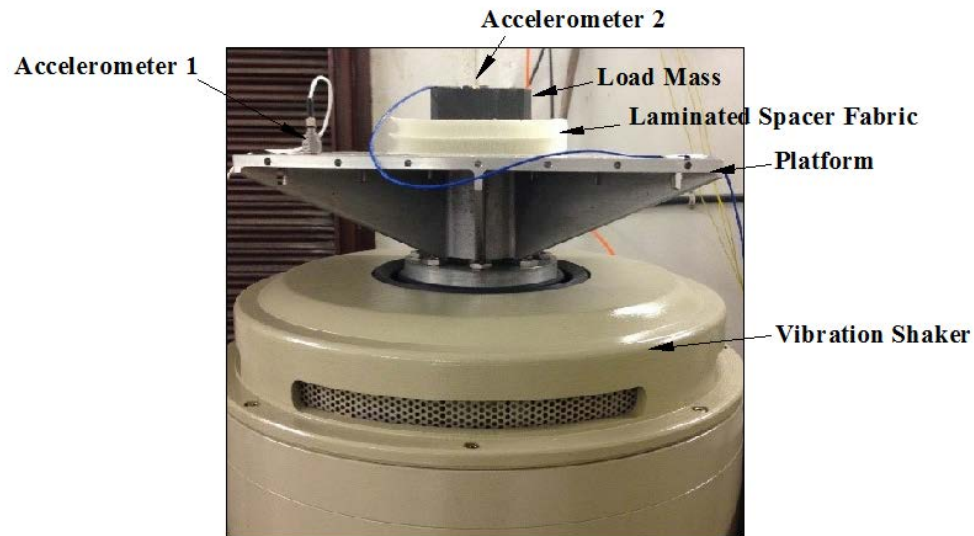


Figure 3.9 Photo of the mass-spacer fabric system and the mounting of two accelerometers.

The size of fabric sample and that of load mass were selected by referring to the International Standard BS EN ISO 13753:2008, “Mechanical vibration and shock. Hand-arm vibration. Method for measuring the vibration transmissibility of resilient materials when loaded by the hand-arm system”. According to this standard, the material to be tested shall contain a circular area of no less than 45 mm in radius; besides, the load block shall be a circular cylinder with a radius of 45 mm and a mass of 2.5 kg. However, due to the nearly orthotropic material properties of weft-knitted spacer fabric structure, it would be appropriate to have fabric samples cut into a square shape rather than a circular one. Consequently, spacer fabric samples used were cut into a size of 150 mm × 150 mm. In order to weaken the edge effect and avoid mass eccentricity, square steel blocks with a surface area (90 mm × 90 mm) smaller than that of spacer fabric samples, but with different masses were used as the load masses.

The shaker was excited by sinusoidal sweeps from 4 Hz to 500 Hz with a sweep rate of 1.0 Oct/min. Each sweep event had a constant excitation level, namely, 0.1g, 0.2g or 0.3g. The profiles of excitation level vs. frequency are shown in Figure 3.10. It should be noted that excitation amplitude decreases as the driving frequency increases. Five different load masses from 1 kg to 5 kg were used. Acceleration transmissibility values at desired frequencies were obtained during tests. Three replications were carried out for each testing condition.

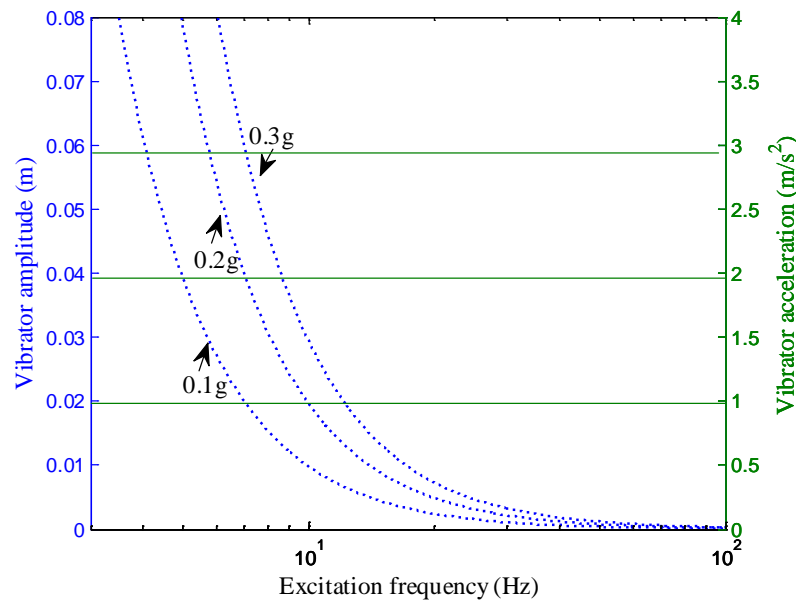


Figure 3.10 Amplitude-frequency curves for three excitation levels, 0.1g, 0.2g and 0.3g.

In addition, in order to better understand how the nonlinear behavior of spacer fabrics affects the vibration isolation performance, a quasi-static compression test was also conducted for the laminated fabrics on an Instron tester 5566 installed with two compression platens. The compression speed was set as 12 mm/min and the maximum compression strain was chosen as 60% of the original fabric thickness. The sample size used was 90 mm × 90 mm, the same as that of load blocks.

3.3.2 Typical transmissibility curve

The vibration isolation performance of the weft-knitted spacer fabrics was evaluated by the acceleration transmissibility T which is defined as the ratio of the acceleration of the load mass to that of the shaker platform. As shown in Figure 3.11, a typical curve of T as a function of the excitation frequency obtained for Spacer-12h when tested under 0.3g excitation level and 2 kg load mass is selected as an example to explain the vibration isolation performance of this type of spacer fabric. The corresponding phase response curve between excitation and response signals is also shown. Although the tests were conducted from 4 Hz to 500 Hz, all the acceleration transmissibility curves shown afterwards are only until 100 Hz to get a better demonstration. From Figure 3.11, it can be seen that under low excitation frequencies, the acceleration transmitted from the platform to the mass approximately equals the excitation level, and the response of load mass is nearly in phase with the platform. However, with increasing the excitation frequency, the transmissibility and the phase angle increase rapidly until the resonance peak. The transmissibility reading above one unit ($T > 1$) indicates that the vibration is amplified. At resonance frequency f_r (15.2 Hz), the transmissibility of the mass-spacer fabric system reaches the peak value T_{\max} (4.1), where the response should have a 90° phase shift (experimental value 87.9°) with reference to the sinusoidal excitation. Further elevating the excitation frequency above f_r , the transmissibility starts to decline. The frequency at which the transmissibility equals one unit ($T = 1$) is called the crossover frequency f_c (30.3 Hz), which defines the boundary between the amplification region and the isolation region. Vibration isolation ($T < 1$) takes effect when the excitation frequency

is larger than f_c .

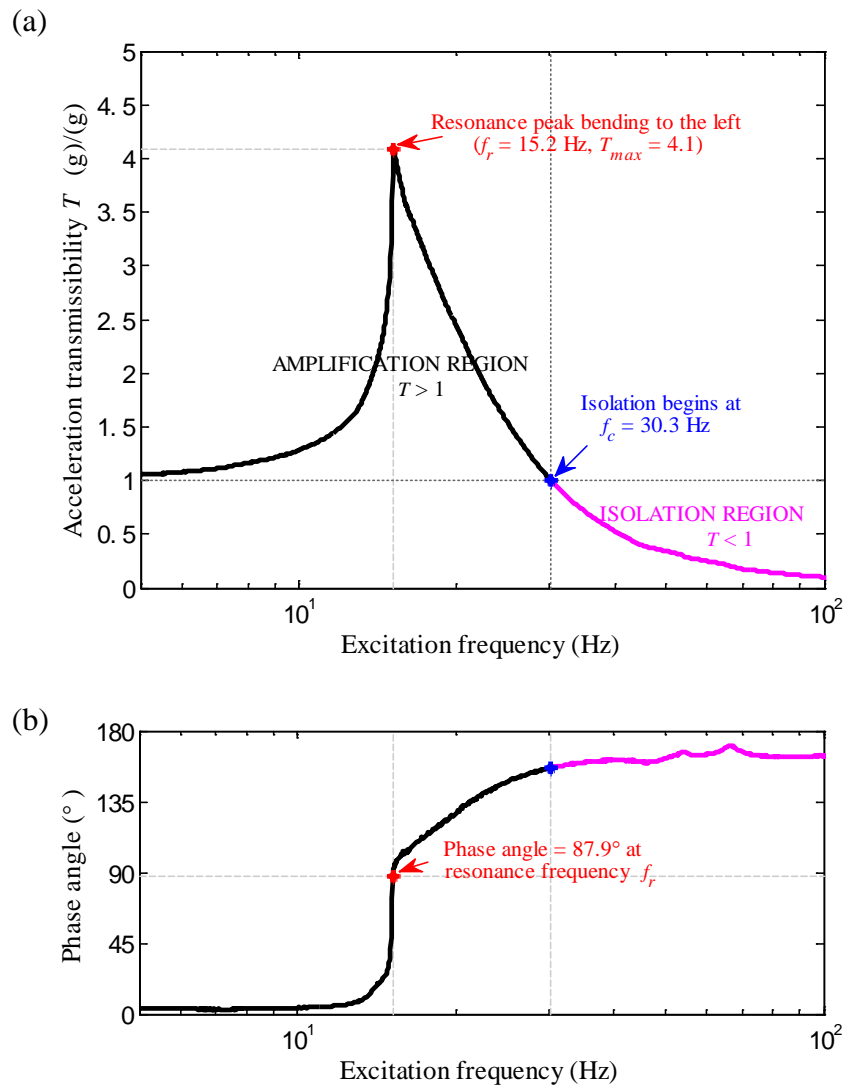


Figure 3.11 (a) Typical acceleration transmissibility curve and (b) the corresponding phase response curve for Spacer-12h under 0.3g excitation level and 2 kg load mass.

To achieve a wider isolation region, the resonance frequency f_r should be reduced. In a linear single-degree-of-freedom (SDOF) system, the curve shape near the resonance peak looks symmetric. In such a kind of system⁹⁸, f_r is related to the dynamic stiffness k_d

and the load mass m which is defined by equation $f_r = \frac{1}{2\pi} \sqrt{\frac{k_d}{m}}$. Observing the curve in Figure 3.11, it can be found that the curve shape near the resonance peak is asymmetric and bent to the left side, indicating that the mass-spacer fabric system is a nonlinear one. Although in a nonlinear system, the calculation of f_r becomes more complicated, f_r is still affected by k_d and m . Besides, under a low excitation level, such a mass-spacer fabric system can be assumed as a linear one. The reduction of f_r implies either decreasing k_d or increasing the load mass. Since the load mass is predefined by the working condition, decreasing k_d should be the only approach to a better isolation performance.

Therefore, an ideal isolator should keep the dynamic stiffness as low as possible. However, due to the nonlinearity of weft-knitted spacer fabric, the value of k_d is affected by the load mass, the fabric thickness and the excitation level. For this reason, Section 3.4 will discuss the effects of these factors on the isolation performance of the mass-spacer fabric system. For better comparison, two physical quantities, i.e. the resonance frequency f_r and the crossover frequency f_c , are selected. Since the amplification region is to be avoided during the use, the peak transmissibility T_{\max} is not a concern in this study.

3.3.3 Sweep rate and direction

The examination of the effect of sweep rate was carried out using three sweep rates

successively, 0.5, 1.0 and 1.5 Oct/min, on one same piece of stacked weft-knitted spacer fabric. The driving frequency varied logarithmically rather than linearly with time. The testing condition of 0.1g excitation level and 2 kg mass was used. Sweeps in both directions were performed, i.e. from lower to upper limit of frequency values and the reverse manner. In Figure 3.12, deviations between forward and backward sweep curves were observed. Regardless of the sequence of the events, backward sweep curves were always higher than forward sweep curves. This was an indication that the deviations were not caused by material fatigue. The difference was the smallest for the lowest sweep rate of 0.5 Oct/min.

Furthermore, a comparison of transmissibility curves showed that the sweep rate did not have a strong influence on the responses overall. But taking a close look at the response curves around resonance peak, a higher forward sweep rate shifted the response curves to the right, while a higher backward sweep rate shifted the response curves to the left. Sweep test is a quasi-steady state technique. With a high sweep rate, the response of system may have not yet reached steady state before the driving frequency moves to the next magnitude. With a low sweep rate, however, the amount of time spent becomes greatly prolonged, thus bringing another problem which involves the fatigue and viscoelasticity of materials. Consequently, a compromise between both requirements for the sweep rate is needed to ensure the reliability of results. Based on an overall consideration, for all of the vibration experiments in the following sections, a sweep rate of 1.0 Oct/min was employed.

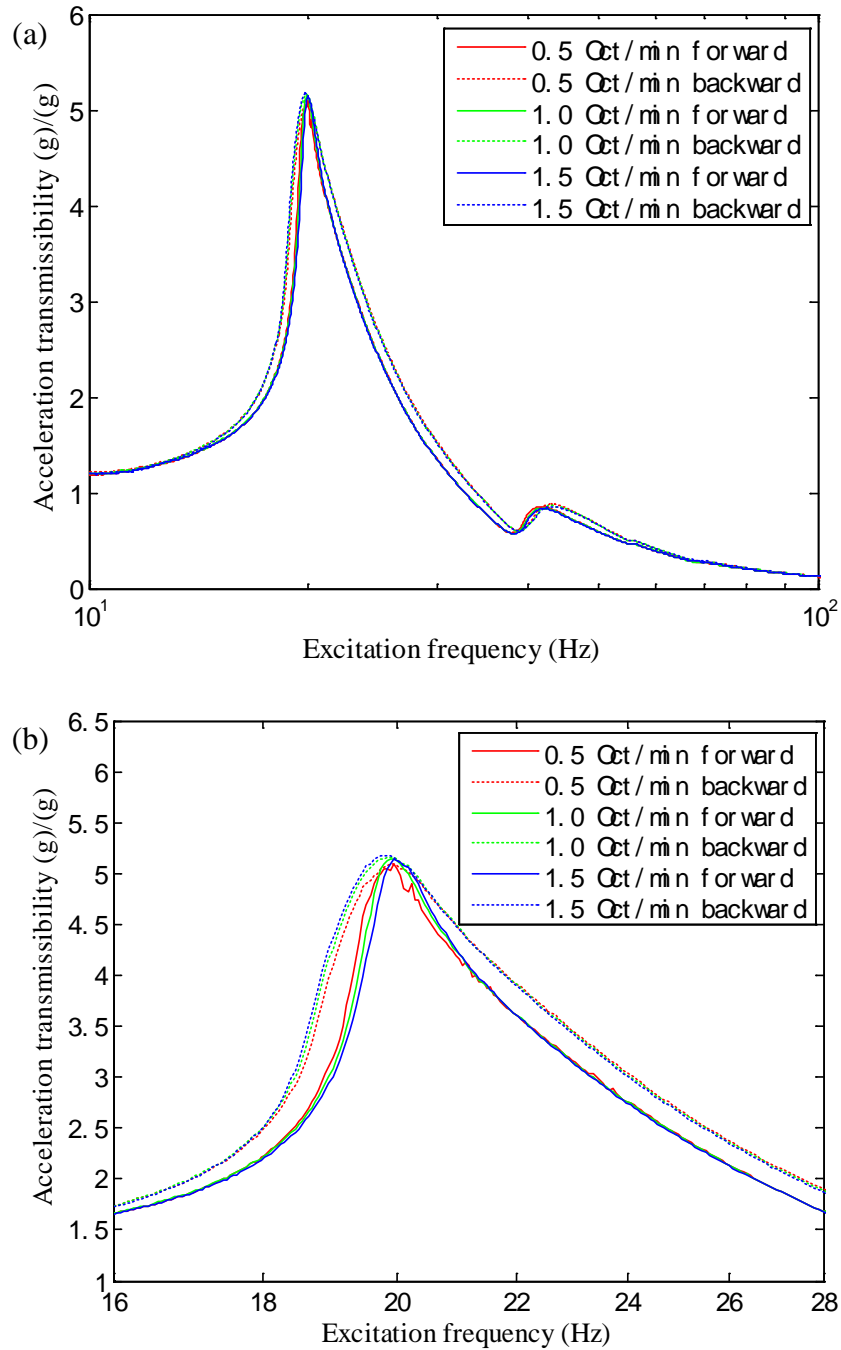


Figure 3.12 Effects of sweep rate and direction, where (b) is a magnified view of (a).

3.3.4 Material fatigue

In order to examine the effect of repeated experiments on the transmissibility curve of one same piece of stacked weft-knitted spacer fabric, ten continuous forward and backward sweep cycles were performed at the same time of five consecutive days. Since the resonance peak bends to the left, the transmissibility curves are of softening type. The values of peak transmissibility and resonance frequency are compared.

As shown in Figures 3.13 and 3.15, as the repetition continues, peak transmissibility increases and resonance frequency decreases within each day. However, as shown in Figure 3.15, given 24 hours' time for relaxation, resonance frequency can be partially recovered. Peak transmissibility in the second day diverges from the main trend. Besides, as in Figure 3.15, within each day, backward sweep results in higher transmissibility in the beginning, but this gap is reduced and reversed as the repetition continues.

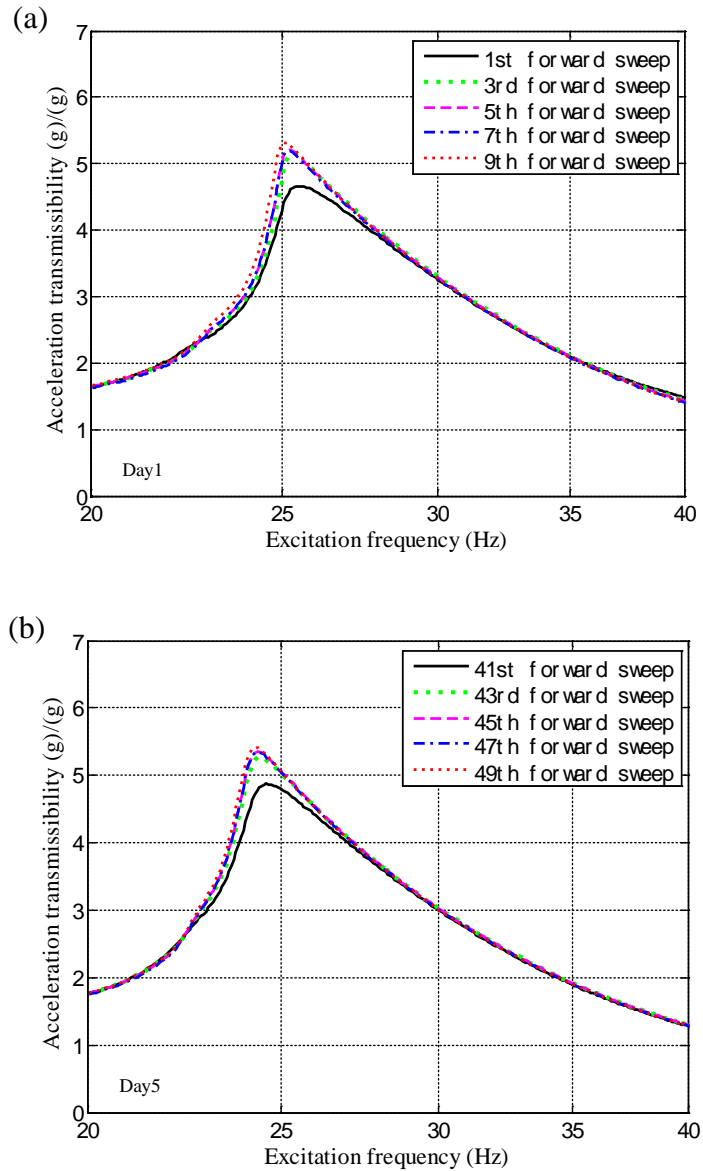


Figure 3.13 Transmissibility curves for the forward sweep events (a) during the 1st day and (b) during the 5th day.

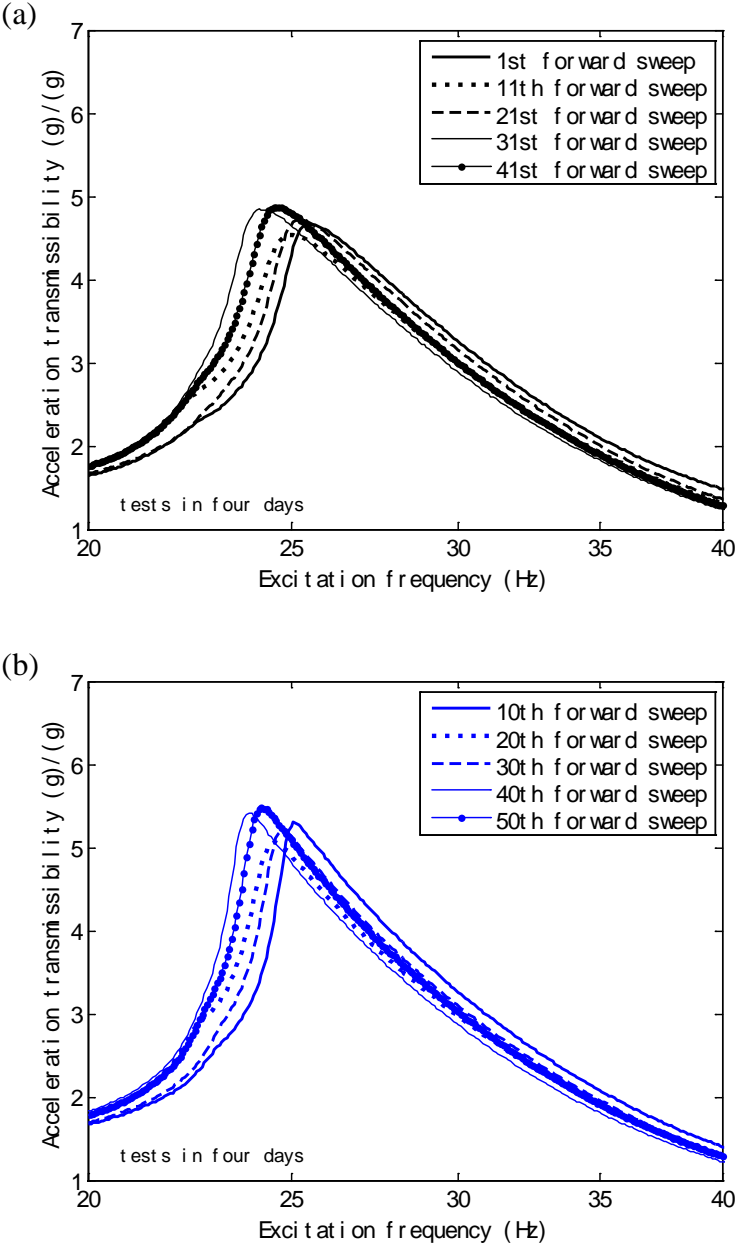


Figure 3.14 Transmissibility curves of (a) the 1st sweep cycles and (b) the 10th sweep cycles for five consecutive days.

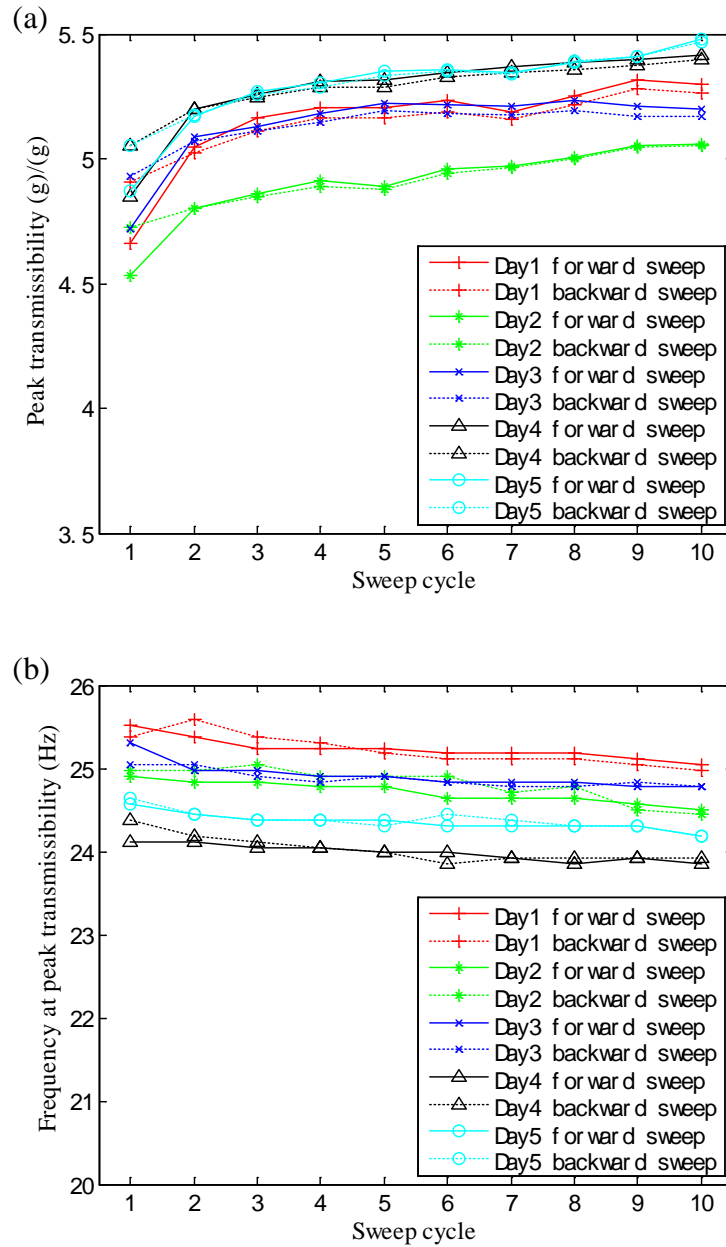


Figure 3.15 Trends of (a) peak transmissibility and (b) resonance frequency for the forward sweep events (in solid lines) and the backward sweep events (in dashed lines) during each of five consecutive days.

3.4 Results and discussion

The effects of fabric thickness, load mass and excitation level on the transmissibility curve and the vibration isolation performance of the mass-spacer fabric system are investigated as follows.

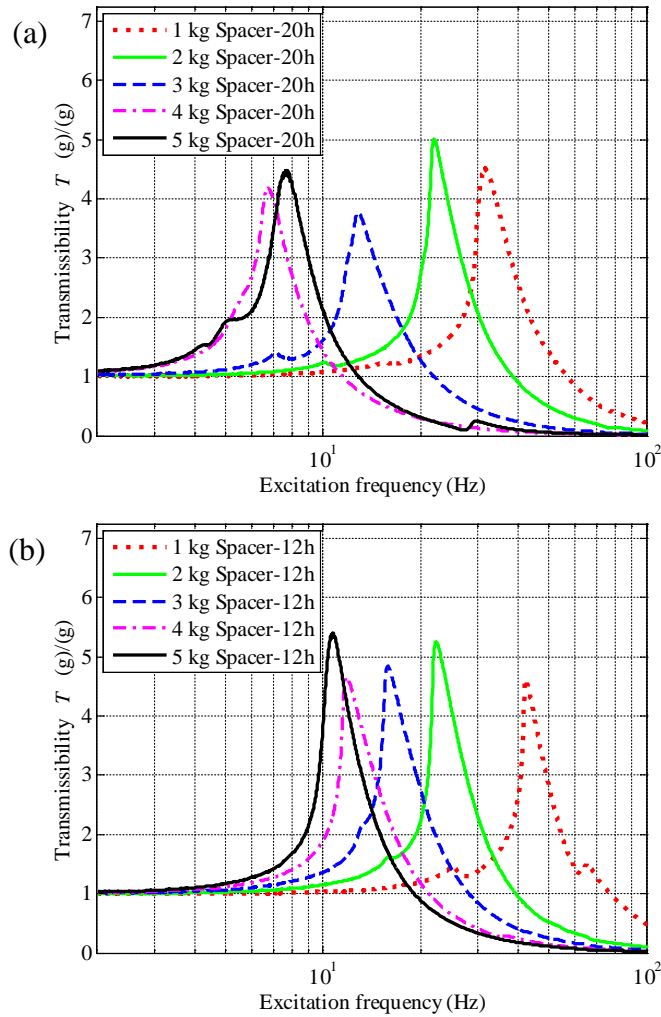
3.4.1 Effect of fabric thickness and load mass

Under the same excitation level, the effect of the fabric thickness on the vibration isolation performance also depends on the load mass due to nonlinear behaviors of spacer fabrics under both static and dynamic loading conditions. In other word, the spacer fabrics will be deformed at different compression strains and will have different stiffness when the load mass changes. In this regard, the effects of the fabric thickness and load mass are discussed together in this section. For ease of discussion, only the testing results for one excitation level of acceleration are presented here. The effect of the excitation level will be discussed in the next section.

Figure 3.16(a) and (b) respectively show the transmissibility curves of Spacer-20h and Spacer-12h with different load masses when the excitation level is kept at 0.1g. It can be seen that the resonance peaks of the transmissibility curves shift to the left side when the load mass increases. This implicates that f_r and f_c decrease with the increase of the load mass (Figure 3.16(c)). However, as shown in Figure 3.16(a), an exceptional case is found for Spacer-20h when the load mass increases from 4 kg to 5 kg. In this case, the transmissibility curve with 5 kg load mass shifts back to the right side instead of shifting

to the left side, resulting in a slight increase of f_r and f_c as shown in Figure 3.16(c).

When observing the effect of the fabric thickness, it can be found that f_r and f_c of Spacer-20h are smaller than those of Spacer-12h, indicating that f_r and f_c decrease with the increase of the fabric thickness.



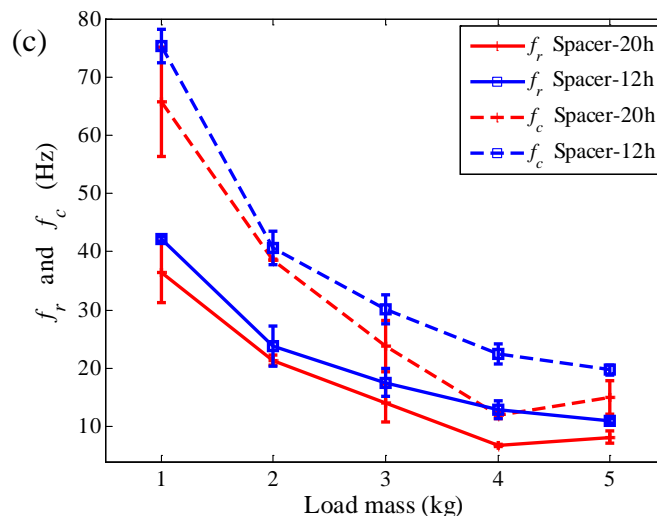


Figure 3.16 (a) and (b) Transmissibility curves under 0.1g excitation level with load mass varied; (c) Variation of f_r and f_c with load mass.

The above phenomena can be explained by stiffness changes of spacer fabrics when the load mass changes. As shown in Figure 3.17, the quasi-static compression curves of both laminated Spacer-20h and Spacer-12h are nonlinear, which indicates that their static stiffness k_s cannot be kept constant under different compression loads. It can be seen that although the compression curves of two spacer fabrics are very different, the variation trends of their static stiffness k_s are very similar. This is that k_s first increases at the very beginning stage, then slightly decreases and finally rapidly increases due to the compaction of the fabric structure under high compression loads. However, the k_s values of two fabrics are different. It should be pointed out that under vibration condition, the dynamic stiffness k_d should be used to explain the vibration isolation performance of spacer fabrics. According to the quasi-static compression curves in Figure 3.17, it can be derived that the compression behavior of two weft-knitted spacer fabrics is similar to that

of damping materials. Therefore, their dynamic stiffness k_d should be different from their static stiffness k_s due to history-dependent mechanical properties under vibration condition. In spite of the nonlinear compressive force-displacement relationship of spacer fabrics, under 0.1g excitation level, the vibration is so localized that the mass-spacer fabric system could be treated as linear. Using $f_r = \frac{1}{2\pi} \sqrt{\frac{k_d}{m}}$, the values of k_d for two spacer fabrics with five load masses were calculated and listed in Table 3.3. It can be seen that the k_d values of Spacer fabric-20h are lower than those of Spacer-12h. This explains why f_r and f_c decrease with the increase of the fabric thickness and the thicker spacer fabric has better vibration isolation than the thinner fabric.

The variation trends of k_d also explain why f_r and f_c decrease with the increase of the load mass because the k_d values also decrease with the increase of the load mass. The exceptional case for Spacer-20h, in which f_r and f_c increases when the load mass increases from 4 kg to 5 kg, can be also explained by k_d value change and static compression curve. As shown in Figure 3.17, when the load mass increases from 4 kg to 5 kg, Spacer-20h changes into the compaction stage with a rapid increase of stiffness. As the effect of the increase of stiffness is higher than that of the increase of load mass, f_r and f_c increases when the load mass increases from 4 kg to 5 kg. Table 3.3 also confirms that the k_d values increase when the load mass increases from 4 kg to 5 kg.

Table 3.3 k_d values of mass-spacer fabric system for a fixed excitation level at 0.1g.

Load mass (kg)		1	2	3	4	5
k_d ($\times 10^4$ N/m)	Spacer-20h	5.26	3.69	2.32	0.74	1.32
	Spacer-12h	7.03	4.96	3.65	2.62	2.40

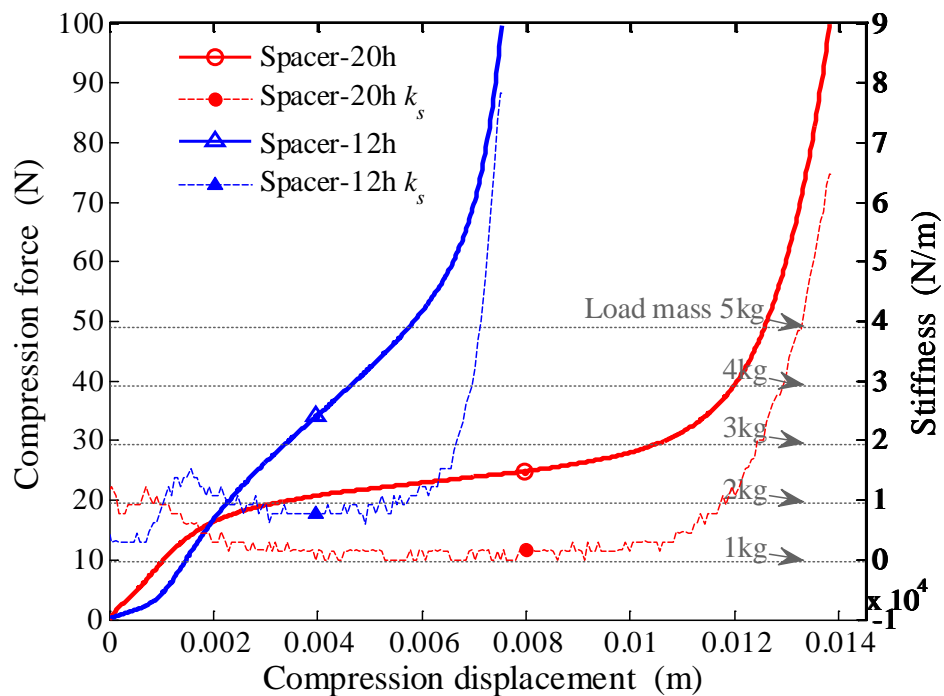


Figure 3.17 Quasi-static compression curves (solid lines ‘—’) and stiffness curves k_s (dashed lines ‘- -’) of spacer fabrics.

3.4.2 Effect of excitation level

The previous section discussed the effects of both the fabric thickness and load mass with a fixed excitation level. In this section, the effect of excitation level is discussed with a

fixed load mass. Figure 3.18(a) and (b) respectively show the transmissibility curves of Spacer-20h and Spacer-12h with different excitation levels when the load mass is kept at 2 kg. It can be seen that the resonance peaks of the transmissibility curves shift to the left side when the excitation level increases. This implicates that f_r and f_c decrease with the increase of the excitation level (Figure 3.18(c)). From Figure 3.18(a) and (b), it can be also found that the shapes of transmissibility curves at the resonance peaks get much bent to the left side when the excitation level increases, indicating that the mass-spacer fabric system becomes more softening. As the increase of softening implicates a decrease of the dynamic stiffness k_d , f_r and f_c decrease with the increase of the excitation level.

From Figure 3.18(c), it can be also found that the f_r and f_c values of Spacer-20h are lower than those of Spacer-12h for all the excitation levels, which confirms again that the thicker spacer fabric has better vibration isolation performance than the thinner spacer fabric. The result in Figure 3.18(c) also shows that the difference in f_r and f_c between two spacer fabrics increase with the increase of excitation level. The reason may be explained by the fact that at low excitation level, the dynamic loads applied to the fabric are relatively smaller and two fabrics work at their low deformation regions where the difference of their stiffness is not high. However, with increasing the excitation level, the dynamic loads applied to the fabric increase and two fabrics will work in different deformation regions where their stiffness gets more important. The detailed explanation needs a further theoretical analysis by considering the nonlinear softening of the mass-spacer fabric system, which will be elaborated in Section 5.2.1 of Chapter 5 on the parametric analysis of theoretical model.

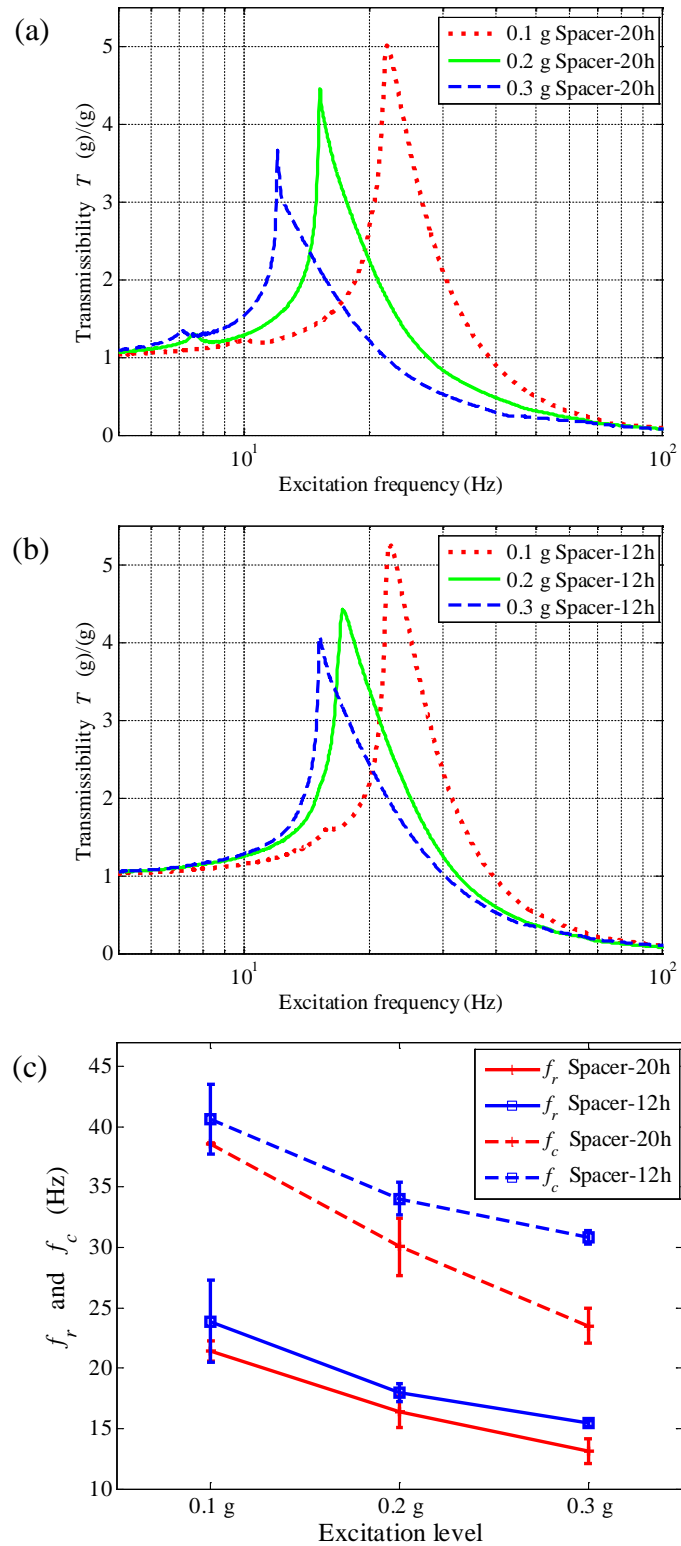


Figure 3.18 (a) and (b) Transmissibility curves under 2 kg load mass with excitation

level varied; (c) Variation of f_r and f_c with load mass.

3.5 Chapter summary

This chapter presents the design and fabrication of weft-knitted spacer fabrics with different thicknesses using an electronic flat knitting machine. Due to the inherent transverse shift of weft-knitted spacer fabric, two pieces were laminated into one sample. The vibration isolation performance of spacer fabric under forced vibration was tested, which is more complicated than that of a linear SDOF system. The effects of fabric thickness, load mass, and excitation level on the transmissibility curve were discussed. According to the results obtained, the following conclusions can be drawn.

- 1) The vibration behaviors of weft-knitted spacer fabrics are not linear due to their nonlinear compression force-displacement relationships which result in different stiffness under different load mass and excitation level.
- 2) Increasing the fabric thickness can result in a decrease of the resonance frequency and crossover frequency due to the reduction of stiffness, and thus improve the vibration isolation performance of spacer fabrics.
- 3) The higher load mass normally results in a smaller resonance frequency and a smaller crossover frequency. However, too high load mass makes fabric compacting, resulting in a higher resonance frequency and a higher crossover frequency due to a rapid increase of the statically-loaded tangential stiffness of fabric.
- 4) Increasing the excitation level results in a smaller resonance frequency and a smaller crossover frequency, and thus a broadened frequency region for vibration isolation. It also results in an enhanced nonlinear softening effect.

CHAPTER 4 PARAMETER IDENTIFICATION BY CURVE

FIT

4.1 Introduction

This chapter builds the equation of motion under forced harmonic excitation using two types of models, one with symmetric elastic force and one with asymmetric elastic force. Frequency-domain solutions are obtained using the harmonic balance method (HBM) with the first-order approximation. Model parameters are identified by curve fit, with discussions on the optimization algorithms used, the goodness of fit concerning two types of models, and the significance of the fractional derivative term.

4.2 Approximate analytical models

4.2.1 Symmetric model with parameters $k_3, k_5, k_7, c, a, \alpha$

To simulate the vibration response of the mass-spacer fabric system under harmonic excitation using a symmetric model, the dynamic equation is first set up as follows

$$m\ddot{x} + c\dot{x} + kx + k_3x^3 + k_5x^5 + k_7x^7 + aD^\alpha x = -mG\cos(\omega t), \quad (4.1)$$

where the term $aD^\alpha x$ is a fractional derivative for explaining the viscoelasticity in spacer fabric, and G is the magnitude of acceleration by the forced oscillation, i.e. the excitation

level. The elastic force is $kx + k_3x^3 + k_5x^5 + k_7x^7$, and the viscous damping force is $c\dot{x}$. Similar equation of motion has been used by Deng⁹ to study the vibration of polyurethane foam. For the nonlinear elastic force, different models have been set up in literature, for instance, the seventh-order polynomial, the fifth-order polynomial, the polynomial plus tangent terms, etc. Including high-order polynomial terms more than necessary may cause overfit, in which case the expression does not optimize but deteriorates the model instead. It is commonly accepted that a seventh-order polynomial can well describe the elastic force of a simple nonlinear system. Furthermore, a polynomial composed of all odd-order terms renders a symmetry of the elastic force-displacement relationship about the origin which represents the oscillations of mass around the pre-stressed position as the reference point for displacement. It should be noted that adding even-orders into the polynomial expression results in an asymmetric model, which has complicated mathematical derivations in the effort to obtain frequency response curves (FRCs). The simplest form of such an asymmetric model will be presented later.

Consider the primary resonance of the system using the symmetric model by Equation (4.1), the response can be written as

$$x(t) = Ae^{j\omega t} + \bar{A}e^{-j\omega t}, \quad (4.2)$$

where $A = A_r + jA_i$, and \bar{A} is the conjugate. The harmonic amplitude is $2|A|$.

With the knowledge of

$$D^\alpha \left\{ e^{j\omega t} \right\} = \omega^\alpha e^{j(\omega t + \frac{\pi}{2}\alpha)}, \quad (4.3)$$

we can equate the coefficients of $e^{j\omega t}$ on both sides of the equation of motion using the harmonic balance method (HBM), and obtain

$$-m\omega^2 A + j c \omega A + k A + a A \omega^\alpha e^{j\frac{\pi}{2}\alpha} + 3k_3 A^2 \bar{A} + 10k_5 A^3 \bar{A}^2 + 35k_7 A^4 \bar{A}^3 = -\frac{mG}{2}. \quad (4.4)$$

This equation can be simplified as

$$PA + jQA = -\frac{mG}{2}. \quad (4.5)$$

Further split into real and imaginary parts,

$$\begin{cases} PA_r - QA_i = -\frac{mG}{2} \\ PA_i + QA_r = 0 \end{cases}, \quad (4.6)$$

and multiplied by \bar{A} , it becomes

$$\begin{cases} P \cdot |A|^2 + \frac{mGA_r}{2} = 0 \\ Q \cdot |A|^2 - \frac{mGA_i}{2} = 0 \end{cases}, \quad (4.7)$$

where

$$\begin{cases} P = -m\omega^2 + k + 3k_3 |A|^2 + 10k_5 |A|^4 + 35k_7 |A|^6 + a\omega^\alpha \cos\left(\frac{\pi}{2}\alpha\right) \\ Q = c\omega + a\omega^\alpha \sin\left(\frac{\pi}{2}\alpha\right) \end{cases}. \quad (4.8)$$

Equation (4.6) can also be squared to obtain

$$\left((-m\omega^2 + k + 3k_3 |A|^2 + 10k_5 |A|^4 + 35k_7 |A|^6 + a\omega^\alpha \cos\left(\frac{\pi}{2}\alpha\right))^2 + (c\omega + a\omega^\alpha \sin\left(\frac{\pi}{2}\alpha\right))^2 \right) \cdot |A|^2 = \frac{m^2 G^2}{4},$$

which is used to recover the harmonic amplitude ($2|A|$) vs. excitation frequency curve after model parameters have been identified by curve fit.

4.2.2 Asymmetric model with parameters: $\beta \ \kappa \ k_3 \ c \ a \ \alpha$

As mentioned earlier, the asymmetric model considers adding even-orders into the polynomial expression for the elastic force-displacement relationship. This asymmetry arises from different sources, such as the ones described in Chapter 2:

- The loaded mass is mistuned (overloaded or underloaded) for an isolator with quasi-zero stiffness, i.e. the static equilibrium position departs from the point of symmetry for the elastic force-displacement relationship.
- An asymmetric excitation force, comprised of a harmonic component and a static component, is applied to an isolator with quasi-zero stiffness.
- For curved beams, the initial curvature gives rise to the quadratic term and the mid-plane stretching gives rise to the cubic term. In such cases, the restoring force containing the quadratic stiffness term $k_2 x^2$ is more realistic in practice, as compared with the one with all odd terms, such as the research carried out by Abolfathi ¹⁵⁰.

In comparison with the symmetric nonlinearity, the quadratic stiffness term takes into account the asymmetry in the restoring force which is more general for real materials and systems. In addition, lower-order nonlinearity terms contribute more to the restoring force than the higher-order terms, thus, the former exhibits higher significance. As a result, the linear-quadratic-cubic stiffness terms are used to build the asymmetric model. Besides,

the highest-order stiffness coefficient is limited to k_3 . The dynamic equation of motion is

$$m\ddot{x} + c\dot{x} + kx + k_2x^2 + k_3x^3 + aD^\alpha x = -mG\cos(\omega t). \quad (4.9)$$

The polynomial elastic force has a relation of equivalence as below

$$kx + k_2x^2 + k_3x^3 = \kappa(x + \delta) + k_3(x + \delta)^3 - \beta, \quad (4.10)$$

which results in

$$\begin{cases} \delta = \frac{k_2}{3k_3} \\ \kappa = k - \frac{k_2^2}{3k_3} \\ \beta = \frac{k \cdot k_2}{3k_3} - \frac{2k_2^3}{27k_3^2} \end{cases}. \quad (4.11)$$

Let the new coordinate be $z(t) = x(t) + \delta$, then after coordinate transformation, the equation of motion becomes

$$m\ddot{z} + c\dot{z} + \kappa z + k_3z^3 + aD^\alpha(z - \delta) = -mG\cos(\omega t) + \beta. \quad (4.12)$$

On the other hand, the fractional derivative of the constant δ is

$$D^\alpha \delta = \delta \lim_{\lambda \rightarrow 0} \frac{\Gamma(\lambda + 1)}{\Gamma(\lambda - \alpha + 1)} \cdot t^{\lambda - \alpha} = \frac{\delta t^{-\alpha}}{\Gamma(1 - \alpha)}, \quad (4.13)$$

where $\alpha \geq 0$, and $t^{-\alpha}$ is a decaying function. Assume the time is adequately long to reach the steady state, which results in $D^\alpha \delta \Big|_{t \rightarrow \infty} = 0$. So we have

$$D^\alpha(z - \delta) = D^\alpha z - D^\alpha \delta = D^\alpha z. \quad (4.14)$$

At last, the equation of motion is transformed into

$$m\ddot{z} + c\dot{z} + \kappa z + k_3 z^3 + aD^\alpha z = -mG\cos(\omega t) + \beta. \quad (4.15)$$

Solving the unknowns $k, k_2, k_3, c, a, \alpha$ in the original equation (4.9) is equivalent to solving the unknowns $\beta, \kappa, k_3, c, a, \alpha$ in Equation (4.15). The advantage of using the transformed form is that it can be treated as an isolator with symmetric elastic force excited by a harmonic force $-mG\cos(\omega t)$ and a constant force β . The resulting steady-state amplitude $z(t)$ contains a harmonic term and a bias term. Assume it has the form

$$z(t) = A_0 + Ae^{j\omega t} + \bar{A}e^{-j\omega t} = A_0 + 2|A|\cos(\omega t + \phi), \quad (4.16)$$

in which $A = A_r + jA_i$. The harmonic amplitude is $2|A|$ and the static displacement is A_0 .

We use the harmonic amplitude vs. excitation frequency curve to perform curve fit and to identify model parameters.

Using the harmonic balance method (HBM), to equate the constants on both sides of Equation (4.15), we have

$$k_3 A_0^3 + 6k_3 A_0 |A|^2 + \kappa A_0 = \beta. \quad (4.17)$$

The static displacement A_0 has only one real root, which is associated with $|A|$ by

$$A_0 = M - \frac{6k_3 |A|^2 + \kappa}{3k_3 M}, \quad (4.18)$$

where

$$M = \left\{ \left[\frac{(6k_3|A|^2 + \kappa)^3}{27k_3^3} + \frac{\beta^2}{4k_3^2} \right]^{1/2} + \frac{\beta}{2k_3} \right\}^{1/3}.$$

Equating the coefficients of $e^{j\omega t}$ on both sides of Equation (4.15), we can obtain

$$3k_3|A|^2 A + 3k_3A_0^2 A + \kappa A + aA\omega^\alpha \cos\left(\frac{\pi}{2}\alpha\right) + jaA\omega^\alpha \sin\left(\frac{\pi}{2}\alpha\right) - m\omega^2 A + jc\omega A = -\frac{mG}{2}. \quad (4.19)$$

Similar as in the symmetric model, the equation above can be simplified as

$$PA + jQA = -\frac{mG}{2}. \quad (4.20)$$

Further split into real and imaginary parts as

$$\begin{cases} PA_r - QA_i = -\frac{mG}{2} \\ PA_i + QA_r = 0 \end{cases}, \quad (4.21)$$

and multiplied by \bar{A} , it becomes

$$\begin{cases} P \cdot |A|^2 + \frac{mGA_r}{2} = 0 \\ Q \cdot |A|^2 - \frac{mGA_i}{2} = 0 \end{cases}, \quad (4.22)$$

where

$$\begin{cases} P = -m\omega^2 + \kappa + 3k_3|A|^2 + 3k_3A_0^2 + a\omega^\alpha \cos\left(\frac{\pi}{2}\alpha\right) \\ Q = c\omega + a\omega^\alpha \sin\left(\frac{\pi}{2}\alpha\right) \end{cases}. \quad (4.23)$$

Equation (4.21) can also be squared to obtain

$$\left((-m\omega^2 + \kappa + 3k_3|A|^2 + 3k_3A_0^2 + a\omega^\alpha \cos(\frac{\pi}{2}\alpha))^2 + (c\omega + a\omega^\alpha \sin(\frac{\pi}{2}\alpha))^2 \right) \cdot |A|^2 = \frac{m^2G^2}{4},$$

which is used to recover the harmonic amplitude ($2|A|$) vs. excitation frequency curve after model parameters have been identified by curve fit. The static displacement A_0 can then be expressed using $|A|$.

4.2.3 Fitness function

Given the expression of harmonic amplitude vs. excitation frequency relationship using either the symmetric model or the asymmetric model, the next procedure is to find the optimal parameter estimates that best describe the vibration behavior of the mass-spacer fabric system by optimization strategy, which can be stated as

$$\min_x \|f(x)\|_2^2 = \min_x \left(\sum_{n=1}^N f_n^2(x) \right), \quad (4.24)$$

where $f_n(x)$ is the fitness function that characterizes the harmonic amplitude vs. excitation frequency relationship, and N is the volume of experimental data. The fitness function has the form of

$$f_n(x) = \sqrt{f_{1,n}^2(x) + f_{2,n}^2(x)}, \quad (4.25)$$

where

$$\begin{cases} f_{1,n}(x) = P \cdot |A|^2 + \frac{mGA_r}{2} \\ f_{2,n}(x) = Q \cdot |A|^2 - \frac{mGA_i}{2} \end{cases} \quad (4.26)$$

For the symmetric model in Section 4.2.1 we have

$$\begin{cases} P = -m\omega^2 + k + 3k_3 |A|^2 + 10k_5 |A|^4 + 35k_7 |A|^6 + a\omega^\alpha \cos\left(\frac{\pi}{2}\alpha\right) \\ Q = c\omega + a\omega^\alpha \sin\left(\frac{\pi}{2}\alpha\right) \end{cases} \quad (4.27)$$

For the asymmetric model in Section 4.2.2 we have

$$\begin{cases} P = -m\omega^2 + \kappa + 3k_3 |A|^2 + 3k_3 A_0^2 + a\omega^\alpha \cos\left(\frac{\pi}{2}\alpha\right) \\ Q = c\omega + a\omega^\alpha \sin\left(\frac{\pi}{2}\alpha\right) \end{cases} \quad (4.28)$$

Experimental data of harmonic amplitude $2|A|$ can be calculated using the data of the

transmissibility T and the phase angle ϕ by the equation $2|A| = \frac{G}{\omega^2} \sqrt{T^2 - 2T \cos \phi + 1}$. By

optimizing the fitness function in Equation (4.25), parameter estimates of $k, k_2, k_3, c, a, \alpha$

in the symmetric model and parameter estimates of $\beta, \kappa, k_3, c, a, \alpha$ in the asymmetric

model can be solved.

4.2.4 Statistical indicator of the goodness of fit (RMSE)

The value of $\min_x \|f(x)\|_2^2$ is also the sum of square error (SSE). As a statistical indicator of the goodness of fit for a model while at the same time considering the effect of data volume, the root mean square error (RMSE) is given as

$$\text{RMSE} = \sqrt{\frac{\text{SSE}}{N}}. \quad (4.29)$$

Another commonly used index for the goodness of fit is the coefficient of determination, which is defined as

$$R^2 = 1 - \frac{\text{SS}_{\text{res}}}{\text{SS}_{\text{tot}}} = 1 - \frac{\sum_{n=1}^N (y_n - f_n)^2}{\sum_{n=1}^N (y_n - \bar{y})^2}, \quad (4.30)$$

where SS_{res} and SS_{tot} are the residual sum of squares and the total sum of squares, y_n and f_n are experimental and fitted values respectively, and \bar{y} is the average of experiment values. However, in a nonlinear system, when the vibration response under a single-frequency harmonic excitation has multiple solutions, the mapping relation between the excitation frequency and the vibration response will not be satisfied. In this case, the response is not a function of excitation frequency, thus, the coefficient of determination R^2 will not be used here.

4.3 Results of data fitting

Results of data fitting using symmetric models and asymmetric models are presented as below. In this study, the highest-order of nonlinearity for the symmetric force is restricted to quintic, so that the symmetric model with unknown parameters $k, k_3, k_5, c, a, \alpha$ contains the same number of parameters as the asymmetric model with unknown parameters $\beta, \kappa, k_3, c, a, \alpha$.

4.3.1 Excitation level

In this section, the levels of the goodness of fit by symmetric models of different structures and asymmetric models of different structures are compared for Spacer-12h under 0.1-0.3g excitation levels and 2 kg load mass conditions. Experimental data of harmonic amplitude vs. excitation frequency were based on a combination of the sweep-up and sweep-down events. It should be noted that some of the harmonic amplitudes for spacer fabric under 0.3g excitation level and 2 kg load mass condition are multi-valued for certain frequency range as shown in Fig 4.1(c), due to the fact that its steady-state response depends on the sweep direction (from low to high frequencies, or from high to low frequencies) of sinusoidal excitation. Experimentally, the unstable solution cannot be observed, while the two stable solutions correspond to the lower and upper paths. The sudden switch from one stable path to the other is called the jump phenomenon. It could take place for nonlinear systems under large excitations.

Symmetric models

Figures 4.1 and 4.2 show parameter estimates and RMSEs using four variants of symmetric models, i.e. with parameters $k, k_3, k_5, c, a, \alpha$, k, k_3, c, a, α , k, k_3, k_5, c , and k, k_3, k_5, a, α , in order to examine the effects of the quintic stiffness k_5 , the viscous damping coefficient C , and the fractional derivative term $aD^\alpha x$.

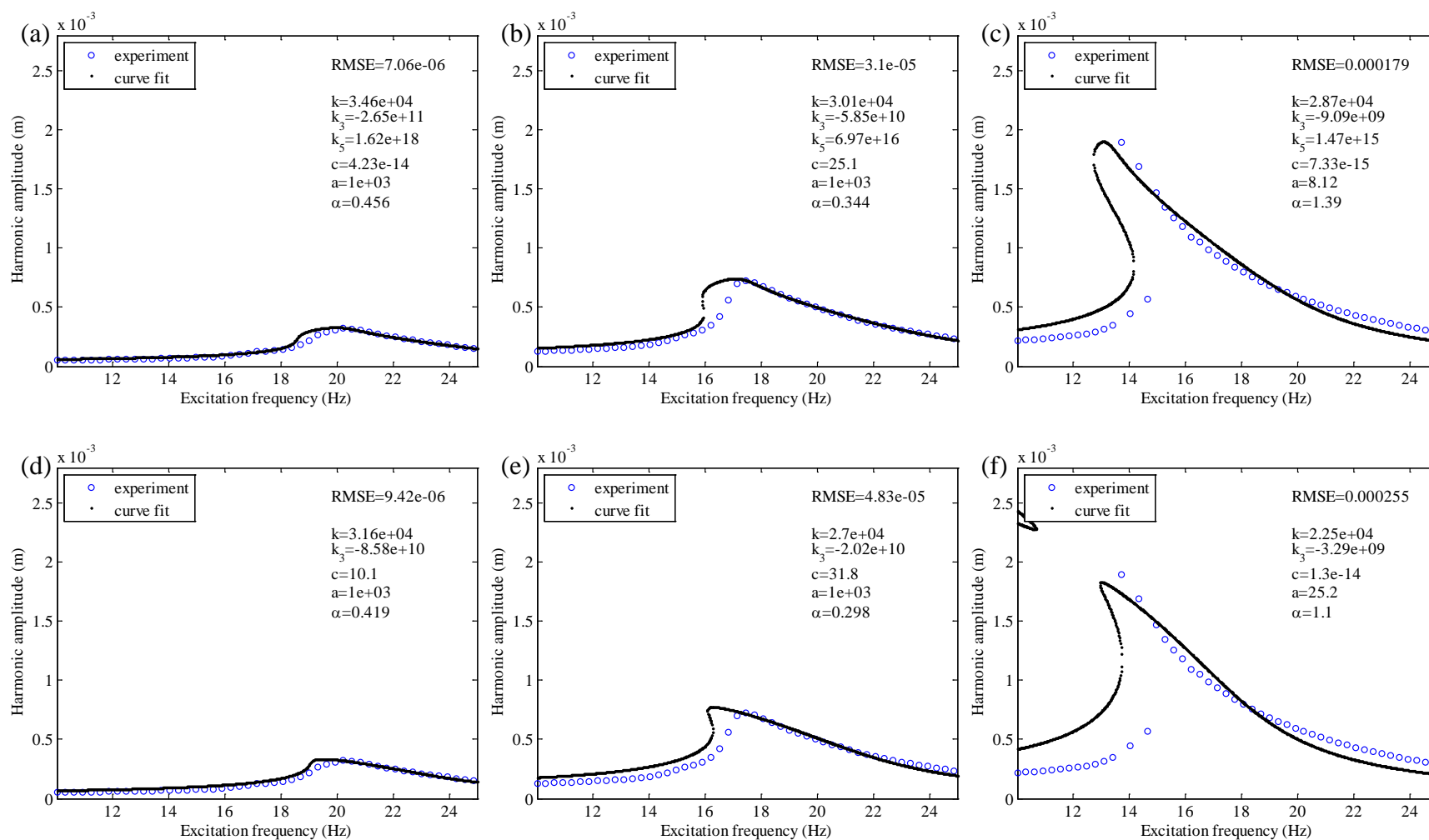


Figure 4.1 Fitting results using the symmetric model with parameters $k, k_3, k_5, c, a, \alpha$ and the one with parameters k, k_3, c, a, α for the conditions of 2 kg load mass and: (a) and (d) 0.1g; (b) and (e) 0.2g; (c) and (f) 0.3g excitation level using Spacer-12h.

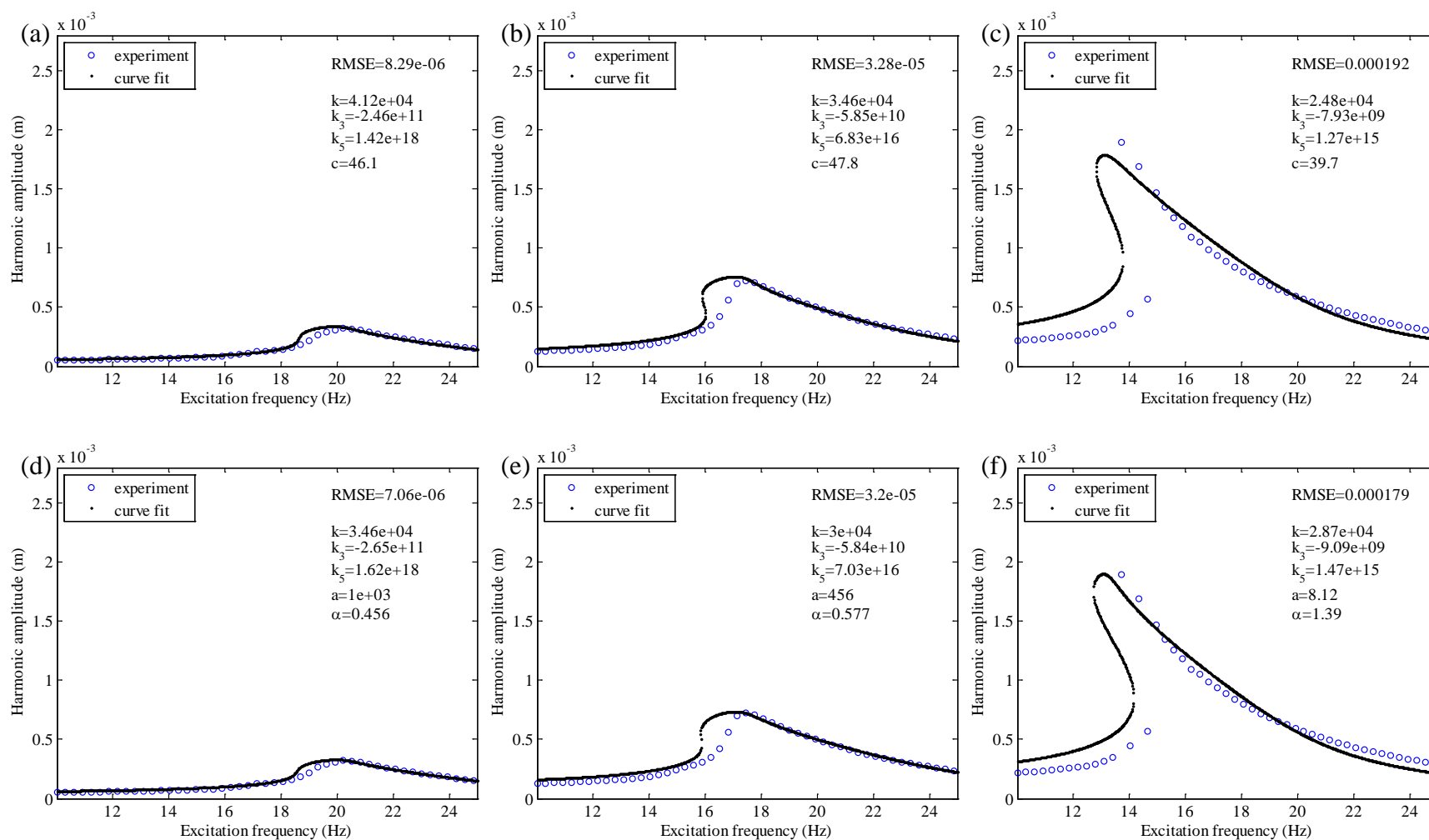


Figure 4.2 Fitting results using the symmetric model with parameters k, k_3, k_5, c and the one with parameters k, k_3, k_5, a, α for the conditions of 2 kg load mass and: (a) and (d) 0.1g; (b) and (e) 0.2g; (c) and (f) 0.3g excitation level using Spacer-12h.

To compare the fitting results of these four variants of symmetric models, Figure 4.3 summarizes their RMSEs. Firstly, it is shown that the symmetric model with six parameters $k, k_3, k_5, c, a, \alpha$ achieves the best curve fit by giving the smallest RMSEs. Secondly, the symmetric model without the quintic stiffness term k_5x^5 , i.e. the one with parameters k, k_3, c, a, α , gives the largest RMSEs, indicating that k_5x^5 is significant for the model. Thirdly, using the model with six parameters $k, k_3, k_5, c, a, \alpha$ results in reduced RMSEs for all three excitation level conditions, as compared with using the model without the fractional derivative term $aD^\alpha x$, i.e. the one with parameters k, k_3, k_5, c . This makes clear the significance of the fractional derivative term for the model. Fourthly, using the model with the fractional derivative term $aD^\alpha x$ alone, i.e. the one with parameters k, k_3, k_5, a, α , gives better curve fit compared with using the model with the viscous damping coefficient c alone, i.e. the one with parameters k, k_3, k_5, c . This also reveals the advantage of using the fractional derivative term to describe the vibration behavior of the mass-spacer fabric system. Last but not least, for 0.1g and 0.3g excitation level conditions, the viscous damping coefficient is redundant, since the model with parameters k, k_3, k_5, a, α gives the same RMSE as the model with parameters $k, k_3, k_5, c, a, \alpha$; however, for the 0.2g excitation level condition, $c\dot{x}$ and $aD^\alpha x$ both helps improve the model structure.

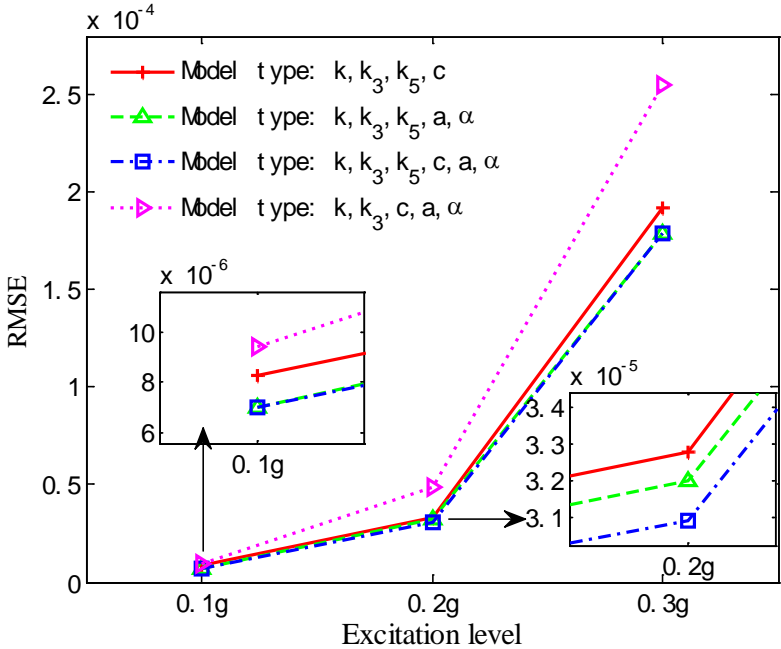
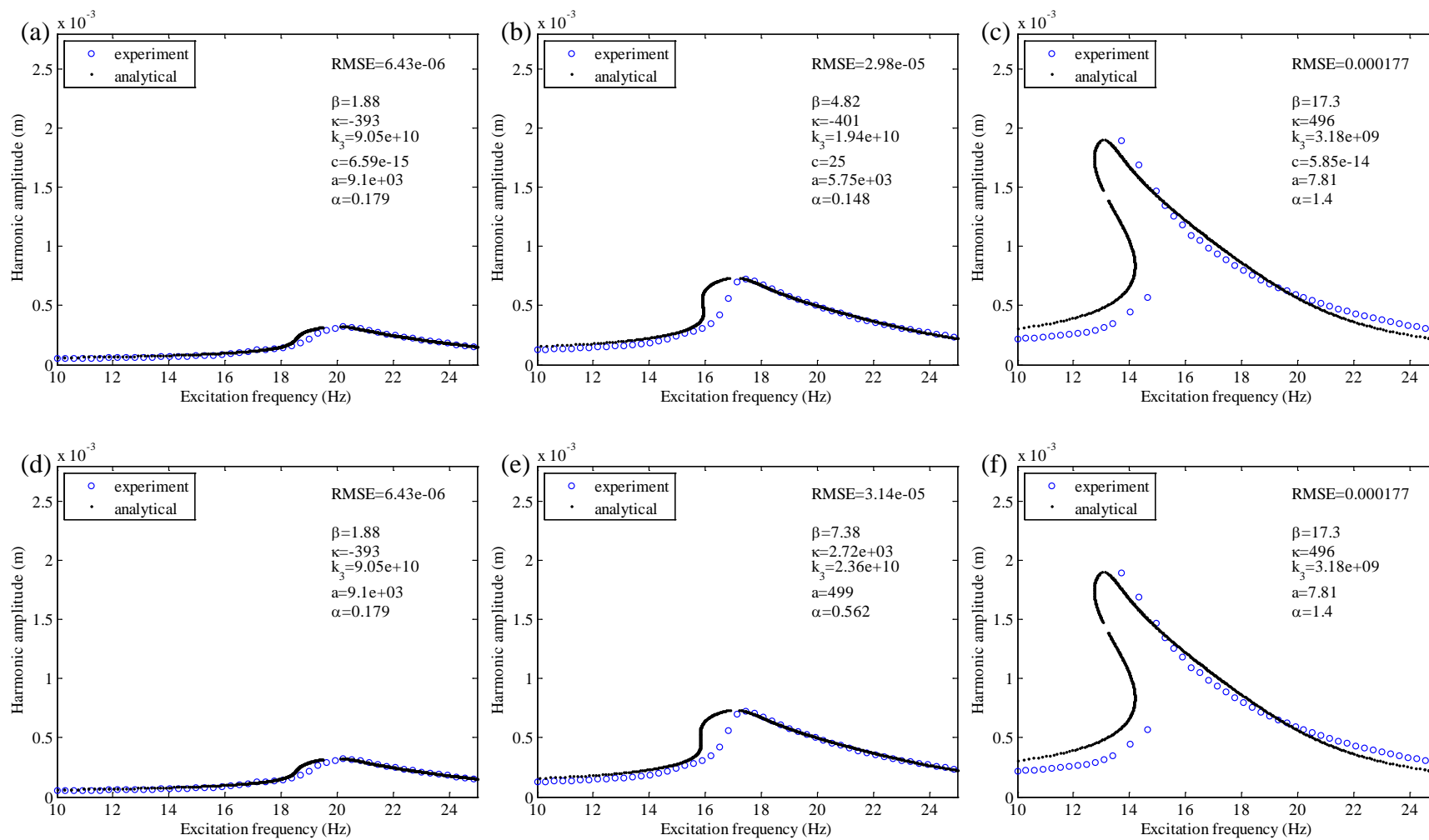


Figure 4.3 Summary of RMSEs from curve fits using four variants of symmetric models.

Asymmetric models

Similarly, parameter estimates and RMSEs under the same excitation level and load mass conditions for the same spacer fabric are shown in Figure 4.4, using three variants of asymmetric models, i.e. with parameters $\beta, \kappa, k_3, c, a, \alpha$, $\beta, \kappa, k_3, a, \alpha$, and β, κ, k_3, c , in order to examine the effects of the viscous damping coefficient C and the fractional derivative term $aD^\alpha x$.



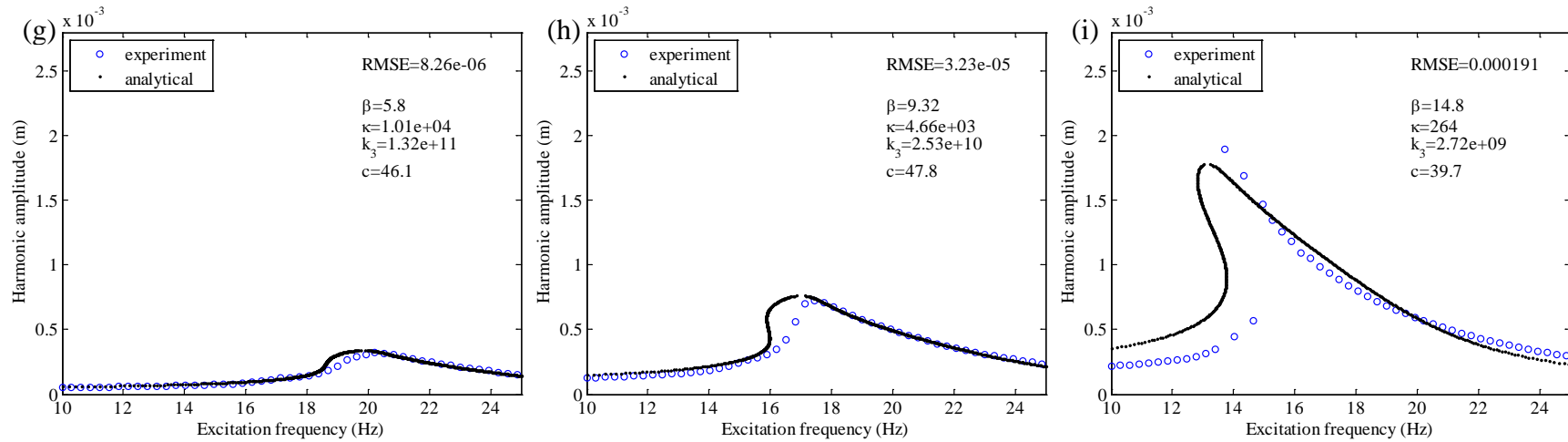


Figure 4.4 Fitting results using the asymmetric model with parameters $\beta, \kappa, k_3, c, a, \alpha$, the one with parameters $\beta, \kappa, k_3, a, \alpha$ and the one with parameters β, κ, k_3, c for conditions of 2 kg load mass and: (a), (d) and (g) 0.1g; (b), (e) and (h) 0.2g; (c), (f) and (i) 0.3g excitation level using Spacer-12h.

Similarly, to compare the fitting results of these three variants of asymmetric models, Figure 4.5 summarizes their RMSEs. Firstly, it is shown that the asymmetric model with six parameters $\beta, \kappa, k_3, c, a, \alpha$ achieves the best curve fit by giving the smallest RMSEs. Secondly, using the model with six parameters $\beta, \kappa, k_3, c, a, \alpha$ results in reduced RMSEs for all three excitation level conditions, as compared with using the model without the fractional derivative term $aD^\alpha x$, i.e. the one with parameters β, κ, k_3, c . This makes clear the significance of the fractional derivative term for the model. Thirdly, using the model with the fractional derivative term $aD^\alpha x$ alone, i.e. the one with parameters $\beta, \kappa, k_3, a, \alpha$, gives better curve fit compared with using the model with the viscous damping coefficient c alone, i.e. the one with parameters β, κ, k_3, c . This again reveals the advantage of using the fractional derivative term to describe the vibration behavior of the mass-spacer fabric system. Last but not least, for 0.1g and 0.3g excitation level conditions, the viscous damping coefficient is redundant, since the model with parameters $\beta, \kappa, k_3, a, \alpha$ gives the same RMSE as the model with parameters $\beta, \kappa, k_3, c, a, \alpha$; however, for the 0.2g excitation level condition, $c\dot{x}$ and $aD^\alpha x$ both help improve the model structure.

The physical significance of the fractional derivative term $aD^\alpha x$ is some combination of the linear elastic force and the viscous damping force when $0 \leq \alpha \leq 1$. Thus, it contributes to both the elastic force and the damping force. When $\alpha = 0$, $aD^\alpha x$ evolves into a linear spring ax ; when $\alpha = 1$, $aD^\alpha x$ evolves into a viscous damper $a\dot{x}$. For the 0.3g excitation

level condition, however, the best-fit value of the fractional order α is larger than one. The extension of the interval ($0 \leq \alpha \leq 2$) makes the physical meaning of α more difficult to be defined. Despite this, it helps improve the model structure to some degree by giving a reduced RMSE.

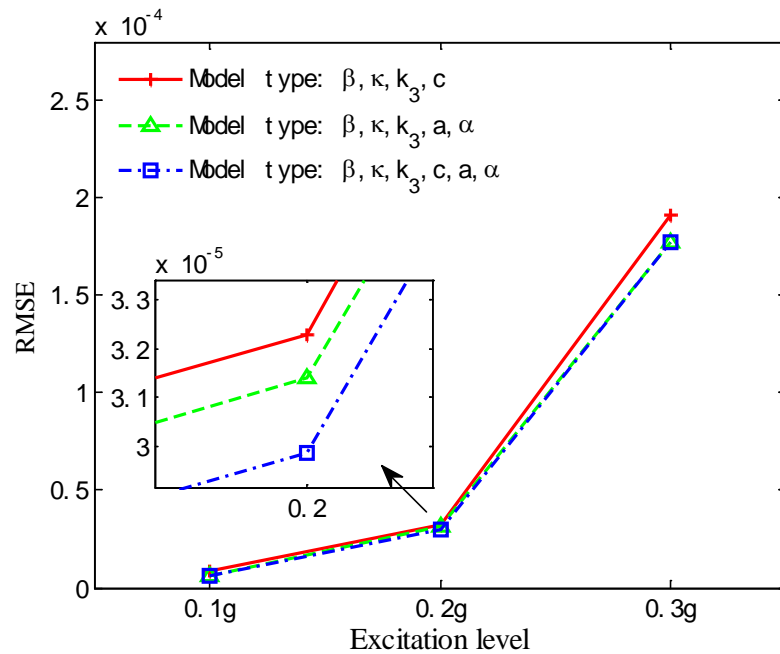


Figure 4.5 Summary of RMSEs from curve fits using three variants of asymmetric models.

Asymmetric vs. symmetric models

In order to find whether the six-parameter asymmetric model $(\beta, \kappa, k_3, c, a, \alpha)$ or the six-parameter symmetric model $(k, k_3, k_5, c, a, \alpha)$ performs better, Figure 4.6 compares their RMSEs. It is shown that two types of model structures have comparable performances. If must, the asymmetric model performs slightly better by giving a bit smaller RMSEs.

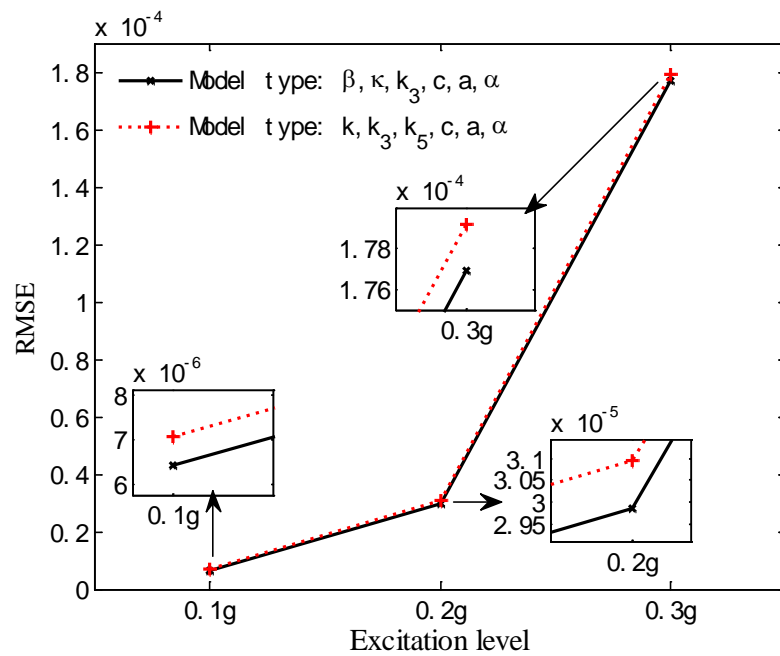


Figure 4.6 Comparison of RMSEs by asymmetric vs. symmetric models.

Reconstructed force-displacement curve

Although the asymmetric and the symmetric types of model structures have comparable performances, their elastic force-displacement relationships are quite different. To reconstruct the elastic force-displacement curves in the form of polynomials by asymmetric and symmetric model types, the fractional derivative term $aD^\alpha x$ is not considered, otherwise it would also contribute to the elastic force. On one hand, using the asymmetric model with parameters β, κ, k_3, c , the corresponding elastic force-displacement curves under 0.1-0.3g excitation levels and 2 kg load mass for Spacer-12h are shown in Figure 4.7(a), expressed as $k(x-\delta) + k_2(x-\delta)^2 + k_3(x-\delta)^3 + \beta$, or $\kappa x + k_3 x^3$ after coordinate transformation, which passes the statically-loaded position at the point (δ, β) . The tangent stiffness k (marked with a dashed line) at this position (marked with a solid dot) is also shown. On the other hand, using the symmetric model with parameters k, k_3, k_5, c , the corresponding elastic force-displacement curves are shown in Figure 4.7(b), expressed as $kx + k_3 x^3 + k_5 x^5$, which passes the statically-loaded position at the origin $(0, 0)$.

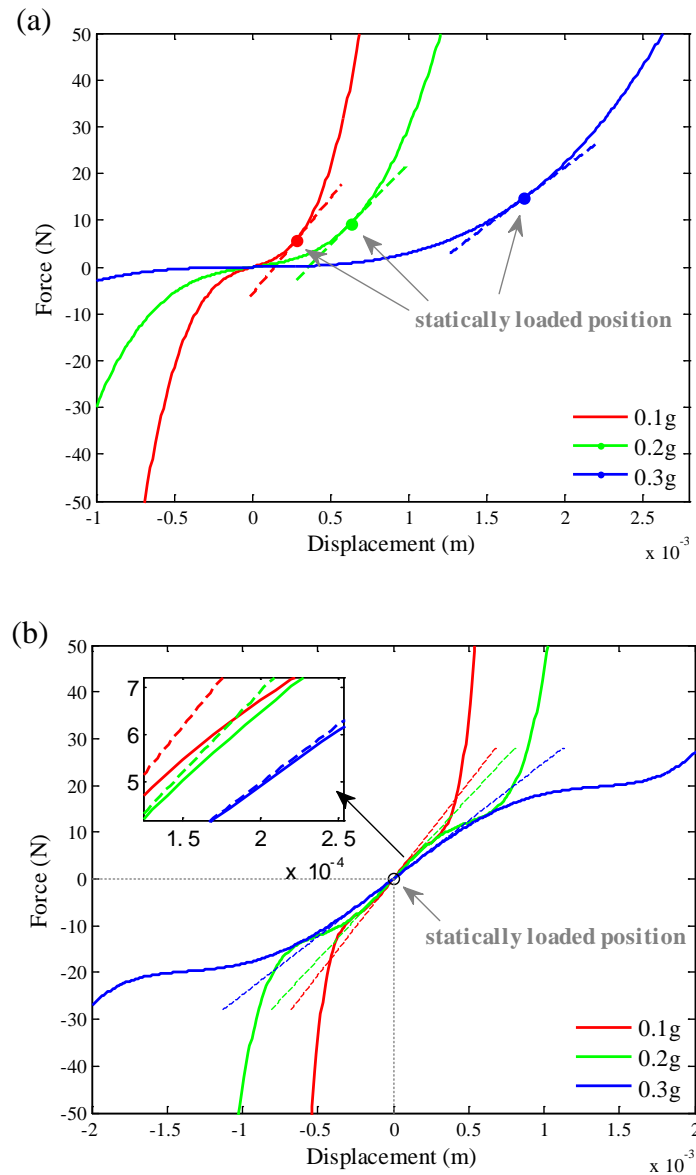


Figure 4.7 Reconstructed elastic force-displacement curves using fitted parameters under 0.1-0.3g excitation levels and 2 kg load mass for Spacer-12h: (a) the asymmetric model with parameters β, κ, k_3, c ; (b) the symmetric model with parameters k, k_3, k_5, c .

The reconstructed elastic force-displacement curves show that, as the excitation level increases from 0.1g to 0.3g, the tangent stiffness k decreases for both the asymmetric model and the symmetric model.

4.3.2 Load mass

Using the experimental data for Spacer-12h under 1-5 kg load mass and 0.1g excitation level conditions, results of data fitting including RMSEs and parameter estimates are presented in Figures 4.9 to 4.12, using two symmetric and two asymmetric model structures. During curve fit, as the location of resonance peak for different load mass varies largely, a unified frequency range for data fitting becomes unsuitable. For each case of load mass, the frequency range is defined as an interval of ± 7 Hz from the frequency value that has peak amplitude.

Figure 4.8 also summarizes the RMSEs for different model structures. It is shown that when the load mass is small, all models result in nearly the same level of the goodness of fit. As the load mass increases, the advantage of using models containing the fractional derivative term appears. Moreover, the symmetric model structures and the asymmetric model structures have comparable levels of performance.

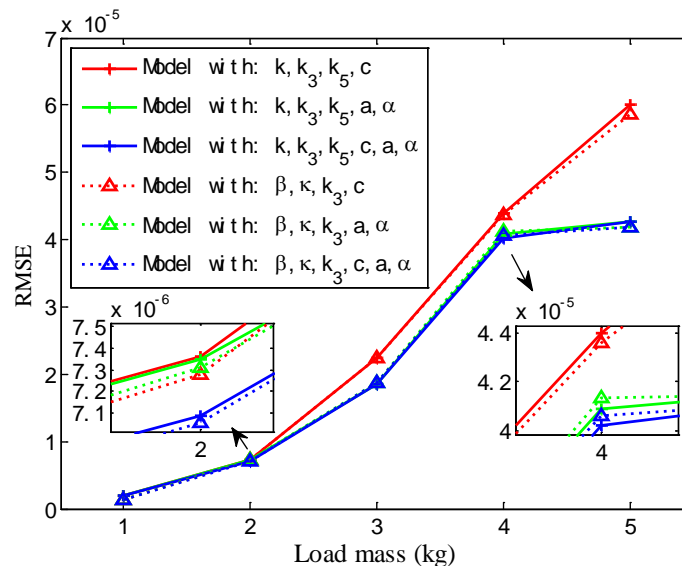


Figure 4.8 Comparison of RMSEs for six model structures for the conditions of 1-5 kg load mass and 0.1g excitation level.

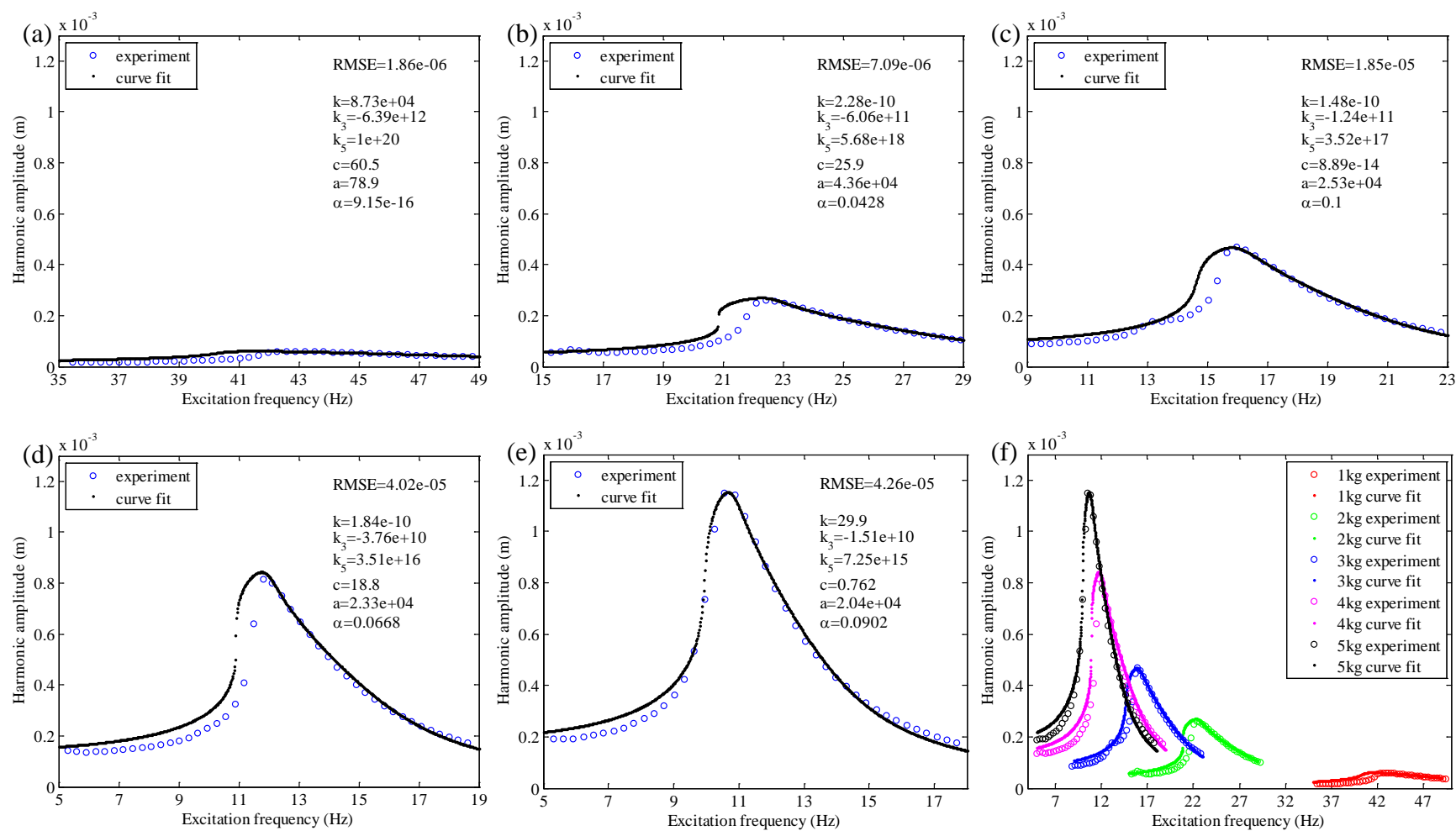


Figure 4.9 Fitting using the symmetric model $k, k_3, k_5, c, a, \alpha$ for the conditions of 0.1g excitation level and the mass of: (a) 1 kg; (b) 2 kg; (c) 3 kg; (d) 4 kg; (e) 5 kg; and (f) is a summary.

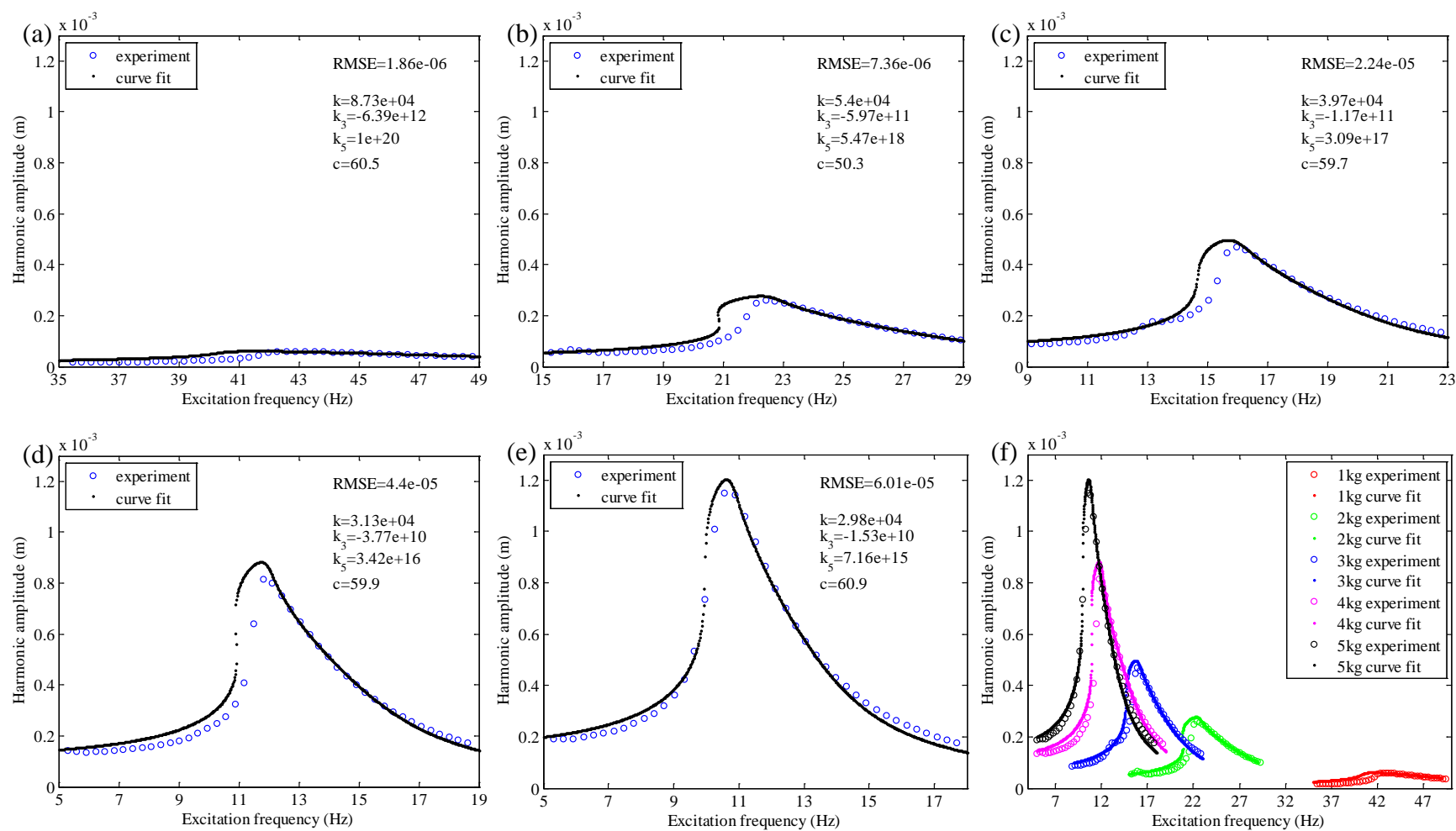


Figure 4.10 Fitting using the symmetric model k, k_3, k_5, c for the conditions of 0.1g excitation level and the mass of: (a) 1 kg; (b) 2 kg; (c) 3 kg; (d) 4 kg; (e) 5 kg; and (f) is a summary.

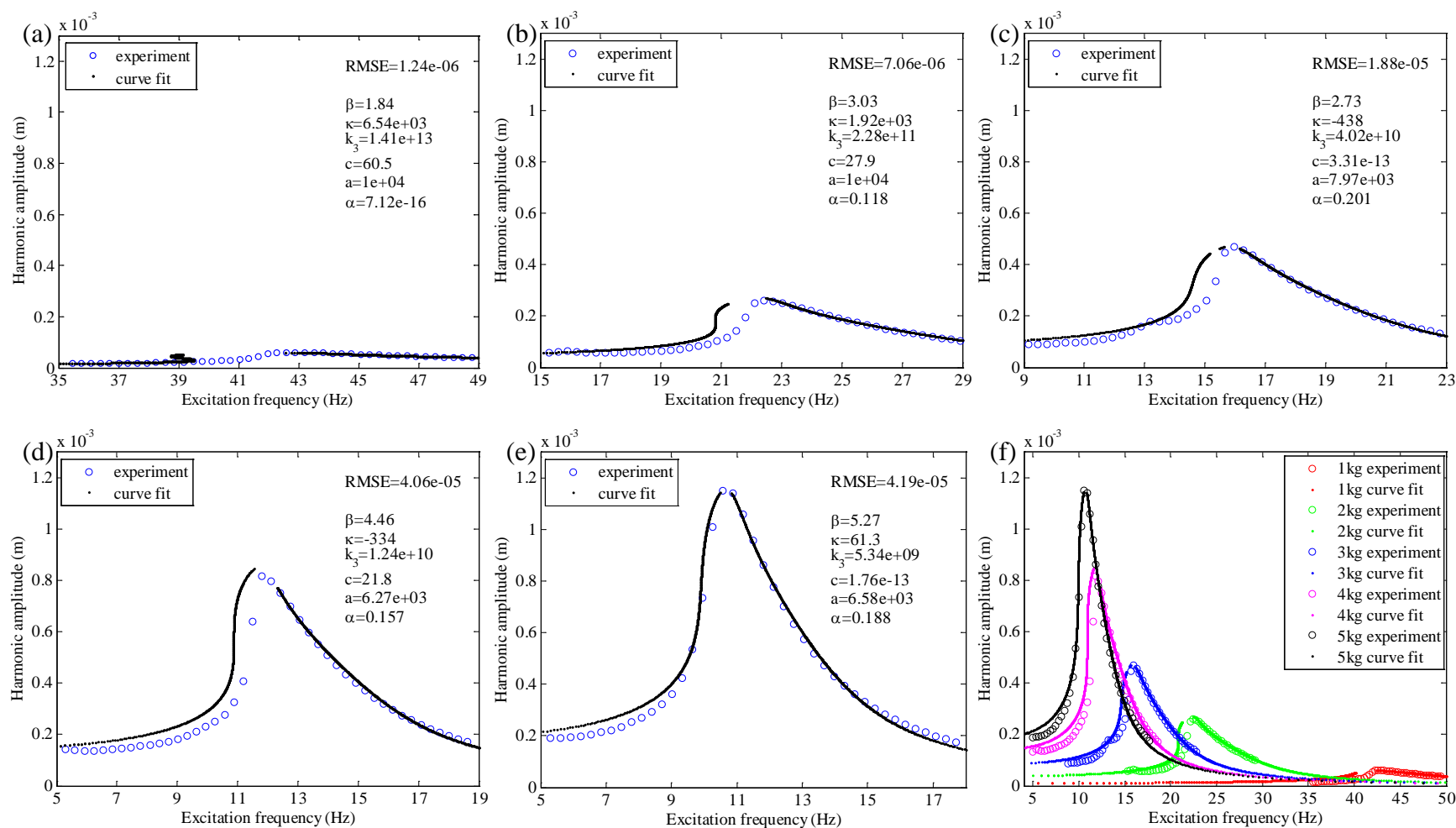


Figure 4.11 Fitting using the asymmetric model $\beta, \kappa, k_3, c, a, \alpha$ for the conditions of 0.1g excitation level and the mass of: (a) 1 kg; (b) 2 kg; (c) 3 kg; (d) 4 kg; (e) 5 kg; and (f) is a summary.

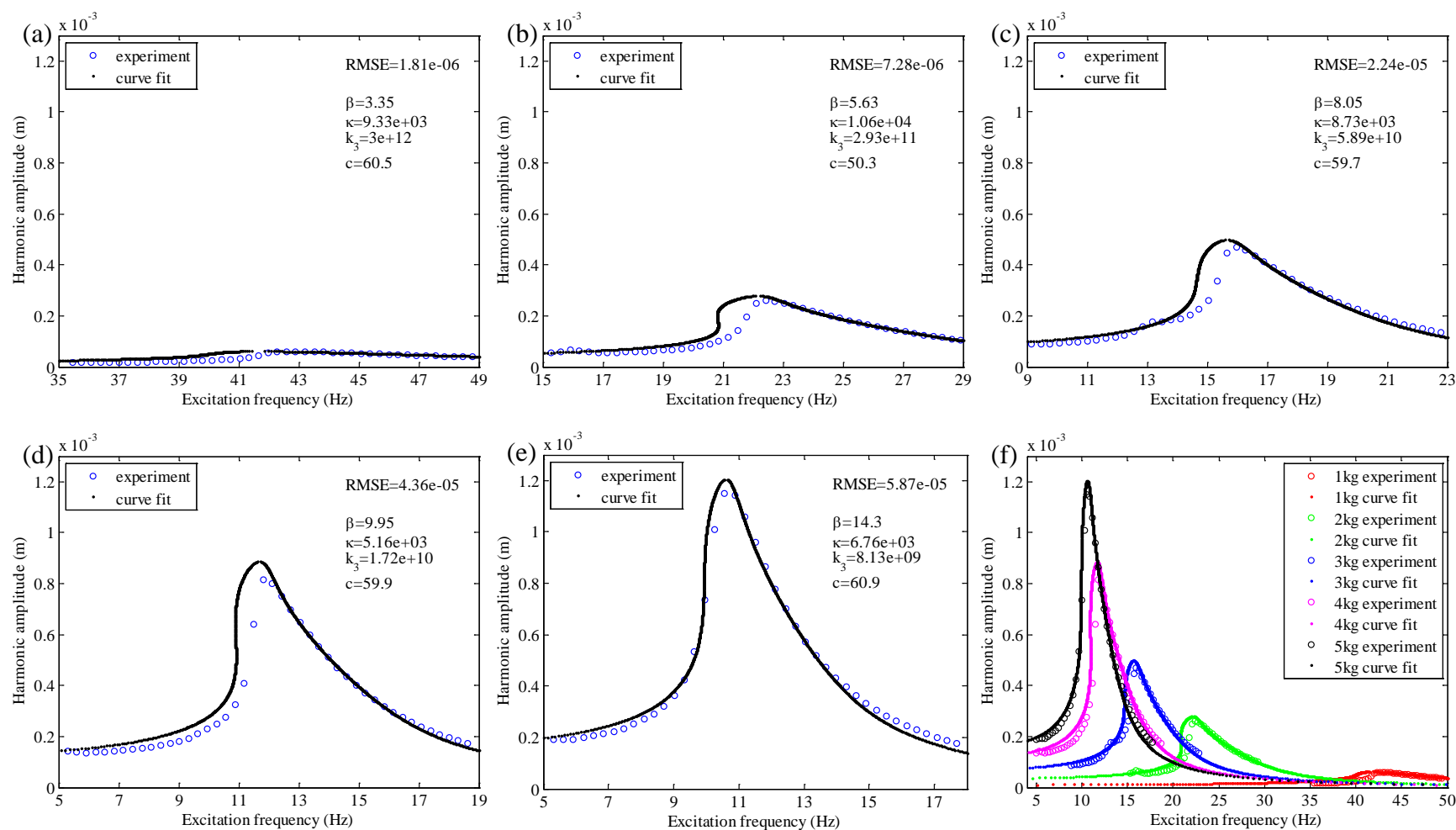


Figure 4.12 Fitting using the asymmetric model β, κ, k_3, c for the conditions of 0.1g excitation level and the mass of: (a) 1 kg; (b) 2 kg; (c) 3 kg; (d) 4 kg; (e) 5 kg, and (f) is a summary.

4.4 Chapter summary

In this chapter, curve fit and parameter identification was performed using symmetric models and asymmetric models under varied excitation level and load mass conditions. For each model structure, the corresponding equation of motion was built to describe the vibration of the mass-spacer fabric system. The steady-state solution was derived in the frequency domain. Experimental results of harmonic amplitude vs. excitation frequency curve were fitted with analytical models using a proper fitness function. Root mean square error (RMSE) was adopted as the indicator of goodness of fit.

A comparison of RMSEs using different models shows that the asymmetric model and the symmetric model have comparable performance. The former performs slightly better. Secondly, including the high-order quintic stiffness coefficient k_5 helps improve the symmetric model. Moreover, the fractional derivative term $aD^\alpha x$ also improves the goodness of fit of models to a certain extent. The term $aD^\alpha x$ outperforms $c\dot{x}$ for describing the vibration behavior of the mass-spacer fabric system. The viscous damping coefficient C was redundant in some cases.

CHAPTER 5 PARAMETRIC ANALYSIS

5.1 Introduction

In this chapter, theoretical analysis concerning the effects of nonlinear stiffness and damping property on the dynamic equation of the system under forced vibration is performed to strengthen the understanding of the vibration response mechanism of weft-knitted spacer fabrics. Two phenomenological models, the symmetric model and the asymmetric model, are considered separately. For the symmetric model, the influence of varying excitation level, viscous damping coefficient, fractional derivative parameters, linear stiffness, cubic stiffness and quintic stiffness on the frequency response curves (FRCs) will be discussed. For the asymmetric model, the influence of varying bias force, linear stiffness and cubic stiffness will be discussed. The FRCs used are the amplitude-frequency response curve and the force transmissibility curve. For the asymmetric model, a static displacement-frequency response curve is also obtained due to the asymmetric elastic force. Concerning the influence of varying stiffness coefficients on vibration response, the corresponding nonlinear force-displacement relationship are also provided.

5.2 Symmetric model

Given the dynamic equation for the nonlinear mass-spacer fabric system under harmonic excitation as

$$m\ddot{x} + c\dot{x} + kx + k_3x^3 + k_5x^5 + k_7x^7 + aD^\alpha x = -mG\cos(\omega t), \quad (5.1)$$

where $aD^\alpha x$ is a fractional derivative for explaining the viscoelasticity in spacer fabric, and G is the excitation level. The solution for the steady-state harmonic response has the form of

$$x(t) = Ae^{j\omega t} + \bar{A}e^{-j\omega t}, \quad (5.2)$$

where $A = A_r + jA_i$, and \bar{A} is the conjugate.

It can also be written as

$$x(t) = 2|A|\cos(\omega t + \phi), \quad (5.3)$$

where

$$\begin{cases} A_r = |A|\cos\phi \\ A_i = -|A|\sin\phi \end{cases} \quad (5.4)$$

From Chapter 4 we have already known that

$$\begin{cases} P \cdot |A|^2 + \frac{mGA_r}{2} = 0 \\ Q \cdot |A|^2 - \frac{mGA_i}{2} = 0 \end{cases}, \quad (5.5)$$

where

$$\begin{cases} P = -m\omega^2 + k + 3k_3|A|^2 + 10k_5|A|^4 + 35k_7|A|^6 + a\omega^\alpha \cos\left(\frac{\pi}{2}\alpha\right) \\ Q = c\omega + a\omega^\alpha \sin\left(\frac{\pi}{2}\alpha\right) \end{cases}. \quad (5.6)$$

Equation (5.5) can also lead to

$$(P^2 + Q^2) \cdot |A|^2 = \frac{m^2 G^2}{4}, \quad (5.7)$$

which is used to recover the harmonic amplitude $2|A|$ under different excitation frequencies with known model parameters.

At resonance, we have $\frac{d|A|}{d\phi} = 0$. So the phase angle at resonance is $\phi = -90^\circ$. Using

$$A_i \Big|_{\phi=-90^\circ} = |A|,$$

$$Q \cdot |A|^2 - \frac{mGA_i}{2} = 0,$$

and

$$Q = c\omega + a\omega^\alpha \sin\left(\frac{\pi}{2}\alpha\right)$$

from Equations (5.4) to (5.6), at resonance, we will have

$$\left[c\omega + a\omega^\alpha \sin\left(\frac{\pi}{2}\alpha\right) \right] \cdot |A|^2 - \frac{mG \cdot |A|}{2} = 0. \quad (5.8)$$

As a result, the locus of harmonic peak at resonance is

$$2 \cdot |A| \Big|_{\phi=-90^\circ} = \frac{mG}{c\omega + a\omega^\alpha \sin\left(\frac{\pi}{2}\alpha\right)}. \quad (5.9)$$

It is observed that the locus of response is not only a function of the excitation frequency, but also a function of the excitation level, load mass, damping coefficient and the fractional derivative term. It does not depend on the stiffness of the system. For simplicity,

the locus line will only appear in figures concerning the effect of changing stiffness terms.

From Equation (5.3), i.e. $x(t) = 2|A|\cos(\omega t + \phi)$, we learn that the force transmitted is also harmonic,

$$f_t = f_{t1} \cos(\omega t + \phi_t). \quad (5.10)$$

Since

$$\begin{aligned} f_t &= c\dot{x} + kx + k_3x^3 + k_5x^5 + k_7x^7 + aD^\alpha x \\ &= -mG \cos(\omega t) - m\ddot{x}, \\ &= -mG \cos(\omega t) + 2m\omega^2 |A| \cos(\omega t + \phi) \end{aligned} \quad (5.11)$$

we have now

$$\begin{cases} f_{t1} \cos \phi_t = -mG + 2m\omega^2 |A| \cos \phi \\ f_{t1} \sin \phi_t = 2m\omega^2 |A| \sin \phi \end{cases} \quad (5.12)$$

So the amplitude of the transmitted force becomes

$$f_{t1} = \sqrt{m^2 G^2 + 4m^2 \omega^4 |A|^2 - 4m^2 \omega^2 G |A| \cos \phi}. \quad (5.13)$$

Using

$$A_r = |A| \cos \phi,$$

$$P \cdot |A|^2 + \frac{mGA_r}{2} = 0,$$

and

$$P = -m\omega^2 + k + 3k_3 |A|^2 + 10k_5 |A|^4 + 35k_7 |A|^6 + a\omega^\alpha \cos\left(\frac{\pi}{2}\alpha\right)$$

from Equations (5.4) to (5.6), the cosine of phase angle can be written as

$$\cos \phi = -\frac{2|A| \cdot \left[-m\omega^2 + k + 3k_3|A|^2 + 10k_5|A|^4 + 35k_7|A|^6 + a\omega^\alpha \cos\left(\frac{\pi}{2}\alpha\right) \right]}{mG}. \quad (5.14)$$

This is substituted into Equation (5.13) to obtain the transmissibility as

$$T = \frac{f_{t1}}{mG} = \sqrt{1 + \frac{8\omega^2|A|^2}{mG^2} \cdot \left[-\frac{m\omega^2}{2} + k + 3k_3|A|^2 + 10k_5|A|^4 + 35k_7|A|^6 + a\omega^\alpha \cos\left(\frac{\pi}{2}\alpha\right) \right]}. \quad (5.15)$$

The locus of peak transmissibility can be obtained by setting the phase angle $\phi = -90^\circ$.

With Equations (5.9) and (5.13), we have

$$T \Big|_{\phi=-90^\circ} = \sqrt{1 + \frac{m^2\omega^4}{\left[c\omega + a\omega^\alpha \sin\left(\frac{\pi}{2}\alpha\right) \right]^2}}. \quad (5.16)$$

It is noticed that the locus of peak transmissibility is a function of the excitation frequency, load mass, damping coefficient and the fractional derivative term. It is, however, not affected by the excitation level and the nonlinear stiffness coefficients of the system. For simplicity, the locus of peak transmissibility will only appear in figures concerning the excitation level and nonlinear stiffness terms.

If we let $G = 0$, we obtain that $P = 0$. By solving the equation

$$0 = P = -m\omega^2 + k + 3k_3|A|^2 + 10k_5|A|^4 + 35k_7|A|^6 + a\omega^\alpha \cos\left(\frac{\pi}{2}\alpha\right), \quad (5.17)$$

a relation between the response amplitude $2|A|$ and the excitation frequency ω is

obtained. This is the backbone curve of response amplitude. It is independent of the excitation level and the damping force (i.e. the imaginary part of the solution). In the following figures, backbone curves of response amplitude are also given. It tells the trend of the peak when increasing the excitation level. It also tells the resonance frequency.

In Sections 5.2.1 to 5.2.6 as follows, the influence of excitation level, viscous damping coefficient, the fractional derivative term, linear, cubic and quintic stiffness coefficients will be presented by giving the harmonic amplitude response curve and the transmissibility curve. Concerning the effects of stiffness coefficients, the corresponding force-displacement curves are also given.

The reference parameter values are obtained by data fitting using the symmetric model with parameters k, k_3, k_5, c for Spacer-12h under the condition of $G_0 = 0.1g$ excitation level and 2 kg load mass. They are listed in Table 5.1. The fractional derivative term $aD^\alpha x$ is not considered, otherwise it would also contribute to the elastic force. However, they are added arbitrarily later in order to examine their effects on the FRCs.

Table 5.1 Parameter estimates by curve fit using the symmetric model.

Model parameter	k_0	k_{3_0}	k_{5_0}	c_0
Value	4.123×10^4	-2.463×10^{11}	1.423×10^{18}	46.15

5.2.1 Effect of excitation level G

As the excitation level is very small, the system oscillates with a very limited amplitude around the statically loaded position. The tangential stiffness at the statically loaded position is the linear stiffness k . When the harmonic amplitude becomes infinitesimal, the backbone curve intercepts with the horizontal axis at the frequency $f_r = \frac{1}{2\pi} \sqrt{\frac{k}{m}}$, which equates to a linear system. As shown in Figure 5.1(a), as the excitation level increases from $0.01g$ to $0.1g$, i.e. from $0.1G_0$ to G_0 , the response curve bends to the left, an indication of stiffness softening. The equivalent stiffness in a softening system is lower than the tangential stiffness at the statically loaded position (i.e. the linear stiffness k), as a result the resonance frequency falls below f_r . As the excitation level further increases from $0.1g$ to $0.3g$, i.e. from G_0 to $3G_0$, the response curve bends to the right, an indication of stiffness hardening, and the corresponding resonance frequency is above f_r . The cubic stiffness has a negative value, accounting for the stiffness softening phenomenon when the excitation level is relatively small; while the quintic stiffness has a positive value, accounting for the stiffness hardening phenomenon when the excitation level is relatively large. This is also verified by the fact that the trend of the backbone curve leans to the left first and then to the right as the harmonic amplitude rises.

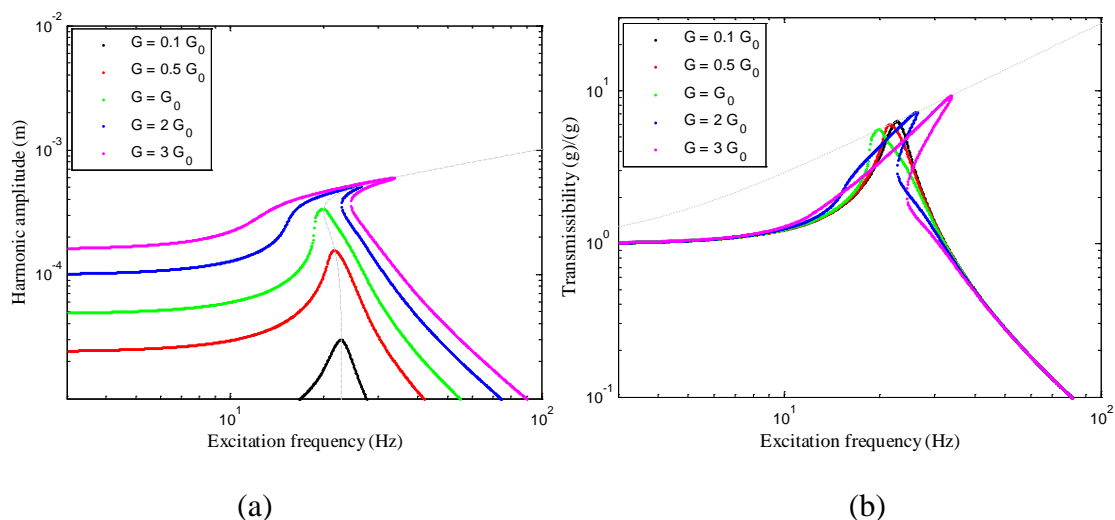


Figure 5.1 Effect of excitation level G on (a) harmonic amplitude $2|A|$ vs. excitation frequency response and (b) acceleration transmissibility T .

Figure 5.1(b) shows the corresponding transmissibility curves. It is learned from Equation (5.16) for the locus of peak transmissibility that, peak transmissibility is positively related with resonance frequency. This confirms the observation that at resonance, a softening system leads to reduced peak transmissibility, while a hardening system leads to elevated peak transmissibility.

On the other hand, as the excitation level is increased to a certain value, multiple solutions under certain excitation frequencies could take place, such as in the condition of $0.2g$ excitation level. Some solutions are unstable and will not be observed in experiments or numerical simulations. As this study is not concerned with the stability analysis of such nonlinear systems, it will not be discussed herein.

5.2.2 Effect of viscous damping coefficient c

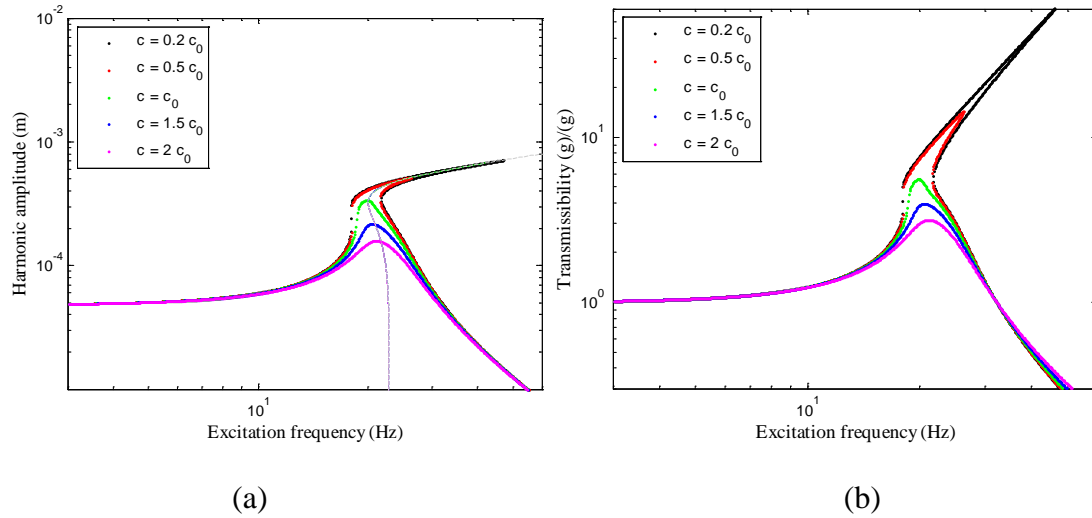


Figure 5.2 Effect of viscous damping coefficient c on (a) harmonic amplitude $2|A|$ vs. excitation frequency response and (b) acceleration transmissibility T .

Figure 5.2 shows clearly that increasing the viscous damping coefficient c leads to reduced response magnitude. This agrees with Equation (5.9) for the locus of harmonic peak and Equation (5.16) for the locus of peak transmissibility which suggest that both the peak harmonic amplitude and the peak transmissibility are negatively related with the viscous damping coefficient c . The damping term has a significant effect on both the harmonic amplitude and the transmissibility around resonance. However, its effect on regions away from resonance frequency is diminished. As a result, increasing damping is one efficient approach to vibration attenuation if resonance is a concern.

5.2.3 Effect of the fractional derivative term (a and α)

The fractional derivative term $aD^\alpha x(t)$ has two parameters, the coefficient a and the fractional derivative order α . It is assumed that $a \geq 0$ and $0 \leq \alpha \leq 2$. Considering the cases when $\alpha = 0$, $\alpha = 1$ and $\alpha = 2$, then this fractional derivative term evolves to the linear stiffness, the viscous damping coefficient and the inertia, respectively. Thus, when the fractional derivative order α is a non-integer between zero and one, it implicates certain combination of a linear spring and a viscous damper. The increase of α reduces the share of stiffness component and uplifts the share of damping component. To evaluate their effects on FRCs, we arbitrarily assume that $a_0 = 1000$ and $\alpha_0 = 0.2$. As shown in Figure 5.3, the increase of α from 0 to $4\alpha_0$ results in increased resonance frequency and reduced peak transmissibility.

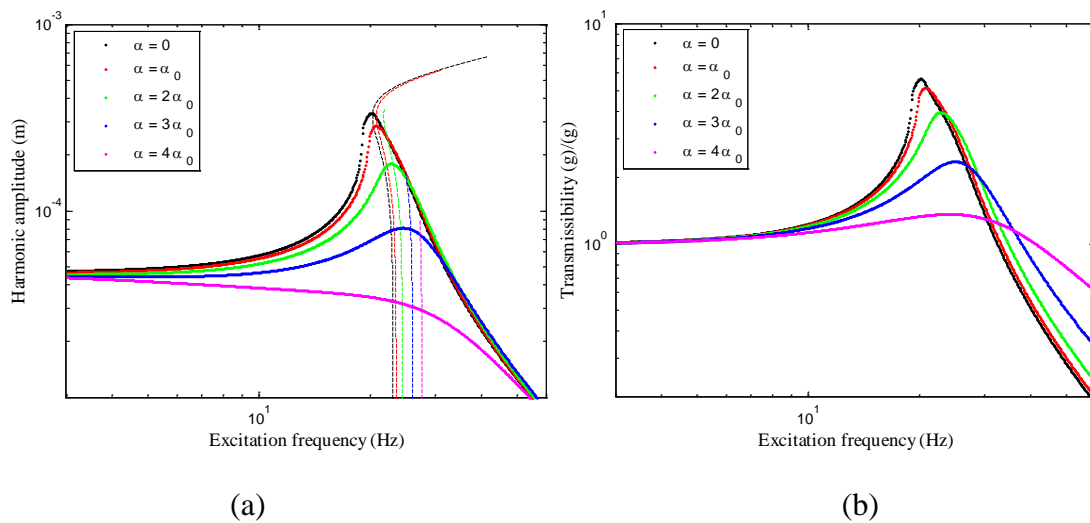


Figure 5.3 Effect of fractional derivative order α on (a) harmonic amplitude $2|A|$ vs. excitation frequency response and (b) acceleration transmissibility T .

On the other hand, it is evident that the increase of the coefficient a uplifts both the share of stiffness component and the share of damping component. As shown in Figure 5.4, the increase of the fractional derivative coefficient a from 0 to $4a_0$ results in increased resonance frequency and reduced peak transmissibility.

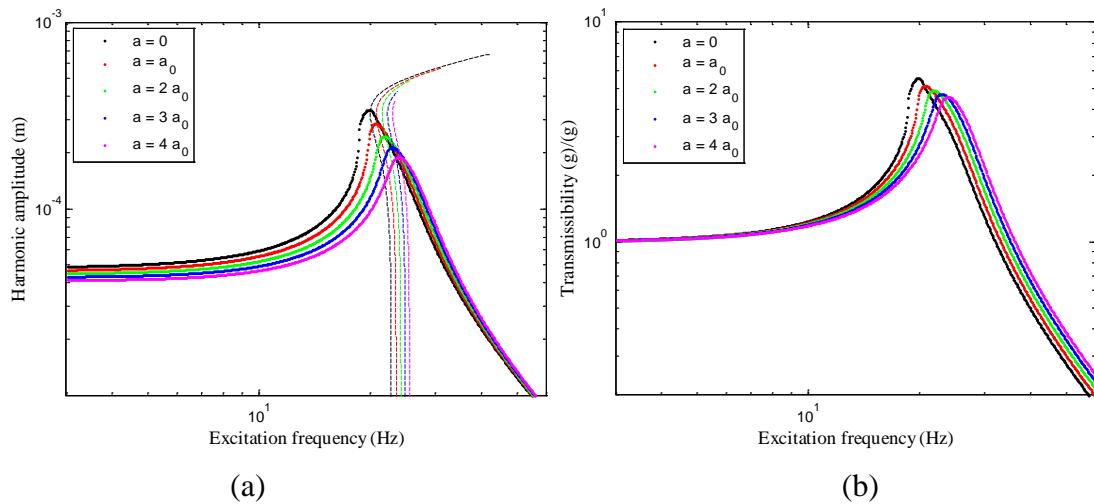


Figure 5.4 Effect of fractional derivative coefficient a on (a) harmonic amplitude $2|A|$ vs. excitation frequency response and (b) acceleration transmissibility T .

5.2.4 Effect of the linear stiffness k

The linear stiffness k is the tangential stiffness of the system at the statically-loaded position. As shown in Figure 5.5(a), the backbone curve intercepts with the horizontal axis

at resonance frequency $f_r = \frac{1}{2\pi} \sqrt{\frac{k}{m}}$. As a result, the increase of linear stiffness k leads

to higher resonance frequency. The increase of linear stiffness k also reduces the peak harmonic amplitude. Examining on the force-displacement curves reconstructed with the stiffness terms $y = kx + k_3x^3 + k_5x^5$, where y represents the force and x represents the displacement. Assuming $k_3 < 0$ and $k_5 > 0$, when the linear stiffness is low, the force-

displacement curve first softens and then hardens. Correspondingly, the amplitude curve and the transmissibility curve bend to the left first and then to the right. As the linear stiffness k increases, the softening phenomenon is weakened. In the corresponding amplitude curve and transmissibility curve, the bending to the left is also weakened, and the bending to the right fades. However, it can be predicted from the backbone curves that as the excitation level increases or the viscous damping coefficient decreases, the frequency response curves will regenerate the bending to the right at resonance.

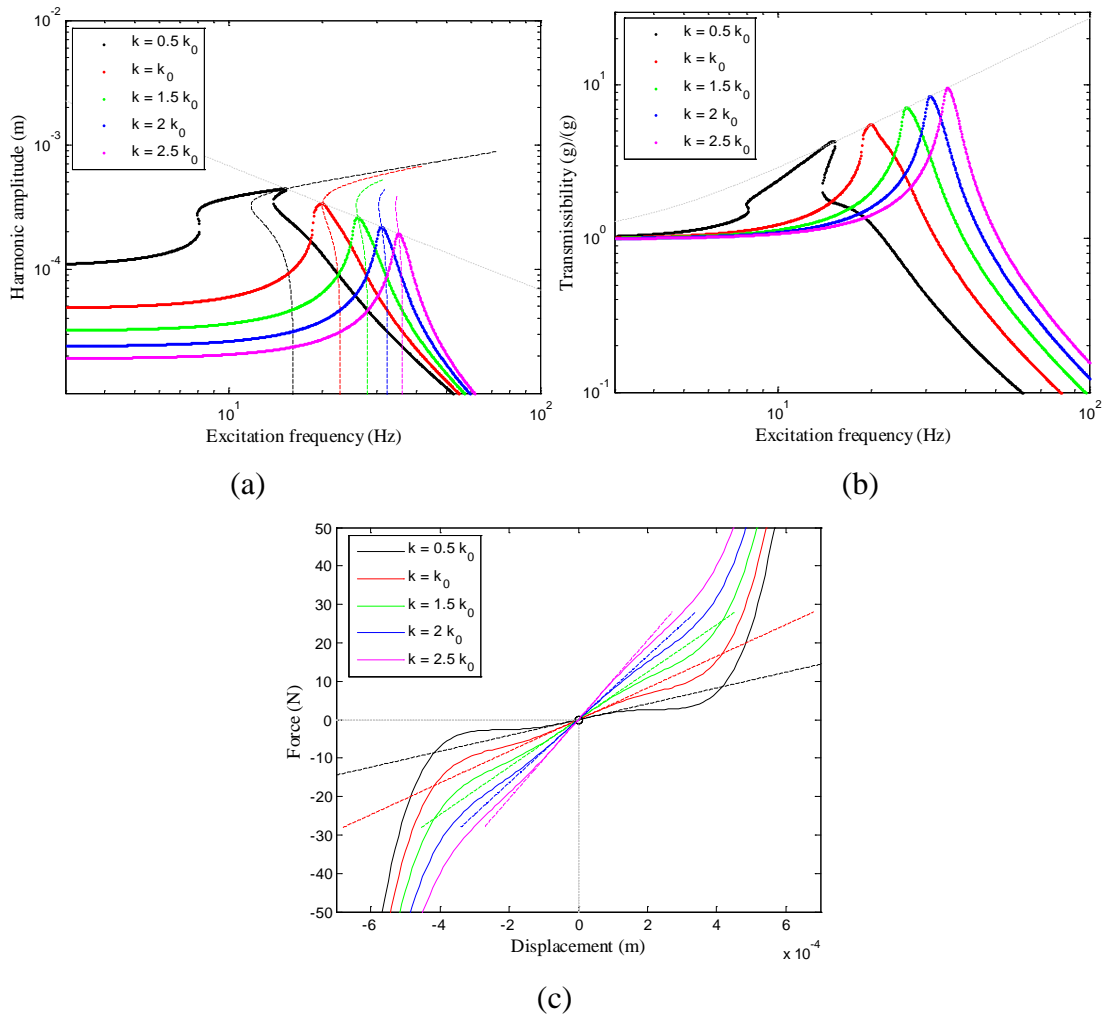


Figure 5.5 Effect of linear stiffness k on (a) harmonic amplitude $2|A|$, (b) acceleration transmissibility T and (c) elastic force $kx + k_3x^3 + k_5x^5$.

5.2.5 Effect of the cubic stiffness k_3

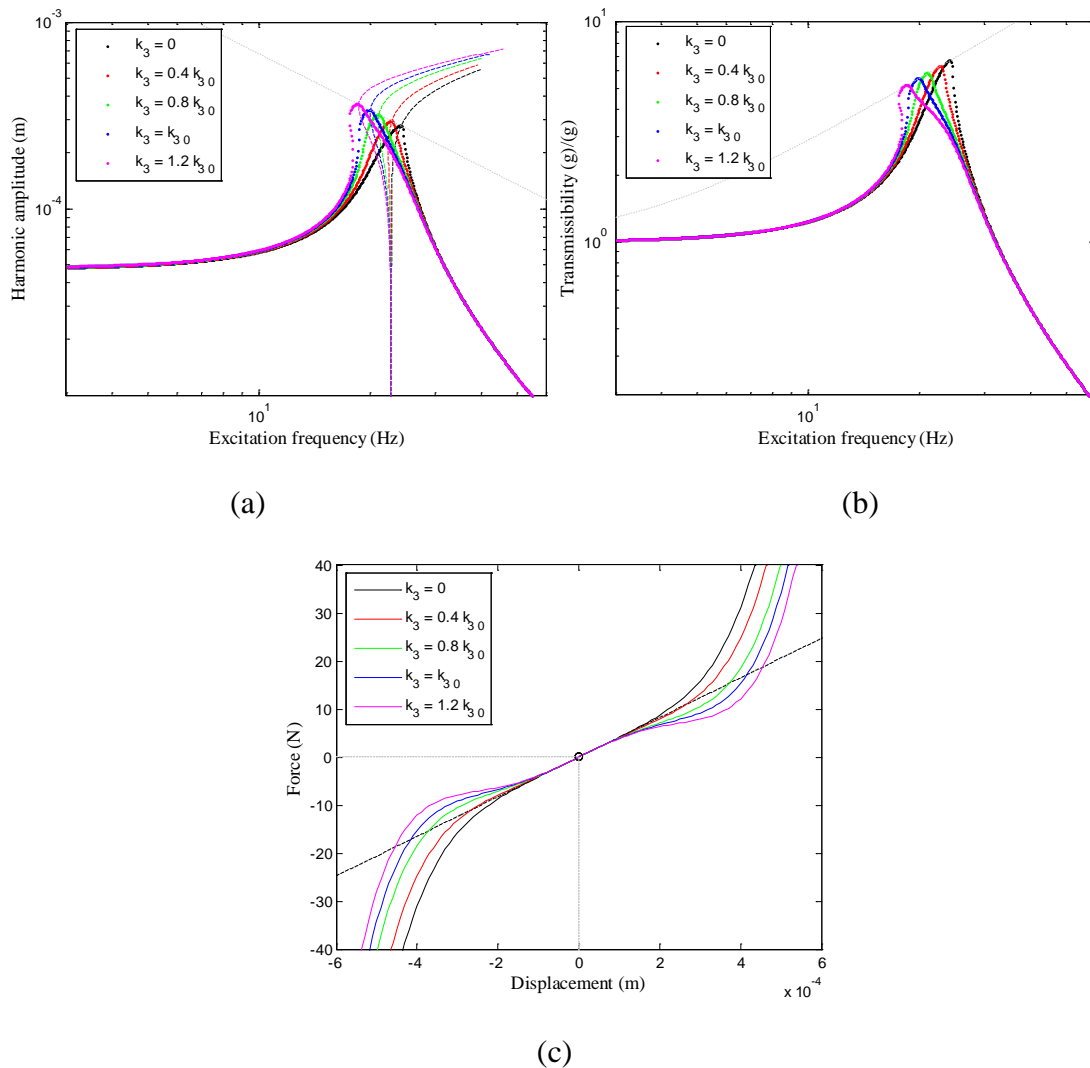


Figure 5.6 Effect of cubic stiffness k_3 on (a) harmonic amplitude $2|A|$, (b) acceleration transmissibility T and (c) elastic force $kx + k_3x^3 + k_5x^5$.

Assuming $k_3 < 0$, the cubic stiffness k_3 is responsible for the softening behavior in the frequency response curves. As shown in Figure 5.6(a), when the cubic stiffness disappears or is small enough, the frequency response curves bends only to the right due to the

dominant effect of the quintic stiffness coefficient $k_5 > 0$. When the cubic stiffness coefficient k_3 increases, the reconstructed force-displacement curve in Figure 5.6(c) experiences a prolonged softening region before entering the hardening region as the force or displacement goes away from the statically-loaded position. The corresponding frequency response curves also reflect stronger softening effect by bending to left. Besides, the peak harmonic amplitude is elevated and the peak transmissibility is reduced.

5.2.6 Effect of the quintic stiffness k_5

Due to the assumption of $k_3 < 0$ and $k_5 > 0$, the effects of k_3 and k_5 are opposite. As shown in Figure 5.7, with the increase of the quintic stiffness coefficient k_5 , the frequency response curve changes from bending to the left to bending to the right. When the quintic stiffness coefficient k_5 is small, the cubic stiffness coefficient k_3 dominates the bending of the resonance peak to the left under current excitation level and damping effect. When the quintic stiffness coefficient k_5 increases, the resonance peak first bends to the left and then to the right under a relatively high excitation level or a relatively small viscous damping effect, which is not in the figure but is predicted from the backbone curve. When the quintic stiffness coefficient k_5 is large enough to counteract the softening effect given by the cubic stiffness coefficient k_3 , pure hardening effect will be observed in the frequency response curves. This also agrees with the pure stiffness hardening in the reconstructed force-displacement curve in Figure 5.7(c).

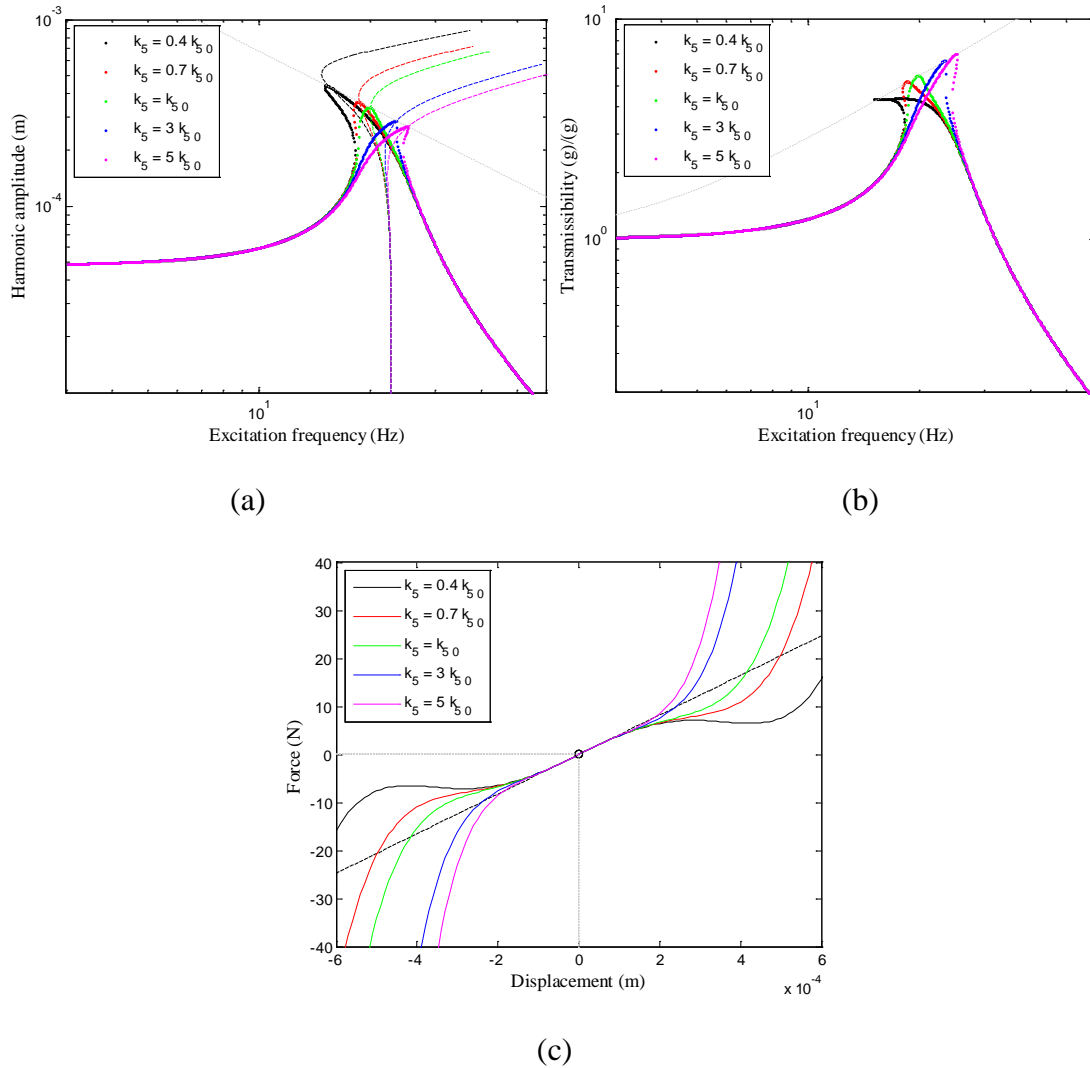


Figure 5.7 Effect of quintic stiffness k_5 on (a) harmonic amplitude $2|A|$, (b) acceleration transmissibility T and (c) elastic force $kx + k_3x^3 + k_5x^5$.

5.3 Asymmetric model

To describe the vibration behavior of the mass-spacer fabric system under harmonic excitation using the asymmetric model, the dynamic equation has the form of

$$m\ddot{x} + c\dot{x} + kx + k_2x^2 + k_3x^3 + aD^\alpha x = -mG\cos(\omega t). \quad (5.18)$$

Let

$$kx + k_2x^2 + k_3x^3 = \kappa(x + \delta) + k_3(x + \delta)^3 - \beta, \quad (5.19)$$

the relationship between two sets of parameters are

$$\begin{cases} \delta = \frac{k_2}{3k_3} \\ \kappa = k - \frac{k_2^2}{3k_3} \\ \beta = \frac{k \cdot k_2}{3k_3} - \frac{2k_2^3}{27k_3^2} \end{cases}. \quad (5.20)$$

The fractional derivative of the constant function is

$$D^\alpha \delta = \delta \lim_{\lambda \rightarrow 0} \frac{\Gamma(\lambda + 1)}{\Gamma(\lambda - \alpha + 1)} \cdot t^{\lambda - \alpha} = \frac{\delta t^{-\alpha}}{\Gamma(1 - \alpha)}, \quad (5.21)$$

where $\alpha \geq 0$, and $t^{-\alpha}$ is a decaying function so that $D^\alpha \delta \Big|_{t \rightarrow \infty} = 0$.

$$\text{Let } z(t) = x(t) + \delta, \quad (5.22)$$

and assume time is adequately long to reach steady state, so we have

$$D^\alpha (z - \delta) = D^\alpha z - D^\alpha \delta = D^\alpha z. \quad (5.23)$$

After coordinate transformation, the equation of motion becomes

$$m\ddot{z} + c\dot{z} + \kappa z + k_3z^3 + aD^\alpha z = -mG\cos(\omega t) + \beta. \quad (5.24)$$

Assume

$$z(t) = A_0 + Ae^{j\omega t} + \bar{A}e^{-j\omega t} = A_0 + 2|A|\cos(\omega t + \phi), \quad (5.25)$$

in which $A = A_r + jA_i$. The harmonic amplitude is $2|A|$ and the static displacement is A_0 .

Using the harmonic balance method (HBM), to equate the constants on both sides of Equation (5.24), we can obtain

$$k_3 A_0^3 + 6k_3 A_0 |A|^2 + \kappa A_0 = \beta. \quad (5.26)$$

The static displacement has only one real root, which is

$$A_0 = M - \frac{6k_3 |A|^2 + \kappa}{3k_3 M}, \quad (5.27)$$

where

$$M = \left\{ \left[\frac{(6k_3 |A|^2 + \kappa)^3}{27k_3^3} + \frac{\beta^2}{4k_3^2} \right]^{1/2} + \frac{\beta}{2k_3} \right\}^{1/3}.$$

Equating the coefficients of $e^{j\omega t}$ on both sides of Equation (5.24), we can obtain

$$3k_3 |A|^2 A + 3k_3 A_0^2 A + \kappa A + aA\omega^\alpha \cos\left(\frac{\pi}{2}\alpha\right) + jaA\omega^\alpha \sin\left(\frac{\pi}{2}\alpha\right) - m\omega^2 A + jc\omega A = -\frac{mG}{2}. \quad (5.28)$$

Let

$$\begin{cases} P = 3k_3 |A|^2 + 3k_3 A_0^2 + \kappa + a\omega^\alpha \cos\left(\frac{\pi}{2}\alpha\right) - m\omega^2 \\ Q = c\omega + a\omega^\alpha \sin\left(\frac{\pi}{2}\alpha\right) \end{cases}, \quad (5.29)$$

Equation (5.28) can be reduced to

$$PA + jQA = -\frac{mG}{2}, \quad (5.30)$$

thus, we have

$$\begin{cases} PA_r - QA_i = -\frac{mG}{2} \\ PA_i + QA_r = 0 \end{cases}. \quad (5.31)$$

The following procedures are mainly identical with those in the earlier symmetric model.

The difference is the static displacement term. The static displacement A_0 can be expressed with $|A|$.

The locus of harmonic peak is identical with that in the symmetric model, i.e. Equation (5.9)

$$2 \cdot |A| \Big|_{\phi=-90^\circ} = \frac{mG}{c\omega + a\omega^\alpha \sin\left(\frac{\pi}{2}\alpha\right)}.$$

Substituting Equation (5.9) into Equation (5.27), the locus of static displacement is solved accordingly.

The transmitted force is composed of a harmonic component and a static component

$$f_t = f_{t0} + f_{t1} \cos(\omega t + \phi_t). \quad (5.32)$$

Since

$$\begin{aligned}
f_t &= c\dot{x} + \kappa x + k_3 x^3 + aD^\alpha x \\
&= \beta - mG \cos(\omega t) - m\ddot{x} \\
&= \beta - mG \cos(\omega t) + 2m\omega^2 |A| \cos(\omega t + \phi)
\end{aligned} \tag{5.33}$$

we have now

$$\begin{cases} f_{t1} \cos \phi_t = -mG + 2m\omega^2 |A| \cos \phi \\ f_{t1} \sin \phi_t = 2m\omega^2 |A| \sin \phi \\ f_{t0} = \beta \end{cases} . \tag{5.34}$$

As there is no contribution of bias term, the transmissibility is expressed in the form of

$$T = \frac{f_{t1}}{mG} . \tag{5.35}$$

Similar as for the symmetric model, with Equations (5.4), (5.5) and (5.29), the transmissibility becomes

$$T = \sqrt{1 + \frac{8\omega^2 |A|^2}{mG^2} \cdot \left[-\frac{m\omega^2}{2} + 3k_3 |A|^2 + 3k_3 A_0^2 + \kappa + a\omega^\alpha \cos\left(\frac{\pi}{2}\alpha\right) \right]} . \tag{5.36}$$

The locus of peak transmissibility is obtained by setting phase angle $\phi = -90^\circ$, and it is identical with the symmetric model, i.e. Equation (5.16)

$$T \Big|_{\phi=-90^\circ} = \sqrt{1 + \frac{m^2 \omega^4}{\left[c\omega + a\omega^\alpha \sin\left(\frac{\pi}{2}\alpha\right) \right]^2}} .$$

If we let $G = 0$, we obtain that $P = 0$. By solving the equation

$$0 = P = 3k_3 |A|^2 + 3k_3 A_0^2 + \kappa + a\omega^\alpha \cos\left(\frac{\pi}{2}\alpha\right) - m\omega^2, \quad (5.37)$$

and substituting A_0 in the form of $|A|$, the relation between the response amplitude $2|A|$ and the excitation frequency ω is obtained. This is the backbone curve of response amplitude.

The parameter estimates by curve fit using the four-parameter model with β, κ, k_3, c are shown in Table 5.2, for the mass-spacer fabric system under the condition of $G_0 = 0.1g$ excitation level and 2 kg load mass. The parameter estimates of k and k_2 from the original equation of motion are also shown. The SI units are used for all of parameters. In the asymmetric model, the effects of the excitation level, the viscous damping coefficient and the fractional derivative term are similar with those in the symmetric model. So, only the effect of the bias term (β) and the stiffness terms (κ, k_3) will be discussed.

Table 5.2 Parameter estimates by curve fit using the asymmetric model.

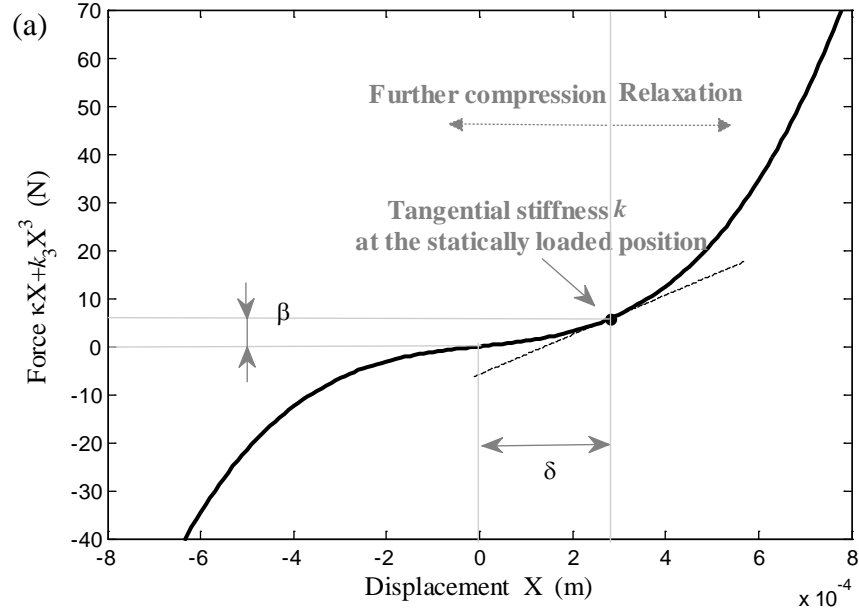
Model parameter	β_0	κ_0	k_{3_0}	c_0	k_0	k_{2_0}
Value	5.797	1.009×10^4	1.319×10^{11}	46.15	4.154×10^4	1.116×10^8

Spacer fabric is pre-stressed by load mass. During harmonic excitation, the compressive displacement for spacer fabric changes dynamically. The emergence of the bias force β

in Equation (5.24) is due to the existence of an asymmetric stiffness term k_2x^2 in the system. The true force-displacement relationship is $y = kx + k_2x^2 + k_3x^3$, i.e. $y = \kappa(x + \delta) + k_3(x + \delta)^3 - \beta$, where y represents the force and x represents the displacement, and which passes the origin $(0,0)$ of the coordinate plane, i.e. the statically-loaded position, and the point $(-\delta, -\beta)$.

In order to trace the frequency response curves under different bias forces β to the nonlinear stiffness terms of the system, we let $X = x + \delta$ and $Y = y + \beta$, so the force-displacement relationship is recast into $Y = \kappa X + k_3X^3$, as shown in Figure 5.8(a), which passes the point (δ, β) , i.e. the statically-loaded position which is marked with a solid dot, and the origin $(0,0)$, i.e. the center of 180° rotational symmetry. The instantaneous stiffness at the statically-loaded position equals k , which is marked with a dashed line. It is also noted that the tangent at the origin equals κ . The physical significance of ΔX is the change of compressive displacement for spacer fabric. To the positive direction ($\Delta X > 0$) of the reference coordinate (δ, β) is the pressure relaxation ($\Delta Y > 0$) process, while to the negative direction ($\Delta X < 0$) is the further compression ($\Delta Y < 0$) process. Due to the asymmetric force-displacement relationship about the statically-loaded position, displacements to the left and to the right exhibit stiffness softening and stiffness hardening characteristics separately, as is shown in Figure 5.8(a). Consequently, the center of harmonic displacement is no longer at the statically-loaded position. We consider the offset distance from the statically-loaded position to the center of oscillation to be called

the static displacement $A_0 - \delta$, the value of which depends on the excitation frequency. It has removed the effect of the constant displacement δ caused by coordinate transformation. It will be shown later that the static displacement $A_0 - \delta$ has negative values, which indicates that the center of oscillation shifts to the further compression direction for spacer fabric ($\Delta X < 0$ and $\Delta Y < 0$), i.e. the stiffness softening part. This is reasonable since a softening system undergoes longer displacement than a hardening system under an identical level of force. The center of oscillation will shift to the softening part to balance out the difference. To comply with practice, the reconstructed elastic force-displacement curve in Figure 5.8(a) is also converted into the compression force vs. compression displacement curve in Figure 5.8(b), when the load mass is 2 kg.



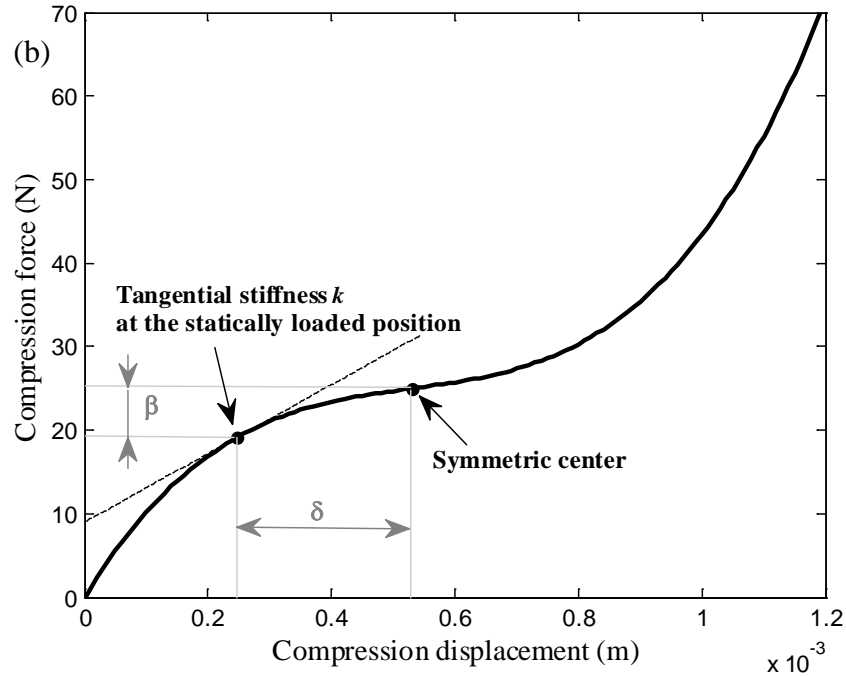


Figure 5.8 (a) Reconstructed elastic force-displacement curve $\kappa X + k_3 X^3$ using fitted parameters of the model with parameters β, κ, k_3, c under 0.1g excitation level; (b) Converted into the compression force vs. compression displacement curve.

5.3.1 Effect of the bias force β

The fitted model parameters satisfy the relations of $k_2 > 0$, $k_3 > 0$ and $\beta > 0$. The parameters κ and k_3 are fixed herein. Since the curve $y = \kappa(x + \delta) + k_3(x + \delta)^3 - \beta$ passes the origin $(0, 0)$, then we have $\beta = \kappa\delta + k_3\delta^3$. Since we have the fitted model parameter $\kappa > 0$, then β will also be positively related with δ , an intermediate parameter generated due to coordinate transformation. On the other hand, Equation (5.20) can be transformed to obtain $k_2 = 3k_3\delta$ and $k = \kappa + 3k_3\delta^2$. Consequently, the bias force

β is positively related with both the linear stiffness k and the quadratic stiffness k_2 . This agrees with our case. Figure 5.9(d) shows that an increase in the bias force β is associated with both an increase in the tangent stiffness k at the statically-loaded position and an increase in the intermediate parameter δ . Therefore, concerned with the frequency responses, the backbone curve will intercept with the horizontal axis at a higher resonance frequency $f_r = \frac{1}{2\pi} \sqrt{\frac{k}{m}}$, as is shown in Figure 5.9(a) and (b) for the frequency response curves of the static displacement $A_0 - \delta$ and the harmonic amplitude $2|A|$.

However, if restricting the conditions by letting $\kappa < 0$, which will be discussed in the next section, the positive relationship between the bias force β and the intermediate parameter δ will not always be founded. We have already known that the tangent equals κ at the origin $(0,0)$, i.e. the center of 180° rotational symmetry, then the force-displacement curve will experience a negative stiffness region about the center of symmetry if $\kappa < 0$. Suppose we have $\kappa = 0$, the curve will experience a quasi-zero stiffness region about the center of symmetry.

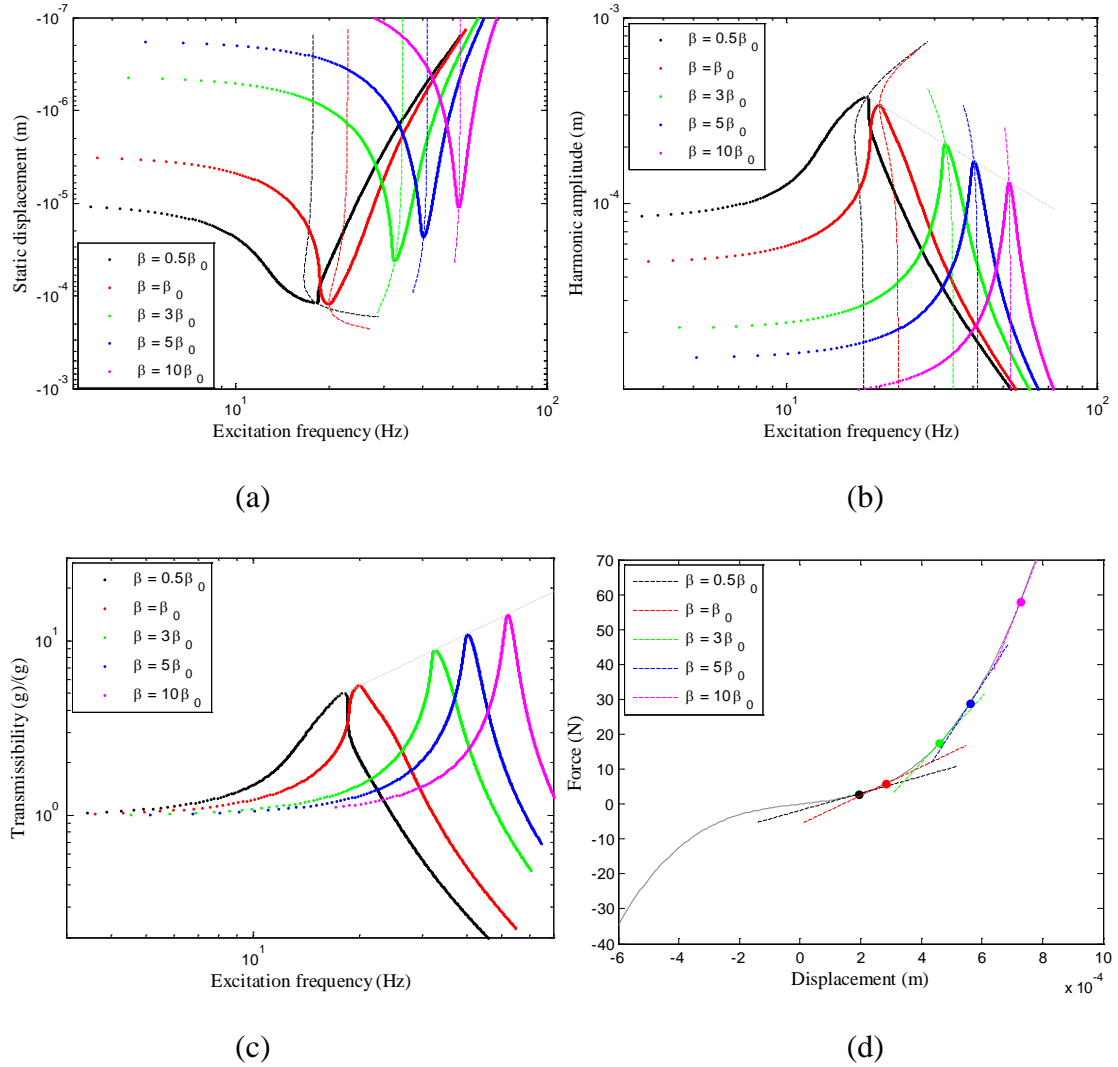


Figure 5.9 Effect of bias force β on (a) static displacement $A_0 - \delta$, (b) harmonic amplitude $2|A|$, (c) acceleration transmissibility T and (d) elastic force $\kappa X + k_3 X^3$.

5.3.2 Effect of the linear stiffness κ

Similarly, we use a recast force-displacement relationship $Y = \kappa X + k_3 X^3$ to examine on the effect of changing the parameter κ on the frequency responses of the mass-spacer fabric system. This curve passes the point (δ, β) , i.e. the statically-loaded position, and

the origin $(0,0)$, i.e. the center of 180° rotational symmetry. The tangent stiffness at the center of symmetry equals \mathcal{K} . From the previous analysis, we already know that the sign of \mathcal{K} determines whether the curve exhibits a positive, a quasi-zero or a negative stiffness region about the center of symmetry.

The fitted model parameters satisfy the relations of $k_2 > 0$, $k_3 > 0$ and $\beta > 0$. With parameters β and k_3 fixed, the aforementioned equation $\beta = \mathcal{K}\delta + k_3\delta^3$ indicates that the stiffness \mathcal{K} will be negatively related with the intermediate parameter δ . On the other hand, Equation (5.20) shows that $k_2 = 3k_3\delta$, so that δ is proportional to k_2 . In brief, as the linear stiffness \mathcal{K} increases, both of the intermediate parameter δ and the quadratic stiffness k_2 will decrease. Equation (5.20) gives the following expression $k = \frac{\beta}{\delta} + 2k_3\delta^2$,

and the derivative is $\frac{dk}{d\delta} = 4k_3\delta - \frac{\beta}{\delta^2}$. When $\frac{dk}{d\delta} > 0$, i.e. $\delta > \sqrt[3]{\frac{\beta}{4k_3}}$, the linear stiffness

k will be positively related with the intermediate parameter δ ; on the contrary, when

$\frac{dk}{d\delta} < 0$, i.e. $\delta < \sqrt[3]{\frac{\beta}{4k_3}}$, the linear stiffness k will be negatively related with the

intermediate parameter δ . Our case belongs to the former situation, in which as \mathcal{K} increases, the linear stiffness k will decrease.

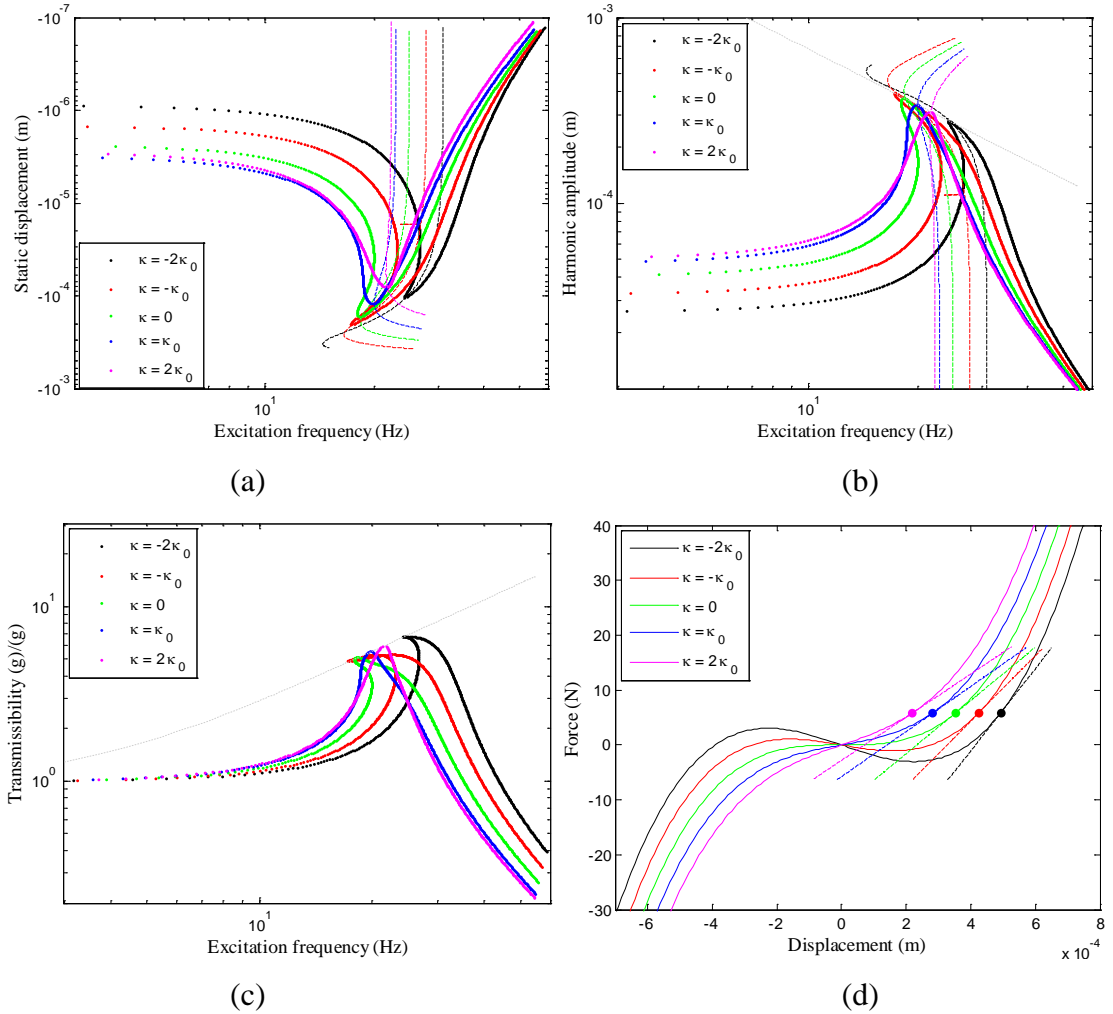


Figure 5.10 Effect of linear stiffness κ on (a) static displacement $A_0 - \delta$, (b) harmonic amplitude $2|A|$, (c) acceleration transmissibility T and (d) elastic force $\kappa X + k_3 X^3$.

This agrees with the observation in Figure 5.10(d), which shows that an increase in the tangent stiffness κ at the center of symmetry is associated with a decrease in the tangent stiffness k at the statically-loaded position which is marked with a solid dot. Therefore, concerned with the frequency responses, the backbone curve will intercept with the horizontal axis at a smaller resonance frequency $f_r = \frac{1}{2\pi} \sqrt{\frac{k}{m}}$, as is shown in Figure

5.10(a) and (b) for the frequency response curves of static displacement $A_0 - \delta$ and harmonic amplitude $2|A|$.

5.3.3 Effect of the cubic stiffness k_3

Once again, we use a recast force-displacement relationship $Y = \kappa X + k_3 X^3$, which passes the point (δ, β) and the origin $(0,0)$, to examine on the effect of changing the cubic stiffness k_3 on the frequency responses of this nonlinear system. The fitted parameters satisfy the relations of $k_2 > 0$, $k_3 > 0$ and $\beta > 0$. The bias force β and the tangent stiffness κ at the center of symmetry are kept constant herein. From the aforementioned equation $\beta = \kappa\delta + k_3\delta^3$ we know that as the cubic stiffness k_3 increases, the intermediate parameter δ decreases. On the other hand, with Equation (5.20) we obtain the expressions $k = \frac{3\beta}{\delta} - 2\kappa$ and $k_2 = \frac{k - \kappa}{\delta}$. Consequently, the cubic stiffness k_3 is positively related with both the linear stiffness k and the quadratic stiffness k_2 . This agrees with our case. Figure 5.11(d) shows that an increase in the cubic stiffness k_3 is associated with an increase in the tangent stiffness k at the statically-loaded position which is marked with a solid dot. Therefore, concerned with the frequency responses, the backbone curve will intercept with the horizontal axis at a higher resonance frequency $f_r = \frac{1}{2\pi} \sqrt{\frac{k}{m}}$, as is shown in Figure 5.11(a) and (b) for the frequency response curves of

the static displacement $A_0 - \delta$ and the harmonic amplitude $2|A|$.

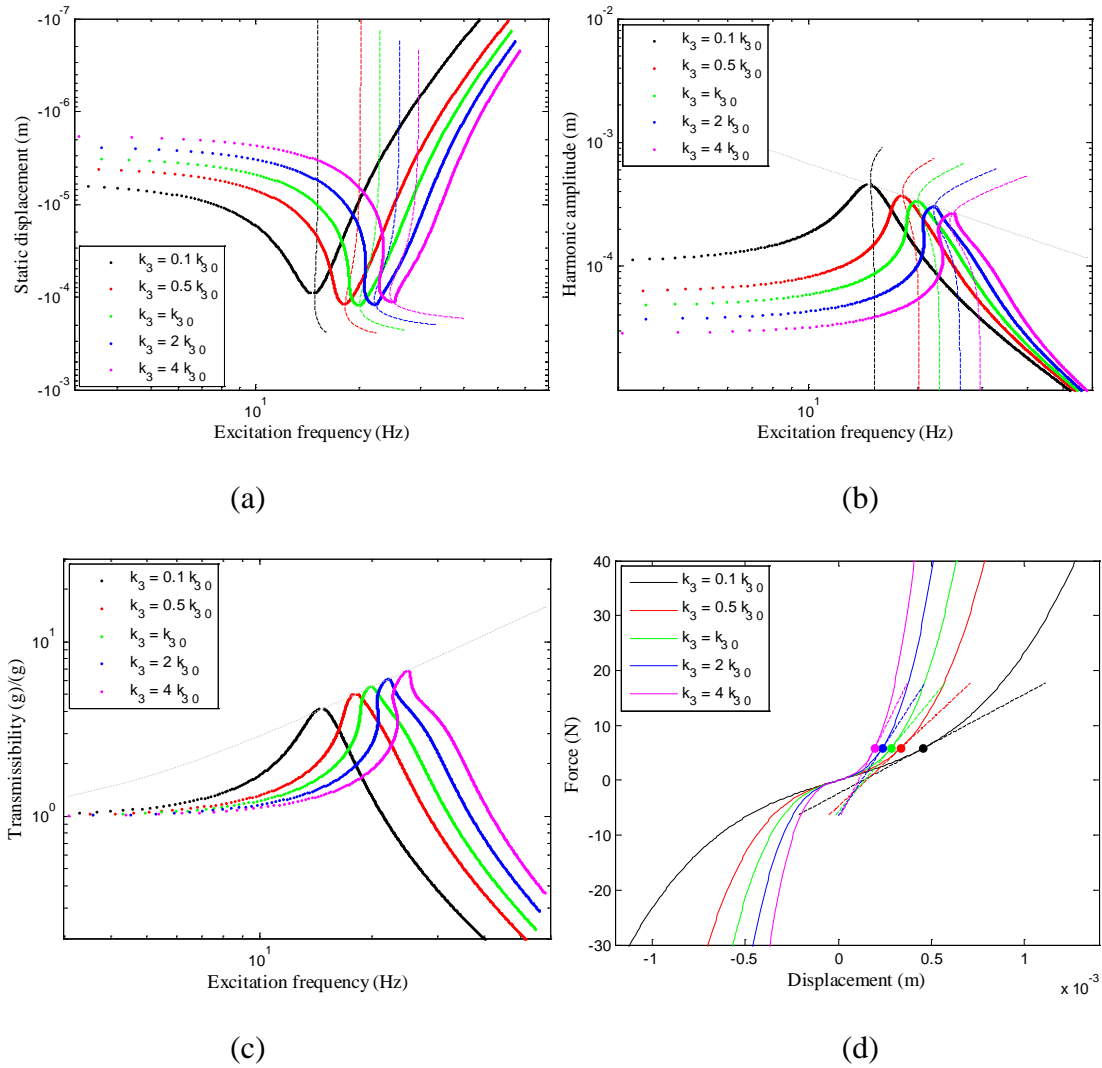


Figure 5.11 Effect of cubic stiffness k_3 on (a) static displacement $A_0 - \delta$, (b) harmonic amplitude $2|A|$, (c) acceleration transmissibility T and (d) elastic force $\kappa X + k_3 X^3$.

5.4 Chapter summary

Parametric analysis has been performed in this chapter using the symmetric model and

the asymmetric model separately. For both models, the amplitude-frequency relationship and force transmissibility relationship are derived from the equation of motion.

In the upper half part, effects of the excitation level G and model parameters $c, a, \alpha, k, k_3, k_5$ are studied for the symmetric model.

- **Excitation level G** : The system can be softening, hardening and mixed softening-hardening depending on the magnitude of excitation level. As the excitation level increases, resonance peak of the frequency response curves (FRCs) becomes softening first and then hardening.
- **Viscous damping coefficient c** : Viscous damping coefficient c can be used to reduce both harmonic amplitude and force transmissibility around resonance region.
- **The fractional derivative term $aD^\alpha x$** : The increase of the fractional order α and the fractional derivative coefficient a result in increased resonance frequency and reduced peak transmissibility.
- **Linear stiffness k** : The increase of linear stiffness k increases the resonance frequency, reduces the peak harmonic amplitude and increases the peak force transmissibility.
- **Cubic stiffness k_3** : Assume the value of cubic stiffness k_3 is negative, it is responsible for the softening behavior in the FRCs, which is characterized by the bending to left for resonance peak. Increasing its absolute value results in elevated peak harmonic amplitude and reduced peak transmissibility.

- **Quintic stiffness k_5** : Assume the value of quintic stiffness k_5 is positive, it is responsible for the hardening behavior in the FRCs. The effect of the positive quintic stiffness k_5 is opposite to the effect of the negative stiffness k_3 . Its significance is manifested at high displacement values.

In the lower half part, effects of model parameters β, κ, k_3 are studied for the asymmetric model. In our case, we have $k_2 > 0$, $k_3 > 0$ and $\beta > 0$.

- **Bias force β** : An increase in the bias force β is associated with an increase in the tangent stiffness k at the statically-loaded position. Therefore, resonance will take place at a higher frequency.
- **Stiffness κ at the center of symmetry** : In our cases, an increase in the tangent stiffness κ at the center of symmetry of elastic force is associated with a decrease in the tangent stiffness k at the statically-loaded position. Therefore, resonance will take place at a lower frequency.
- **Cubic stiffness k_3** : An increase in the cubic stiffness k_3 is associated with an increase in the tangent stiffness k at the statically-loaded position. Therefore, resonance will take place at a higher frequency.

CHAPTER 6 NUMERICAL SIMULATION

6.1 Introduction

In Chapter 5, approximate analytical solutions of the amplitude-frequency relationship are obtained by the harmonic balance method with the first-order approximation. For the symmetric model with parameters $k, k_3, k_5, c, a, \alpha$, the amplitude-frequency response is composed of harmonic components. For the asymmetric model with parameters $\beta, \kappa, k_3, c, a, \alpha$, the amplitude-frequency response is composed of a harmonic component and a static component. In this chapter, numerical simulations will be carried out to solve the equation of motion described by both symmetric and asymmetric models. The results will be compared with approximate analytical solutions. Secondly, whether model parameters obtained for one excitation level can predict the vibration behavior for a different excitation level will be investigated. Following this, the bifurcation and chaotic behaviors of the mass-spacer fabric are studied numerically using the asymmetric model with excitation frequency, excitation level and fractional order varied.

6.2 Periodic solutions

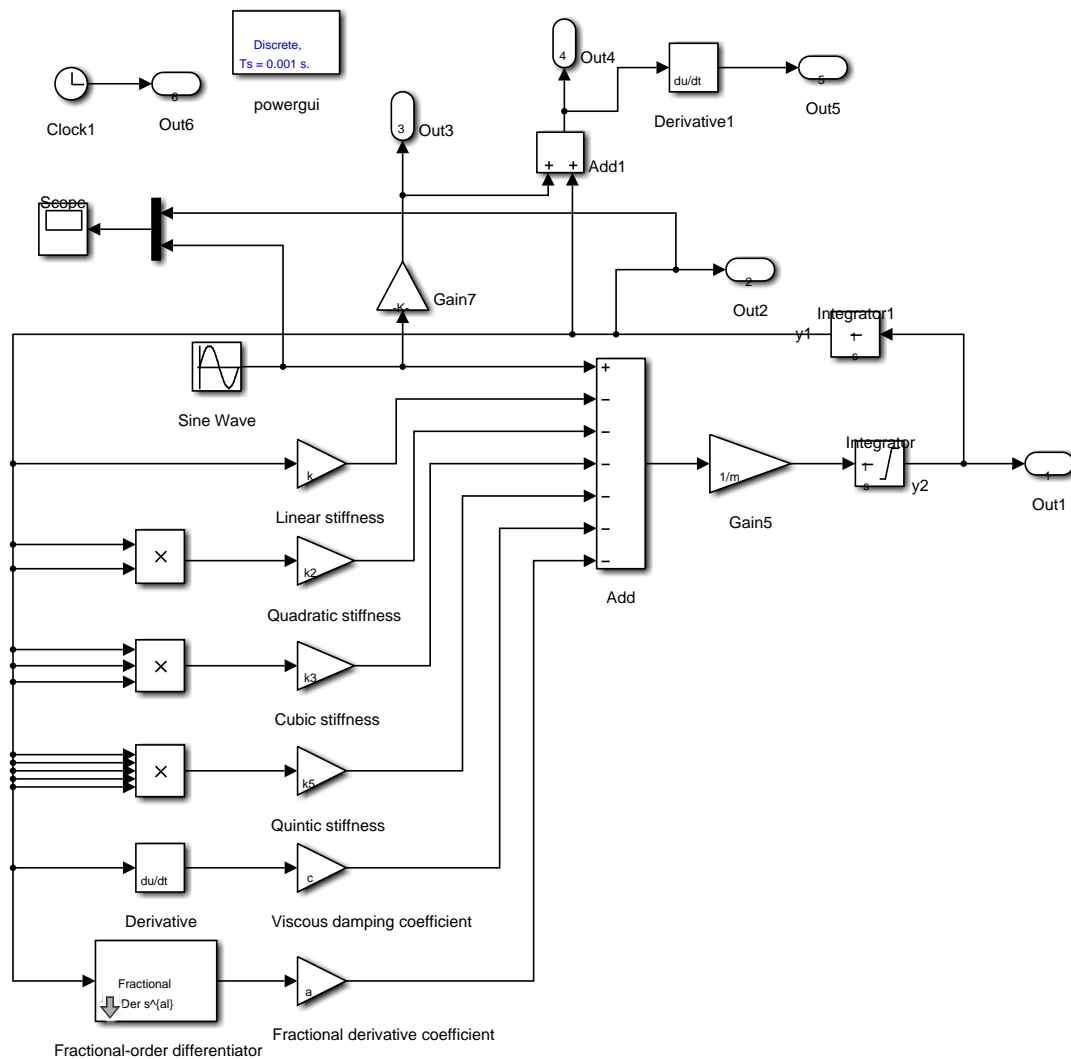


Figure 6.1 MATLAB/Simulink block diagram, with the Oustaloup filter^{151, 152}

implemented for the approximation of the fractional derivative operator.

With model parameters identified in Chapter 4, the MATLAB/Simulink block diagram as shown in Figure 6.1 is utilized to obtain numerical results of the equation of motion described by both symmetric and asymmetric models, for Spacer-12h under the conditions of 0.1-0.3g excitation levels and 2 kg load mass. The ode3 solver with a fixed step size

0.001 s is adopted. The simulation time is 100 s in order for the response to achieve the steady state. The fractional-order operator is approximated using the 4th-order Oustaloup filter^{151, 152}, and the frequency range of interest is [0.001 1000] rad/sec.

Figure 6.2 shows the numerical result of the static component $A_0 - \delta$ and the harmonic component $2|A|$ of the amplitude-frequency responses using the asymmetric model with parameters β, κ, k_3, c , in comparison with the experimental data and the approximation by harmonic balance method (HBM). As described in Chapter 5, the static component $A_0 - \delta$ is the offset distance from the statically-loaded position to the center of oscillation, which has removed the effect of the constant displacement δ caused by coordinate transformation. The negative value of $A_0 - \delta$ indicates that the center of oscillation shifts to the further compression direction for spacer fabric, i.e. to the stiffness softening region. For this asymmetric model structure, the numerical results and the HBM approximation agrees well at relatively high excitation frequencies. However, a discrepancy between them occurs at relatively low excitation frequencies of around 10 Hz, which is caused by an even order second harmonic. In comparison, when the symmetric model with parameters k, k_3, k_5, c is used as in Figure 6.4(a), numerical results agrees very well with the HBM approximation for all excitation frequencies. Time-domain numerical representations will be used later in Figures 6.5 and 6.6 to explain the discrepancy.

Adding the fractional derivative term into the previous asymmetric model, Figure 6.3 shows the numerical result in comparison with the experimental data and the HBM

approximation using the asymmetric model with parameters $\beta, \kappa, k_3, c, a, \alpha$. In this case, the numerical result has an evident difference with the HBM approximation at the resonance peak and the high-frequency region. In comparison, Figure 6.4(b) uses the symmetric model with parameters $k, k_3, k_5, c, a, \alpha$. The same phenomenon occurs for this model structure.

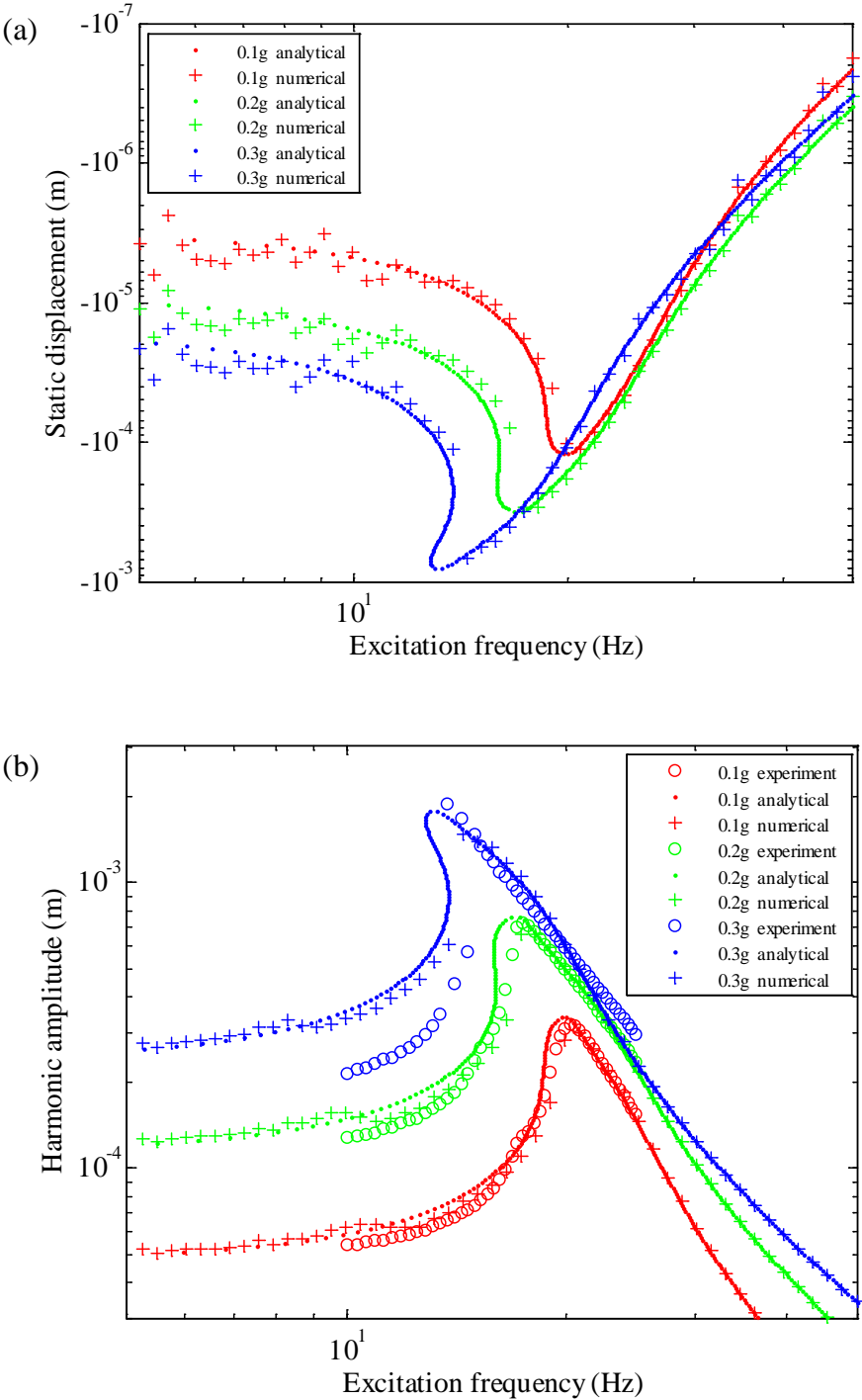


Figure 6.2 Numerical result ('+') in comparison with the experimental data ('o') and the HBM approximation ('•') using the asymmetric model with parameters β, κ, k_3, c : (a) static displacement; (b) harmonic amplitude.

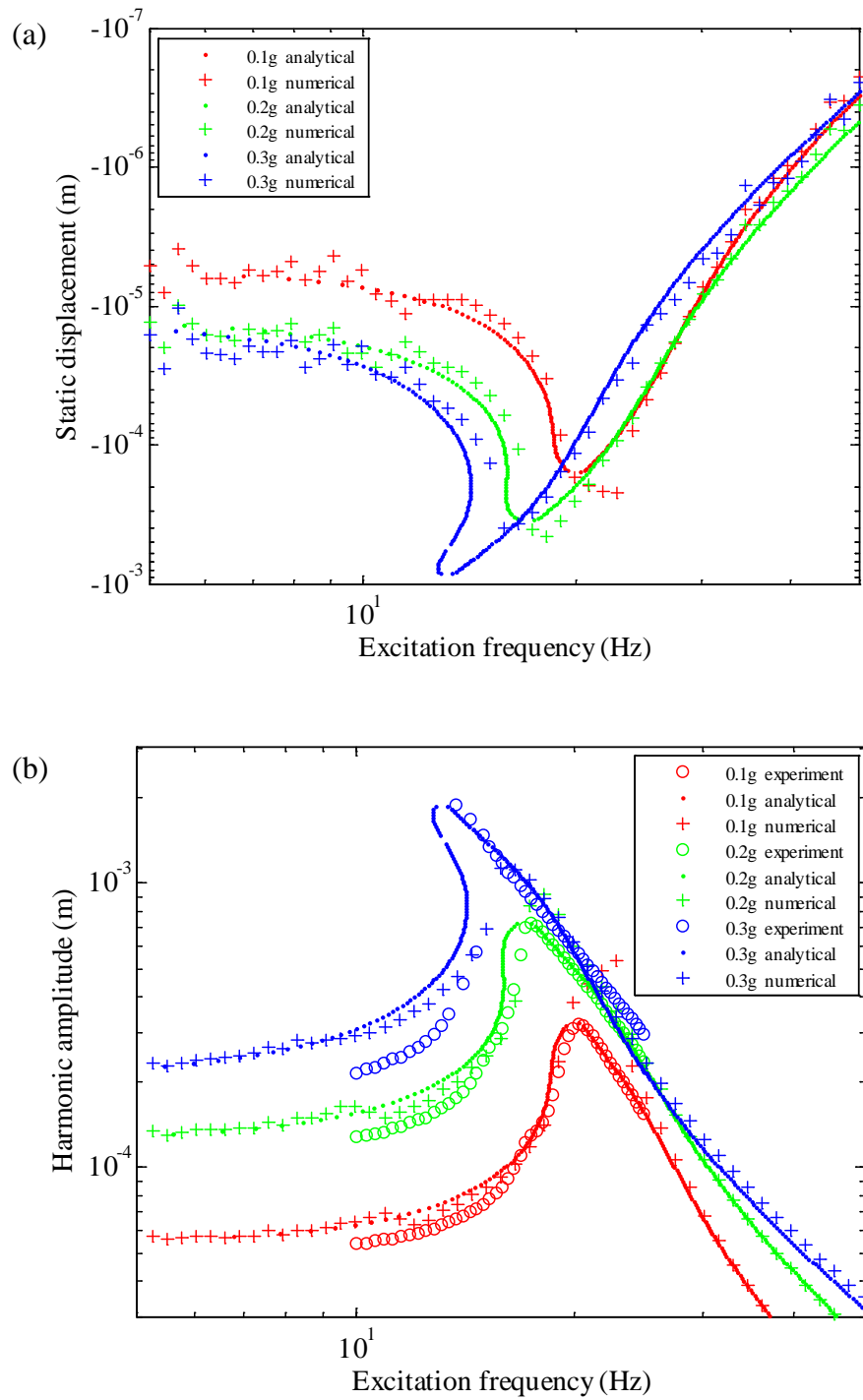


Figure 6.3 Numerical result ('+') in comparison with the experimental data ('o') and the HBM approximation ('•') using the asymmetric model with parameters

$\beta, \kappa, k_3, c, a, \alpha$: (a) static displacement; (b) harmonic amplitude.

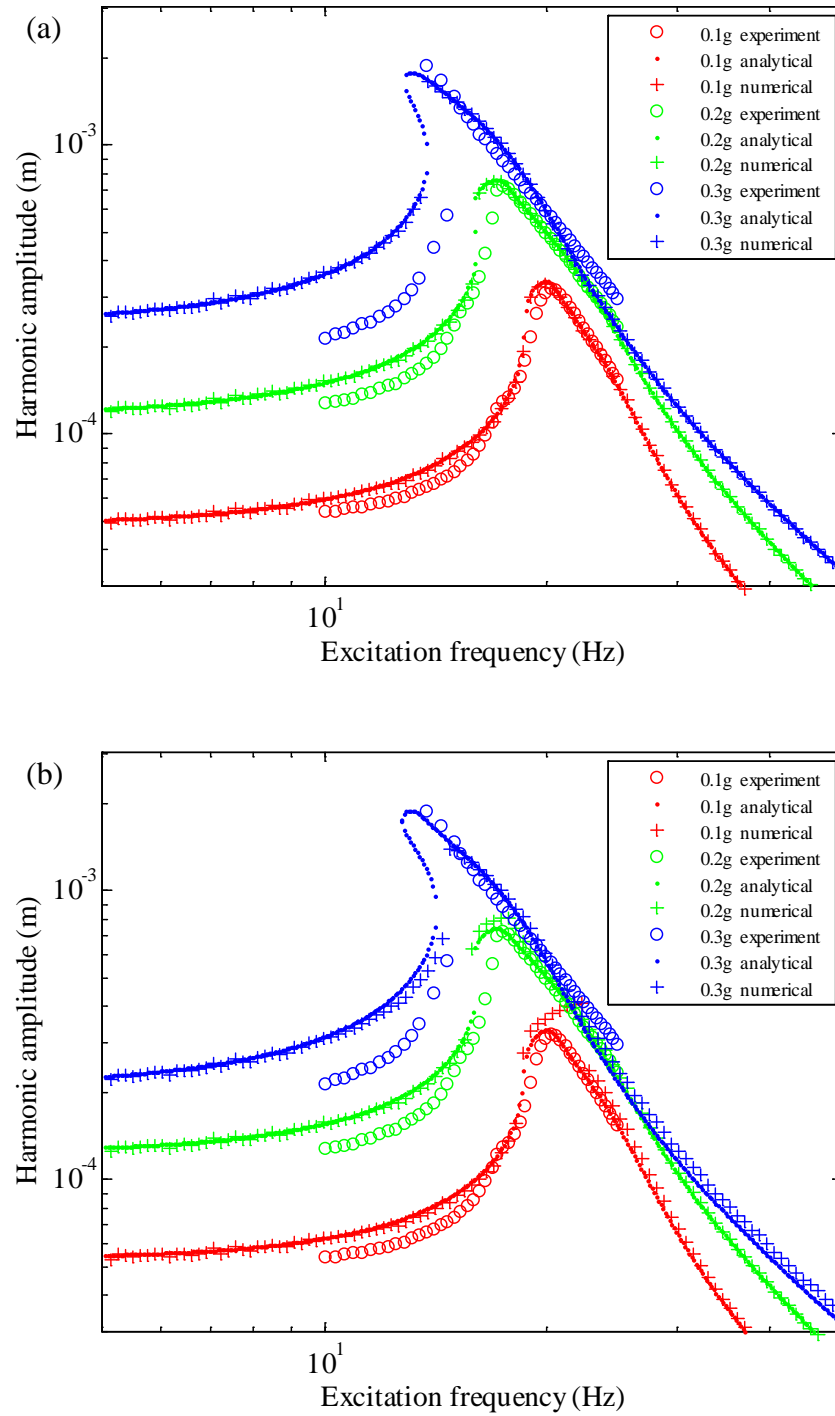


Figure 6.4 Numerical result ('+') in comparison with the experimental data ('o') and the HBM approximation ('•') of harmonic amplitude using (a) the symmetric model with parameters k, k_3, k_5, c ; (b) the symmetric model with parameters $k, k_3, k_5, c, a, \alpha$.

Using the asymmetric model with the same set of parameter estimates of β, κ, k_3, c as used in Figure 6.2 for the fabric Spacer-12h under 0.1g excitation level and 2 kg loaded mass (shown in red), numerical techniques are applied to obtain the periodic solutions for the dynamic displacement of spacer fabric in the time domain. Figure 6.5 shows the time series, phase portrait and Fourier amplitude spectrum for the steady-state solutions under different excitation frequencies. The time series diagram contains the displacement of vibration platform and the displacement of fabric deformation. Phase portrait depicts the trajectories of a dynamic system in the state space, in which the horizontal and vertical axes represent the state variables of displacement and velocity herein. The closed trajectory in the phase portrait is a limit cycle. For a linear system under sinusoidal excitation force, the limit cycle appears as an oval. However, the limit cycle becomes distorted in a nonlinear system as here. The peak at the driving frequency Ω and the peak at zero frequency in the Fourier amplitude spectrum represents the primary harmonic and the static displacement, respectively. The magnitudes of peak_h and peak_s are both marked in the spectrum. The peak_s being an absolute value does not reflect the real sign of the static displacement. In fact, the center of limit cycle in the phase portrait tends to the negative part of displacement signifying that the static displacement is negative, which agrees with the observations in Figure 6.2(a).

On the other hand, the asymmetric period shape shown in the time series and the symmetry-breaking trajectory in the phase portrait suggest an even order harmonic distortion, which is caused by the quadratic stiffness term in the elastic force. This even order harmonic is represented by a peak at frequency 2Ω , i.e. twice the driving frequency,

in the Fourier amplitude spectrum. As the frequency increases from 8 to 12 Hz, this peak becomes stronger. Then, it fades with further increase of excitation frequency. This explains the discrepancy between the approximate analytical solution and the numerical solution occurring at relatively low excitation frequencies of around 10 Hz in the amplitude-frequency curves of Figure 6.2.

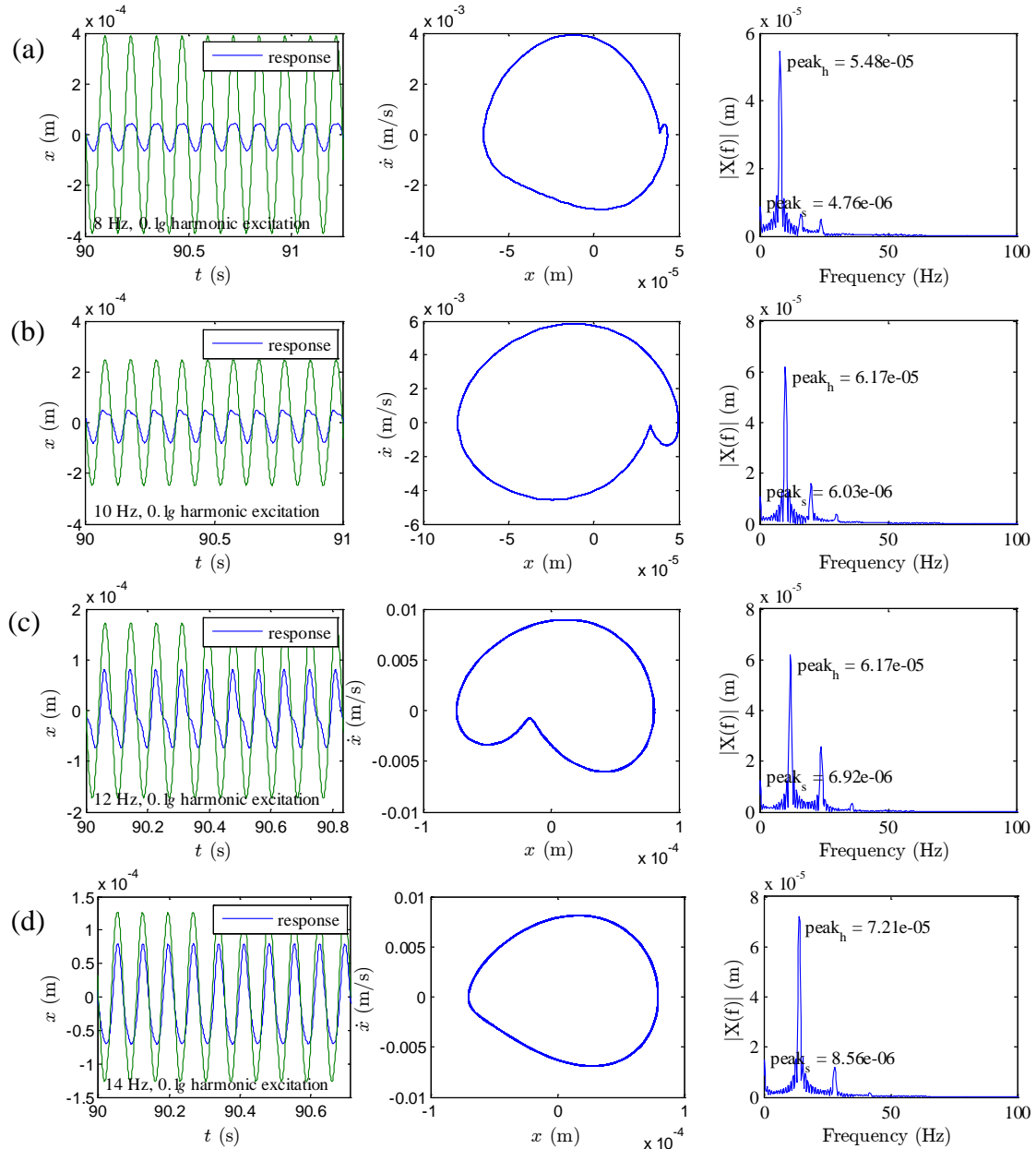


Figure 6.5 Time series, phase portrait and Fourier amplitude spectrum for the dynamic displacement of spacer fabric using the asymmetric model with parameters β, κ, k_3, c .

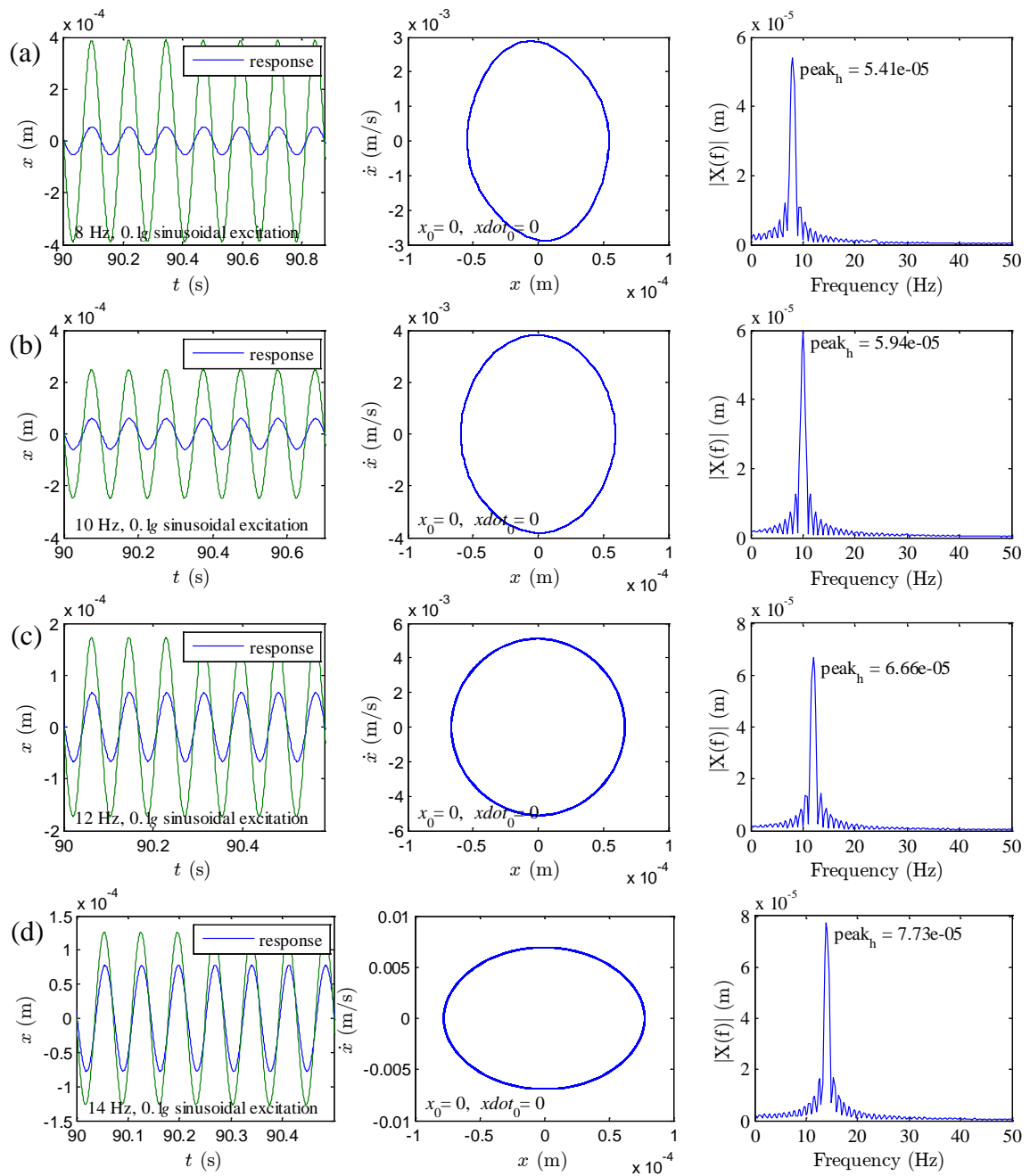


Figure 6.6 Time series, phase portrait and Fourier amplitude spectrum for the dynamic displacement of spacer fabric using the symmetric model with parameters k, k_3, k_5, c .

In contrast, using the symmetric model with the same set of parameter estimates of k, k_3, k_5, c as used in Figure 6.4(a) for the fabric Spacer-12h under 0.1g excitation level

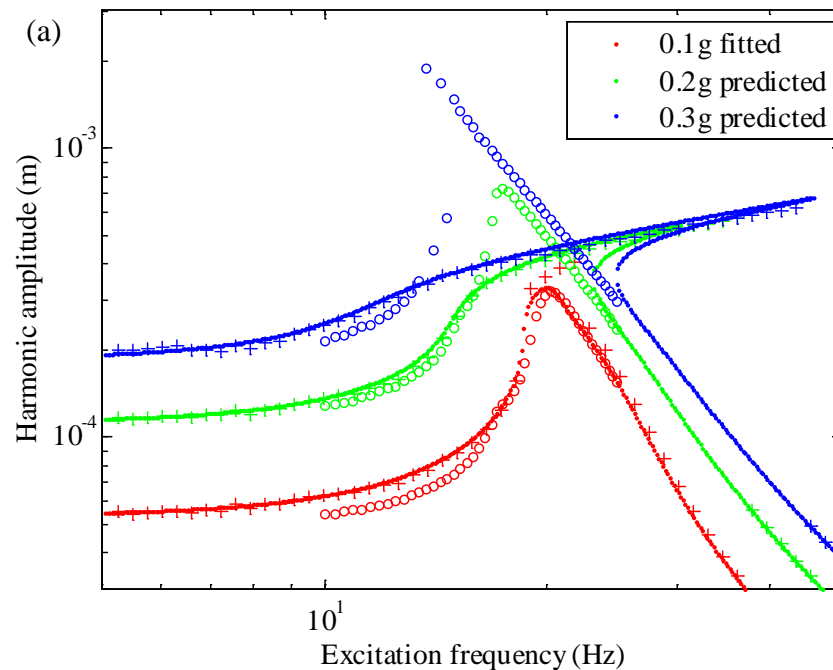
and 2 kg loaded mass (shown in red), the time-domain numerical representations are shown in Figure 6.6 when the excitation frequency varies from 8 to 14 Hz. Due to the fact that stiffness terms in the equation of motion are all odd, the steady-state solutions only present harmonics of odd order as seen in the Fourier spectrum. Moreover, the DC component noticed earlier in the asymmetric model does not show in the current symmetric model, which is confirmed by the consistency of approximate analytical solutions and numerical solutions in Figure 6.4(a).

6.3 Model predictability

This section is to examine whether model parameters identified by fitting a model with experimental data of one excitation level can be used to predict the frequency responses for the other excitation levels. Experimental data used is for Spacer-12h under the conditions of 0.1-0.3g excitation levels and 2 kg load mass. Figures 6.7 and 6.8 are concerned with numerical and HBM predictions using the symmetric model with parameters $k, k_3, k_5, c, a, \alpha$ and the asymmetric model with parameters $\beta, \kappa, k_3, c, a, \alpha$. With model parameters identified by fitting models with data of the 0.1g excitation level as shown in Figures 6.7(a) and 6.8(a), the predicted resonance peaks for 0.2g and 0.3g conditions have a hardening tendency, which diverges greatly from experimental observations of a softening behavior. However, the predictions agree with the experimental results in the non-resonant regions to a certain degree. It is also noted that for the asymmetric model as shown in Figure 6.8(a), in the non-resonant regions around 10 Hz exhibit evident second-harmonics. Next, with model parameters identified by

fitting models with data of the 0.3g excitation level as shown in Figures 6.7(c) and 6.8(c), the predictions underestimate the resonance frequencies for the 0.1g and 0.2g conditions.

It is concluded that parameter estimates from one excitation level cannot be used to predict the vibration behavior for a different excitation level, regardless of using a symmetric or an asymmetric model. For small excitation levels, the fitted nonlinear stiffness coefficients can only describe a narrow range of the elastic force-displacement curve. Thus, it is not difficult to understand that parameter estimates from low excitation levels cannot predict the vibration behavior for high excitation levels. The other way round, parameter estimates from high excitation levels also cannot predict the vibration behavior for low excitation levels.



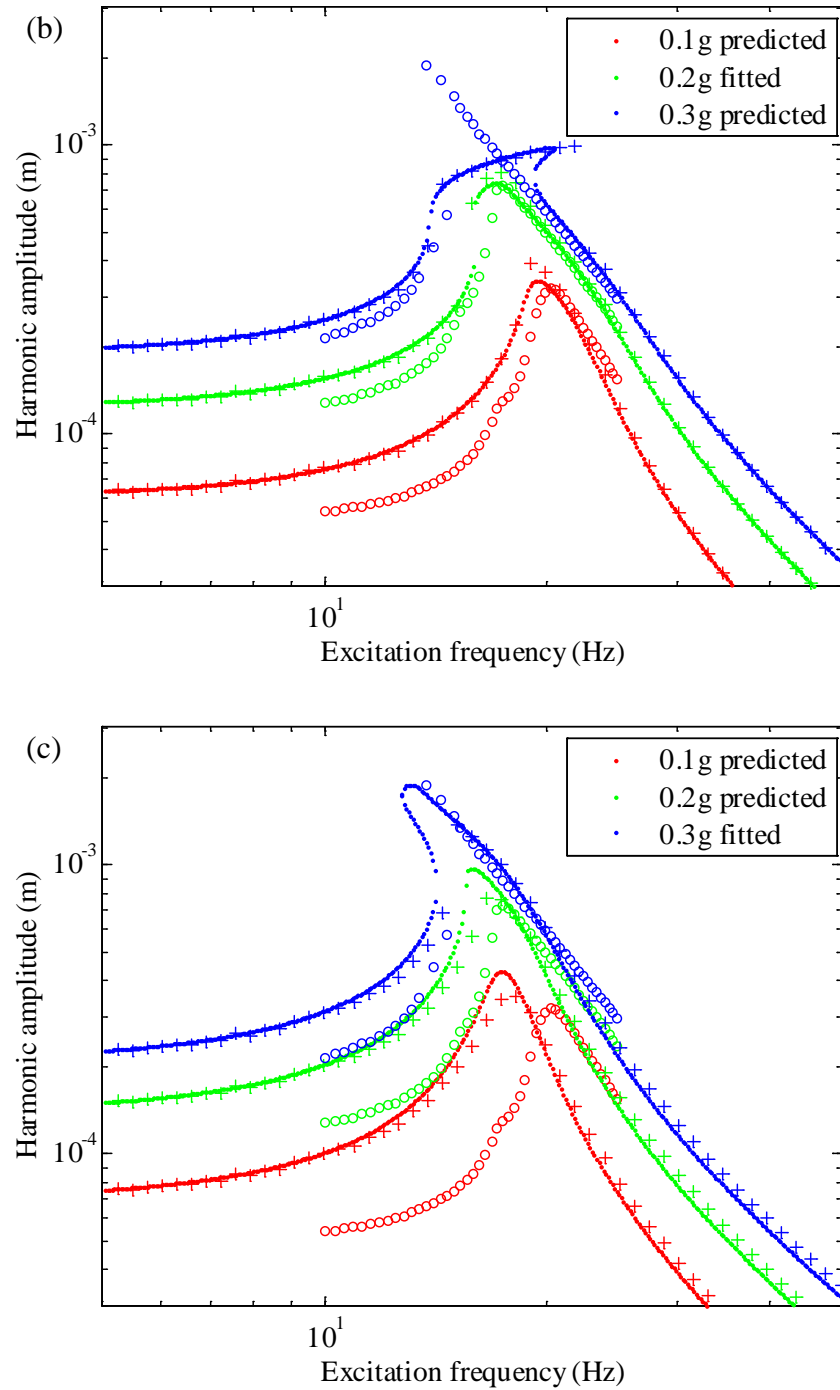
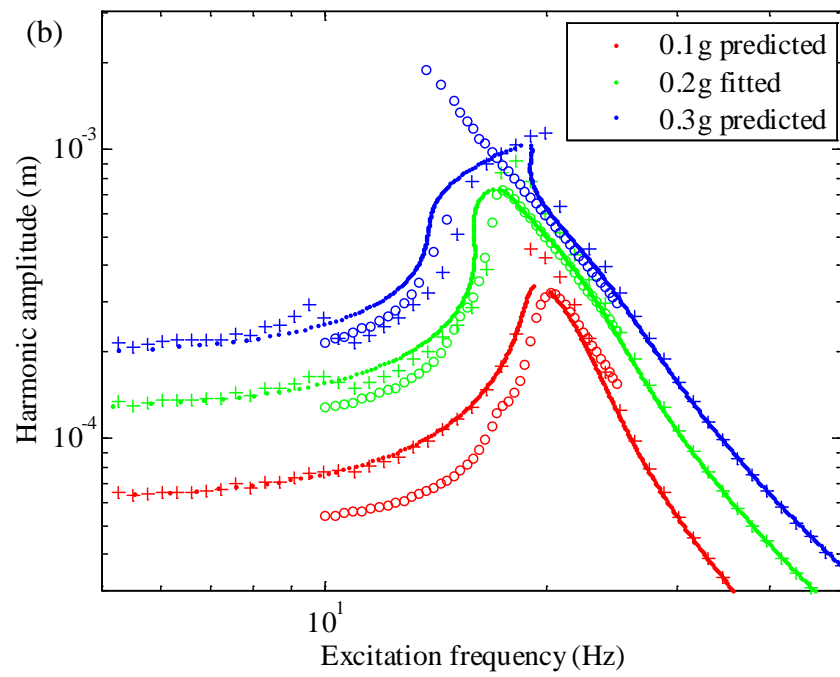
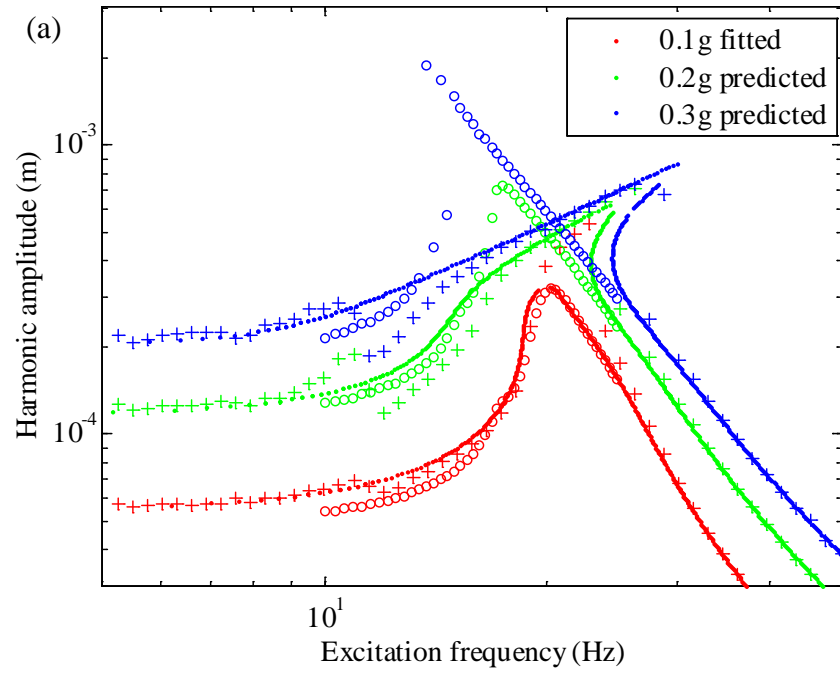


Figure 6.7 Numerical predictions ('+') and approximate analytical predictions ('•') for

the other two excitation levels using the symmetric model with parameters

$k, k_3, k_5, c, a, \alpha$ identified by fitting with experimental data ('o') of (a) the 0.1g

excitation level; (b) the 0.2g excitation level; (c) the 0.3g excitation level.



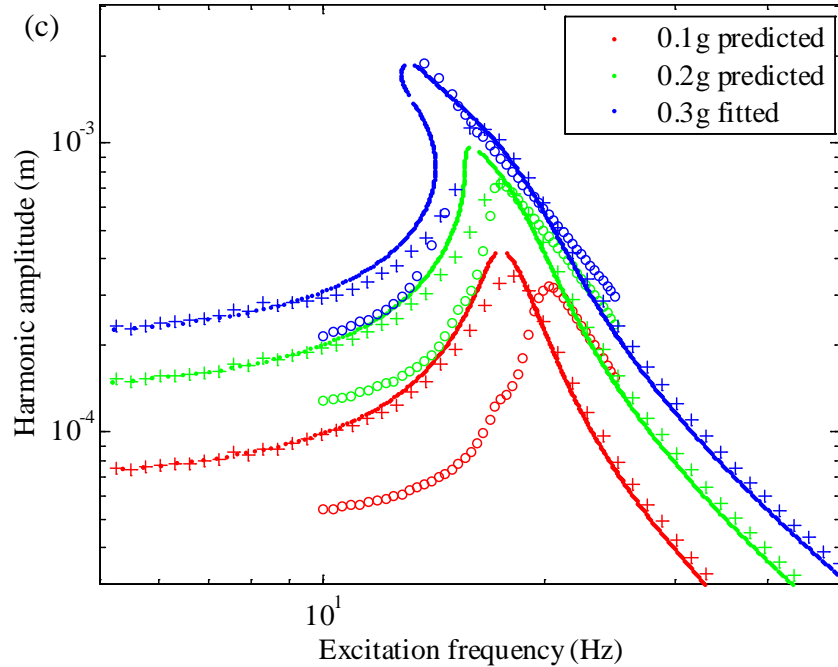


Figure 6.8 Numerical predictions ('+') and approximate analytical predictions ('•') for the other two excitation levels using the asymmetric model with parameters $\beta, \kappa, k_3, c, a, \alpha$ identified by fitting with experimental data ('o') of (a) the 0.1g excitation level; (b) the 0.2g excitation level; (c) the 0.3g excitation level.

6.4 Bifurcation and chaotic motions

Although chaos was not observed during experiments, we would like to numerically study the bifurcation and chaotic behaviors of the mass-spacer fabric system. Model parameters identified by fitting experimental data with the asymmetric model without the fractional derivative term are used herein. Experimental data was obtained for the stacked fabric Spacer-12h under 0.1g excitation level and 2 kg load mass. The equation of motion has the form of $m\ddot{x} + c\dot{x} + kx + k_2x^2 + k_3x^3 = -mG\cos(\omega t)$ or after coordinate transformation

$m\ddot{z} + c\dot{z} + \kappa z + k_3 z^3 = -mG\cos(\omega t) + \beta$, in which the relationship of the original and the transformed model parameters can be found in Equation (5.20). The parameter estimates by curve fit are listed in Table 5.2. The SI units are used for all of parameters. The following section studies the bifurcation and chaos of the system using bifurcation diagram with excitation frequency, excitation level and the fractional order varied.

6.4.1 Bifurcation vs excitation frequency

The equation of motion is numerically solved with time step increment 0.001 s. At each value of the excitation frequency, the values of x of the Poincaré map for the first 90 s simulation time are discarded to remove the initial transient effect from the steady-state response, and the values of x for the next 10 s simulation time are plotted on the bifurcation diagram. Figure 6.9 shows the bifurcation diagrams when the excitation frequency is varied from 5 to 40 Hz with step size 0.2 Hz. The amplitude of excitation level is 0.1g, 0.4g, 0.6g and 1.0g, respectively, in which 1.0g represents one unit of gravitational acceleration, 9.81 m/s^2 . It is shown that as the amplitude of excitation level is small, no bifurcation and chaos is observed within the simulated frequency range. When the excitation level increases, the phenomenon of period doubling bifurcation takes place.

In order to inspect the variations of system dynamics over time, the steady-state time series, Phase portrait, Poincaré map, and Fourier amplitude spectrum with the initial condition $(x_0, \dot{x}_0) = (0, 0)$ are presented in Figure 6.10 with different magnitudes of excitation frequency and excitation level. Under 30 Hz excitation frequency as in Figure

6.10(a) and (c), the Phase portrait forms a closed loop, the shape of which is not oval indicating that the time-series response is also not perfectly sinusoidal. The Poincaré map shows a period-one oscillation at the driving frequency. The Fourier amplitude spectrum shows the response of a static displacement component due to the asymmetric elastic force. As the excitation frequency increases to 35 Hz as in Figure 6.10(b) and (d), the Phase portrait evolves into a closed double-loop, and the Poincaré map shows a period-two oscillation. The Fourier amplitude spectrum contains an additional peak at one half of the driving frequency. This interprets the phenomenon of period doubling bifurcation in Figure 6.9(c) and (d).

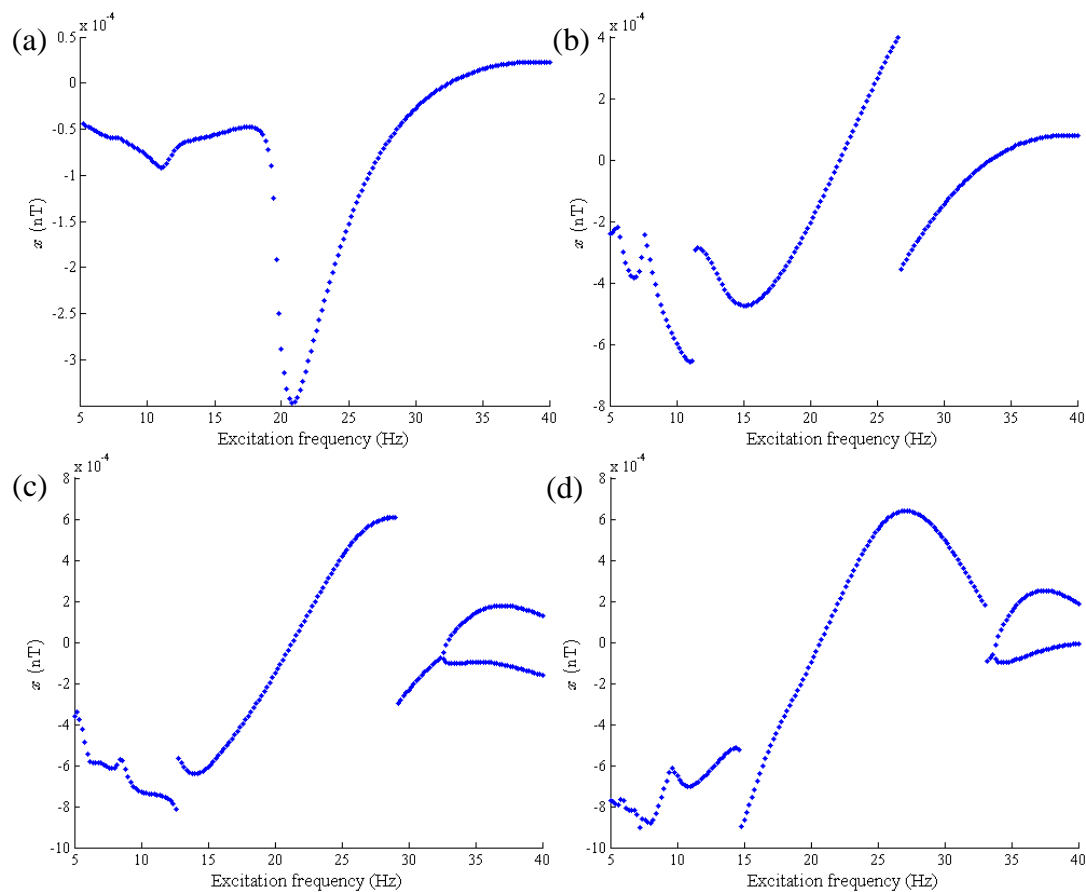


Figure 6.9 Bifurcation diagram with respect to excitation frequency under different excitation levels: (a) 0.1g; (b) 0.4g; (c) 0.6g; (d) 1.0g.

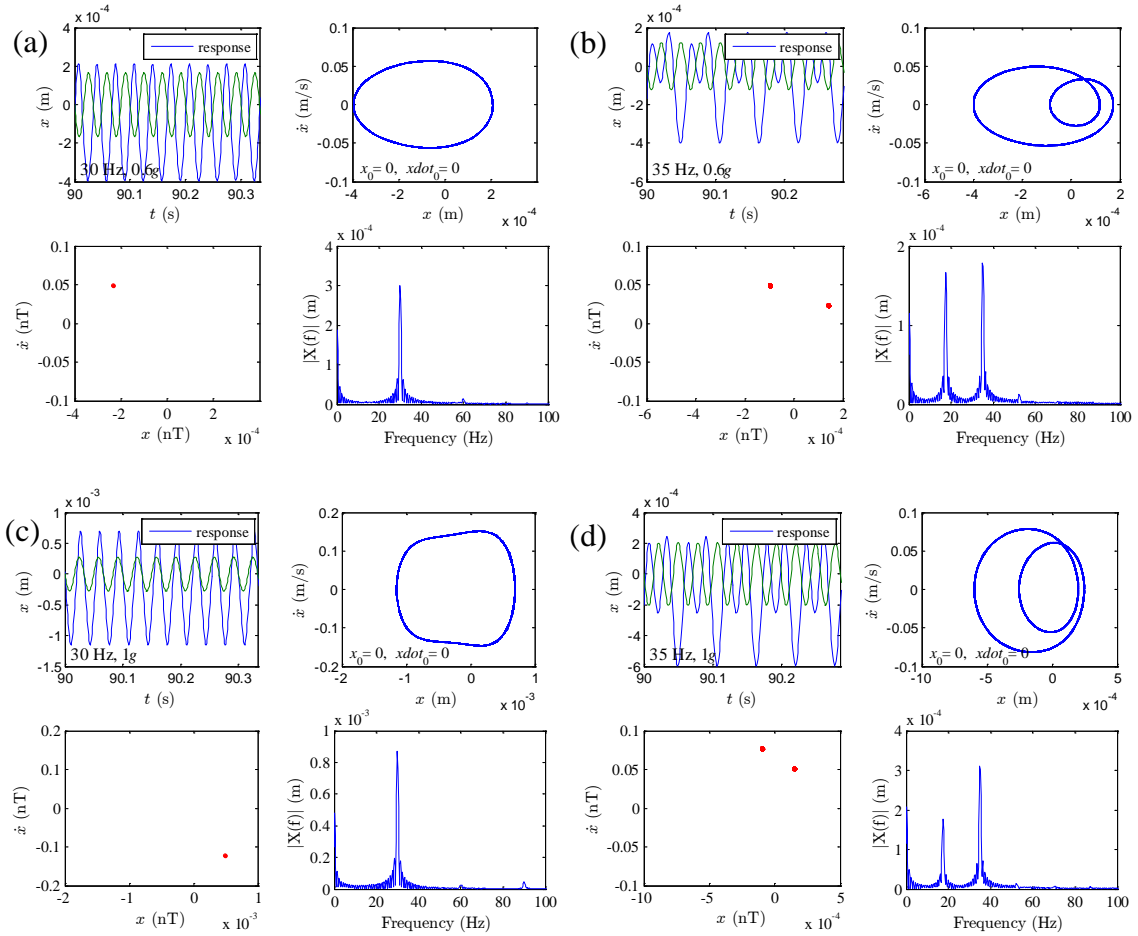


Figure 6.10 Time series, phase portrait, Poincaré map and Fourier amplitude spectrum for the dynamic displacement of spacer fabric using the asymmetric model with parameters β, κ, k_3, c , under the excitation frequency and the excitation level of: (a) 30 Hz, 0.6g; (b) 35 Hz, 0.6g; (c) 30 Hz, 1.0g; (d) 35 Hz, 1.0g.

6.4.2 Bifurcation vs excitation level

Similarly, at each value of the excitation level, the values of x of the Poincaré map for the first 90 s simulation time are discarded and those for the next 10 s simulation time are used. Figure 6.11 shows the bifurcation diagrams when the amplitude of excitation level

is varied from 0 to 20 m/s^2 with step size 0.04 m/s^2 . No bifurcation and chaos is observed at 25 Hz. However, period doubling bifurcation takes place at three other frequencies, 35 Hz, 40 Hz and 50 Hz. At 35 Hz also presents an inverse period doubling bifurcation. At 50 Hz, period doubling bifurcations take place for twice resulting in period-four oscillations as the excitation level is increased. It is noted that all these modes belong to periodic motions of the system.

The non-periodic behavior takes place when the excitation frequency is 40 Hz. Under this condition, the period doubling bifurcation cascade leads to chaotic motions with the increase of excitation level. The first period doubling bifurcation takes place at excitation level about 4 m/s^2 . The period-two oscillation lasts until the second period doubling bifurcation at about 10.5 m/s^2 . The next period doubling bifurcation takes place at about 12 m/s^2 , which can be viewed clearly in Figure 6.12.

As shown in Figure 6.11(c), the system leaves chaos through a route of sudden transition from chaotic to period-one motion when the excitation level is increased to above 14 m/s^2 . With further increasing the excitation level, it enters another chaotic zone through a sudden transition and leaves it by an inverse period doubling bifurcation. Then, the system returns to a period-one motion.

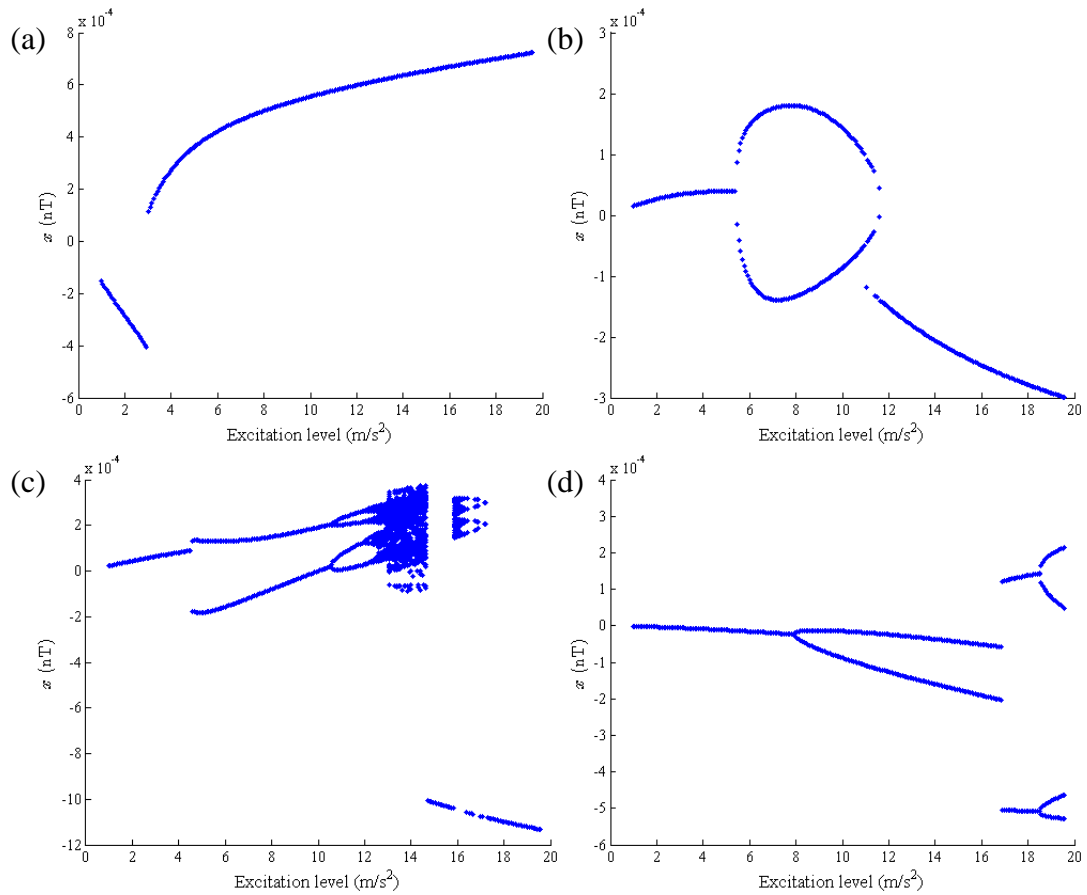


Figure 6.11 Bifurcation diagram with respect to excitation level under different excitation frequencies: (a) 25 Hz; (b) 35 Hz; (c) 40 Hz; (d) 50 Hz.

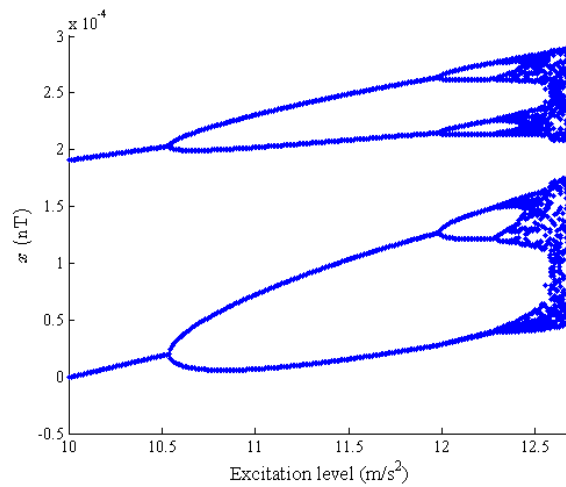


Figure 6.12 Magnified bifurcation diagram in Figure 6.11(c) regarding excitation level under 40 Hz excitation frequency, showing period doubling bifurcation cascade to chaos.

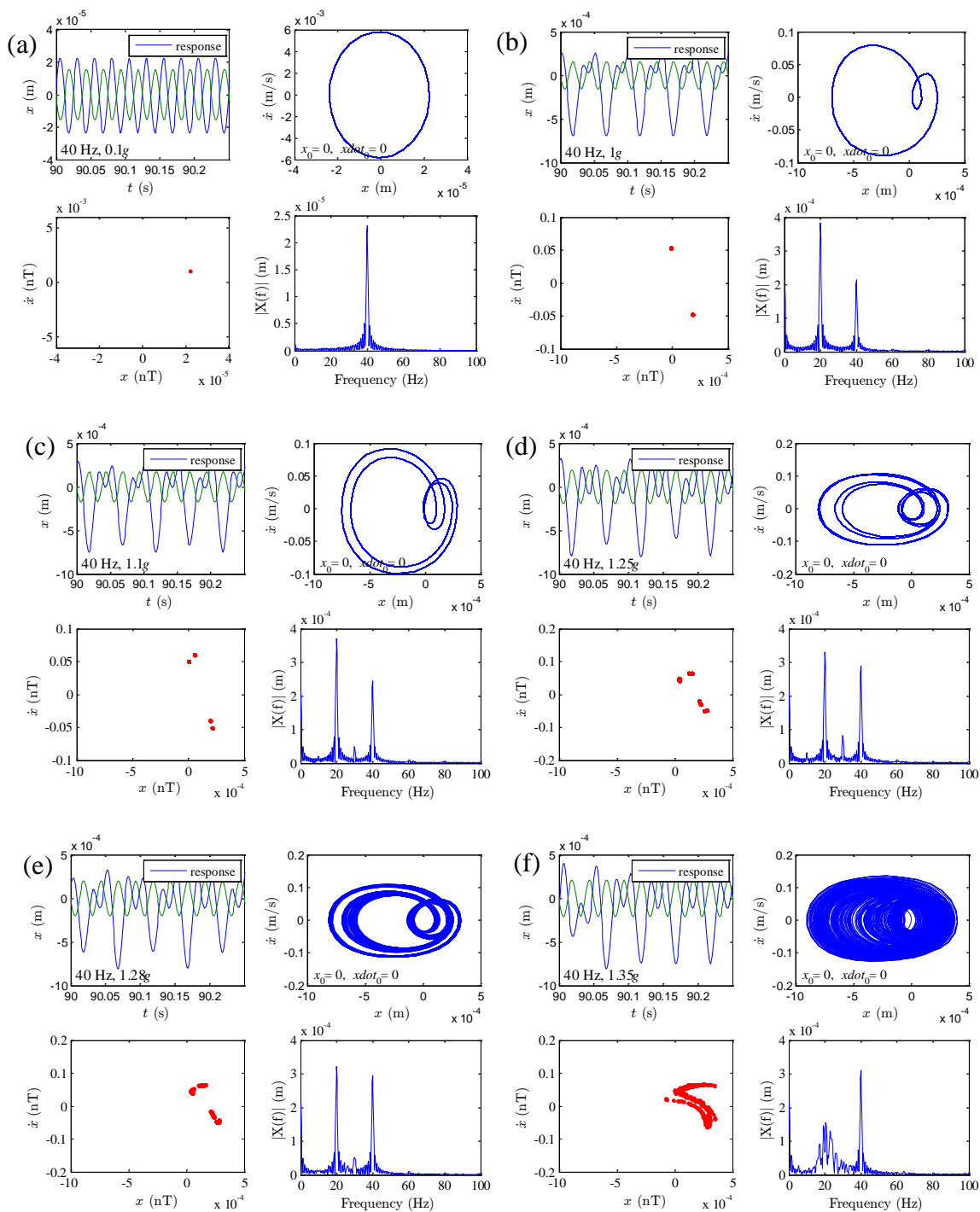


Figure 6.13 Time series, phase portrait, Poincaré map and Fourier amplitude spectrum for the dynamic displacement of spacer fabric using the asymmetric model with parameters β, κ, k_3, c , under 40 Hz excitation frequency and the excitation level is: (a) 0.10g; (b) 1.00g; (c) 1.10g; (d) 1.25g; (e) 1.28g; (f) 1.35g.

Figure 6.13(a)-(f) shows the steady-state time series, Phase portrait, Poincaré map, and Fourier amplitude spectrum for a period-one motion, period-two motion, period-four motion, period-eight motion, transition to chaos and chaotic motion when the excitation frequency is 40 Hz and the amplitude of excitation level is 0.10g, 1.00g, 1.10g, 1.25g, 1.28g and 1.35g, respectively. The corresponding amplitude of excitation level in the SI unit is provided in Table 6.1. The chaotic motion is manifested by a strange attractor in the Poincaré map in Figure 6.13(f). The energy of the Fourier spectrum for chaos is not only concentrated in the peaks, but also distributed in a wide frequency domain.

Table 6.1 Unit conversion: $1g = 9.81 \text{ m/s}^2$. The 1g is one gravitational acceleration.

Unit	(a)	(b)	(c)	(d)	(e)	(f)
g	0.10	1.00	1.10	1.25	1.28	1.35
m/s^2	0.98	9.81	10.79	12.26	12.56	13.24

6.4.3 Bifurcation vs fractional order

To investigate the effect of the fractional derivative term $aD^\alpha x$ on the chaotic behavior of the system, the fractional derivative coefficient α is arbitrarily assigned to have the value of 5, 10, 20 and 40. As Figure 6.11(c) has shown that the chaotic motions take place under 40 Hz excitation frequency when the model does not contain the fractional derivative term, the same condition of excitation frequency and 1.35g excitation level is used here. The bifurcation diagrams are shown in Figure 6.14 when the fractional order α is varied from 0 to 1.8 with step size $\Delta\alpha = 0.01$.

The fractional order α shows a strong effect on the dynamics of system. When the fractional order α is small, chaotic motion takes place. As it increases, the system leaves chaos through an inverse period doubling bifurcation and becomes periodic. The system is stabilized when it approaches 1.8. Besides, as the fractional derivative coefficient \mathcal{A} increases, the system can be stabilized with a relatively smaller fractional order α .

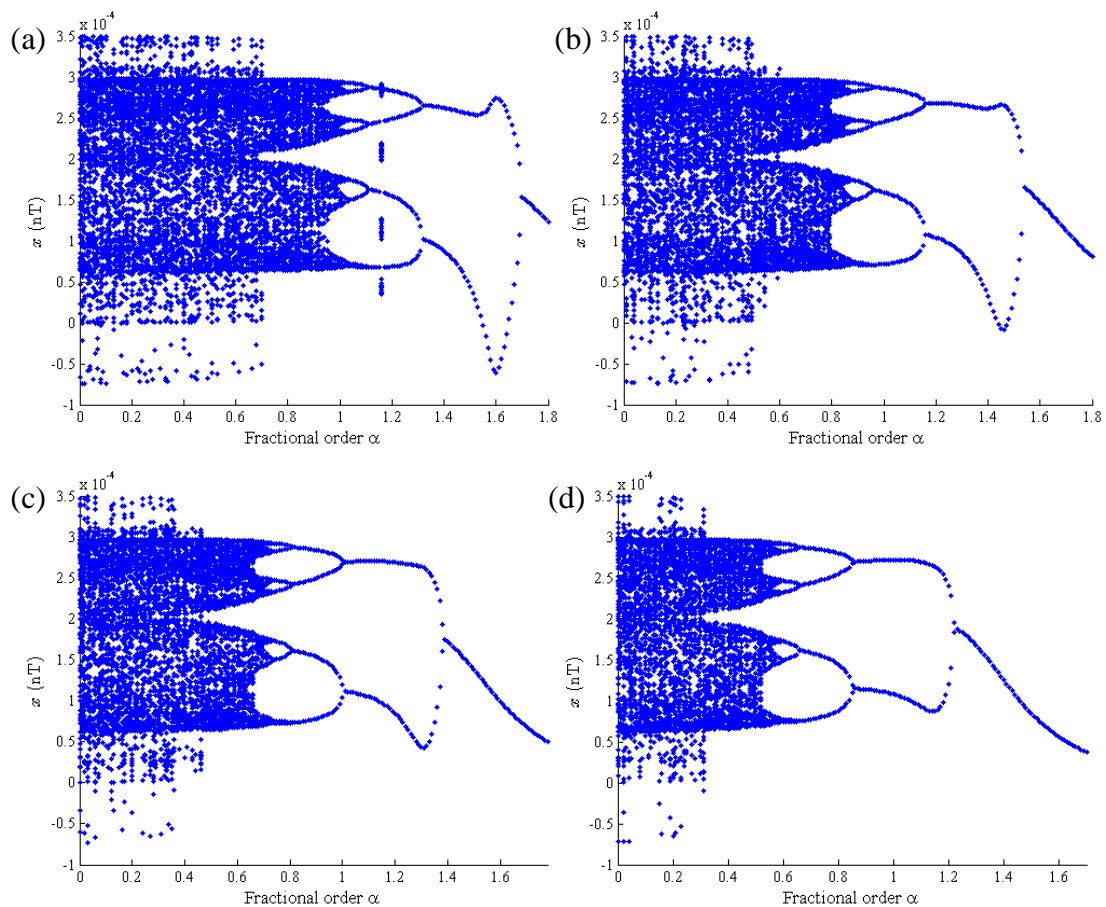


Figure 6.14 Bifurcation diagram with respect to the fractional order under 1.35g excitation level and 40 Hz excitation frequency when the coefficient of the fractional derivative term \mathcal{A} is: (a) 5; (b) 10; (c) 20; (d) 40.

6.5 Chapter summary

In this chapter, numerical simulations with regard to the regular behavior and the chaotic behavior of the mass-fabric system are performed.

- The amplitude-frequency curves obtained by numerical simulation are compared with those obtained by approximate analytical solution, for both the symmetric models and the asymmetric models. For the symmetric models, two approaches achieve high consistency. However, for the asymmetric models, two approaches have a little inconsistency where exists an even order harmonic distortion.
- Parameter estimates from one excitation level cannot be used to predict the vibration behavior for a different excitation level, regardless of using a symmetric or an asymmetric model.
- Bifurcation and chaotic behaviors are studied using the asymmetric model with excitation frequency, excitation level and fractional order varied. Period doubling bifurcation to chaos and inverse period doubling bifurcation to periodic motion are observed numerically. The fractional derivative term can remove chaotic motion when the fractional derivative coefficient a and the fractional order α are large.

CHAPTER 7 CONCLUSIONS AND FUTURE WORK

7.1 Conclusions

Human body is sensitive to vibrational environments. Compared with conventional anti-vibration materials such as rubber and polyurethane foams, weft-knitted spacer fabric provides better thermophysiological comfort to the human body due to its air and moisture management, softness and handle. However, studies on the vibration isolation performance of weft-knitted spacer fabrics are still needed. In order to promote its application for the protection of human body from vibration exposure, this study aimed at a comprehensive understanding of frequency responses of the nonlinear mass-spacer fabric system under forced harmonic excitation.

Effects of fabric structure, load mass and excitation level on the isolation performance were analyzed experimentally. The mechanism of how nonlinear stiffness influence its vibration was related with the quasi-static compression behavior. Suitable analytical models were built to describe the vibration behavior of the system. Experimental observations and analytical models offered a fundamental perspective for the development of weft-knitted spacer fabric as vibration isolator in the future. Moreover, numerical investigations also uncovered the possibility of irregular vibration behaviors of the system. The fulfilled goals are summarized as follows.

7.1.1 Improved thickness of spacer fabric

The main approach for achieving good vibration isolation is to reduce the dynamic stiffness of the isolation material. To reduce the stiffness of weft-knitted spacer fabrics for achieving small resonance frequencies during vibration, the use of thicker spacer fabrics is recommended. Thick weft-knitted spacer fabrics were manufactured on the electronic flatbed knitting machine with limited adjustment of the distance between two needle beds, by employing longer linking distance of spacer monofilaments to knit the spacer layer and elastic yarns to knit the outer layers.

7.1.2 Effects influencing the isolation performance

The vibration isolation performances of these fabrics were experimentally investigated revealing the effects of fabric structure, load mass and excitation level on the acceleration transmissibility curve of the mass-spacer fabric system. Due to the nonlinear elastic force of weft-knitted spacer fabric, the response of the system is complex, different from a linear mass-spring-damper model. Thicker fabric has a better isolation performance by having a lower resonance frequency and a lower crossover frequency. Higher excitation level results in a broadened isolation region and an enhanced nonlinear effect. A high load mass makes fabric compact leading to a rapid increase of the statically-loaded tangential stiffness of fabric and resulting in a high resonance frequency and a high crossover frequency.

7.1.3 Improved performance of analytical model

Analytical models to describe the periodic response of system under forced harmonic excitation were built. Symmetric polynomial and asymmetric polynomial were used for the nonlinear elastic force. The fractional derivative term and the viscous damping term were used for the viscoelasticity. Approximate analytical solutions for the harmonic amplitude vs. excitation frequency curve were obtained using harmonic balance method (HBM). The performances of different models were compared by evaluating their levels of the goodness of fit. The asymmetric polynomial and the fractional derivative term help improve the model performance. However, parameter estimates from one excitation level cannot be used to predict the vibration behavior for a different excitation level, regardless of using a symmetric or an asymmetric model. This is one of the limitations of the present analytical models.

7.1.4 Effects of nonlinear stiffness coefficients on frequency response curves

Due to the nonlinear elastic force-displacement relationship of weft-knitted spacer fabric, bending of resonance peak was caused. The resonance frequency also changes with the conditions of excitation level and load mass. Influences of nonlinear stiffness coefficients on frequency response curves (FRCs) of the mass-spacer fabric system were studied through parametric analysis. Concerning the order and the sign of stiffness coefficients on the FRCs, under small excitations, the linear stiffness is responsible for the system dynamics. When the linear stiffness increases, the resonance frequency and peak force transmissibility are also increased, but the peak harmonic amplitude for spacer fabric is

reduced. As the excitation becomes larger, nonlinear stiffness terms exhibit their influences. Negative odd-order stiffness causes softening behavior in the FRCs, characterized by peak bending to the left. Its increase resulted in elevated peak harmonic amplitude and reduced peak transmissibility. To the opposite, positive odd-order stiffness causes hardening behavior in the FRCs characterized by peak bending to the right. The system can also be mixed softening-hardening if positive and negative nonlinearities both exist, but it also depends on the magnitude of excitation level.

Odd-order nonlinearities such as cubic stiffness result in balanced vibration response for displacement away from the statically-loaded position. However, even order nonlinearities such as quadratic stiffness result in biased vibration response. From the numerical result of Fourier amplitude spectrum, a static displacement component exists for such a system. Besides the static displacement and the primary harmonic at the excitation frequency Ω , an even order second harmonic takes place at frequency 2Ω , i.e. twice the excitation frequency. This is also indicated by the little inconsistency of numerical result and approximate analytical solution by using the asymmetric model.

7.1.5 Bifurcation and chaotic behavior of the nonlinear system

Except for the periodic behavior, the bifurcation and chaotic behavior of the system was also predicted by numerical method with varied excitation frequency, excitation level and fractional order using the asymmetric model. Period doubling bifurcation to chaos and inverse period doubling bifurcation to periodic motion were observed. Besides, increasing the fractional order α and the fractional derivative coefficient a stabilized the

originally chaotic motion into the regular periodic motion.

7.2 Limitations

The limitations of this study are discussed as follows.

7.2.1 Model predictability

Model parameters identified by curve fit can only work for the current excitation level. Using the same set of model parameters fails to predict the vibration behaviors for other excitation levels. For instance, the fractional derivative term improves model prediction only under the high excitation force condition. For relatively low excitation levels, however, it does not improve the model significantly. Thus, a universal analytical model is not found.

7.2.2 Phenomenological models

The construction of phenomenological models considering the polynomial elastic force does not stem directly from material and structural properties of weft-knitted spacer fabrics, but is based on the empirical observation of the bending of resonance peak through experiment. As a result, the model may lack sufficient structures to capture the features of vibration behavior accurately. A different modeling approach revealing the inherent mechanism of how structural and material properties act on system dynamics is called for. To build such a model, elastic modulus and thickness of yarns need to be known,

and the deformation mechanism of three-dimensionally curved monofilaments with proper assumptions of initial and boundary conditions need to be discovered. However, this approach is challenging in that the quasi-static deformation mechanism of spacer fabric may not necessarily represent the elastic force under vibration conditions.

7.2.3 Fabric instability

Although the thickness of weft-knitted spacer fabric used in this study is increased, spacer monofilaments are loosely tucked with outer layers. Strictly speaking, the spacer is composed of parallel successions of two-dimensionally wavy structures of spacer monofilaments. This causes the instability of fabric under large vibration levels. In contrast, spacer monofilaments in the warp-knitted spacer fabric are tightly restrained by knit stitches. Besides, the monofilaments form a true three-dimensional spacer structure. Thus, warp-knitted spacer fabric is relatively more stable in general.

7.2.4 Experiment condition

This study focuses on the steady-state vibration of the mass-spacer fabric system under sinusoidal sweeps with fixed excitation force across the frequency band. However, sinusoidal sweeps with fixed excitation amplitude across the frequency band has not been studied, for which the FRCs will be different from the former case due to the nonlinear elastic force of the system. Moreover, the transient and steady-state time histories of vibration signals are not recorded in this study. Nevertheless, they are important because time-domain data contains rich information on system dynamics.

7.3 Recommendations for future work

The recommendations for future work emerging from this study are presented as follows.

7.3.1 Model improvement

The phenomenological models used in this study can be improved to better describe the vibration behavior. Suggested directions for model modification include adding other types of damping such as hysteretic damping and quadratic damping, and using more complex forms of elastic force such as full orders of nonlinear stiffness terms. On the other hand, models revealing the inherent relationship between material and geometric properties of spacer fabric and the vibration dynamics can be built.

7.3.2 Statistical analysis

In this research, spacer fabric was designed with fabric structure, i.e. the linking distance of spacer monofilament varied. In addition to this, material and geometric properties of spacer monofilament and outer layer yarns have also significant effects on the vibration behavior, which has not been studied yet. Hence, a great variety of weft-knitted spacer fabrics can be designed and manufactured by varying needle density, yarn materials, the diameter and the linking distance of spacer monofilament, etc. Statistical analysis of variance can be performed to find statistically significant variables that act on the vibration behavior of spacer fabric.

7.3.3 Applied research

Utilizing the anti-vibration performance of weft-knitted spacer fabric, products such as cushion packaging materials and anti-vibration gloves can be produced. Thus, vibration risks such as shock and vibration of packages during transportation and hand arm vibration from operating hand-held power tools can be analyzed through experiments in response to these types of excitations. It is noted that under these application conditions, lateral vibrations also exist besides vertical vibration. Moreover, for the application study, the anti-vibration performance using weft-knitted spacer fabric can be comparatively studied with warp-knitted spacer fabric and conventional cushion materials such as rubber and polyurethane foam.

7.3.4 Time history

Due to the rich information contained in the time domain signals, experimental time signals can be compared with time histories obtained by numerical method. It applies not only for steady-state responses, but also for transient responses before the system enters steady state, and also for transient responses under shock conditions, since transient dynamics is vital for system stability in such circumstances.

Appendixes

Introduction

Appendixes 1-6 are all concerned with the data fitting.

In Appendixes 1 and 2, curve fit using the model with parameters $k, k_3, k_5, c, a, \alpha$ was adopted as an example to study the effects of frequency range and frequency step size on the level of the goodness of fit (indicated by RMSE) for Spacer-12h under the conditions of 0.1-0.3g excitation level and 2 kg load mass, based on which determines proper frequency range and step size for this study.

In Appendix 3, through the goodness of fit test (indicated by visual comparisons) for the harmonic amplitude vs. excitation frequency curve obtained by two kinds of fitness function, a suitable fitness function was selected for this study.

In Appendix 4, RMSEs obtained by the method of least squares was compared with those by the different evolution algorithm used in Chapter 4. The former is a local optimization method, which depends on the choices of initial values and bounds of unknown model parameters. In contrast, the latter achieves solutions more efficiently and is free of choosing an initial value, and more importantly, it results in a higher level of the goodness of fit.

In Appendix 5, the effect of the initial value of the fractional order on the level of the goodness of fit was examined using the method of least squares.

In Appendix 6, the relative standard error (RSE) for an individual model parameter was used as the performance indicator of model parameter.

Appendix 1 Frequency range

The driving frequency for the sinusoidal sweep experiment covers a wide range, which results in a large quantity of data. However, the characteristic domain which is representative of the vibration behavior for a system locates around the resonance. In order to highlight the features in the region of resonance, a proper frequency range of training data set, i.e. the experimental data used for fitting, should be defined. However, if an improper training set is used, the apparent relationship outside the selected frequency range cannot be predicted by using the model parameters identified. Thus, a validation set is required to test the serviceability of the fitted model by examining the variability of the goodness of fit, and to decide which frequency range of training data to take. Here the validation set has a frequency range of 10-25 Hz.

In Figure A.1, the model with parameters $k, k_3, k_5, c, a, \alpha$ is used. The solid lines are the RMSEs for the training set, while the dotted lines are those for the validation set as reference. A large variation between these two RMSEs indicates the selected frequency range has an unsatisfactory performance. Frequency ranges of 5-20 Hz, 5-25 Hz, 5-30 Hz,

10-25 Hz and 10-30 Hz resulted in the smallest variations in RMSEs between the training set and the validation set for all of three excitation levels. These frequency ranges performed better than other ones. Finally, the frequency range of 10-25 Hz was selected as the default.

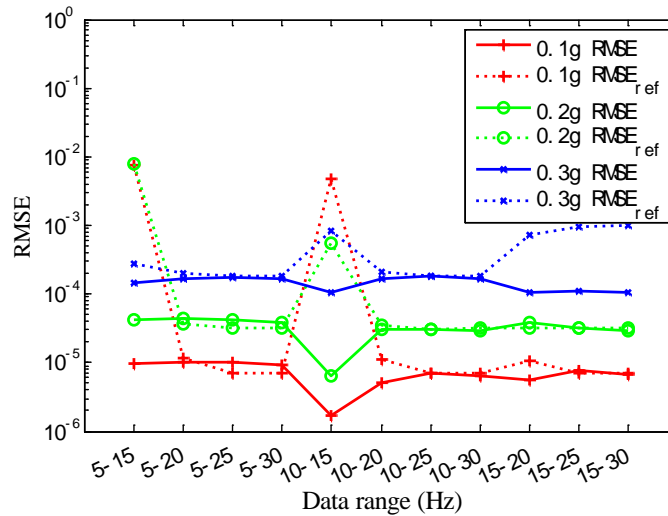


Figure A.1 Effect of frequency range on the RMSE using the model with parameters

$$k, k_3, k_5, c, a, \alpha.$$

Appendix 2 Frequency step size

Similar as in the previous discussion on selecting a proper frequency range of training data set, this section will determine the number of data points used in the training set. As described in Chapter 3, the raw data obtained by sweep experiment was recorded on a logarithmic scale. For curve fitting, it was converted into the linear scale format by interpolation. The resulting data resolution was 0.01 Hz per increment of frequency values. Due to the high resolution of data, the noise is also absorbed during fitting, which could

lead to over-fitting. To avoid this, a proper data resolution needs to be defined. As shown in Table A.1, the frequency step size was varied and the corresponding number of data points used was calculated. A similar approach as in the previous section was employed for the validation of various candidate frequency step sizes. A frequency step size of 31 was used for the validation purpose.

In Figure A.2, the model with parameters $k, k_3, k_5, c, a, \alpha$ is used. The solid and dotted lines are the RMSEs for the training set and the validation set, respectively. When the frequency step size was small, i.e. with a high number of data points, the RMSEs obtained by the candidate step size were almost identical with the ones obtained by the validation set. However, as the candidate step size became larger, a large variation between these two RMSEs emerged, an indication of poor performance with the use of the candidate step size. As a result, a frequency step size of 31 was selected as the default, as it ensures the performance of the fitted model and at the same time contains fewer number of data points.

Table A.1 Nine candidate frequency step sizes.

Frequency step size	1	3	5	15	31	93	155	217	279
Data resolution (Hz)	0.01	0.03	0.05	0.15	0.31	0.93	1.55	2.17	2.79
Number of data points	1500	500	300	100	49	17	10	7	6

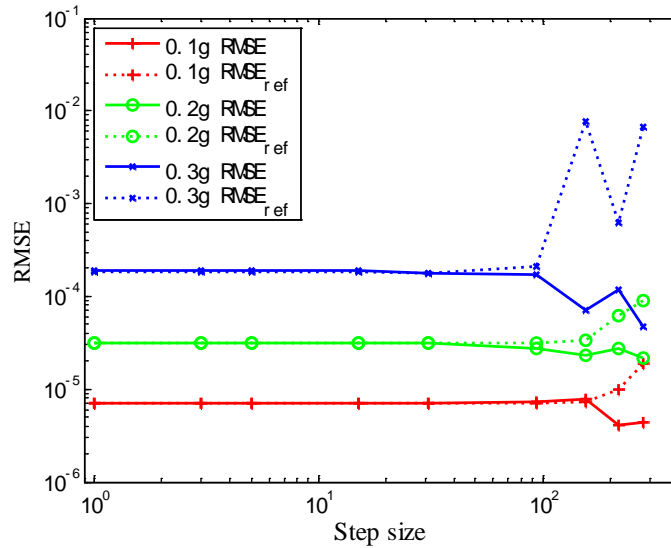


Figure A.2 Effect of frequency step size on the RMSE using the model with parameters

$$k, k_3, k_5, c, a, \alpha .$$

Appendix 3 Fitness function

The harmonic amplitude vs. excitation frequency relationship can be formulated in two different forms, as discussed in Chapter 4. Correspondingly, the fitness function has also two forms. The one used as default in Chapter 4 is based on Equation (4.7), which belongs to the fitness function Type I and has the form of

$$\begin{cases} f_{1,n} = \left(P \cdot |A|^2 + \frac{mG_e A_r}{2} \right) \cdot |A|^u \\ f_{2,n} = \left(Q \cdot |A|^2 - \frac{mG_e A_i}{2} \right) \cdot |A|^u \end{cases}, \quad (\text{A.1})$$

where the weighing factor $u = 0, \pm 1, \pm 2, \dots$

On the other hand, Equation (4.7) can also be squared to obtain

$$(P^2 + Q^2) \cdot |A|^2 = \frac{m^2 G_e^2}{4}, \quad (\text{A.2})$$

which is used to recover the harmonic amplitude ($2|A|$) vs. excitation frequency curve.

Based on Equation (A.2), we obtain the fitness function Type II in the form of

$$f_n = \left[(P^2 + Q^2) \cdot |A|^2 - \frac{m^2 G_e^2}{4} \right] \cdot |A|^d, \quad (\text{A.3})$$

where the weighing factor $d = 0, \pm 1, \pm 2, \dots$

To evaluate the performances of fitness functions Type I and Type II considering weighing factors, the experimental data of harmonic amplitude vs. frequency curve under 0.3g excitation level and 2 kg load mass for Spacer-12h is used. The fitted curves using the asymmetric model with parameters $\beta, \kappa, k_3, c, a, \alpha$ are shown in Figures A.3 and A.4; and the fitted curves using the symmetric model with parameters $k, k_3, k_5, c, a, \alpha$ are shown in Figures A.5 and A.6. Results show that the fitness function Type II weighs the low-amplitude fitting more heavily than the fitness function Type I does. Type I mostly has worse fitting in the low-amplitude region, especially in the low-frequency part. The asymmetric model with parameters $\beta, \kappa, k_3, c, a, \alpha$ alleviates this issue to some degree. However, Type I gives better fit than Type II at resonance. Secondly, the inclusion of weighing factor may cause under-fitting ($u = -1, d = -1$) or over-fitting ($u = 1, d = 1$). Therefore, the weighing factor is not considered for this study (i.e. let $u = 0, d = 0$). Given an overall consideration, the fitness function Type I (with $u = 0$) is selected as the default for this study.

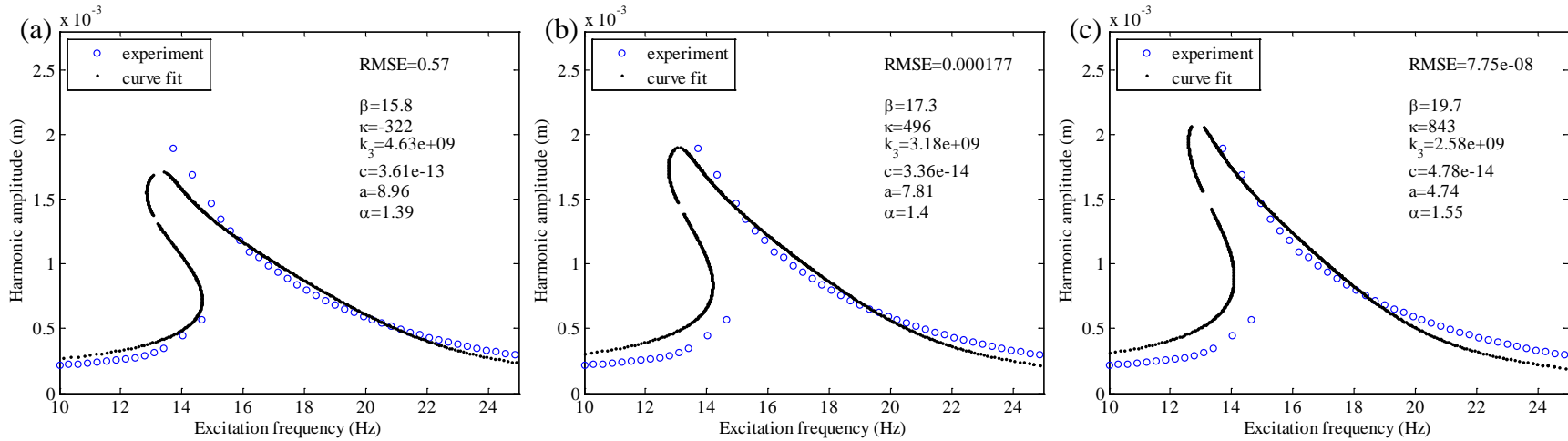


Figure A.3 Fitness function Type I for the asymmetric model $\beta, \kappa, k_3, c, a, \alpha$ with weighing factor: (a) $u = -1$; (b) $u = 0$; (c) $u = 1$.

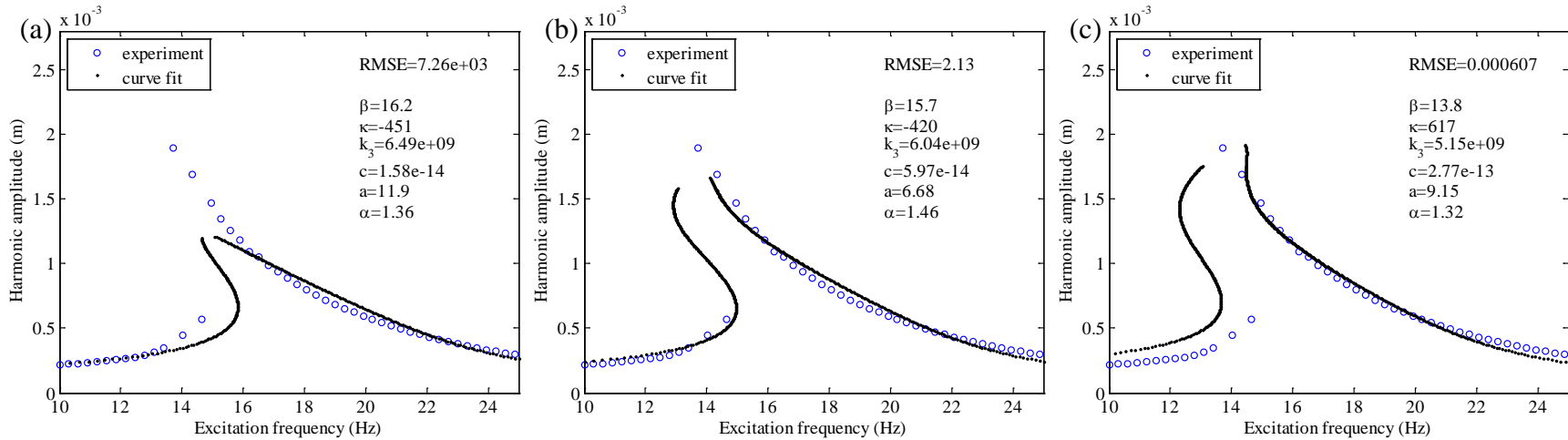


Figure A.4 Fitness function Type II for the asymmetric model $\beta, \kappa, k_3, c, a, \alpha$ with weighing factor: (a) $d = -1$; (b) $d = 0$; (c) $d = 1$.

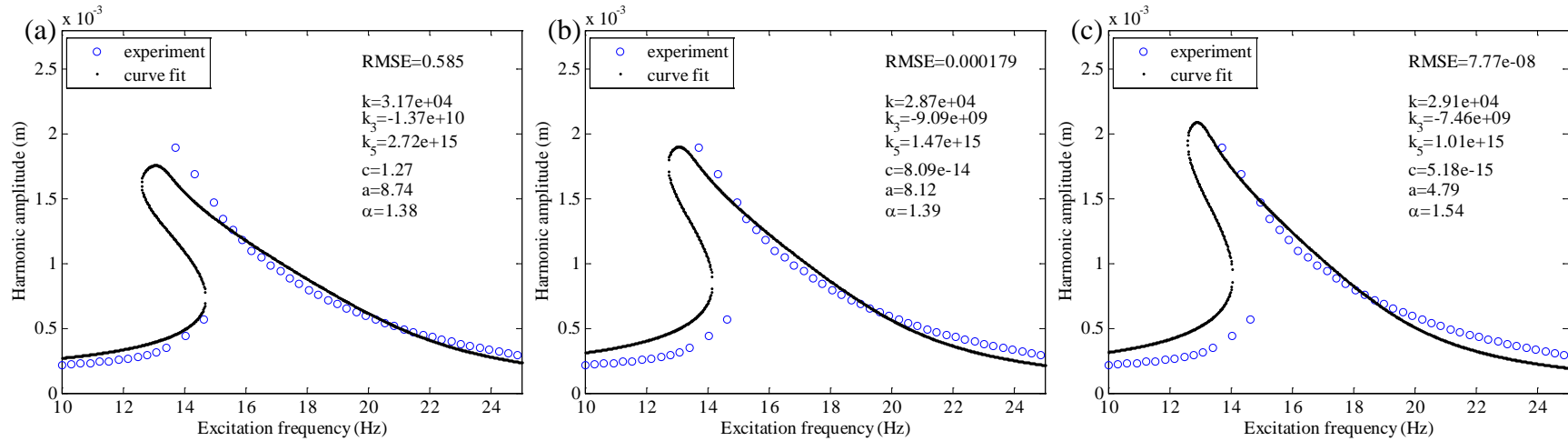


Figure A.5 Fitness function Type I for the symmetric model $k, k_3, k_5, c, a, \alpha$ with weighing factor: (a) $u = -1$; (b) $u = 0$; (c) $u = 1$.

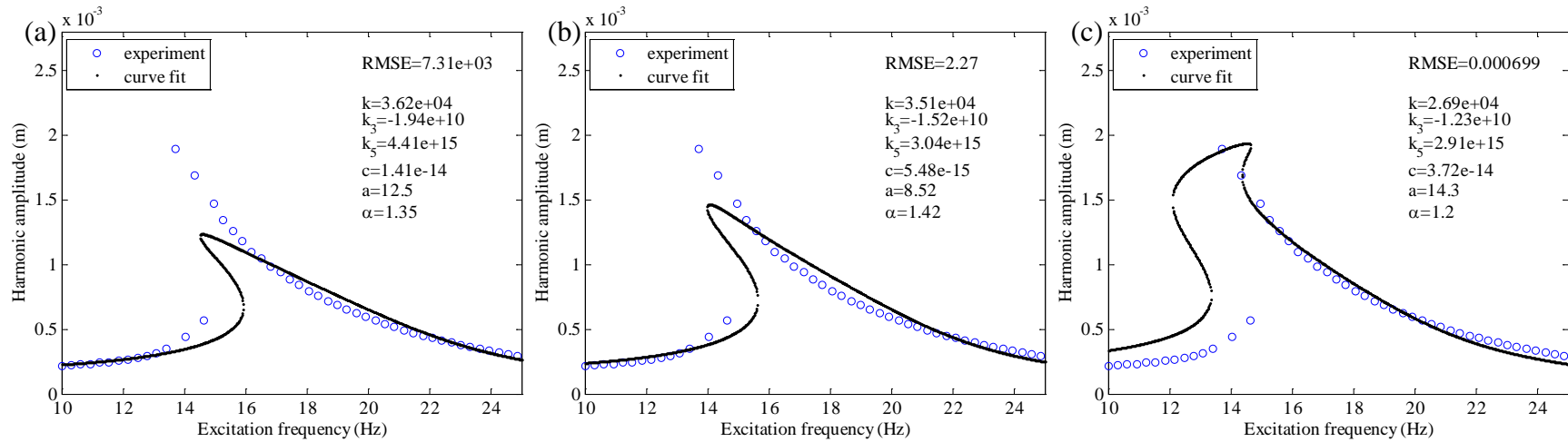


Figure A.6 Fitness function Type II for the symmetric model $k, k_3, k_5, c, a, \alpha$ with weighing factor: (a) $d = -1$; (b) $d = 0$; (c) $d = 1$.

Table A.2 also summarizes the RMSEs for the model with parameters $k, k_3, k_5, c, a, \alpha$ and the model with parameters $\beta, \kappa, k_3, c, a, \alpha$ using different fitness functions. It again confirms that the asymmetric model performs better than the symmetric model.

Table A.2 The goodness of fit (RMSEs) using different fitness functions.

RMSE		Model with parameters $k, k_3, k_5, c, a, \alpha$	Model with parameters $\beta, \kappa, k_3, c, a, \alpha$
Fitness function type I	$u = -1$	0.585	0.57
	$u = 0$	0.000179	0.000177
	$u = 1$	7.77e-08	7.75e-08
Fitness function type II	$d = -1$	7.31e+03	7.26e+03
	$d = 0$	2.27	2.13
	$d = 1$	0.000699	0.000607

Appendix 4 Optimization algorithm: least squares vs. jDE

For data fitting, we have adopted a differential evolution (jDE) algorithm, developed by Brest et al. ¹⁵³, and Zhang and Sanderson ¹⁵⁴. The jDE algorithm runs efficiently and is free of choosing an initial value. Relatively, the method of nonlinear least-squares, which is a local optimization strategy, requires multiple attempts to achieve a best solution with adjustments of scaling factors, initial values and bounds of the unknown parameters, and the maximum number of function evaluations. Table A.3 makes a comparison of the features of the jDE algorithm and the method of least squares.

Table A.3 Comparison of the jDE algorithm and the method of least squares.

Items	jDE	Least squares
Range of bounds	Finite	Infinite/Finite
Lower and upper bounds	Can be identical	Must be different
Initial value needed?	No	Yes
Elapsed time to run the program	Shorter	Longer
The goodness of fit achieved	Equal/Better	for reference
Convenience (Is the definition of fitness function model-based?)	High (No)	Low (Yes)
Applicability to asymmetric models (nonlinearly constrained optimization)	Applicable	Inapplicable
Type of optimization	Global	Local

In order to compare the performances of two algorithms, experimental data for Spacer-12h under the conditions of 0.1-0.3g excitation levels and 2 kg load mass is used for curve fit, using the model with parameters $k, k_3, k_5, c, a, \alpha$. For the method of least squares, the maximum number of function evaluations of 5×10^6 is verified to be adequate, otherwise premature solution may arise. Besides, to increase its efficiency by reducing the number of iterations involved and to broaden the search range, scaling factors for stiffness coefficients are used. With improper scaling factors, although a local minimum may be achieved, the RMSE obtained can be too large, an indication of under-fitting. After multiple tests, the scaling factors for the linear, cubic, quintic and seventh-order stiffness coefficients are chosen to be 10^4 , 10^{10} , 10^{16} and 10^{22} , in order to obtain an optimized

solution of model parameters.

Figure A.7 compares the RMSEs obtained by the method of least squares and by the jDE algorithm. Results show that the latter gives a smaller RMSE. Hence, the jDE algorithm is used as the default in Chapter 4, due to its improved efficiency and goodness of fit.

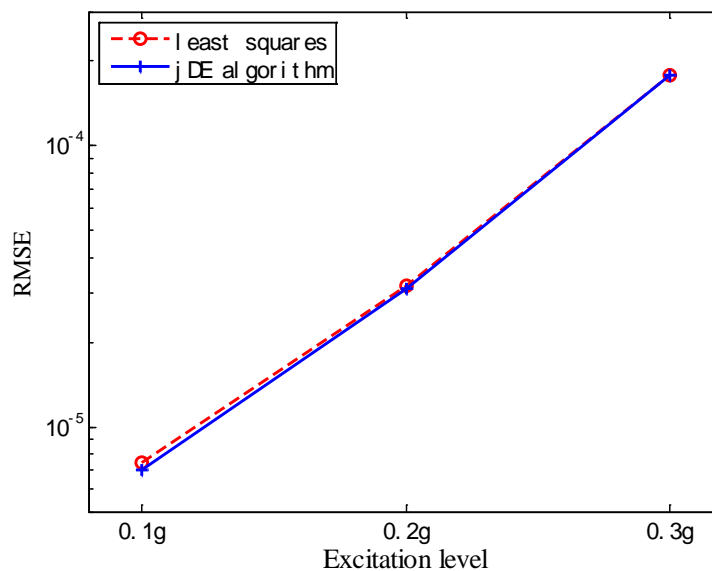


Figure A.7 RMSEs obtained by two algorithms.

For the asymmetric model, the method of least squares has an improved performance when the initial values of unknown model parameters are given not arbitrarily but by using parameter estimates from the jDE algorithm. This indicates the incapability of least squares method (hard to escape local minima), and also indicates the complexity of the solutions of data fitting using an asymmetric model. In fact, using the method of least squares for asymmetric models can be very tricky with regards to the initial value and the bounds, especially for the fractional order α . At times, the result equals the one obtained

by the jDE algorithm; at other times, the result can be much better than the initial values given by the jDE algorithm if the initial values are not good enough. This is the case when the fractional derivative term exists.

Appendix 5 The initial value of the fractional order α

In spite of the weaknesses of the method of least squares, it is a common and easy-to-use algorithm provided in the Optimization Toolbox in MATLAB. Its optimization performance is affected by the choice of initial values of the unknown model parameters. In order to check the dependence of parameter estimates and the RMSE on the initial value of the fractional order α_0 , Figure A.8 shows the results of curve fit for Spacer-12h under 0.3g excitation level and 2 kg load mass using the model with parameters $k, k_3, k_5, c, a, \alpha$ with α_0 varied, accurate to the first decimal. The bound of α is set as $0 \leq \alpha \leq 2$. The initial values for other model parameters are kept constant, i.e. $k_0 = 1$, $k_{3_0} = 1$, $k_{5_0} = 1$, $c_0 = 1$, and $a_0 = 1$.

Two kinds of parameter estimates are obtained. In Figure A.8(a), the fractional derivative coefficient a approximately equals zero and the viscous damping coefficient c is responsible for the damping of the system. Herein, the fractional derivative term $aD^\alpha x$ is redundant. In Figures A.8(b)-(f), in contrast, the viscous damping coefficient c approximately equals zero and the fractional derivative term $aD^\alpha x$ is responsible for the

damping of the system. Parameter estimates are similar for these five cases. Besides, as compared with the result in Figure A.8(a), i) the RMSE is much reduced, ii) the goodness of fit in the low-amplitude-low-frequency region of the curve has also evident improvement, and iii) the goodness of fit at the resonance peak is also slightly optimized. Herein, the fractional derivative term $aD^\alpha x$ is not redundant and it starts to exert its significance to the model.

It is noted that the currently used MaxIter (5×10^6) and MaxFunEvals (5×10^6) in the optimization procedure are sufficiently large, and the TolFun (10^{-20}) and TolX (10^{-18}) are sufficiently small for the trust-region-reflective algorithm to achieve a local minimum. The number of iterations is also below the threshold. Therefore, a reasonable explanation for obtaining different and unstable solutions of parameter estimates is the method of least squares itself, as it gives local optimization solutions.

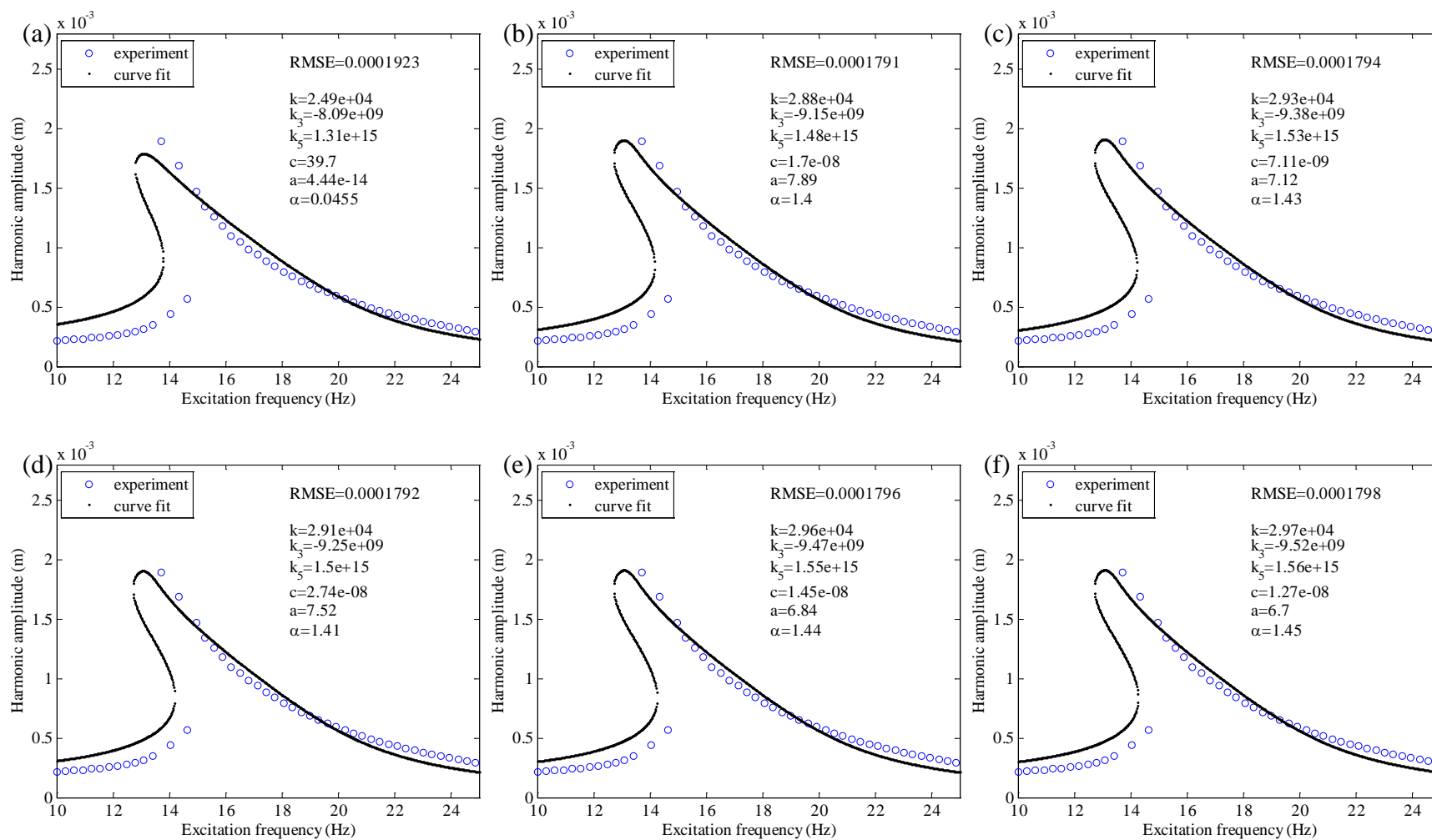


Figure A.8 RMSE depends on the initial value of α : (a) $\alpha_0 = 0.1$; (b) $\alpha_0 = 0.2$; (c) $\alpha_0 = 0.4$; (d) $\alpha_0 = 0.5$; (e) $\alpha_0 = 0.8$; (f) $\alpha_0 = 1.0$.

Appendix 6 The relative standard error (RSE)

As the physical meaning of the viscous damping term $c\dot{x}$ is overlapped with the fractional derivative term $aD^\alpha x$, the robustness of the model structure containing both terms should be examined. However, although the root mean square error (RMSE) is the statistical indicator of the goodness of fit for a model, this index cannot tell whether a model structure is robust or not. Instead, the relative standard error (RSE) is used.

As long as the data volume is sufficiently large, the relationship between the confidence interval (CI), the standard error (SE) and the relative standard error (RSE) has the form

$$\begin{cases} 95\% \text{ CI} = \bar{x} \pm 1.96 \cdot \text{SE} \\ \text{Relative standard error (RSE)} = \frac{\text{Standard error (SE)}}{\bar{x}} \end{cases}, \quad (\text{A.4})$$

where \bar{x} is the value of model parameter identified by data fitting. The 95% confidence interval for each model parameter was obtained using the `nlparci` command for the nonlinear least squares parameter estimates in MATLAB. Then, the RSE is obtained by applying the above relationship.

RMSEs and parameter estimates obtained using the models with parameters $k, k_3, k_5, c, a, \alpha$, k, k_3, k_5, c , and k, k_3, k_5, a, α for the conditions of 0.1-0.3g excitation levels and 2 kg load mass are shown in Figures A.9-A.11. The RSE for an individual model parameter is shown in percentages and given in parentheses following the value of parameter estimate. RSEs of all parameters for one model structure are also shown in one separate figure.

The model with the parameters k, k_3, k_5, c gives the worst prediction due to its largest RMSE. Apparently, adding the fractional derivative term $aD^\alpha x$ in the model improves the goodness of fit, but at the cost of large RSEs for parameters c , a and α . The viscous damping coefficient c becomes redundant for the 0.3g excitation level condition. Nevertheless, for the 0.1g and 0.2g excitation levels, the viscous damping coefficient c has helped improve the model by reducing the RMSE.

On the other hand, the linear stiffness coefficient k is limited to positive values during fitting. The RSE for k has increased due to the introduction of the fractional derivative term into the model. Furthermore, the RSEs for the cubic stiffness coefficient k_3 and the quintic stiffness coefficient k_5 are always relatively small, regardless of the model type. The negative value of k_3 characterizes the softening nonlinearity which relates to the resonance peak bent to the left. The positive value of k_5 accounts for the hardening nonlinearity in the elastic force-displacement relationship. When the excitation level is further increased to a sufficiently large magnitude, the resonance peak will bend to right.

In overall, the RSEs for stiffness coefficients maintain relatively small; while the RSEs for the damping component depends on model structure. The model with parameters $k, k_3, k_5, c, a, \alpha$ gives best fit but causes the largest RSEs.

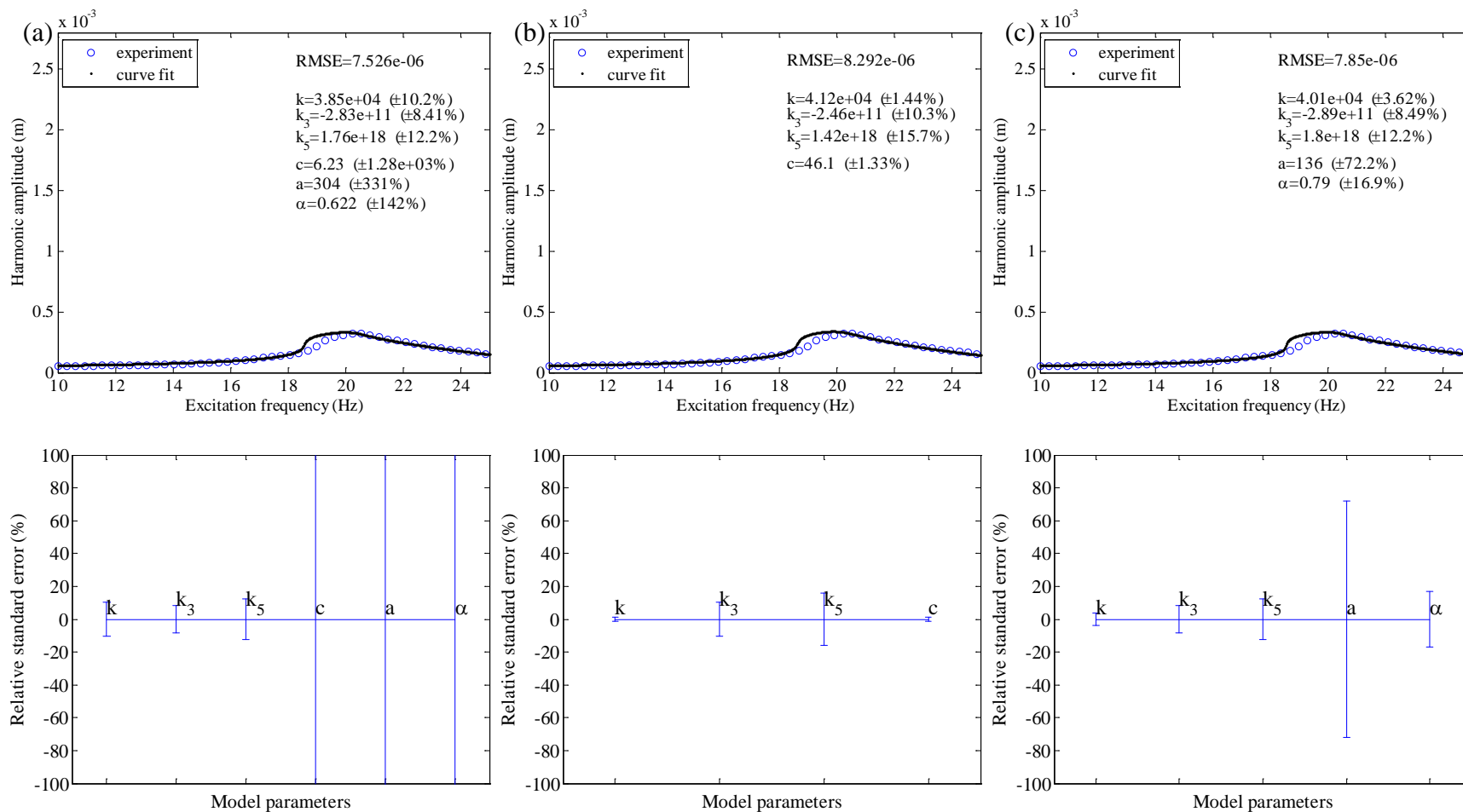


Figure A.9 RMSE and RSEs obtained using (a) the model with parameters $k, k_3, k_5, c, a, \alpha$; (b) the model with parameters k, k_3, k_5, c ; (c) the model with parameters k, k_3, k_5, a, α , for the 0.1g excitation level condition.

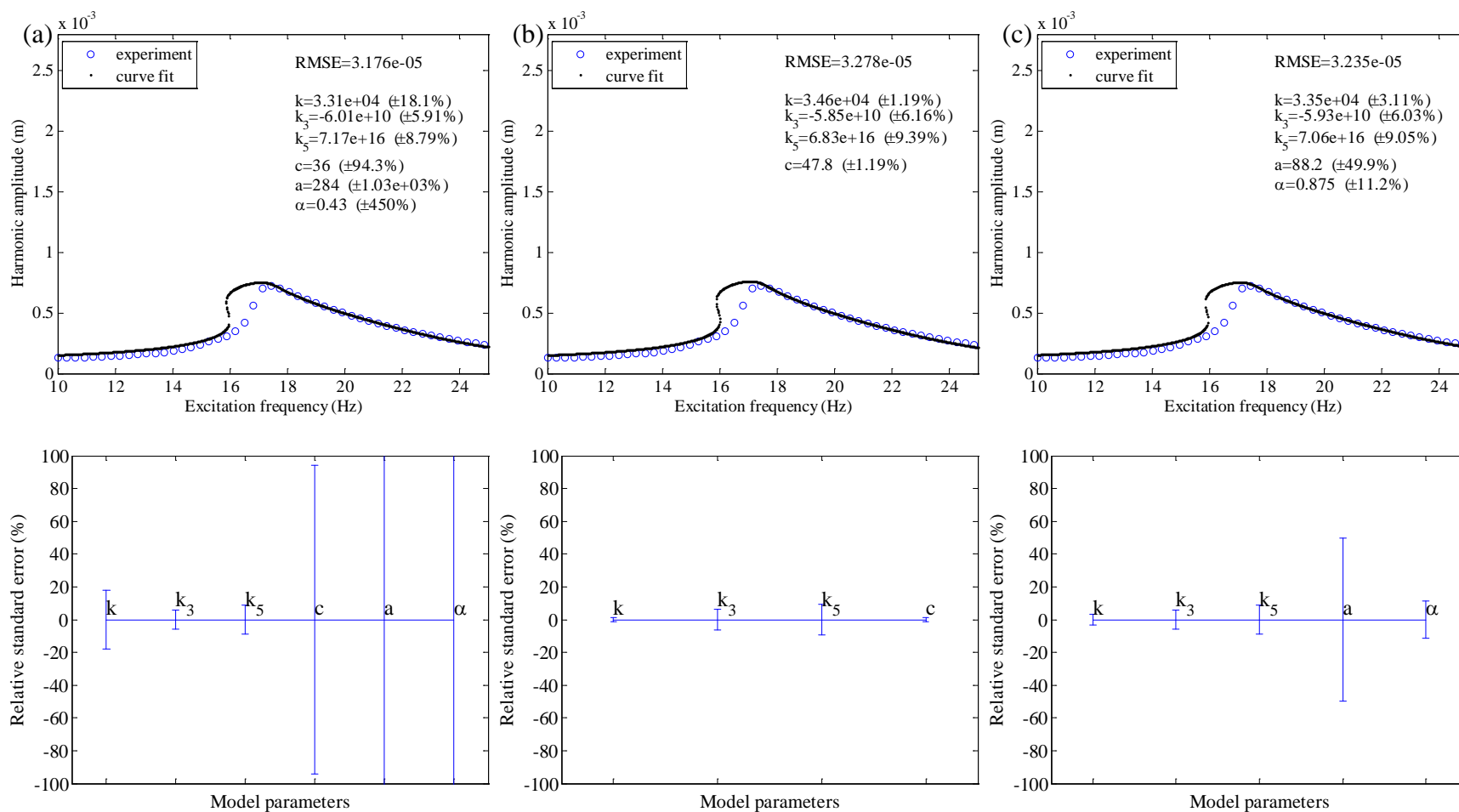


Figure A.10 RMSE and RSEs obtained using (a) the model with parameters $k, k_3, k_5, c, a, \alpha$; (b) the model with parameters k, k_3, k_5, c ; (c) the model with parameters k, k_3, k_5, a, α , for the 0.2g excitation level condition.

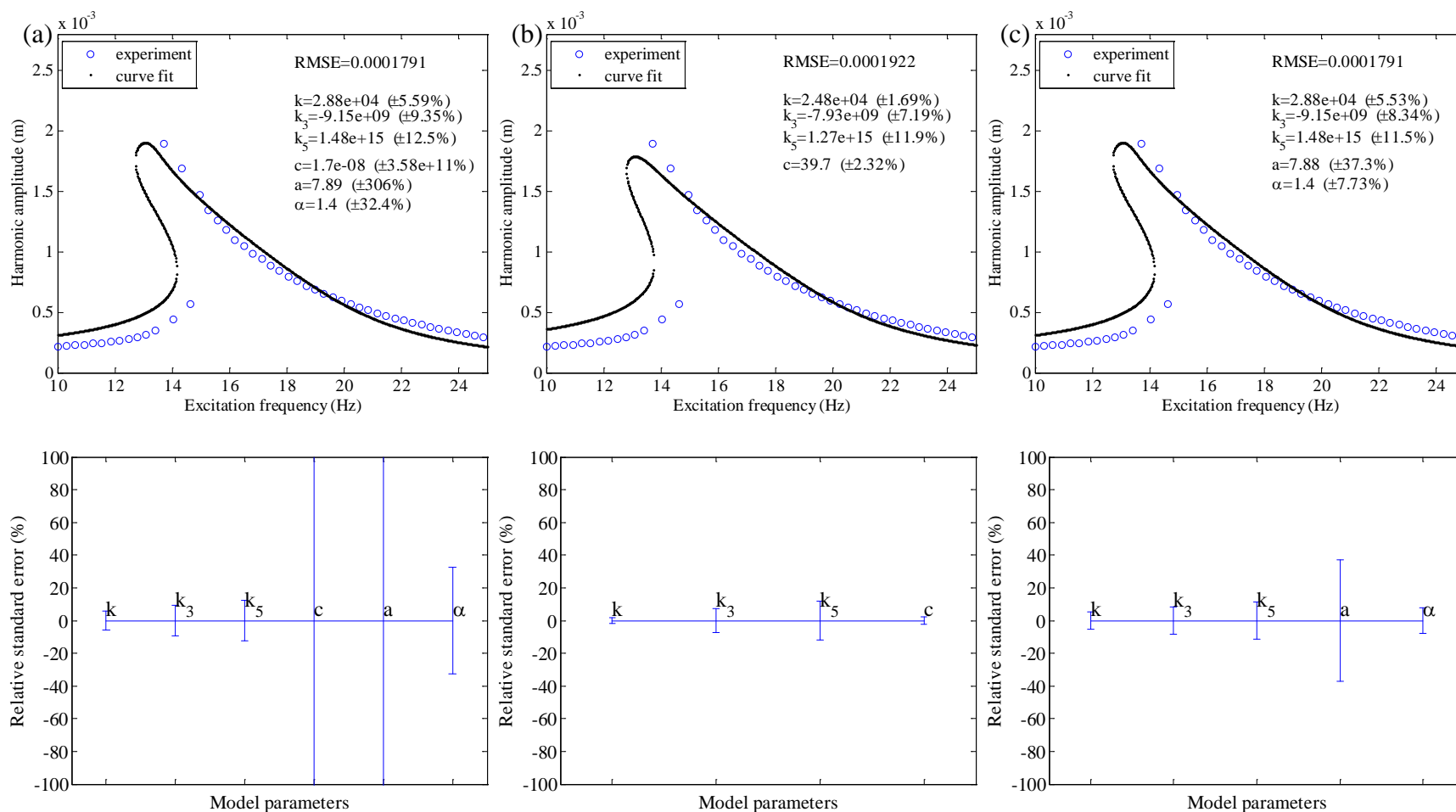


Figure A.11 RMSE and RSEs obtained using (a) the model with parameters $k, k_3, k_5, c, a, \alpha$; (b) the model with parameters k, k_3, k_5, c ; (c) the model with parameters k, k_3, k_5, a, α , for the 0.3g excitation level condition.

References

1. Arabzadeh F, Sheikhzadeh M, Ghane M, Hejazi SM and Arabzadeh F. Mathematical modeling of spacer fabrics under impulsive loading. *Journal of the Textile Institute*. 2012; 103: 1031-41.
2. Blaga M, Seghedin N-E and Ciobanu AR. Weft knitted spacer fabrics response to vibrations. *14th Autex World Textile Conference*, . Bursa, Turkey 2014.
3. Blaga M, Seghedin N-E and Ciobanu AR. Warp knitted fabrics behaviour under dynamic testing. *Industria Textilă*. 2013; 64: 334-41.
4. Liu Y and Hu H. Vibration isolation performance of warp-knitted spacer fabrics. *Fiber Society spring conference*, . Hong Kong 2011, p. 63-4.
5. Liu Y and Hu H. Vibration isolation behaviour of 3D polymeric knitted spacer fabrics under harmonic vibration testing conditions. *Polymer Testing*. 2015; 47: 120-9.
6. Walter TR, Richards AW and Subhash G. A unified phenomenological model for tensile and compressive response of polymeric foams. *Journal of Engineering Materials and Technology*. 2009; 131: 1-6.
7. Gao D and Lu F-d. Nonlinear dynamic analysis of series cushioning system made with expanded polyethylene and corrugated paperboard. *Advances in Mechanical Engineering*. 2013; 5: 816951.
8. Deng R, Davies P and Bajaj AK. Flexible polyurethane foam modelling and identification of viscoelastic parameters for automotive seating applications. *Journal of Sound and Vibration*. 2003; 262: 391-417.

9. Deng R. Modeling and characterization of flexible polyurethane foam. PhD Thesis. *Purdue University*. 2004.
10. Liu Y. A study of warp-knitted spacer fabrics as cushioning materials for human body protection. PhD Thesis. *The Hong Kong Polytechnic University*. 2013.
11. Pamuk G, Ceken F, Icten BM and Karakuzu R. Mechanical properties of spacer fabric-reinforced composites knitted from glass yarn. *Journal of Composite Materials*. 2011; 45: 1741-8.
12. Bruer SM, Powell N and Smith G. Three-Dimensionally Knit Spacer Fabrics: A Review of Production Techniques and Applications. *Journal of Textile and Apparel, Technology and Management*. 2005; 4: 1-29.
13. Anand S. Spacers - at the technical frontier. *Knitting International - Leicester*. 2003; 1305: 38-41.
14. Davies A and Williams J. The Use of spacer fabrics for absorbent medical applications. *Journal of Fiber Bioengineering and Informatics* 2009; 1: 321-30.
15. Onal L. Structure and applications of 3D Knitted Spacer Fabrics. *Textile Congress*. Istanbul 2004.
16. Roye A and Gries T. 3-D textiles for advanced cement based matrix reinforcement. *Journal of Industrial Textiles*. 2007; 37: 163-73.
17. Jiang G. Development and application of warp-knitted space fabric. *Shanghai Textile Science & Technology*. 2003; 31: 27-9.
18. Włodarczyk B and Kowalski K. Technology and Properties of Distance Five-layered Double-Weft-Knitted Fabrics with Elastomeric Threads. *Fibres & Textiles in Eastern Europe*. 2014; 22: 68-73.

19. Piekłak K and Mikołajczyk Z. Original Concept of a New Multicomb Warp-knitting Machine for Manufacturing Spatial Knitted Fabrics. *Fibres & Textiles in Eastern Europe*. 2009; 17: 76-80.
20. Dias T and Delkumburewatte GB. Analysis of water absorbency into knitted spacer structures. *The Journal of the Textile Institute*. 2010; 101: 143-53.
21. Heide M, Möhring U, Hänsel R, Stoll M, Wollina U and Heinig B. Antimicrobial-Finished Textile Three-Dimensional Structures. *Current Problems in Dermatology*. 2006; 33: 179-99.
22. Milosavljević S and Škundrić P. Contribution of textile technology to the development of modern compression bandages. *Chemical Industry and Chemical Engineering Quarterly*. 2007; 13: 88-102.
23. Bagherzadeh R, Montazer M, Latifi M, Sheikhzadeh M and Sattari M. Evaluation of comfort properties of polyester knitted spacer fabrics finished with water repellent and antimicrobial agents. *Fibers and Polymers*. 2007; 8: 386-92.
24. Wollina U, Heide M, Müller-Litz W, Obenauf D and Ash J. Functional textiles in prevention of chronic wounds, wound healing and tissue engineering. *Current Problems in Dermatology*. 2003; 31: 82-97.
25. Delkumburewatte GB and Dias T. Porosity and capillarity of weft knitted spacer structures. *Fibers and Polymers*. 2009; 10: 226-30.
26. Wollina U, Heide M and Swerev M. Spacer Fabrics—A Potential Tool in the Prevention of Chronic Wounds. *Exogenous Dermatology*. 2002; 1: 276-8.

-
27. Pereira S, Anand SC, Rajendran S and Wood C. A study of the Structure and Properties of Novel Fabrics for Knee Braces. *Journal of Industrial Textiles*. 2007; 36: 279-300.
28. Bartels VT. Thermal comfort of aeroplane seats: influence of different seat materials and the use of laboratory test methods. *Applied Ergonomics*. 2003; 34: 393-9.
29. Mao N and Russell SJ. The thermal insulation properties of spacer fabrics with a mechanically integrated wool fiber surface. *Textile Research Journal*. 2007; 77: 914-22.
30. Rajan TP, Souza LD, Ramakrishnan G and Zakriya GM. Comfort properties of functional warp-knitted polyester spacer fabrics for shoe insole applications. *Journal of Industrial Textiles*. Published online before print November 4, 2014, doi: 10.1177/1528083714557056.
31. Rajan TP, Souza LD, Ramakrishnan G, Kandhavadi P and Vigneswaran C. Influence of porosity on water vapor permeability behavior of warp knitted polyester spacer fabrics. *Journal of Industrial Textiles*. Published online before print June 25, 2014, doi: 10.1177/1528083714540697.
32. Tong S-f, Yip J, Yick K-l and Yuen C-wM. Exploring use of warp-knitted spacer fabric as a substitute for the absorbent layer for advanced wound dressing. *Textile Research Journal*. 2015; 85: 1258-68.
33. Morrissey MP and Rossi RM. The effect of metallisation, porosity and thickness on the thermal resistance of two-layer fabric assemblies. *Journal of Industrial Textiles*. 2015; 44: 912-23.

-
34. Montazer M and Jolaei MM. Novel spacer three-dimensional polyester fabric with β -cyclodextrin and butane tetra carboxylic acid. *The Journal of the Textile Institute*. 2010; 101: 165-72.
35. Onggar T, Shayed MA, Hund R-D and Cherif C. Silvering of three-dimensional polyethylene terephthalate textile material by means of wet-chemical processes. *Textile Research Journal*. 2015; 85: 658-70.
36. Yip J and Ng SP. Study of three-dimensional spacer fabrics: Molding properties for intimate apparel application. *Journal of Materials Processing Technology*. 2009; 209: 58-62.
37. Menges A. Integral Computational Design for Composite Spacer Fabric Structures. *eCAADe 27 - Session 09: Modes of Production*. Stuttgart University, Germany, 2009, p. 289-97.
38. Funke HL, Gelbrich S, Ehrlich A, Ulke-Winter L and Kroll L. Anisotropic fibre-reinforced plastics as formworks for single and double-curved textile reinforced concrete. *Journal of Materials Science Research*. 2015; 4: 36-45.
39. Funke HL, Gelbrich S, Ehrlich A, Ulke-Winter L and Kroll L. Unsymmetrical Fibre-Reinforced Plastics for the Production of Curved Textile Reinforced Concrete Elements. *Open Journal of Composite Materials*. 2014; 4: 191-200.
40. Berglin L and Zetterblom M. Textile Sound Structures. *Ambience08-International Scientific Conference*. 2-3 of June 2008.
41. Dias T, Monaragala R, Needham P and Lay E. Analysis of sound absorption of tuck spacer fabrics to reduce automotive noise. *Measurement Science and Technology*. 2007; 18: 2657-66.

-
42. Dias T, Monaragala R and Lay E. Analysis of thick spacer fabrics to reduce automobile interior noise. *Measurement Science and Technology*. 2007; 18: 1979-91.
43. Han F, Chen H, Zhang W, Lv T and Yang Y. Influence of 3D spacer fabric on drying shrinkage of concrete canvas. *Journal of Industrial Textiles*. Published online before print November 27, 2014, doi: 10.1177/1528083714562087.
44. Han F, Chen H, Jiang K, Zhang W, Lv T and Yang Y. Influences of geometric patterns of 3D spacer fabric on tensile behavior of concrete canvas. *Construction and Building Materials*. 2014; 65: 620-9.
45. Stegmaier T, Linke M and Planck H. Bionics in textiles: flexible and translucent thermal insulations for solar thermal applications. *Philosophical Transactions of the Royal Society A: Mathematical, Physical and Engineering Sciences*. 2009; 367: 1749-58.
46. Soin N, Shah TH, Anand SC, et al. Novel “3-D spacer” all fibre piezoelectric textiles for energy harvesting applications. *Energy & Environmental Science*. 2014; 7: 1670-9.
47. Wang Z and Hu H. A finite element analysis of an auxetic warp-knitted spacer fabric structure. *Textile Research Journal*. 2015; 85: 404-15.
48. Wang Z and Hu H. 3D auxetic warp-knitted spacer fabrics. *Physica Status Solidi (B)*. 2014; 251: 281-8.
49. Wang Z, Hu H and Xiao X. Deformation behaviors of three-dimensional auxetic spacer fabrics. *Textile Research Journal*. 2014; 84: 1361-72.
50. Ye X, Hu H and Feng X. Development of the warp knitted spacer fabrics for cushion applications. *Journal of Industrial Textiles*. 2008; 37: 213-23.

-
51. Ye X, Figueiro R, Hu H and de Araújo M. Application of warp-knitted spacer fabrics in car seats. *Journal of the Textile Institute*. 2007; 98: 337-44.
52. Ye X, Hu H and Feng X. An experimental investigation on the properties of the spacer knitted fabrics for pressure reduction. *Research Journal of Textile and Apparel*. 2005; 3: 52-7.
53. Liu Y and Hu H. Compression property and air permeability of weft-knitted spacer fabrics. *The Journal of the Textile Institute*. 2011; 102: 366-72.
54. Yip J and Chung LS. Study on the Physical Properties of Three-dimensional Spacer Fabrics.
55. Yip J and Ng SP. Study of three-dimensional spacer fabrics: Physical and mechanical properties. *Journal of Materials Processing Technology*. 2008; 206: 359-64.
56. Mecit D and Roye A. Investigation of a testing method for compression behavior of spacer fabrics designed for concrete applications. *Textile Research Journal*. 2009; 79: 867-75.
57. Armakan DM and Roye A. A study on the compression behavior of spacer fabrics designed for concrete applications. *Fibers and Polymers*. 2009; 10: 116-23.
58. Liu Y and Hu H. An Experimental Study of Compression Behavior of Warp-knitted Spacer Fabric. *Journal of Engineered Fibers and Fabrics*. 2014; 9: 61-9.
59. Supel B and Mikołajczyk Z. Model of the connector for 3D distance knitted fabric fastened by articulated joints. *Fibres & Textiles in Eastern Europe*. 2008; 16: 77-82.
60. Supel B and Mikołajczyk Z. Model of the Compressing Process of a One-and Two-Side Fastened Connector of a 3D Distance Knitted Fabric. *Fibres & Textiles in Eastern Europe*. 2008; 16: 44-8.

-
61. Supeł B and Mikołajczyk Z. Modelling the Process of the Compression of Distance Knitted Fabrics in the Aspect of 'Elastica Curves'. *Fibres & Textiles in Eastern Europe*. 2010; 18: 52-5.
62. Miao XH and Ge MQ. The compression behaviour of warp knitted spacer fabric. *Fibres & Textiles in Eastern Europe*. 2008; 16: 90-2.
63. Sheikhzadeh M, Ghane M, Eslamian Z and Pirzadeh E. A modeling study on the lateral compressive behavior of spacer fabrics. *Journal of the Textile Institute*. 2010; 101: 795-800.
64. Du Z and Hu H. A study of spherical compression properties of knitted spacer fabrics Part I: Theoretical analysis. *Textile Research Journal*. 2012; 82: 1569-78.
65. Köllner A and Völlmecke C. Analytical modelling of the in-plane compressive behaviour of pile fibres in Spacer Fabric Composites. *the Proceedings in Applied Mathematics and Mechanics*. Wiley Online Library, 2014, p. 197-8.
66. Liu Y and Hu H. Compressive mechanics of warp-knitted spacer fabrics. Part I: a constitutive model. *Textile Research Journal*. 2016; 86: 3-12.
67. Zhang LZ, Jiang GM, Miao XH and Cong HL. Three-dimensional Computer Simulation of Warp Knitted Spacer Fabric. *Fibres & Textiles in Eastern Europe*. 2012; 3: 56-60.
68. Piekłak K and Mikołajczyk Z. Spatial Model of the Structure of Warp-Knitted 3D Distance Fabrics. *Fibres & Textiles in Eastern Europe*. 2008; 5: 83-9.
69. Lee G, Rajendran S and Anand S. New single-layer compression bandage system for chronic venous leg ulcers. *British Journal of Nursing*. 2009; 18: S4-S18.

-
70. Vassiliadis S, Kallivretaki A, Psilla N, Provatidis C, Mecit D and Roye A. Numerical Modelling of the Compressional Behaviour of Warp-knitted Spacer Fabrics. *Fibres & Textiles in Eastern Europe*. 2009; 17: 56-61.
71. Kyosev Y and Renkens W. Computational mechanics models of warp knitted structures for tension and compression under small deformations. *IV European Conference on Computational Mechanics*. Palais des Congrès, Paris, France: ECCM, 2010.
72. Helbig FU. Gestaltungsmerkmale und mechanische Eigenschaften druckelastischer Abstandsgewirke. PhD Thesis. *Die Technische Universität Chemnitz* 2006.
73. Hou X, Hu H, Liu Y and Silberschmidt V. Nonlinear Compression Behavior of Warp-Knitted Spacer Fabric: Effect of Sandwich Structure. *Computers Materials and Continua*. 2011; 23: 119-34.
74. Hou X, Hu H and Silberschmidt V. A study of computational mechanics of 3D spacer fabric: factors affecting its compression deformation. *Journal of Materials Science*. 2012; 47: 3989-99.
75. Qian J, Miao X and Shen Y. Experimental Study and Simulation on Compression Character of Warp Knitted Spacer Fabrics. *Computers Materials and Continua*. 2012; 27: 179-88.
76. Brisa VJD, Helbig F and Kroll L. Numerical characterisation of the mechanical behaviour of a vertical spacer yarn in thick warp knitted spacer fabrics. *Journal of Industrial Textiles*. 2015; 45: 101-17.

-
77. Liu Y and Hu H. Finite element analysis of compression behaviour of 3D spacer fabric structure. *International Journal of Mechanical Sciences*. 2015; 94: 244-59.
78. Guo X, Long H and Zhao L. Investigation on the impact and compression-after-impact properties of warp-knitted spacer fabrics. *Textile Research Journal*. 2013; 83: 904-16.
79. Liu Y, Au WM and Hu H. Protective properties of warp-knitted spacer fabrics under impact in hemispherical form. Part I: Impact behavior analysis of a typical spacer fabric. *Textile Research Journal*. 2014; 84: 422-34.
80. Marques M, Terroso M, Freitas R, Marques AnT, Gabriel J and Simoes R. A procedure for a mechanical evaluation of an undefined osteo-protective material. *Accident Analysis & Prevention*. 2015; 75: 285-91.
81. Liu Y and Hu H. Compressive mechanics of warp-knitted spacer fabrics. Part II: a dynamic model. *Textile Research Journal*. 2015; 85: 2020-9.
82. Lu Z, Wu L, Gu B and Sun B. Numerical simulation of the impact behaviors of shear thickening fluid impregnated warp-knitted spacer fabric. *Composites Part B: Engineering*. 2015; 69: 191-200.
83. Winterflood J, Barber T and Blair DG. Using Euler buckling springs for vibration isolation. *Classical and Quantum Gravity*. 2002; 19: 1639-45.
84. Winterflood J, Blair DG and Slagmolen B. High performance vibration isolation using springs in Euler column buckling mode. *Physics Letters A*. 2002; 300: 122-30.
85. Virgin LN and Davis RB. Vibration isolation using buckled struts. *Journal of Sound and Vibration*. 2003; 260: 965-73.

-
86. Liu X, Huang X and Hua H. On the characteristics of a quasi-zero stiffness isolator using Euler buckled beam as negative stiffness corrector. *Journal of Sound and Vibration*. 2013; 332: 3359-76.
87. Friswell MI and Flores EIS. Dynamic isolation systems using tunable nonlinear stiffness beams. *The European Physical Journal Special Topics*. 2013; 222: 1563-73.
88. Shoup TE. Shock and vibration isolation using a nonlinear elastic suspension. *Aiaa Journal*. 1971; 9: 1643-5.
89. Yabuno H and Tsumoto K. Experimental investigation of a buckled beam under high-frequency excitation. *Archive of Applied Mechanics*. 2007; 77: 339-51.
90. Winterflood J. High performance vibration isolation for gravitational wave detection. PhD Thesis. *University of Western Australia*. 2001.
91. Winterflood J, Barber TA and Blair DG. Mathematical analysis of an Euler spring vibration isolator. *Physics Letters A*. 2002; 300: 131-9.
92. Chin EJ, Lee KT, Winterflood J, Ju L and Blair DG. Low frequency vertical geometric anti-spring vibration isolators. *Physics Letters A*. 2005; 336: 97-105.
93. Platus DL and Ferry DK. Negative-stiffness vibration isolation improves reliability of nanoinstrumentation. *Laser Focus World*. 2007; 43: 107.
94. Platus DL. Negative-stiffness-mechanism vibration isolation systems. In *SPIE's International Symposium on Optical Science, Engineering, and Instrumentation*. International Society for Optics and Photonics, 1999, p. 98-105.
95. Shahan D, Fulcher B, Seepersad CC, Haberman M and Wilson PS. Robust Design of Negative Stiffness Elements Fabricated by Selective Laser Sintering. *Proceedings of*

the 22nd Annual International Solid Freeform Fabrication Symposium—An Additive Manufacturing Conference. Austin, TX 2011.

96. Ahn HJ. Performance limit of a passive vertical isolator using a negative stiffness mechanism. *Journal of Mechanical Science and Technology*. 2008; 22: 2357-64.
97. Bažant ZP and Cedolin L. Stability of structures. *Elastic, inelastic, fracture and damage theories (1st ed)* Oxford University Press, New York. 1991.
98. Carrella A, Brennan MJ and Waters TP. Static analysis of a passive vibration isolator with quasi-zero-stiffness characteristic. *Journal of Sound and Vibration*. 2007; 301: 678-89.
99. Kovacic I, Brennan MJ and Waters TP. A study of a nonlinear vibration isolator with a quasi-zero stiffness characteristic. *Journal of Sound and Vibration*. 2008; 315: 700-11.
100. Carrella A, Brennan MJ, Kovacic I and Waters TP. On the force transmissibility of a vibration isolator with quasi-zero-stiffness. *Journal of Sound and Vibration*. 2009; 322: 707-17.
101. Carrella A, Brennan MJ and Waters TP. Optimization of a Quasi-Zero-Stiffness Isolator. *Journal of Mechanical Science and Technology*. 2007; 21: 946-9.
102. Carrella A, Brennan MJ, Waters TP and Shin K. On the design of a high-static–low-dynamic stiffness isolator using linear mechanical springs and magnets. *Journal of Sound and Vibration*. 2008; 315: 712-20.
103. Pasala DTR, Sarlis AA, Nagarajaiah S, Reinhorn AM, Constantinou MC and Taylor D. Adaptive Negative Stiffness: A New Structural Modification Approach for Seismic Protection. *Journal of Structural Engineering*. 2012; 139: 1112-23.

-
104. Le TD and Ahn KK. A vibration isolation system in low frequency excitation region using negative stiffness structure for vehicle seat. *Journal of Sound and Vibration*. 2011; 330: 6311-35.
105. Lee CM, Goverdovskiy VN and Temnikov AI. Design of springs with “negative” stiffness to improve vehicle driver vibration isolation. *Journal of Sound and Vibration*. 2007; 302: 865-74.
106. Lee CM and Goverdovskiy VN. A multi-stage high-speed railroad vibration isolation system with “negative” stiffness. *Journal of Sound and Vibration*. 2012; 331: 914-21.
107. Park ST and Luu TT. Techniques for optimizing parameters of negative stiffness. *Proceedings of the Institution of Mechanical Engineers, Part C: Journal of Mechanical Engineering Science*. 2007; 221: 505-10.
108. Robertson W, Cazzolato B and Zander A. Theoretical analysis of a non-contact spring with inclined permanent magnets for load-independent resonance frequency. *Journal of Sound and Vibration*. 2012; 331: 1331-41.
109. Zhou N and Liu K. A tunable high-static–low-dynamic stiffness vibration isolator. *Journal of Sound and Vibration*. 2010; 329: 1254-73.
110. Elías-Zúñiga A and Martínez-Romero O. Transient and Steady-State Responses of an Asymmetric Nonlinear Oscillator. *Mathematical Problems in Engineering*. 2013; 2013: 1-9.
111. Carrella A, Brennan MJ, Waters TP and Lopes V. Force and displacement transmissibility of a nonlinear isolator with high-static-low-dynamic-stiffness. *International Journal of Mechanical Sciences*. 2012; 55: 22-9.

-
112. Kalmár-Nagy T and Balachandran B. Forced harmonic vibration of a Duffing oscillator with linear viscous damping. *The Duffing Equation: Nonlinear Oscillators and their Behaviour*. 2011: 139-73.
113. Duffing G. *Erzwungene Schwingungen bei veränderlicher Eigenfrequenz und ihre technische Bedeutung*. No. 41-42. R, Vieweg & Sohn 1918.
114. Moon FC. Chaotic vibrations: an introduction for applied scientists and engineers. *Research supported by NSF, USAF, US Navy, US Army, and IBM New York, Wiley-Interscience*. 1987, p. 322.
115. Shen Y, Yang S, Xing H and Gao G. Primary resonance of Duffing oscillator with fractional-order derivative. *Communications in Nonlinear Science and Numerical Simulation*. 2012; 17: 3092-100.
116. Rega G, Benedettini F and Salvatori A. Periodic and chaotic motions of an unsymmetrical oscillator in nonlinear structural dynamics. *Chaos, Solitons & Fractals*. 1991; 1: 39-54.
117. Sheu L-J, Chen H-K, Chen J-H and Tam L-M. Chaotic dynamics of the fractionally damped Duffing equation. *Chaos, Solitons & Fractals*. 2007; 32: 1459-68.
118. Cao J, Ma C, Xie H and Jiang Z. Nonlinear dynamics of duffing system with fractional order damping. *Journal of Computational and Nonlinear Dynamics*. 2010; 5: 041012.
119. El-Sayed AMA, El-Raheem ZFE and Salman SM. Discretization of forced Duffing system with fractional-order damping. *Advances in Difference Equations*. 2014; 2014: 1-12.

-
120. Carrella A, Brennan MJ and Waters TP. Force transmissibility of a nonlinear vibration isolator with high-static-low-dynamic-stiffness. *6th EUROMECH Nonlinear Dynamics Conference* Saint Petersburg, Russia 2008.
121. Milovanovic Z, Kovacic I and Brennan MJ. On the displacement transmissibility of a base excited viscously damped nonlinear vibration isolator. *Journal of Vibration and Acoustics*. 2009; 131: 054502.
122. Le TD and Ahn KK. Experimental investigation of a vibration isolation system using negative stiffness structure. *International Journal of Mechanical Sciences*. 2013; 70: 99-112.
123. Huang X, Liu X, Sun J, Zhang Z and Hua H. Vibration isolation characteristics of a nonlinear isolator using Euler buckled beam as negative stiffness corrector: A theoretical and experimental study. *Journal of Sound and Vibration*. 2014; 333: 1132-48.
124. Huang X, Liu X and Hua H. On the characteristics of an ultra-low frequency nonlinear isolator using sliding beam as negative stiffness. *Journal of Mechanical Science and Technology*. 2014; 28: 813-22.
125. Kovacic I, Brennan MJ and Lineton B. On the resonance response of an asymmetric Duffing oscillator. *International Journal of Non-Linear Mechanics*. 2008; 43: 858-67.
126. Kovacic I and Brennan MJ. Forced harmonic vibration of an asymmetric Duffing oscillator. *The Duffing Equation: Nonlinear Oscillators and their Behaviour*. 2011: 277-322.
127. Mayoof FN and Hawwa MA. Chaotic behavior of a curved carbon nanotube under harmonic excitation. *Chaos, Solitons & Fractals*. 2009; 42: 1860-7.

-
128. Friswell MI, Ali SF, Bilgen O, Adhikari S, Lees AW and Litak G. Non-linear piezoelectric vibration energy harvesting from a vertical cantilever beam with tip mass. *Journal of Intelligent Material Systems and Structures*. 2012; 23: 1505-21.
129. Ghayesh MH and Amabili M. Nonlinear dynamics of axially moving viscoelastic beams over the buckled state. *Computers & Structures*. 2012; 112: 406-21.
130. Somnay RJ and Ibrahim RA. Nonlinear dynamics of a sliding beam on two supports under sinusoidal excitation. *Sadhana*. 2006; 31: 383-97.
131. Busby HR and Weingarten VI. Non-linear response of a beam to periodic loading. *International Journal of Non-Linear Mechanics*. 1972; 7: 289-303.
132. Ravindra B and Mallik AK. Performance of non-linear vibration isolators under harmonic excitation. *Journal of Sound and Vibration*. 1994; 170: 325-37.
133. Kadji HGE, Orou JBC and Wofo P. Regular and chaotic behaviors of plasma oscillations modeled by a modified Duffing equation. *Physica Scripta*. 2008; 77: 025503.
134. Kovacic I, Brennan MJ and Lineton B. Effect of a static force on the dynamic behaviour of a harmonically excited quasi-zero stiffness system. *Journal of Sound and Vibration*. 2009; 325: 870-83.
135. Benedettini F, Rega G and Salvatori A. Prediction of bifurcations and chaos for an asymmetric elastic oscillator. *Chaos, Solitons & Fractals*. 1992; 2: 303-21.
136. Virgin LN. On the harmonic response of an oscillator with unsymmetric restoring force. *Journal of Sound and Vibration*. 1988; 126: 157-65.
137. Yang JH and Zhu H. Vibrational resonance in Duffing systems with fractional-order damping. *Chaos: An Interdisciplinary Journal of Nonlinear Science*. 2012; 22: 013112.

-
138. Bagley RL and Torvik PJ. A theoretical basis for the application of fractional calculus to viscoelasticity. *Journal of Rheology*. 1983; 27: 201-10.
139. Ge Z-M and Ou C-Y. Chaos synchronization of fractional order modified duffing systems with parameters excited by a chaotic signal. *Chaos, Solitons & Fractals*. 2008; 35: 705-17.
140. Eldred LB, Baker WP and Palazotto AN. Kelvin-Voigt versus fractional derivative model as constitutive relations for viscoelastic materials. *AIAA journal*. 1995; 33: 547-50.
141. Wei Z and Shimizu N. Numerical Algorithm for Dynamic Problems Involving Fractional Operators. *JSME International Journal Series C*. 1998; 41: 364-70.
142. Shokooh A and Suárez L. A comparison of numerical methods applied to a fractional model of damping materials. *Journal of Vibration and Control*. 1999; 5: 331-54.
143. Barbosa RS, Machado JAT, Vinagre BM and Calderon AJ. Analysis of the Van der Pol oscillator containing derivatives of fractional order. *Journal of Vibration and Control*. 2007; 13: 1291-301.
144. Xue D and Chen Y. *Solving applied mathematical problems with MATLAB*. CRC Press, 2008.
145. Koh CG and Kelly JM. Application of fractional derivatives to seismic analysis of base-isolated models. *Earthquake Engineering & Structural Dynamics*. 1990; 19: 229-41.
146. Failla G and Pirrotta A. On the stochastic response of a fractionally-damped Duffing oscillator. *Communications in Nonlinear Science and Numerical Simulation*. 2012; 17: 5131-42.

-
147. Ge Z-M and Ou C-Y. Chaos in a fractional order modified Duffing system. *Chaos, Solitons & Fractals*. 2007; 34: 262-91.
148. Ogam G, Groby J-P and Ogam E. A non-linear vibration spectroscopy model for structures with closed cracks. *International Journal of Non-Linear Mechanics*. 2014; 59: 60-8.
149. Dal F. Multiple time scales solution of an equation with quadratic and cubic nonlinearities having fractional-order derivative. *Mathematical and Computational Applications*. 2011; 16: 301-8.
150. Abolfathi A. Nonlinear vibration isolators with asymmetric stiffness. PhD Thesis. *University of Southampton*. 2012.
151. Oustaloup A. La commande CRONE, Commande robuste d'ordre non entier, Hermes (Traité des Nouvelles Technologies-Série Automatique), Paris. ISBN 2-86601-289-5, 1991.
152. Oustaloup A, Levron F, Mathieu B and Nanot FM. Frequency-band complex noninteger differentiator: characterization and synthesis. *Circuits and Systems I: Fundamental Theory and Applications, IEEE Transactions on*. 2000; 47: 25-39.
153. Brest J, Greiner S, Boskovic B, Mernik M and Zumer V. Self-adapting control parameters in differential evolution: A comparative study on numerical benchmark problems. *Evolutionary Computation, IEEE Transactions on*. 2006; 10: 646-57.
154. Zhang J and Sanderson AC. JADE: adaptive differential evolution with optional external archive. *Evolutionary Computation, IEEE Transactions on*. 2009; 13: 945-58.